Department
Chemie und Pharmazie

Friedrich-Alexander-Universität
Naturwissenschaftliche Fakultät

Adsorption Dynamics of Hydrocarbons on Ionic Liquid Interfaces Studied by Molecular Beam Techniques

Adsorptionsdynamik von Kohlenwasserstoffen auf Grenzflächen Ionischer Flüssigkeiten untersucht mittels Molekularstrahltechniken

Der Naturwissenschaftlichen Fakultät
der Friedrich-Alexander-Universität Erlangen-Nürnberg

zur Erlangung des Doktorgrades Dr. rer. nat.

vorgelegt von
LEONHARD WINTER
aus Nürnberg

Als Dissertation genehmigt von der Naturwissenschaftlichen Fakultät
der Friedrich-Alexander-Universität Erlangen-Nürnberg

Tag der mündlichen Prüfung: 16.10.2023

Vorsitzender des Promotionsorgans: Prof. Dr. Wolfgang Achtziger

Gutachter:
Prof. Dr. Hans-Peter Steinrück
Prof. Dr. Peter Wasserscheid
Prof. Dr. Hans-Joachim Freund (Fritz-Haber-Institut, Berlin)

Table of Contents

Published Papers

[P1] **On the Dynamic Interaction of *n*-Butane with Imidazolium-Based Ionic Liquids**

R. G. Bhuin, L. Winter, M. Lexow, F. Maier, H.-P. Steinrück

Angew. Chem. Int. Ed. **2020**, *59*, 14429-14433

Die Dynamische Wechselwirkung von *n*-Butan mit Imidazolium-Basierten Ionischen Flüssigkeiten

R. G. Bhuin, L. Winter, M. Lexow, F. Maier, H.-P. Steinrück

Angew. Chem., **2020**, *132*, 14536-14541

The author’s contributions are the molecular beam measurements, data analysis and interpretation, preparation of the figures and translation into German.

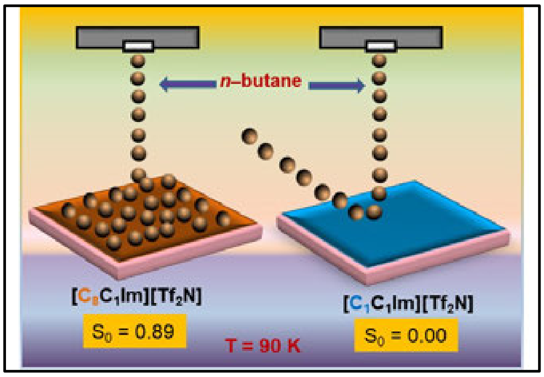

[P2] **On the Adsorption of *n*-Butane on Alkyl Imidazolium Ionic Liquids with Different Anions Using a New Molecular Beam Setup**

L. Winter, R. G. Bhuin, M. Lexow, F. Maier, H.-P. Steinrück

J. Chem. Phys., **2020**, *153*, 214706

The author’s contributions are the molecular beam measurements, data analysis and interpretation, preparation of the figures and writing of the original draft.

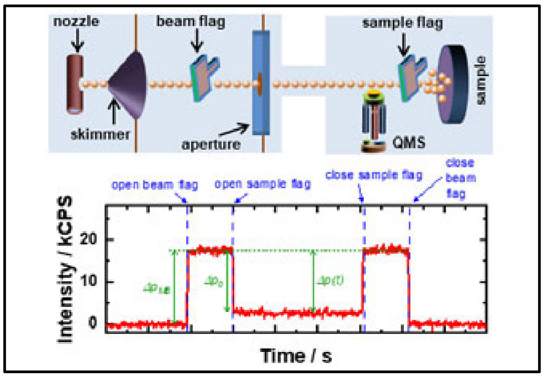

[P3] *n*-Butane, *iso*-Butane and 1-Butene Adsorption on Imidazolium-Based Ionic Liquids Studied with Molecular Beam Techniques

L. Winter, R. G. Bhuin, F. Maier, H.-P. Steinrück

Chem. Eur. J., **2021**, *27*, 17059-17065

The author's contributions are the molecular beam measurements, data analysis and interpretation, preparation of the figures and writing of the original draft.

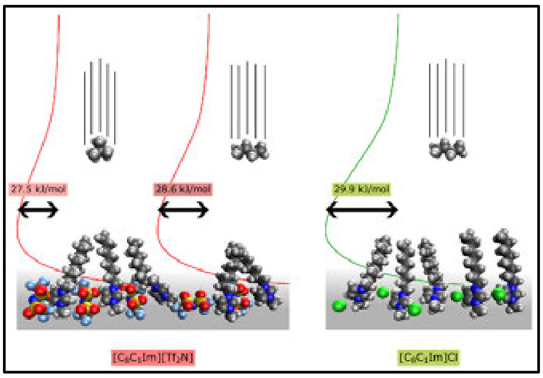

[P4] Tailoring the Selectivity of 1,3-Butadiene versus 1-Butene Adsorption on Pt(111) by Ultrathin Ionic Liquid Films

L. Winter, S. Trzeciak, C. C. Fernández, S. Massicot, T. Talwar, F. Maier, D. Zahn, H.-P. Steinrück

ACS Catal., **2023**, *13*, 10866-10877

The author's contributions are the molecular beam and XPS measurements, molecular beam and XPS data analysis and interpretation, preparation of the figures (except Figure 5) and writing of the original draft.

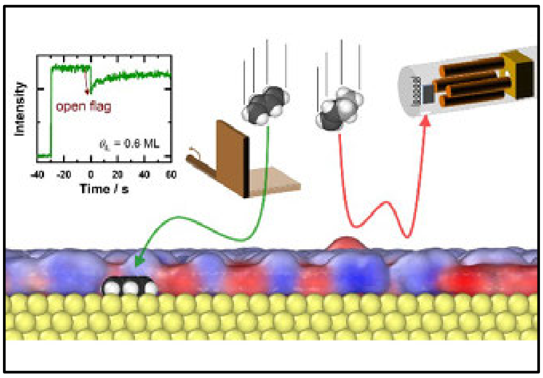

Acknowledgment/Danksagung

Niemand schreibt seine Dissertation ohne die Unterstützung anderer. Deshalb möchte ich mich bei einer ganzen Reihe an Personen herzlichst bedanken.

An erster Stelle natürlich bei Prof. Dr. Hans-Peter Steinrück, der mir die Möglichkeit gegeben hat, meine Doktorarbeit an seinem Lehrstuhl und in seiner Gruppe zu schreiben. Eine Gruppe, in der man einige Freiheiten und Möglichkeiten (Stichwort Finanzierung) hat. Seine Expertise und Erfahrung mit Oberflächen, ILs, XPS und Molekularstrahlen kommt einem manchmal fast unheimlich vor. Dabei waren die Diskussionen immer konstruktiv und ich habe so einiges gelernt. Dank gebührt ihm auch für die Gespräche über meine persönliche berufliche Zukunft in letzter Zeit.

Ein besonderer Dank gilt auch Dr. Florian Maier, der sich als Leiter der IL-Gruppe in einem für den akademischen Mittelbau nicht selbstverständlichen Maße in die Forschung einbringt, d.h. bei den oben erwähnten konstruktiven Diskussionen immer mit eigenen Ideen dabei war. Auch in der für uns alle nicht ganz einfachen Pandemiezeit, war es hauptsächlich er, der den Umgang damit am Lehrstuhl gemanagt hat.

Other special thanks also to Dr. Radha Gobinda Bhuin, who shared his newly built vacuum chamber with me. Working together was always uncomplicated and a joy and I appreciate the trust he put into a UHV greenhorn like me.

Of course another special thanks to Dr. Cynthia C. Fernández, who brought a lot of Latin vibes and fun to the lab after I was working alone for about two years (most of it under COVID conditions); also her scientific input into the latest project should not be underestimated, and I am glad I can put the ILID chamber into her safe hands. I also want to thank her and Timo Talwar for printing and submitting my thesis while I was on a conference and on vacation in the United States.

Danke auch an alle weiteren Mitglieder der IL-Gruppe, Dr. Matthias Lexow, Dr. Bettina Heller, Dr. Sunghwan Shin, Dr. Francesco Greco, Dr. Manuel Meusel, Dr. Ulrike Paap, Dr. Simon Jaekel, Dr. Jade Barreto, Stephen Massicot, Timo Talwar, Afra Gezmis, Daniel Hemmeter und Rajan Adhikari, für die angenehme Arbeitsatmosphäre und dass man sich immer Materialen oder helfende Hände ausleihen konnte.

Ein großer Dank gebührt auch Bernd Kreß und Hans-Peter Bäumler, die mit ihrer Erfahrung, ihrem Werkzeug und ihren magischen Händen alle technischen Probleme lösen können. Bernd Kreß war auch federführend für das Design, die Planung und die Installation der ILID-Kammer verantwortlich; Hans-Peter Bäumler für die Organisation und Installation des elektronischen Zubehörs. Ihr Beitrag zum sozialen Zusammenhalt am Lehrstuhl und dem Gelingen der Feiern sollte an der Stelle auch erwähnt sein.

Ein weiterer Dank allen, die den Lehrstuhl am Laufen halten: Der akademische Oberrat Dr. Andreas Bayer, die Sekretärinnen Susana Kreß und Andrea Meixner-Wolf, das Werkstattteam unter der Leitung von Friedhold Wölfel, die Praktikumsteams mit Dorjkhand Rudolph, Corinne Wiegner, Sebastian Heiß, Andrea Buchner, Gertrud Weiß und Martin Kolacyak und die IT-Betreuung durch Norman Anja Schmidt.

Ebenso möchte ich allen weiteren Mitgliedern des Lehrstuhls für die schöne Zeit danken. Besonders Michael Moritz für die unkomplizierte und kollegiale gemeinsame Betreuung des XPS-Versuchs. Und auch Prof. Dr. Christian Papp und Dr. Ole Lytken für die anregenden Diskussionen im Lehrstuhlseminar.

Ein weiterer Dank auch an meine Kooperationspartner vom CCC, Prof. Dr. Dirk Zahn und Simon Trzeciak, die sich auf mein Projekt eingelassen haben und innerhalb sehr kurzer Zeit anspruchsvolle Simulationen umgesetzt haben.

Dankeschön auch an Dr. Nicola Taccardi, Dr. Julian Mehler und Daniel Kremitzl vom CRT für die Synthese von ILs.

Zu guter Letzt gilt ein Dank natürlich auch meiner Familie und meinen Freunden für die Unterstützung außerhalb der Wissenschaft.

1 Introduction

Ionic Liquids (ILs) are a class of compounds consisting solely of cations and anions, while at the same time possessing a low melting point. Many ILs are even liquid below room temperature.[1-2] Although substances fulfilling this definition are known for more than a century,[3] the scientific field of "ionic liquids" only started to develop in the 1990s[4-5]. In the beginning, ILs were seen as "green" alternatives for conventional bulk chemicals,[6-8] like solvents,[9-11] electrolytes,[12-15] lubricants[16-17] or scavengers[18-20]. Due to their tunable physicochemical properties, they also have been adapted to more specific applications, for example, sensors,[21-22] lubricant additives,[23] pharmaceuticals,[24-26] or in catalysis[27-32]. These applications fully exploit their potential using only small amounts, so the environmental footprint is acceptable, even if the "green" label for ILs came increasingly under debate in recent years.[33-39]

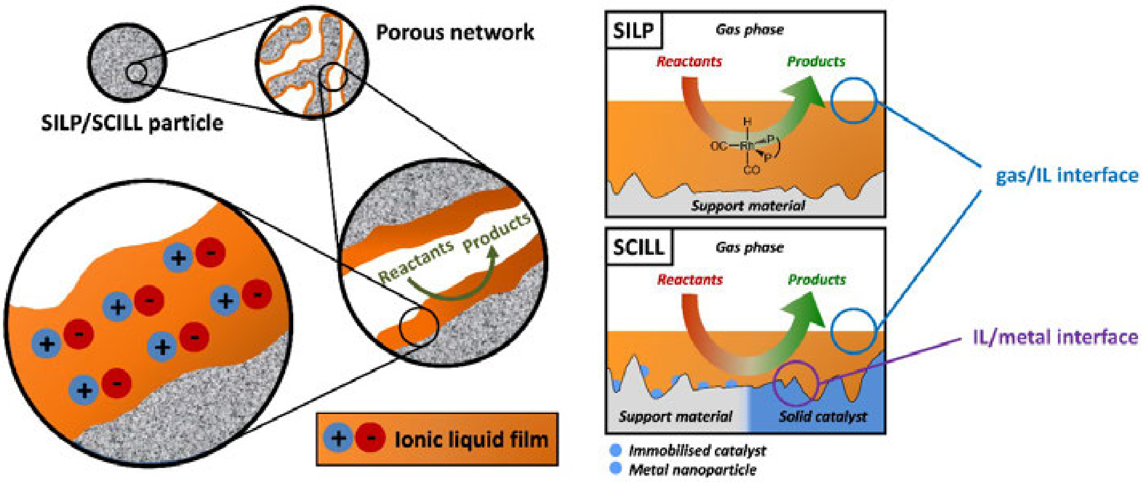

Figure 1.1: For catalysis, thin IL films can be immobilized on a porous support. In SILP systems, a homogenous catalyst is dissolved inside of the IL, in SCILL systems, the catalytically active site is located at the IL/metal interface of a solid catalyst (particle). The transfer of reactant and product molecules across the gas/IL interface is crucial for both approaches. Adapted with permission from Ref[40].

In catalysis, ILs can be used as bulk solvents in a biphasic approach, but also in smaller amounts as thin layers on porous supports (see Figure 1.1).[30-31] From a practical point of view, these heterogeneous systems can be handled like traditional supported solid catalysts, which facilitates adaptation to existing reactors and product-catalyst separation eventually paving the way to commercial applications.[41-42] Two conceptually different approaches can be distinguished: In Supported Ionic Liquid Phase (SILP) catalysis,[43] an originally homogenous catalyst – typically a metal complex – is dissolved in an IL phase immobilized on an inert porous support, which increases the mobile phase/IL interface area and simplifies product separation.[30-31, 44-45] In the Solid Catalyst with Ionic Liquid Layer (SCILL) approach,[46] a traditional heterogeneous catalyst, often metal nanoparticles dispersed on a support, is modified by a thin IL film.[30-31, 47]

Typically, SCILL is used to improve the selectivity of hydrogenation reactions,[46-48] for example the 1,3-butadiene hydrogenation to produce 1-butene.[49-52] In the industrial application of this reaction, the 1,3-butadiene content of 1-butene streams must be pushed to < 5 ppm, without the formation of too many byproducts, mainly *n*-butane.[53-56] Different solubility of the competing reactants in the IL film was proposed to be responsible for the SCILL effect in the earlier literature.[46-47] However, the selectivity of SCILL-catalysts can be larger than explainable by taking into account only solubility differences.[50] Moreover, the onset of the SCILL effect is already observable for only minor amounts of IL used in the catalyst preparation, far less than is needed for the formation of a three-dimensional IL phase.[50] Therefore, the SCILL effect is nowadays often attributed to site blocking and/or ligand effects of the IL ions interacting with the catalyst and/or the reactants in the vicinity of the IL/solid interface. Despite different concepts, however, a thorough understanding of the SCILL effect is still lacking.[48, 50, 57-58]

In this context, understanding and controlling the properties of the IL/metal interface is thus highly desired. Molecular-level insights can be gained by studying suitable model systems, especially ultrathin IL films on metal substrates prepared by physical vapor deposition (PVD).[59] These surface science studies under ultra-high vacuum (UHV) conditions revealed surprising growth,[60-61] wetting[62-64] and exchange[65-67] phenomena, along with unexpected structural changes[68] and reactions with the metal surface[68-71]. Furthermore, also the mass transfer across the gas/IL interface plays a crucial role in the SCILL and SILP systems. Therefore, the structure of the vacuum/IL interface has been thoroughly investigated using different surface science techniques like X-ray reflectivity[72-73], direct recoil spectrometry[74-75], Rutherford backscattering[75-76], low energy ion scattering[77-78], reactive atom scattering[79-80], sum frequency generation vibrational spectroscopy,[81-82] X-ray photoelectron spectroscopy (XPS)[40, 83-89] and molecular dynamics simulations[90-92]. In this way, a rather comprehensive picture of the static properties of the vacuum/IL interface has been achieved.

In contrast, the interaction dynamics of gas molecules with the gas/IL interface has only been investigated for selected examples: In a molecular beam study of CO_2 scattering from imidazolium-based IL surfaces at room temperature, two distinctive pathways could be deconvoluted – trapping/desorption (TD) and inelastic scattering (IS). In particular, it was found that with increasing alkyl chain length and decreasing anion size, the probability for the TD pathway increases.[93-94] NO scattering shows similar trends as CO_2, and moreover interesting rotational, vibrational and electronic effects, because of its uncommon open-shell electronic structure.[95-96] Oxygen atoms can be scattered inelastically and/or reactively forming OH and H_2O from pyrrolidinium- and imidazolium-based ILs. For both cation classes, the probability of reactive scattering increases with increasing alkyl chain length and decreasing anion size.[79, 97-99] Moreover, on frozen $[C_2C_1Im][Tf_2N]$ and $[C_8C_1Im][BF_4]$, water adsorbs with an initial trapping probability close to zero, which then increases with increasing water coverage.[100]

The work presented in this thesis are – to the best of my knowledge – the first studies on the dynamic interactions of IL interfaces with gaseous hydrocarbons, the most common feedstock in SCILL and SILP applications.[30-31] Chapter 4.1 will describe the dynamics of hydrocarbon trapping on gas/IL interfaces and how it is influenced by the structure of the cation, anion and hydrocarbon. Chapter 4.2 will then discuss how the interaction strength between the hydrocarbon and the IL interface, i.e. the desorption energy, can be quantified. The results of this analysis will be correlated with the IL surface structure in Chapter 4.3. Finally, Chapter 4.4 will address the dynamics of hydrocarbon sticking at the gas/IL/metal interface, which is considered to be a model system for a SCILL catalyst. The results presented in this work are the first ones obtained with a new molecular beam setup specifically dedicated to the investigation of Ionic Liquid Interface Dynamics (ILID). Since the construction of components, commissioning and characterization of the new ILID machine was a part of this thesis, the experimental details will be thoroughly discussed in Chapter 3.

2 Fundamentals

2.1 Molecular Beam Techniques

2.1.1 Fundamentals of Molecular Beams

First described by Louis Dunoyer in 1911[101] and a few years later implemented in the Nobel-prize-winning studies of Otto Stern and Walther Gerlach,[102] molecular beams are almost as old as vacuum technology.[103] They are essentially formed by a controlled "leak", that is, via the expansion of a gas through a small opening into vacuum. In contrast to ion beams, molecular beams consist of uncharged molecules, moving in a spatially directed fashion in a collision-free environment.[104]

Molecular beams can be divided into two classes: effusive beams (also known as thermal or Knudsen beams) and supersonic beams (sometimes called free jets).[105] In the simplest setup, effusive beams are generated by the effusion of a gas from a heated oven through a small orifice. For effusive beams, the Knudsen number discriminating the two beam conditions, $Kn = \lambda/d$ (λ: mean free path of the molecules, d: diameter of the orifice), is considerably larger than one. Therefore, after leaving the oven, the gas molecules no longer collide with each other. As a consequence, the Maxwell-Boltzmann distribution remains the same as initially in the Knudsen cell.[106]

Since the focus of this thesis is on supersonic molecular beams, the related background will be described in more detail in the following. For supersonic beams, Kn is much smaller than one, i.e., a lot of collisions between molecules occur during beam formation. To generate such a beam, a gas is allowed to flow from a stagnation tube with higher pressure p_0 through a nozzle into a chamber of lower pressure p_b. If p_0/p_b is larger than $\left(\frac{\gamma+1}{2}\right)^{\frac{\gamma}{\gamma-1}}$ (which is < 2.1 for all gases),[107] the gas molecules accelerate to supersonic speed and a complex shock wave structure forms at a certain distance from the nozzle.[108] In molecular beam setups, the formation of these shock waves is omitted by extracting the molecular beam with a skimmer (a conical-formed aperture) placed at a short distance from the nozzle (see Figure 2.1a). Since heat transfer during the expansion process is usually negligible, the beam formation can be treated as an adiabatic, isentropic expansion.[107] Therefore, the sum of enthalpy and (directed) kinetic energy remains constant:

$$h + \frac{Mv^2}{2} = h_0 = const. \tag{2.1}$$

Thereby, h is the molar enthalpy, M the molar mass, v the velocity of the (directed) mass flow and h_0 the molar enthalpy before the expansion. During the expansion, energy is efficiently transferred through collisions from the internal energy (undirected kinetic, rotational and vibrational energy) into directed kinetic energy. With increasing distance to the nozzle, the velocity of the gas molecules in the propagation direction increases quickly, while at the same time their temperature decreases (see Figure 2.1b).

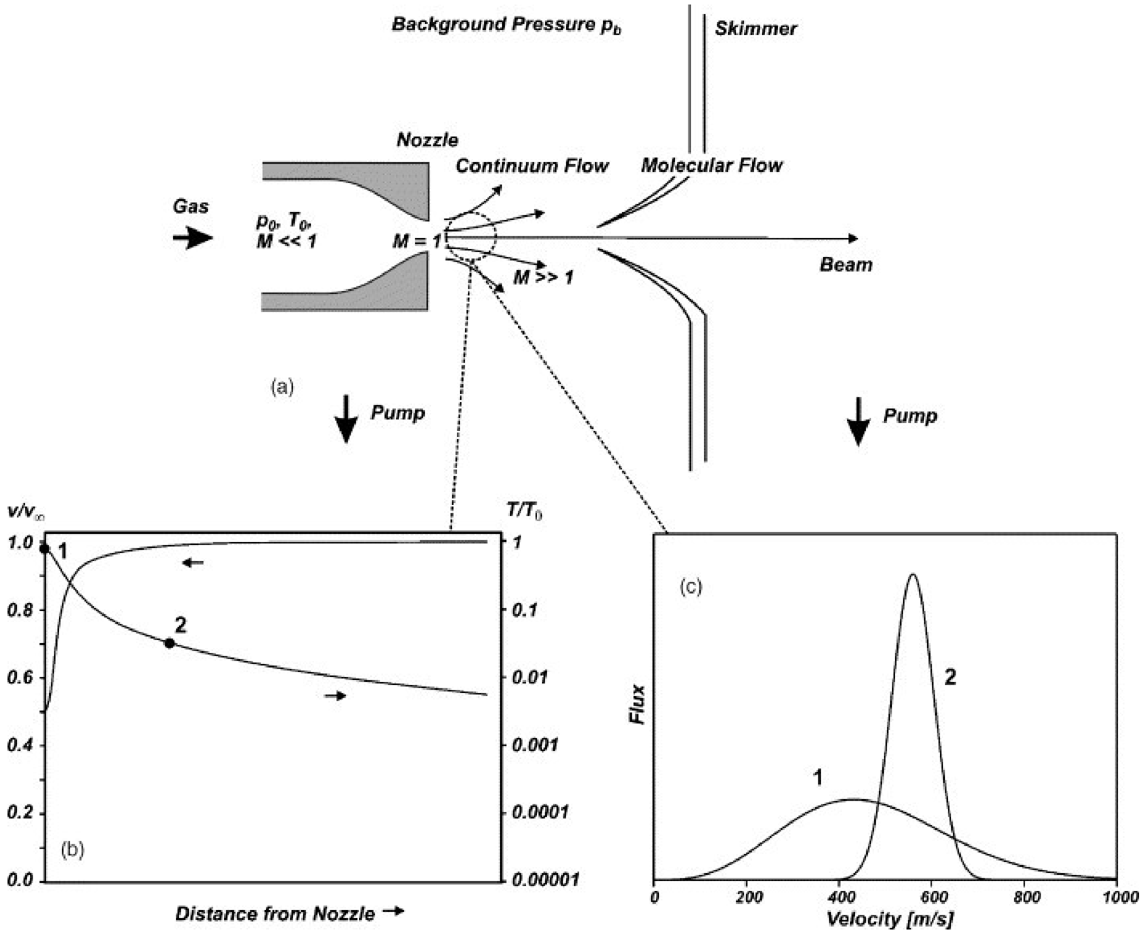

Figure 2.1: a) Expansion of a gas through a nozzle into the vacuum chamber. The skimmer placed at a short distance to the nozzle prevents shock wave formation and extracts the molecular beam. **b)** With increasing distance from the nozzle, the velocity increases until approaching v_∞, while the temperature decreases. **c)** In comparison to the initial Maxwell-Boltzmann distribution (1), the velocity distribution in the supersonic beam is narrowed (2). Reproduced with permission from Ref[104].

The upper limit for the terminal velocity is full conversion of internal energy into directed kinetic energy:

$$v_\infty = \sqrt{\frac{2h_0}{M}} = \sqrt{\frac{2c_pT_0}{M}} \tag{2.2}$$

Consequently, the reachable velocity depends on the nozzle temperature T_0 and the nature of the gas, that is, its isobaric molar heat capacity c_p and molar mass M.[109]

For monoatomic gases, v_∞ is a good approximation for the experimentally achievable velocity. For other gases, also the vibrational and rotational degrees of freedom have to be taken into account, which complicates the prediction of their experimental velocity. In the range of typical nozzle temperatures, the vibrational degrees of freedom are often only partially active, which further complicates the estimation of the flow velocity.[107] With the proceeding expansion of the gas, the collision frequency decreases rapidly. Thus, after about 10^2 to 10^3 collisions per molecule, the transition from continuum to free molecular flow occurs. As a rule of thumb, this is sufficient for the energy transfer from the translational and rotational degrees of freedom into directed movement, but insufficient for the vibrational degrees of freedom.[107, 109]

Since the free molecular flow is collision-free, the molecules are frozen in a non-equilibrium state, which can be characterized by the temperature parallel $T_\parallel$ and perpendicular $T_\perp$ to the streamline. In typical molecular beam setups, a narrow (but finite) velocity distribution is achieved (see Figure 2.1c) and $T_\parallel$ and $T_\perp$ can even be pushed below 1 K.[110] Further cooling of $T_\perp$ can be achieved by exploiting a geometrical effect: The molecules with highest $T_\perp$ have a momentum perpendicular to the flow direction of the molecular beam, so they drift away from the center of the beam and thus can be sorted out by a downstream aperture.[107]

In principle, only a nozzle, a skimmer and an expansion chamber are required to form a supersonic molecular beam. However, because a considerable gas flow into the expansion chamber is required, usually several differential pumping stages are needed to keep the final pressure low enough for UHV experiments.[111]

2.1.2 Sticking Coefficient Measurements

The sticking coefficient *S* is defined as the probability for an incoming molecule to stick to, that means adsorb on, a sample surface. In this work, *S* is called trapping probability if the adsorption occurs through physisorption rather than chemisorption, which is in line with the nomenclature most often found in the literature.[112] *S* can be measured using the direct method of King and Wells,[113] which requires a supersonic molecular beam and a set of flags (i.e. mechanical shutters). Figure 2.2 shows a sketch of the setup together with an exemplary measurement curve obtained during such an experiment. The partial pressure of the molecule of interest in the analysis chamber is followed by recording a representative *m*/*z* with a quadrupole mass spectrometer (QMS). The experimental procedure is based on a sequence of opening and closing two flags (marked by dashed lines in Figure 2.2).

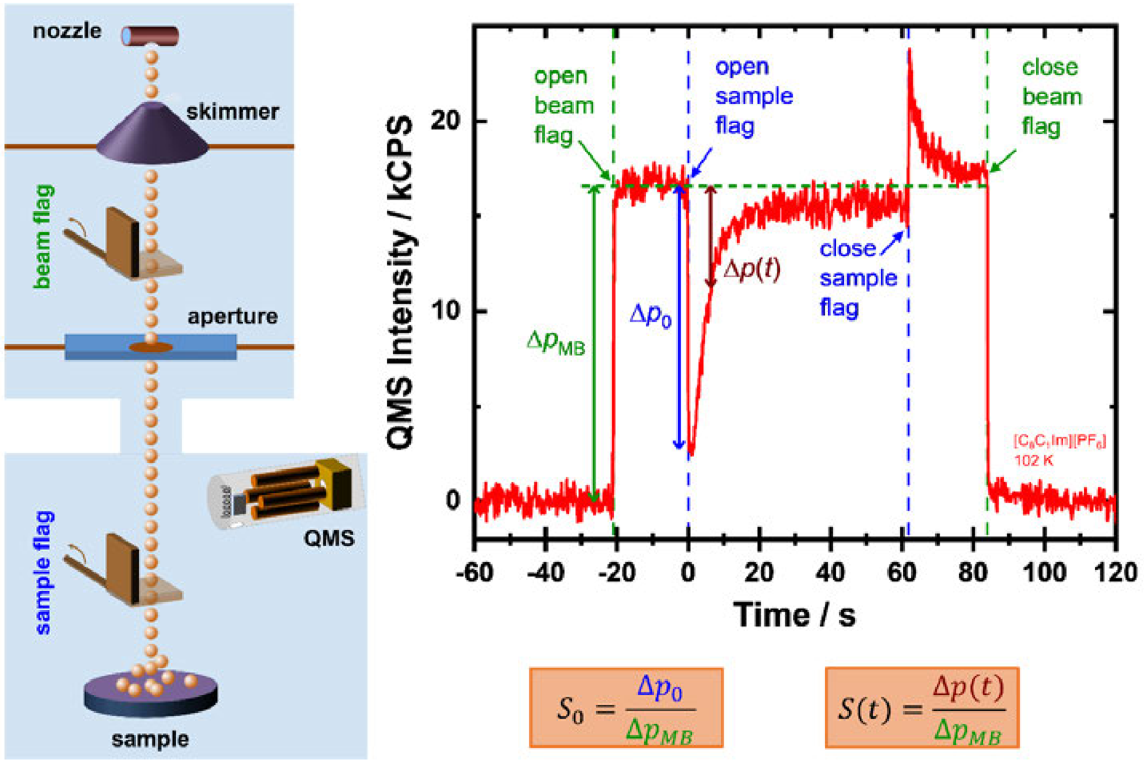

Figure 2.2: Sketch of the molecular beam setup used in this work (left side) together with an exemplary measurement curve (right side). The initial sticking coefficient S_0 and the time-dependent sticking coefficient $S(t)$ can be determined from the partial pressure differences Δp_{MB}, Δp_0 and $\Delta p(t)$ measured with the quadrupole mass spectrometer (QMS). Adapted from Ref[114] under license CC BY 4.0.

At the beginning of the measurement ($t = -40$ s), the beam flag blocks the molecular beam in an upper differential pumping stage, so that the partial pressure in the analysis chamber is zero. At $t = -20$ s, the beam flag is opened, so the molecular beam can enter the analysis chamber, where it is scattered off the inert sample flag. This results in a pressure increase Δp_{MB} in the analysis chamber. At $t = 0$ s, the sample flag is opened and now the molecular beam can hit the sample surface. If the incoming molecules stick to the sample surface, an initial pressure drop Δp_0 is observed. The initial sticking coefficient S_0 is then determined from the ratio of Δp_0 and Δp_{MB}:

$$S_0 = \frac{\Delta p_0}{\Delta p_{MB}} \tag{2.3}$$

S_0 refers to the adsorption on the uncovered surface, that is, at zero adsorbate coverage. With progressing time, a certain coverage builds up on the surface, which often changes the sticking coefficient. These changes are proportional to the changes in partial pressure, so that, in analogy to S_0, a time-dependent sticking coefficient $S(t)$ can be determined from $\Delta p(t)$:

$$S(t) = \frac{\Delta p(t)}{\Delta p_{MB}} \tag{2.4}$$

In the example shown in Figure 2.2, a steady-state situation is reached after ≈ 30 s. Steady state means that the adsorption rate from the molecular beam and the desorption rate into the chamber background become equal. As a result, the partial pressure returns back to the level it had before opening the sample flag. In such cases, where the desorption rate is not negligible, the sticking coefficients or trapping probabilities determined by the approach of King and Wells are often called “net” sticking coefficients or “net” trapping probabilities S^{net}. In these cases, they do not give a measure for the probability of an individual molecule to adsorb or scatter, but rather represent the overall balance between adsorption and desorption rate.

When the sample flag is closed again at $t = 60$ s, the molecular beam is again scattered from it. In the example shown in Figure 2.2, this causes an increase in the partial pressure curve, which arises from the molecules desorbing from the still-present adsorbate layer. In the last step, the beam flag is closed at $t \approx 80$ s and the partial pressure returns to zero.

The experimental technique described above works with the assumption that the pumping speed of the chamber is constant during the measurement. Depending on the investigated system, adsorption on the chamber walls and the (cooled) manipulator can be a major component of the total pumping speed of the chamber. If the adsorption rate to the chamber walls is coverage-dependent, the assumption of constant pumping speed is no longer fulfilled. To account for this effect, in this work an empirical correction for the effect of non-constant pumping speed was successfully applied, where necessary, using a correction originally proposed by Stefan Kneitz,[115] and described in detail in the Supporting Information of [P4] (see Appendix 8.4). When the new ILID apparatus was characterized in the context of this thesis, another experimental artifact was found: If the liquid nitrogen cooling is running, an apparent sticking coefficient of ≈ 0.05 is measured for systems, where no sticking on the sample surface is expected. Therefore, a correction ("base line correction") was applied, so that an apparent sticking coefficient of 0.05 results in a corrected sticking coefficient of 0.00, while an apparent sticking coefficient of 1.00 still is reported as a corrected sticking coefficient of 1.00.

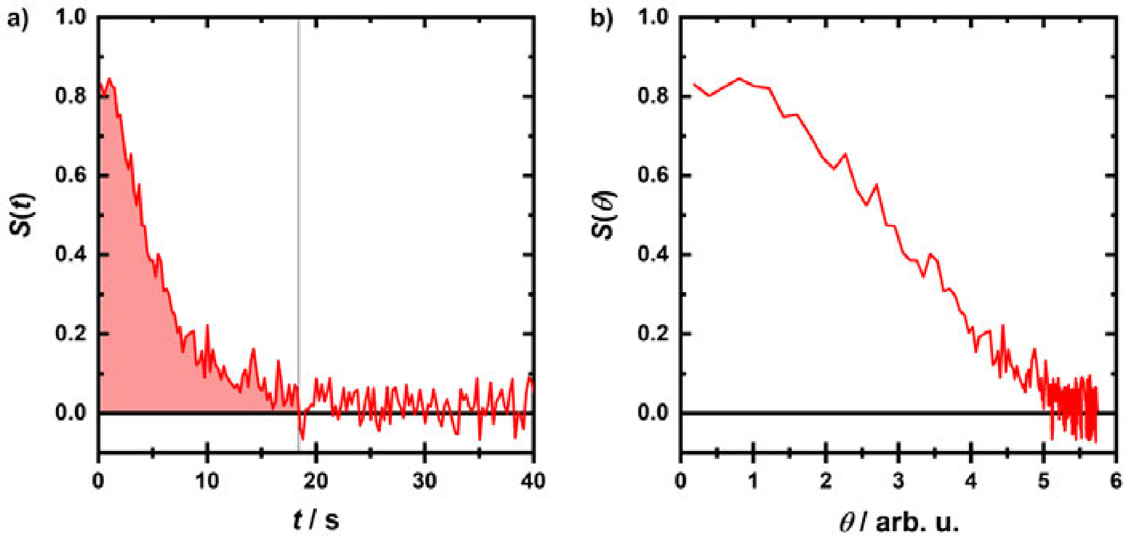

Figure 2.3: a) Plot of the time-dependent sticking coefficient $S(t)$, as it was extracted from the raw data shown in Figure 2.2. The light red area illustrates the integration procedure to determine the uncalibrated coverage θ. **b)** Plot of the coverage-dependent sticking coefficient $S(\theta)$ following from the data shown in a).

As it was introduced earlier, S can be determined for any time t of the experiment, so the raw data can be converted into an $S(t)$ versus t plot. Figure 2.3a shows such a plot, which in this case is based on the raw data shown in Figure 2.2. To discuss changes in the sticking coefficient, it is however often more straightforward to analyze the coverage dependency of the sticking coefficient. The absolute coverage Θ_{abs} (in units of molecules cm^{-2}) adsorbed after a certain time t is given by

$$\Theta_{abs} = R_{imp} \int_0^t S(t)\, dt \tag{2.5}$$

with R_{imp} being the impinging flux of the molecular beam (in molecules $\mathrm{cm}^{-2}\ \mathrm{s}^{-1}$). Since measuring accurate absolute values for R_{imp} is difficult, in this work, the absolute coverage Θ_{abs} will not always be used, but rather an uncalibrated relative coverage, θ, which can be determined from integrating $S(t)$:

$$\theta = \frac{\Theta_{abs}}{R_{imp}} = \int_0^t S(t)\, dt \tag{2.6}$$

θ can then be used to create an $S(\theta)$ versus θ plot (see Figure 2.3b).

2.2 X-Ray Photoelectron Spectroscopy

X-ray Photoelectron Spectroscopy (XPS) is one of the most powerful and frequently applied surface science techniques. The physical foundations and measurement principles of XPS are thoroughly described in a couple of textbooks, e.g., the ones from Briggs and Seah[116], Hüfner[117] or van der Heide[118]. Due to the small inelastic mean free path λ of electrons in matter, photoelectrons are emitted without energy losses only from the first molecular layers of a solid or liquid sample, making XPS a surface-sensitive technique. 96% of the signal is obtained from electrons traveling less than 3λ through the sample material, which is used as a cutoff to define the information depth ID:[118]

$$ID = 3\lambda \cos(\vartheta) \tag{2.7}$$

As Equation (2.7) shows, ID depends also on the emission angle ϑ relative to the surface normal, because photoelectrons emitted at a grazing angle have to travel along a larger distance to escape the sample material (see Figure 2.4). Angle-Resolved XPS (ARXPS) can therefore be used to gain information about the surface composition of a sample. For ILs, measurements in 0° emission angle (ID = 7-9 nm) are dominated by the bulk composition, while measurements in 80° emission (ID = 1-1.5 nm) reflect the surface composition.[119] In Chapter 4.3, this difference in ID will be used to correlate the surface composition obtained by ARXPS with desorption energies determined from temperature-dependent trapping probability measurements.

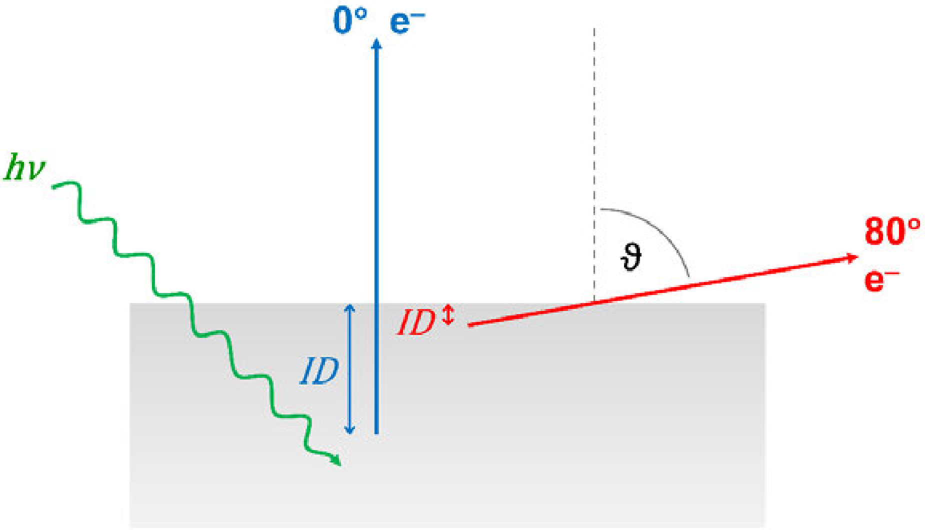

Figure 2.4: Sketch of the 0° emission geometry (left) and the 80° emission geometry (right).

In the context of PVD-prepared ultrathin IL films on metal substrates, XPS can be used to determine the thickness of the IL film, which is also expressed as the IL coverage θ_{IL}. This approach is based on the exponential attenuation of the substrate signal, caused by the adsorbed IL. An ideal two-dimensional (2D) IL layer with thickness d will lead to a decreased substrate signal I_{d}, as compared to the signal of the uncovered substrate I_0:[59, 120]

$$\frac{I_d}{I_0} = e^{-\frac{d}{\lambda \cos(\vartheta)}} \tag{2.8}$$

In this case, λ is the inelastic mean free path of photoelectrons with the kinetic energy characteristic for the respective substrate signal in ILs.[66, 120-124] In literature,[120] the thickness, h, of one IL monolayer (ML) is often estimated by

$$h = \sqrt[3]{V_m} = \sqrt[3]{\frac{M}{N_A\,\rho}} \tag{2.9}$$

where V_{m} is the bulk molecular volume, N_{A} the Avogadro constant, M the molar mass, and ρ the bulk density of the respective IL. Following this estimation, the IL coverage $\theta_{\mathrm{IL}} = 1$ ML is defined as the amount of IL that corresponds to the substrate damping expected from an ideal 2D film with thickness h. In a simple model, such a monolayer has the same density as the IL bulk and is composed of pairs of anions and cations, vertically on top of each other. On metal surfaces, ILs typically form a wetting layer, i.e., a closed layer of anions and cations adsorbed next to each other in a checkerboard arrangement, with an ideal coverage of 0.5 ML.[125] However, because of specific ion/substrate interactions, the resulting adsorption geometry, long-range ordered structure, and a different density, the actual IL coverage needed to form a closed wetting layer can vary from this bulk-derived value.

3 Experimental Details

3.1 Molecular Beam Chamber ILID [P2]

The experiments presented in this thesis are the first ones performed with the newly developed molecular beam apparatus denoted as “ILID” (Ionic Liquid Interface Dynamics; see Figure 3.1). The instrument consists of (1) a preparation chamber for sample introduction, cleaning and *in situ* sample preparation (see Chapter 3.1.1), and an attached IL evaporator (see Chapter 3.1.2), (2) an analysis chamber for measurements (see Chapter 3.1.3), and (3) a three-stage molecular beam setup to generate the supersonic molecular beam (see Chapter 3.1.4). In the Supporting Information of [P2] (see Appendix 8.2) and in Appendix 8.5 further details about the apparatus can be found. These include additional characterization data, technical drawings and a detailed sketch of the pumping system.

3.1.1 Preparation Chamber and Manipulator

Inside the apparatus, the sample can be moved using a manipulator (VAb PM 25-800) with a cryostat for cooling with liquid N_2. Type K (chromel/alumel) thermocouples are used to measure the temperatures of the sample and the cryostat. The sample can be heated up to ≈ 450 K by indirect radiation heating using a filament located below the sample plate. To reach higher temperatures of up to ≈ 1200 K, electron bombardment heating from the back side is also possible. Samples can be introduced into the UHV chamber via a load lock. For this purpose, a transferable sample holder system with very reliable temperature readings was adopted for the instrument. The respective single-crystal or a polycrystalline Ni block as support for macroscopic IL samples (in both cases $12 \times 12 \times 4\ \mathrm{mm}^3$) is mounted with a U-shaped molybdenum clamp on a tantalum ground plate. The thermocouple is placed inside a small hole (0.4 mm diameter, 3 mm depth) of the support; a setup of insulated wires and plates provides a connection to the thermocouple contacts of the sample stage on the manipulator head. In that way, a reliable and accurate measurement of relative sample temperatures (±1 K) is possible, with an estimated absolute temperature accuracy of ±3 K. For the preparation of single crystals, the preparation chamber is also equipped with a sputter gun (SPECS IQE 11/35), a 4-grid LEED (low energy electron diffraction) setup (SPECS ErLEED 150), and leak valves for gas dosing.

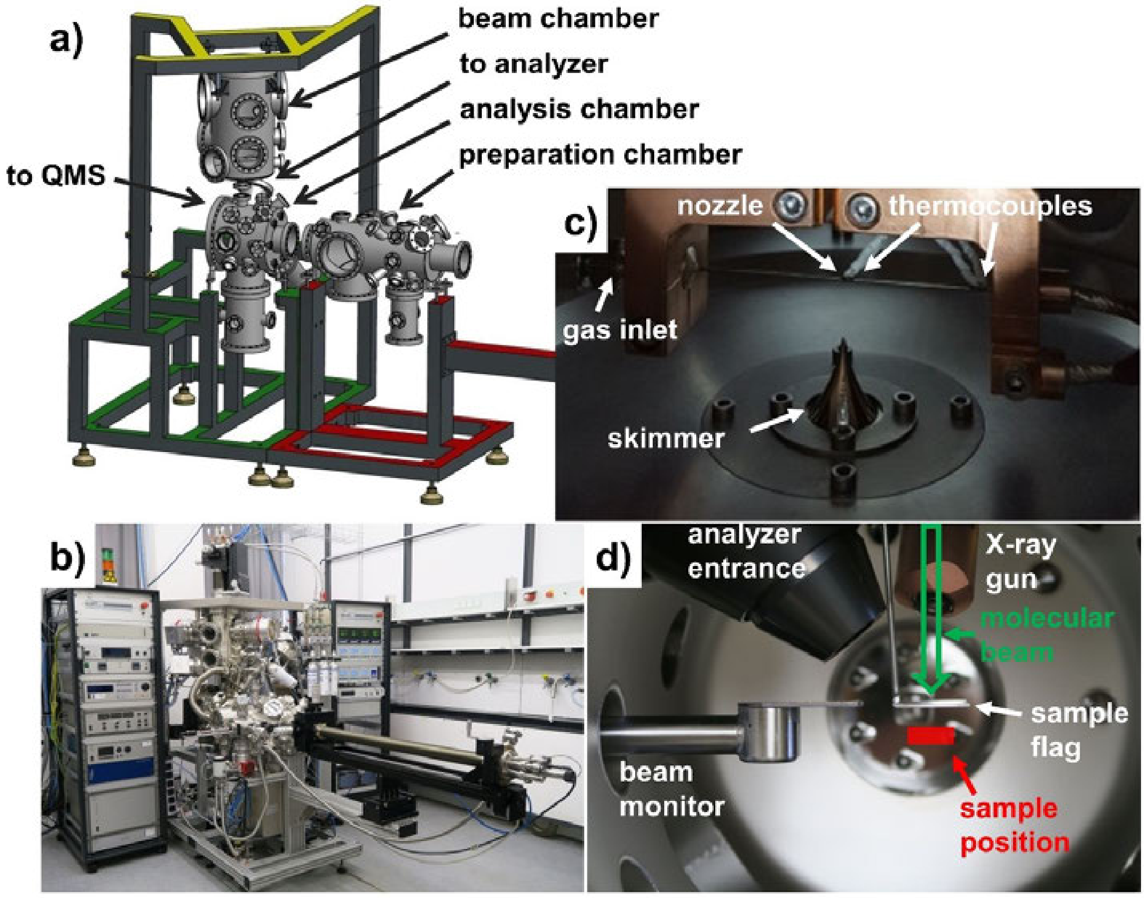

Figure 3.1: **a)** Sketch of the three main parts of the ILID apparatus: preparation (red), analysis (green) and molecular beam chamber (yellow). **b)** Image of the complete setup. **c)** View inside the first pumping stage of the beam chamber. An *xyz*-movable molybdenum tube (which can be heated) is mounted between two copper holders, its nozzle (⌀ = 100 µm; not visible by the eye) is located next to the central thermocouple a few centimeters above the skimmer. **d)** Picture of the inside of the analysis chamber; the sample position and the direction of the molecular beam are indicated. The QMS is not visible in this picture. Reproduced from Ref[114] under license CC BY 4.0.

3.1.2 Ionic Liquid Evaporator

For the preparation of ultrathin IL films by PVD, a home-built IL evaporator[66] is attached to the preparation chamber, separated by a gate valve. A Knudsen cell is mounted inside a water-cooled body, which can be moved into the preparation chamber using a *z*-shift. Heating can be performed by using a tantalum filament (0.25 mm diameter), which is exposed to the surrounding only at the bottom of the setup, but shielded by a copper cylinder at the top. With this setup, the risk for decomposition of IL (which tends to creep out of the crucible) at the hot filament is considerably mitigated.

3.1.3 Analysis Chamber

In the analysis chamber (see Figure 3.1d), a hemispherical electron analyzer (SPECS PHOIBOS 100 1D-DLD) and a dual-anode X-ray gun (SPECS XR 50) are mounted to perform XPS measurements (see Chapter 2.2). A quadrupole mass spectrometer (QMS) with a cross beam ionization source and a secondary electron multiplier as detector (Hiden Analytical 3F RC 301 PIC) is used to perform sticking coefficient measurements, which also require a sample flag (see Chapter 2.1.2). A further component of the analysis chamber is the so-called beam monitor: It is a small volume mounted on an *xyz*-manipulator separated from the analysis chamber by an orifice of 1.0 mm.[107] The stagnation pressure building up inside the beam monitor can be measured with a hot-filament ionization gauge. Measuring this pressure, when the molecular beam covers the orifice, allows one to determine the flux and profile of the molecular beam (see Chapter 3.2.1).

3.1.4 Molecular Beam

The supersonic molecular beam (see Chapter 2.1.1) comprises three differential pumping stages. Stage 1 contains a molybdenum stagnation tube with an inner diameter of 0.7 mm (see Figure 3.1c). A laser-cut round hole in the tube with 100 µm diameter serves as nozzle. Its position can be adjusted in three directions, and it can be resistively heated. The copper holders of the tube are water-cooled, so that heating to high temperatures of up to 1300 K is possible. Gases can be fed over an inlet system featuring three mass flow controllers (Bronkhorst EL-FLOW Prestige), which allow for using also gas mixtures. Stages 1 and 2 are separated by a skimmer (Ni; opening diameter: 0.5 mm; Beam Dynamics, Inc.). The beam flag required for sticking coefficient measurements is placed in stage 2, so the scattered gas molecules are almost completely pumped away, and only a very small pressure leaks into the analysis chamber. Between stages 2 and 3, a changeable aperture (diameter 1.1, 1.9, 2.6 or 3.7 mm) can be inserted, which allows one to adjust the beam diameter and the position of the beam spot on the sample (see Chapters 3.2.1 and 3.2.2).

3.2 Molecular Beam Characterization

3.2.1 Gas Flux Measurements [P2]

The gas flux in the molecular beam can be measured using the beam monitor mounted in the analysis chamber. Similarly to the principle of a Pitot tube, the pressure in the beam monitor rises, if the molecular beam is impinging onto the orifice of the beam monitor. In equilibrium, the incoming gas flux R_{in} is equal to the outgoing flux R_{out}:

$$R_{out} = R_{in} = R_{MB} + R_{bp} \tag{3.1}$$

R_{in} can be expressed as the sum of two components, one originating from the background pressure of the analysis chamber, R_{bp}, and one from the incoming molecular beam, R_{MB}. With the assumption that the gas in the molecular beam, in the background and in the beam monitor consists only of one kind of molecules (with mass m) and assuming that the temperature T in both chambers is the same and constant, we obtain:

$$R_{MB} = R_{out} - R_{bp} = \frac{p_{MB} - p_{bgr}}{\sqrt{2\pi\, m\, k_B\, T}} = \frac{\Delta p}{\sqrt{2\pi\, m\, k_B\, T}} \tag{3.2}$$

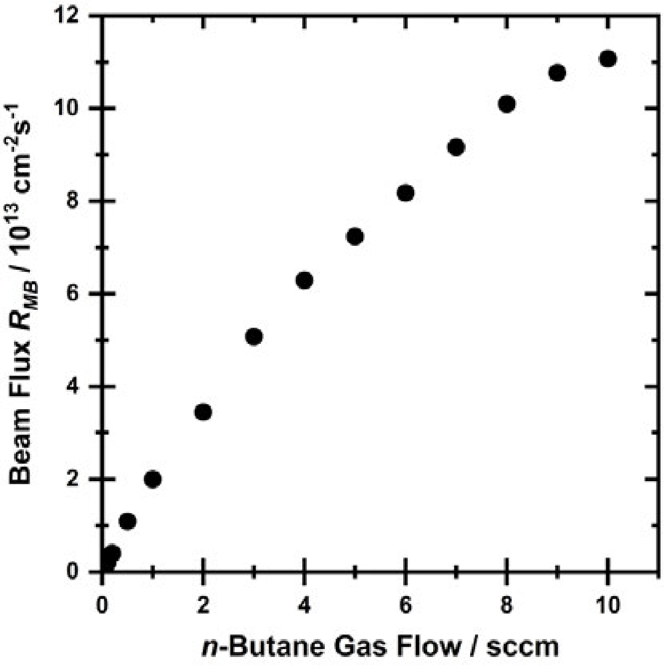

Figure 3.2: Beam flux of *n*-butane measured with the method described in this chapter as a function of the gas flow set in the mass flow controller. Reproduced from Ref[114] under license CC BY 4.0.

To determine the beam flux, it is only required to measure p_{bgr}, the pressure measured in the beam monitor with the molecular beam blocked by the closed sample flag in front of the beam monitor orifice, and p_{MB}, the beam monitor pressure measured with the open sample flag, i.e., the central part of the molecular beam passes the orifice. Figure 3.2 shows the *n*-butane beam flux measured according to this procedure plotted against the set gas flow.

3.2.2 Flux Profiles [P2]

The beam monitor can also be used to measure a lateral profile map of the beam intensity in the sample plane. Figure 3.3 shows a typical example of such a map for an *n*-butane beam (gas flow: 1.0 sccm, beam aperture diameter: 1.1 mm). In this case, 182 Δp values were recorded one after the other along a grid of beam monitor positions, while the valve to the additional pumping in the beam monitor was left open to decrease equilibration time. Note that for this reason, the Δp values from this experiment cannot be converted into flux like described in Chapter 3.2.1, but still allow for determining a profile map. As expected, the beam is round and symmetrical with only minor intensity variation in its center. Due to the finite diameter of the beam monitor orifice (1.00 mm), the beam appears to be broadened in Figure 3.3. The black solid lines in the insets of Figure 3.3 indicate how much broadening is expected by showing a convolution of a rectangular intensity profile (indicated by dashed lines) and the broadening function of the beam monitor orifice ($\varnothing = 1.0$ mm). The agreement of the solid lines with the data points suggests that the beam has indeed a very sharp rectangular intensity profile of 3.4 mm diameter. From an analogous measurement using the beam-defining orifice with a diameter of 1.9 mm, the beam diameter in the sample plane was determined to be 5.9 mm. This shows that the beam diameter in the sample plane is by a factor of 3.1 larger than the beam-defining orifice, which fits the expectations from the geometrical parameters: The distance from the sample plane to the beam-defining aperture (487 mm) is also by a factor of 3.1 larger than the distance from the beam defining aperture to the skimmer (159 mm).

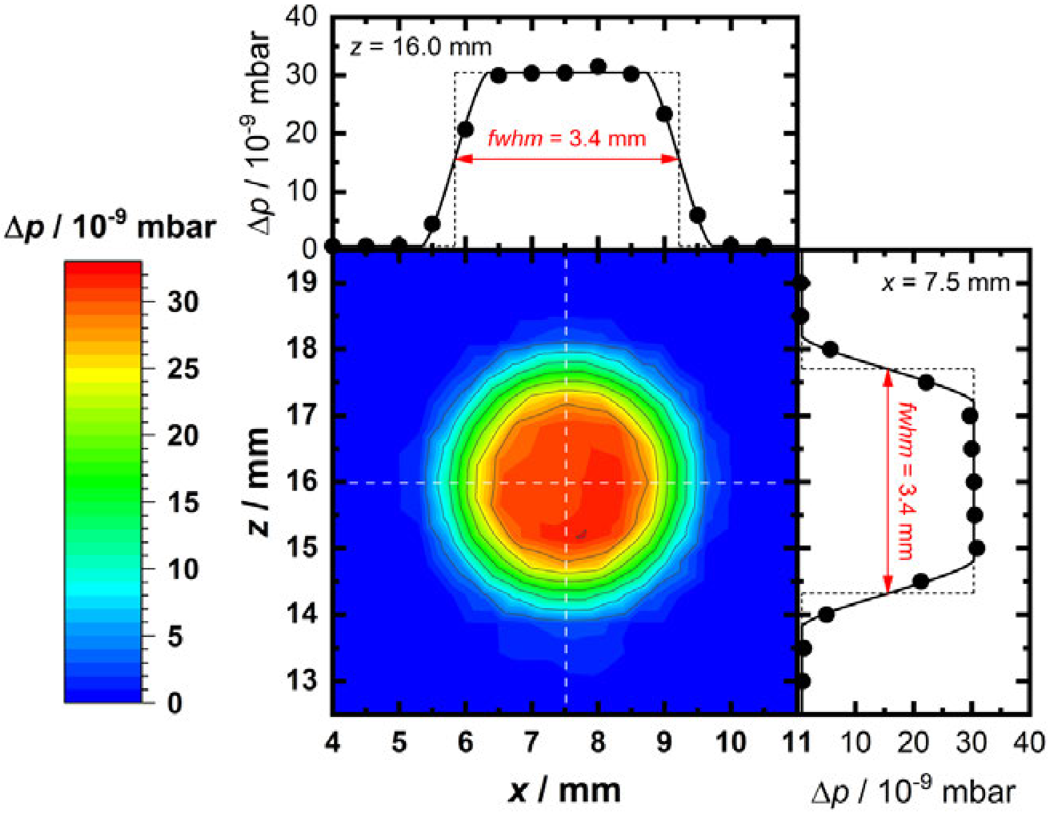

Figure 3.3: Contour plot of the intensity of the *n*-butane molecular beam (1.0 sccm gas flow, beam defining orifice with a diameter of 1.1 mm) measured with the beam monitor. The top inset shows the beam profile in *x*-direction at $z = 16.0$ mm and the right inset the beam profile in *z*-direction at $x = 7.5$ mm. The white dashed lines in the contour plot indicate the location of the beam profiles. The black solid lines in the insets show the convolution of the theoretically expected broadening function of the beam monitor orifice and a rectangular beam profile (see dashed lines). Reproduced from Ref[114] under the license CC BY 4.0.

3.2.3 Sample Positioning

Finding a suitable measurement position for the molecular beam experiments is not straightforward: Although the beam can be mapped using the beam monitor, the sample cannot be brought into the beam position in a simple way. That is because the beam monitor is mounted on a different manipulator as the sample and transformation from one coordinate system to the other is not possible with satisfying accuracy. Furthermore, optimizing the sample position by maximizing the sticking coefficient is not possible. The reason is that the sample is surrounded by metal surfaces at cryogenic temperatures (if liquid nitrogen cooling is used), on which most test molecules will show a high sticking coefficient. Even if the molecular beam misses the sample stage completely, an apparent sticking coefficient is observed, because the molecular beam is then directed straight into the entry of the turbomolecular pump. However, the sticking coefficient can still be used if the opposite strategy is applied: An *n*-butane beam is expected to adsorb on the surrounding cold metal surfaces, but not on the sample (and its surrounding holder) if the sample is heated to 300 K. Figure 3.4 shows how the sticking coefficient of an *n*-butane beam with 3.4 mm diameter changes when the measurement position is varied. Out of the dimensions of the sample holder, it is possible to construct an expected behavior. Matching the expected behavior with the measured data allows one to locate the molecular beam in the sample coordinate system and find a suitable measurement position.

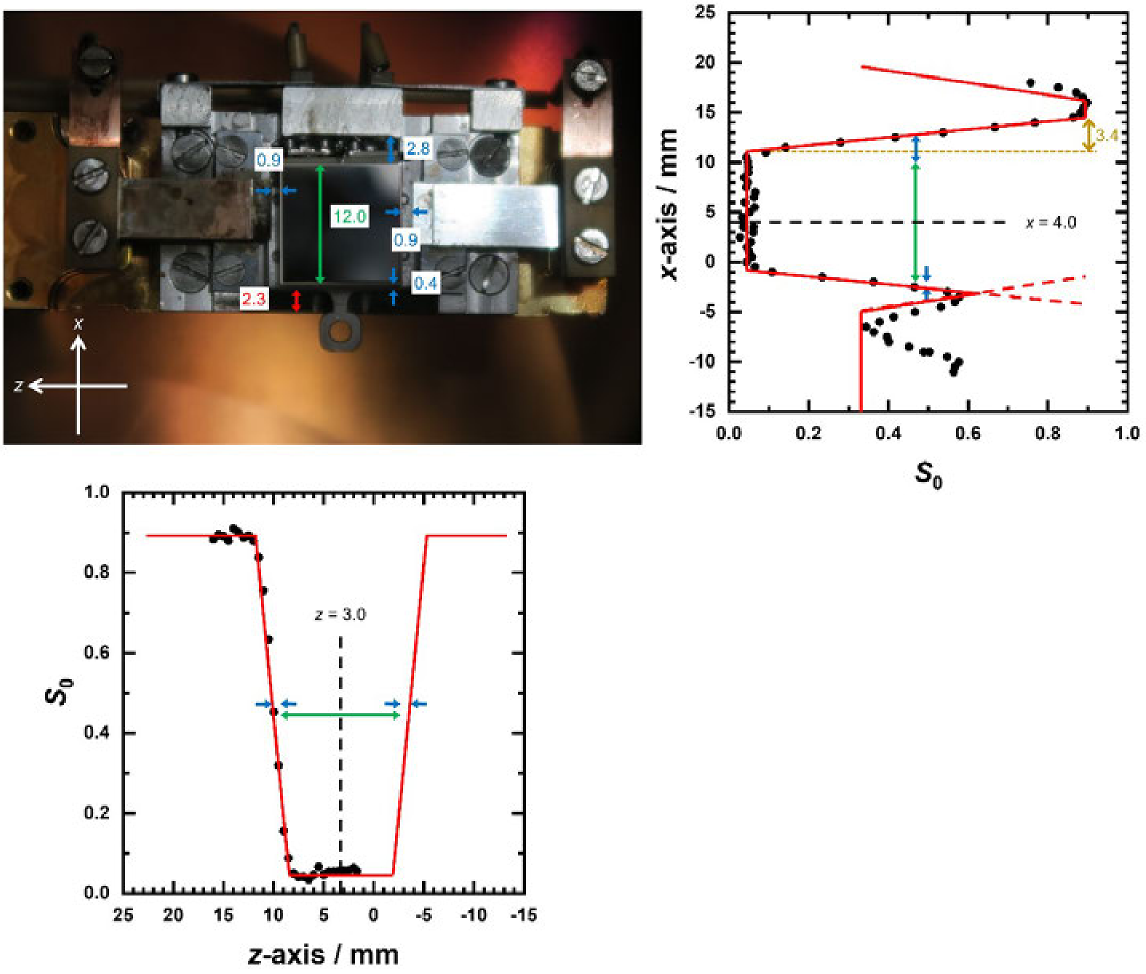

Figure 3.4: Picture of the sample stage, with the dimension of the sample (green) and its holder (blue). The changes in the sticking coefficient are displayed on the right (*x*-axis) and bottom (*z*-axis) together with the expected behavior (red lines) taking into account the diameter of the beam (3.4 mm marked in yellow). The chosen measurement positions are marked with black dashed lines. All dimensions are given in millimeters.

4 Results

4.1 C4-Hydrocarbon Trapping on Imidazolium-Based Ionic Liquids [P1-3]

The following chapter describes the systematic investigation of the trapping dynamics of C4-hydrocarbons – *n*-butane and closely related compounds – physisorbing on imidazolium-based ILs. Imidazolium-based ILs are probably the most common class of ILs (see Figure 4.1). Typically, the imidazolium cation is substituted on both nitrogen atoms, commonly with two alkyl groups, with one of them often being methyl. In contrast, a greater variety of structures is used as anions – from simple halides to highly fluorinated ones like $[Tf_2N]^-$.

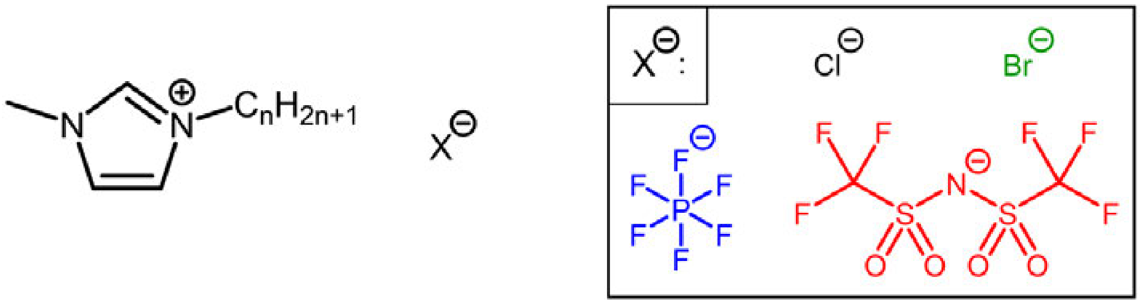

Figure 4.1: General structure of imidazolium-based ILs $[C_nC_1Im]X$ (left side) and different anions used in this thesis (right side).

4.1.1 Effect of Alkyl Chain Length [P1-2]

As introduced in Chapter 2.1.2, the trapping probability S can be measured by the direct method of King and Wells.[113] Figure 4.2 shows corresponding measurements for *n*-butane adsorbing on $[C_8C_1Im][Tf_2N]$ (a) and $[C_3C_1Im][Tf_2N]$ (b). After opening the sample flag at $t = 0$, at 90 K the signal for both ILs drops to a lower constant value, which is attributed to a constant trapping probability $S(t)$ of ≈ 0.9. With increasing surface temperature, $S(t)$ becomes time- and therefore coverage-dependent: For example, at 98 K the signal first drops at $t = 0$, but then immediately starts to rise again (more pronounced for $[C_3C_1Im][Tf_2N]$). This increase is attributed to an increase in the desorption rate of already adsorbed molecules, which yields a decrease of the net trapping probability $S^{net}(t)$ (see also Chapter 2.1.2). After closing the sample flag at $t \approx 60$ s, a higher *n*-butane signal than before opening the sample flag is observed, which indicates that desorption from the *n*-butane covered IL surface continues.

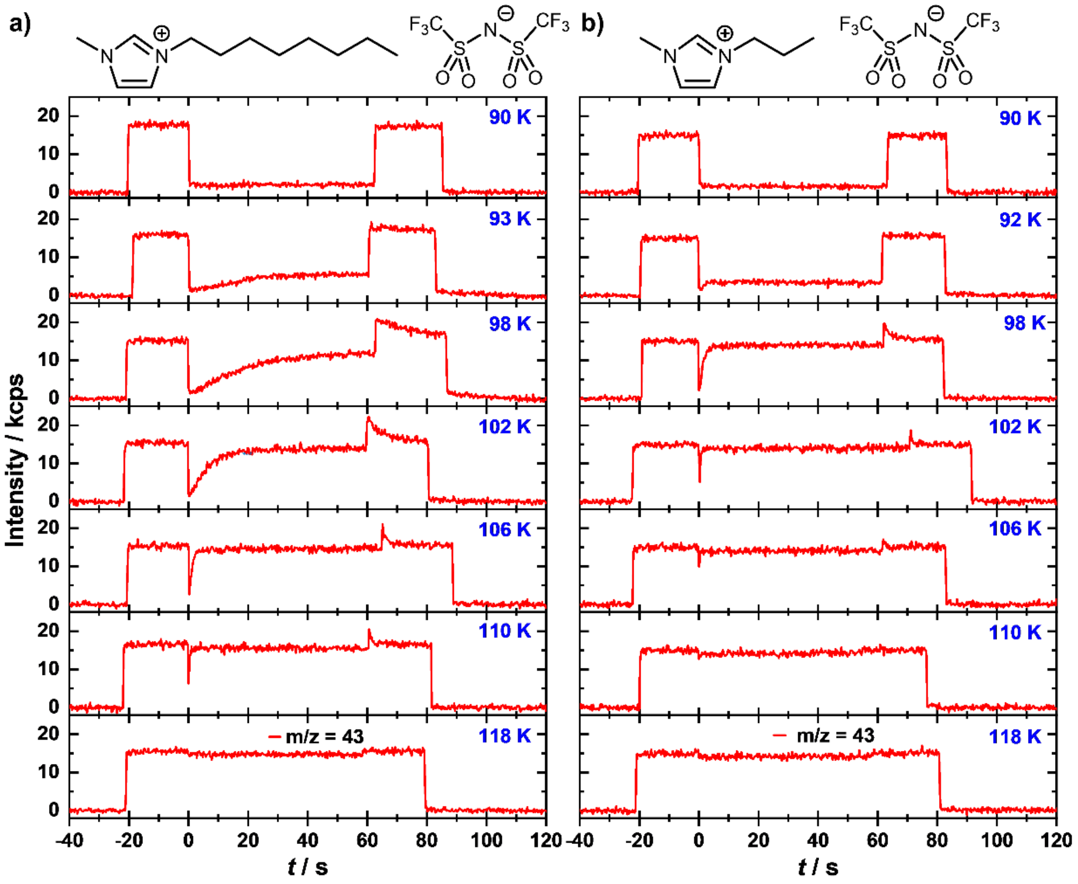

Figure 4.2: King and Wells measurement curves for the adsorption of *n*-butane on frozen $[C_8C_1Im][Tf_2N]$ (**a**) and $[C_3C_1Im][Tf_2N]$ (**b**), recorded at selected temperatures. The *n*-butane partial pressure was measured by following $m/z = 43$, the most intense signal of *n*-butane's mass spectrum. Adapted from Ref[126] under the license CC BY-NC-ND 4.0.

Figure 4.2 already shows that the length of the alkyl chain used as substituent at one nitrogen atom of the imidazolium core of the IL cation has an effect on the trapping probability of *n*-butane. For example, at 106 K, *n*-butane shows an initial trapping probability $S_0^{net} = 0.74$ on $[C_8C_1Im][Tf_2N]$, but on $[C_3C_1Im][Tf_2N]$ it only has an S_0^{net} of 0.30. To obtain more detailed insights, the temperature-dependency of S_0^{net} is therefore systematically investigated for two sets of ILs: $[C_nC_1Im][Tf_2N]$ with $n = 1, 2, 3, 4$ and 8, and $[C_nC_1Im][PF_6]$ with $n = 2, 4$ and 8.

In the first step, the temperature-dependent S_0^{net} of *n*-butane on $[C_8C_1Im][Tf_2N]$ will be discussed (Figure 4.3a, black squares): Until 102 K, S_0^{net} stays constant at ≈ 0.9 and starts to decrease for higher temperatures. At the characteristic temperature $T_{50\%}$ ($[C_8C_1Im][Tf_2N]$) = 110 K, S_0^{net} is decreased to 50% of its initial level. This decrease of S_0^{net} can be explained by the onset of desorption from the adsorbed layer: Since desorption already sets in during the time to measure the first data point (0.50 s), a smaller net trapping probability S_0^{net} is observed. The characteristic temperature $T_{50\%}$ is thus a measure for the interaction strength between *n*-butane and the IL surface.

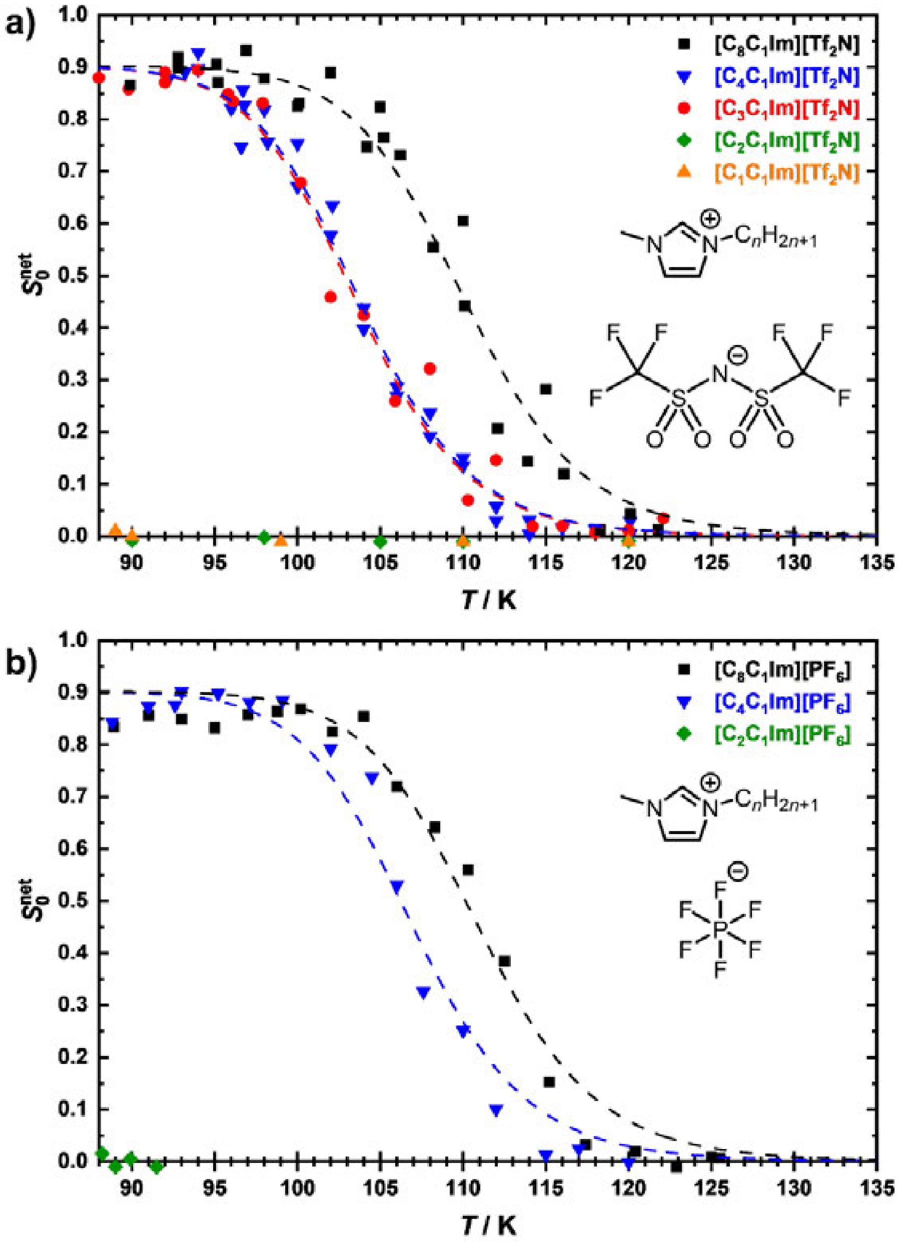

Figure 4.3: Temperature-dependent initial trapping probability S_0^{net} of *n*-butane on imidazolium-based ILs with different alkyl chain lengths. **a)** The set for the $[Tf_2N]^-$ anion, **b)** the one for the $[PF_6]^-$ anion. The dashed lines are fits to the data using the model described in Chapter 4.2.2. Adapted from Ref[114] under the license CC BY 4.0.

In a next step, I discuss the analogs with shorter alkyl chain lengths, $[C_4C_1Im][Tf_2N]$ and $[C_3C_1Im][Tf_2N]$: These two show an almost identical behavior (Figure 4.3a, blue triangles and red circles); compared to $[C_8C_1Im][Tf_2N]$ the curves are shifted by ≈ 6 K to lower temperature. S_0^{net} stays constant until ≈ 96 K and then decreases to zero with $T_{50\%}$ ($[C_{3/4}C_1Im][Tf_2N]$) = 104 K. If the alkyl chain is further shortened to ethyl ($[C_2C_1Im][Tf_2N]$) or methyl ($[C_1C_1Im][Tf_2N]$), no trapping is observed even at ≈ 90 K (green diamonds and orange triangles).

A similar trend can be seen for the series of ILs with the $[PF_6]^-$ anion. $[C_8C_1Im][PF_6]$ (see black squares in Figure 4.3b) and $[C_4C_1Im][PF_6]$ (blue triangles) show an overall analogous behavior as $[C_8C_1Im][Tf_2N]$, $[C_4C_1Im][Tf_2N]$ and $[C_3C_1Im][Tf_2N]$: A constant $S_0^{net} \approx 0.9$ for temperatures below 100 K, and then a drop-down to zero above a particular temperature. The characteristic temperatures are $T_{50\%}$ = 111 K for $[C_8C_1Im][PF_6]$ and $T_{50\%}$ = 107 K for $[C_4C_1Im][PF_6]$. The larger $T_{50\%}$ value for the IL with the longer alkyl chain agrees with the trend found for the series with the $[Tf_2N]^-$ anion. On $[C_2C_1Im][PF_6]$ (green diamonds), one does not observe *n*-butane trapping even in the temperature range of multilayer condensation, as was also the case for $[C_2C_1Im][Tf_2N]$ and $[C_1C_1Im][Tf_2N]$.

An interesting observation is the completely different trapping behavior of *n*-butane on ILs with longer ($n \geq 3$) and shorter ($n \leq 2$) alkyl chains. On ILs with $n \geq 3$, *n*-butane adsorbs with a large trapping probability of ≈ 0.9 at temperatures up to 96-102 K. Since *n*-butane multilayers start to desorb just above 90 K, the trapping observed at higher temperatures indicates that on the surfaces of ILs with $n \geq 3$ individual *n*-butane molecules are stronger bound than in the multilayer. In contrast, for the ILs with $n \leq 2$ no trapping of *n*-butane is observed even at the lowest investigated temperature, which indicates that the adsorption energy is smaller than the condensation energy. Thus, single *n*-butane molecules are only weakly bound on the IL surface and desorb after a short residence time. Notably, while multilayers (i.e., condensed *n*-butane) are known to be stable at $T \leq 90$ K, no *n*-butane multilayer formation is experimentally observed on the ILs with $n \leq 2$. An explanation for this result is that condensation nuclei are needed for multilayer growth. To allow for the formation of such stable nuclei, the statistical chance of a sufficient number of molecules encountering each other needs to be high enough, which requires a minimum coverage on the surface. However, even at the lowest studied temperature, the residence time of *n*-butane on the surfaces of ILs with $n \leq 2$ is too short to form such stable nuclei.

The decrease of $T_{50\%}$ with decreasing alkyl chain length and the absence of trapping on ILs with $n \leq 2$ can be attributed to weaker van-der-Waals interactions with shorter alkyl chains. In a simple picture, the surfaces of the ILs are composed of negatively charged anions, positively charged imidazolium-headgroups and non-polar alkyl chains.[92, 97] The fact that no trapping is observed for ILs with $n \leq 2$ shows that the attractive forces between *n*-butane and the polar headgroups and also the methyl and ethyl chains are very weak. However, upon increasing the alkyl chain length, trapping becomes feasible, because of the stronger van-der-Waals forces between *n*-butane and the non-polar alkyl chains: The longer the alkyl chain, the stronger the interactions as can be seen by an increase of $T_{50\%}$ with increasing chain length.

4.1.2 Effect of Anion [P2-3]

Figure 4.4 shows the S_0^{net} of *n*-butane on two sets of imidazolium-based ILs, one based on the octyl chain (a), the other on the butyl chain (b). Within each set, the anion is varied between Cl^-, Br^-, $[PF_6]^-$ and $[Tf_2N]^-$. The effect of stronger van-der-Waals interactions with the longer octyl chain (as discussed in Chapter 4.1.1) is evident from the fact that the curves for the $[C_8C_1Im]X$ series in Figure 4.4a are shifted to higher temperature compared to their corresponding ones for the $[C_4C_1Im]X$ series in Figure 4.4b. Additionally, Figure 4.4 demonstrates the influence of the anion, that is, $T_{50\%}$ increases with decreasing size of the anion, in the order $[Tf_2N]^- < [PF_6]^- < Br^- \approx Cl^-$. As will be more thoroughly discussed in Chapter 4.3, this effect is not attributed to interactions between the anion and *n*-butane, but rather to the different surface structures induced by the anions, which are characterized by a different degree of orientation of the alkyl chains towards the vacuum.

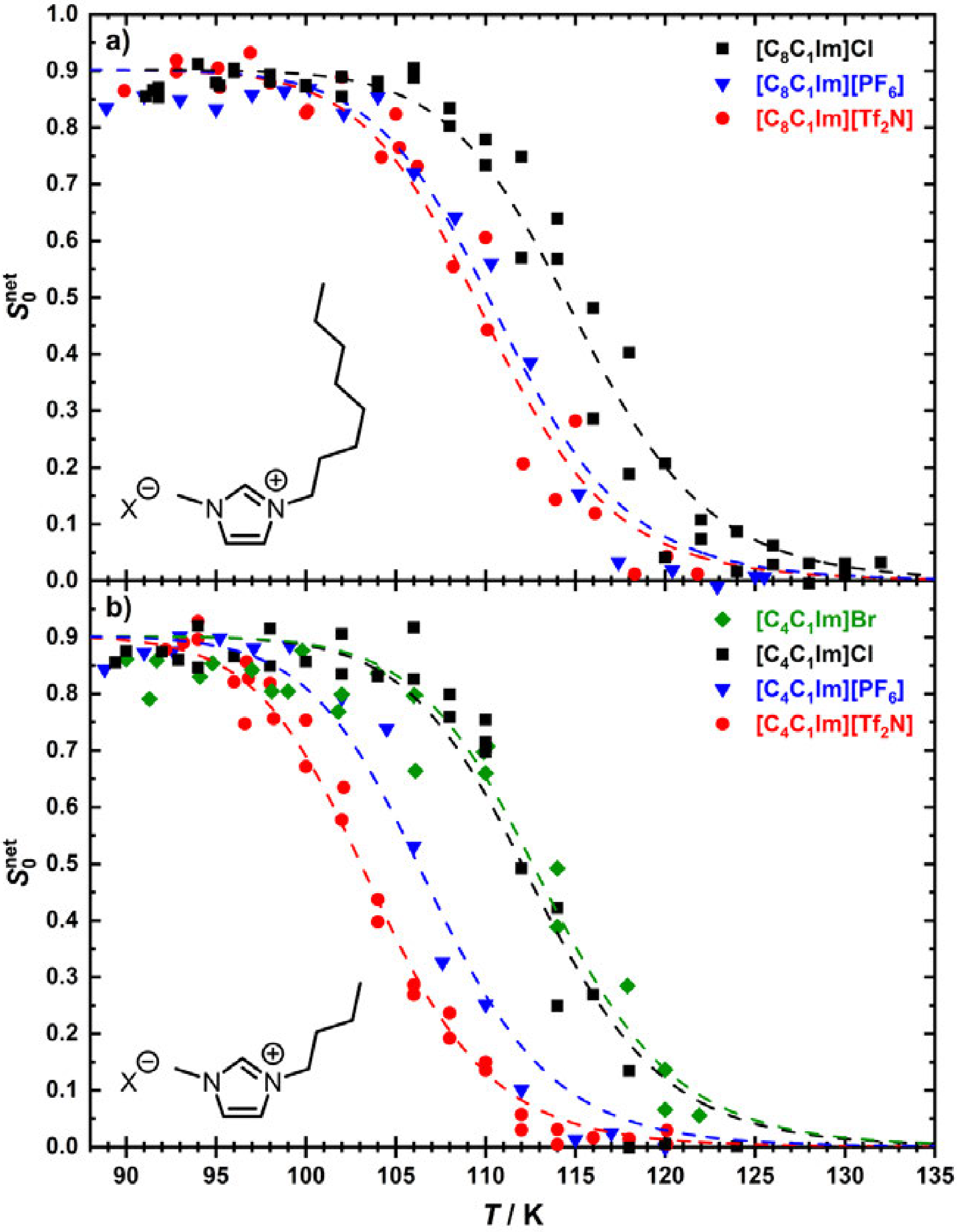

Figure 4.4: Temperature-dependent initial trapping probabilities S_0^{net} of *n*-butane on $[C_8C_1Im]X$ (**a**) and $[C_4C_1Im]X$ (**b**). X^- is varied between $[Tf_2N]^-$, $[PF_6]^-$, Br^- and Cl^-. The dashed lines are fits to the data using the model described in Chapter 4.2.2. Adapted from Ref[127] under the license CC BY-NC-ND 4.0.

4.1.3 Effect of Hydrocarbon [P3]

In Chapters 4.1.1 and 4.1.2, the influence of the IL structures on the trapping of *n*-butane as a model hydrocarbon was discussed. It will be shown in this chapter that the nature of the adsorbing hydrocarbon also influences the adsorption dynamics by comparing the trapping of *n*-butane with two other C4-hydrocarbons – *iso*-butane and 1-butene. The temperature-dependent initial trapping probabilities of these three hydrocarbons on [C_8C_1Im][Tf_2N] are shown in Figure 4.5.

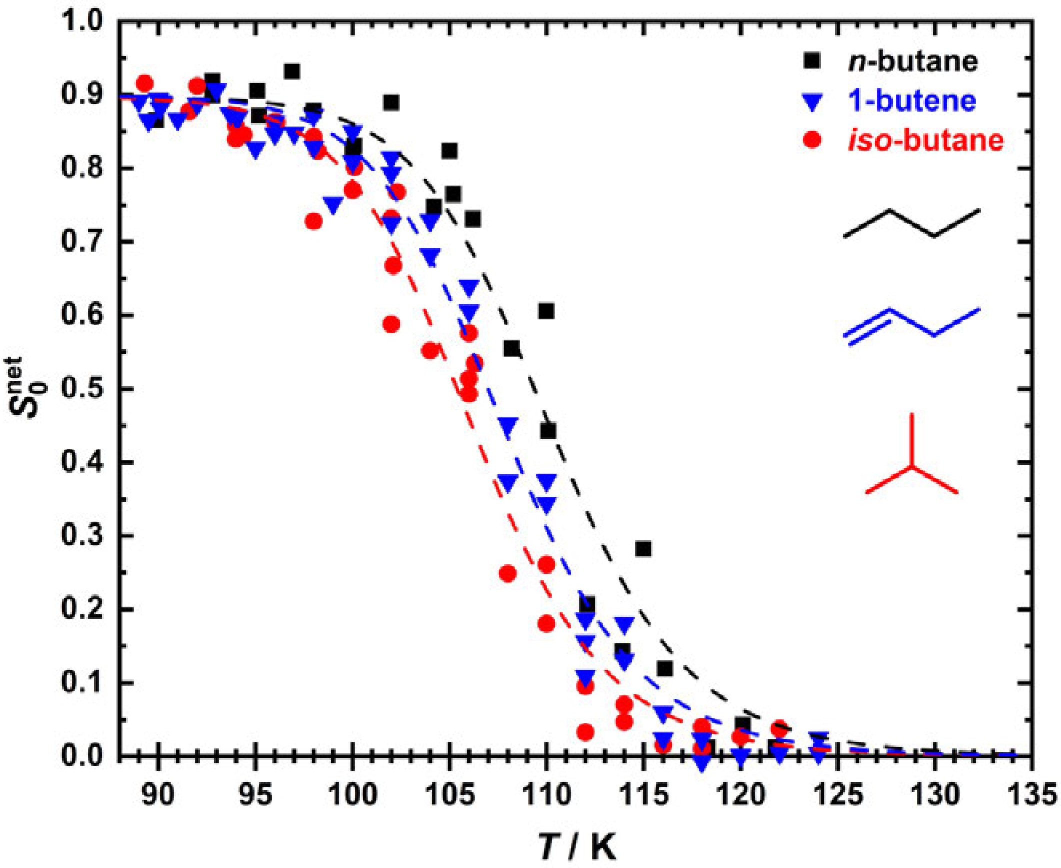

Figure 4.5: Temperature-dependent initial trapping probabilities of *iso*-butane, 1-butene and *n*-butane on [C_8C_1Im][Tf_2N]. The dashed lines are fits to the data using the model described in Chapter 4.2.2. Adapted from Ref[127] under the license CC BY-NC-ND 4.0.

At $T \approx 90$ K, all three hydrocarbons adsorb with the same trapping probability of $S_0^{net} \approx 0.9$. Thus, thermal accommodation at our experimental conditions has the same efficiency in all three cases, although principally the different structures could lead to different energy transfer mechanisms. With increasing temperature, the S_0^{net} of *iso*-butane and 1-butene show a similar decrease as the S_0^{net} of *n*-butane. However, the decrease is shifted by ≈ 2 K (1-butene) or ≈ 4 K (*iso*-butane) to lower temperature. The observed behavior reveals that the interaction strength between the $[C_8C_1Im][Tf_2N]$ surface and the hydrocarbons decreases in the order *n*-butane > 1-butene > *iso*-butane, which can be correlated with the trend in the enthalpies of vaporization of the pure hydrocarbons.[128] They decrease in the same order, because of decreasing dispersion forces between one molecule and its neighbors of the same kind. In a simple picture, this can be explained by more efficient intermolecular alignment of elongated compared to ball-like molecules. For the IL surface, a similar situation can be expected: The longish *n*-butane molecule will align better with the ILs' octyl chains than the ball-like *iso*-butane, with 1-butene lying somewhere in between.

4.2 Determination of the Desorption Energy [P1-2]

This chapter introduces two different strategies developed in this thesis to determine the desorption energy of *n*-butane from IL surfaces. As mentioned above, *n*-butane physisorbs on the IL, that is, it is bound to the IL surface by van-der-Waals interactions. Since physisorption is a non-activated process, the determined value for the desorption energy is equal to the binding energy to the surface.[129]

4.2.1 Arrhenius-Type Approach [P1]

The method introduced in this subchapter is based on analyzing the coverage-dependent net trapping probability $S^{\text{net}}(\theta)$. While the definition of $S(\theta)$ as “pure” trapping probability only considers the adsorption process, the actually measured quantity is a “net” trapping probability $S^{\text{net}}(\theta)$ representing the balance between the adsorption rate and the desorption rate (normalized to the impingement rate):

$$S^{net}(\theta) = \frac{R_{ads}(\theta) - R_{des}(\theta)}{R_{imp}} \tag{4.1}$$

As explained in Chapter 2.1.2, the coverage can be obtained by integrating the time-dependent trapping probability $S^{\text{net}}(t)$. In that way, a plot of $S^{\text{net}}(\theta)$ of *n*-butane on $[C_8C_1Im][Tf_2N]$ can be created for different temperatures (see Figure 4.6a). At 90 K, $S^{\text{net}}(\theta)$ stays constant at ≈ 0.9, independent of the coverage θ. This means that desorption is negligible and *n*-butane multilayers grow after completion of the first layer – and that with the same trapping probability. At higher temperatures, $S^{\text{net}}(\theta)$ decreases with increasing θ, because the desorption rate is now not negligible anymore. The desorption rate is expected to increase with increasing coverage, so $S^{\text{net}}(\theta)$ should decrease until the first layer is filled. The approximate coverage required to fill the first layer is marked by a vertical dotted line in Figure 4.6a.

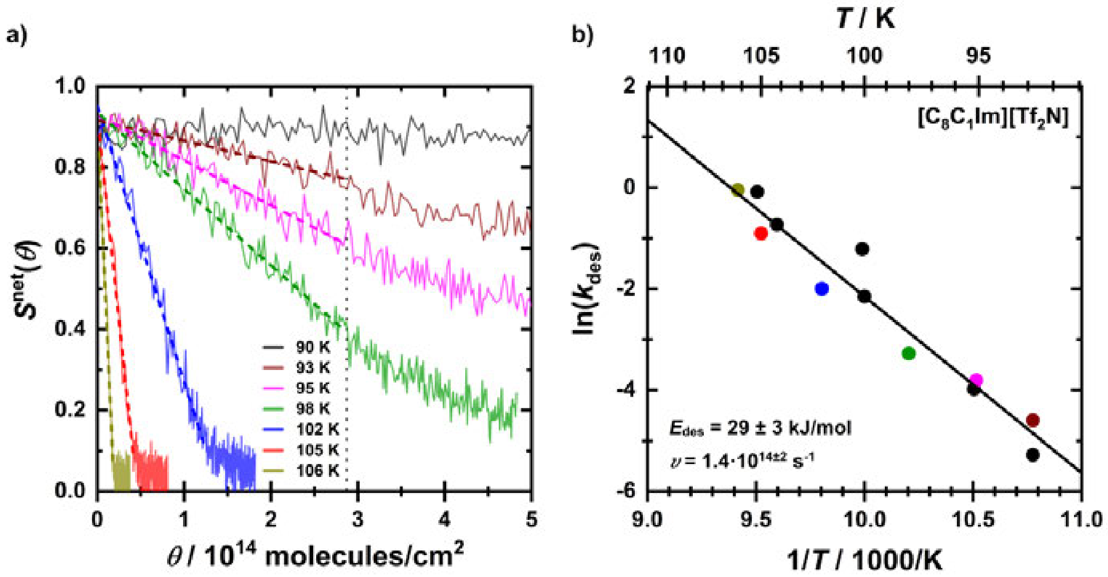

Figure 4.6: a) Coverage-dependent net trapping probability $S^{net}(\theta)$ of *n*-butane on [C_8C_1Im][Tf_2N] for different temperatures. The dashed lines indicate linear fits to the data. The estimated coverage to fill the first layer is indicated by a vertical dotted line. The underlying estimation follows the assumption that the *n*-butane saturation coverage on Ni(111) at 102 K is equal to $2.87 \cdot 10^{14}$ molecules/cm^2 (The lateral density of a free-standing *n*-butane layer).[130] **b)** Arrhenius analysis of the rate constants determined from the linear fits to a). The colored symbols in b) correspond to the respective curves in a). Adapted from Ref[126] under the license CC BY-NC-ND 4.0.

Figure 4.6a shows that $S^{net}(\theta)$ decreases linearly in the low-coverage regime, which can be explained by a simple model: The first assumption of the model is that $S(\theta)$ does not change with coverage in the measured temperature range, which can be directly observed for the case at 90 K (black curve), where desorption is negligible. With this assumption a constant adsorption rate follows:

$$R_{ads} = S(\theta)\, R_{imp} = S_0\, R_{imp} \tag{4.2}$$

With time, an increasing surface coverage θ builds up. Assuming simple first-order desorption, the desorption rate R_{des} is given by:[129]

$$R_{des} = \theta\, \nu\, e^{-\frac{E_{des}}{R\,T}} \tag{4.3}$$

If the desorption energy E_{des} and the pre-exponential frequency factor ν are coverage-independent, a linear decrease of $S^{net}(\theta)$ with increasing θ is expected from combining (4.1), (4.2) and (4.3):

$$S^{net}(\theta) = \frac{S_0\, R_{imp} - \theta\, \nu\, e^{-\frac{E_{des}}{R\,T}}}{R_{imp}} = S_0 - \frac{\nu\, e^{-\frac{E_{des}}{R\,T}}}{R_{imp}}\, \theta \tag{4.4}$$

From linear fits to the data (see dashed lines in Figure 4.6a), $k_{des} = \nu\, e^{-\frac{E_{des}}{R\,T}}$ can be extracted. The k_{des} for the different temperatures are then analyzed in an Arrhenius plot (see Figure 4.6b). The linear fit results in a desorption energy $E_{des} = 29 \pm 3$ kJ/mol and a pre-exponential factor $\nu = 1.4 \cdot 10^{14 \pm 2}$ s^{-1}.

4.2.2 Initial Trapping Probability Approach [P2]

In this subchapter, an alternative method to determine the trapping probability is introduced. As discussed previously, desorption is negligible at low temperatures ($T \leq 90$ K). Therefore, the net trapping probability at low temperature (in our case 90 K), S^{LT}, represents also the trapping probability in its narrow sense:

$$S^{LT} = \frac{R_{ads}}{R_{imp}} \Leftrightarrow R_{ads} = S^{LT} \cdot R_{imp} \tag{4.5}$$

Using the assumption, that R_{ads} is constant in the temperature range of interest (in our case 90 to 130 K), one obtains:

$$S^{net} = \frac{S^{LT} \cdot R_{imp} - R_{des}}{R_{imp}} = S^{LT} - \frac{R_{des}}{R_{imp}} \tag{4.6}$$

In this chapter, the focus will now be put on the trapping probability in the low coverage limit S_0^{net}. Precisely, the low coverage is regarded as the time interval $[0; t_m]$ required to measure the first data point after opening the sample flag: t_m in this case is the measurement time per data point, that is, 0.5 s. In this short time interval, a small coverage θ_0 already adsorbs on the surface, which results in a certain desorption rate $R_{des,0}$. During the time interval, θ_0 and $R_{des,0}$ will increase, so they can be approximated by their values in the middle of the time interval, i.e., at $t_m/2$. Using Equations (4.3) and (2.5), one obtains:

$$R_{des,0} = \theta\left(t = \frac{t_m}{2}\right) \nu\, e^{-\frac{E_{des}}{RT}} = R_{imp} \left(\int_0^{\frac{t_m}{2}} S_0^{net}\, \mathrm{d}t \right) \nu\, e^{-\frac{E_{des}}{RT}} \tag{4.7}$$

Approximating S_0^{net} as a constant in this short time interval, it follows:

$$R_{des,0} = R_{imp}\, S_0^{net}\, \frac{t_m}{2}\, \nu\, e^{-\frac{E_{des}}{RT}} \tag{4.8}$$

Combining with Equation (4.6) and solving for S_0^{net} yields:

$$S_0^{net} = S^{LT} - \frac{R_{des,0}}{R_{imp}} = S^{LT} - S_0^{net}\,\frac{t_m}{2}\,\nu\,e^{-\frac{E_{des}}{RT}} \tag{4.9}$$

$$\Rightarrow S_0^{net} = \frac{S^{LT}}{1 + \frac{t_m}{2}\,\nu\,e^{-\frac{E_{des}}{RT}}} \tag{4.10}$$

Equation (4.10) is a model that can describe the data shown in Figures 4.3, 4.4 and 4.5 very well. S^{LT} thereby is the value of the measurement at LT (in our case ≈ 0.9) and t_m is given by the experimental conditions. The two remaining unknowns, E_{des} and ν, are strongly coupled, so that simultaneous fitting does not give reliable results. It is, however, possible to use the pre-exponential factor $\nu = 1.4 \cdot 10^{14\pm2}$ 1/s determined in Chapter 4.2.1 for *n*-butane on $[C_8C_1Im][Tf_2N]$, under the assumption that this pre-factor is applicable to all “hydrocarbon on IL” systems studied in this work.

Table 4.1: Overview of the desorption energies of *n*-butane on ILs consisting of different cations (columns) and anions (rows). The desorption energy was determined from $S_0^{\mathrm{net}}(T)$ as described in this chapter. The relative uncertainty is estimated to be ±0.3 kJ/mol.

E_{des} / kJ/mol	$[C_3C_1Im]^+$	$[C_4C_1Im]^+$	$[C_8C_1Im]^+$
$[Tf_2N]^-$	26.8	26.9	28.6
$[PF_6]^-$		27.7	28.8
Br^-		29.4	
Cl^-		29.3	29.9

The desorption energies resulting from fits to the data in Figures 4.3 and 4.4 are summarized in Table 4.1. Due to the uncertainty in the prefactor and the absolute temperature scale, the absolute uncertainty of the desorption energies is estimated to ±2 kJ/mol. However, when comparing differences in desorption energy values the uncertainty is estimated to ±0.3 kJ/mol. The agreement between the result for $[C_8C_1Im][Tf_2N]$, which is 28.6±2 kJ/mol, and the corresponding desorption energy determined in Chapter 4.2.1, which was 29±3 kJ/mol, is very good. The analysis from Chapter 4.2.1 has the advantage, that it can provide values for E_{des} and ν at the same time. However, this Arrhenius-type approach can only be applied, if (a) the trapping probability (in its narrow sense) is coverage-independent over a considerable coverage range, and (b) the desorption rate is measurable, but also low enough to enable the formation of a considerable adsorbate layer. Especially the latter prerequisite is not fulfilled for all ILs studied in this work so that the systematic comparison in Chapter 4.3 will rely on values determined by the initial trapping probability approach presented in this chapter.

Note that Table 4.1 shows two trends: Firstly, E_{des} increases in the rows from left to right, which is with increasing alkyl chain length. Secondly, E_{des} increases down the columns, which is with decreasing size of the anion. These effects will be more thoroughly discussed in the following chapter by making a correlation with the structuring of the alkyl chains at the IL surface.

4.3 Correlation of Desorption Energy and Surface Structure [P3]

As it was mentioned in the previous chapters, the *n*-butane desorption energy increases with decreasing anion size. The anion size of different ILs with the same cation can be easily quantified by the molecular volume, which can be determined from literature density data.[131] Figure 4.7a shows the corresponding plot of E_{des} versus molecular volume. E_{des} decreases steeply from the halide anions to $[PF_6]^-$ and then more shallow towards $[Tf_2N]^-$. This holds for both groups of ILs that were investigated – $[C_8C_1Im]X$ and $[C_4C_1Im]X$. This empirical correlation is, however, not a satisfying explanation, since a surface-related quantity like E_{des} should depend on surface properties rather than the bulk property molecular volume.

Previous theoretical and experimental studies suggest that the size of the anion strongly influences the degree of surface enrichment of alkyl chains of the cation pointing towards the vacuum.[75, 79, 92, 97, 119, 132-137]. Angle-resolved X-ray photoelectron spectroscopy (see also Chapter 2.2) can be conveniently used to quantify the degree of alkyl chain enrichment. This can be done by looking at the C 1s region, where two distinct peaks of the $[C_nC_1Im]^+$ cation are observed; one for the carbon atoms bound to at least one nitrogen atom (called C_{hetero}) and one for the carbon atoms only bound to carbon and hydrogen (called C_{alkyl}). From the stoichiometry of the IL, the intensity ratio of the peaks $I_{\mathrm{C\ 1s}}(C_{\mathrm{alkyl}})$ / $I_{\mathrm{C\ 1s}}(C_{\mathrm{hetero}})$ is expected to be 7:5 = 1.4 for $[C_8C_1Im]X$ and 3:5 = 0.6 for $[C_4C_1Im]X$. The measurements in the more bulk sensitive 0° emission angle agree with these theoretically expected values, but for measurements in the surface-sensitive emission angle of 80°, ratios higher than the nominally expected ones were obtained.[119, 132-133] The peak ratios at 80° emission can be used to compare the different degrees of alkyl chain enrichment for different ILs. Their analysis showed that the degree of enrichment increases with increasing chain length[132] and with decreasing anion size[133]. The anion size effect is explained by a denser packing of the imidazolium cations if they are built into an ionic sublayer with smaller anions, leading to a denser packing of the protruding alkyl chains. In Figure 4.7b, literature values of $I_{\mathrm{C\ 1s}}(C_{\mathrm{alkyl}})$ / $I_{\mathrm{C\ 1s}}(C_{\mathrm{hetero}})$ ratios are plotted versus the molecular volume for selected ILs.

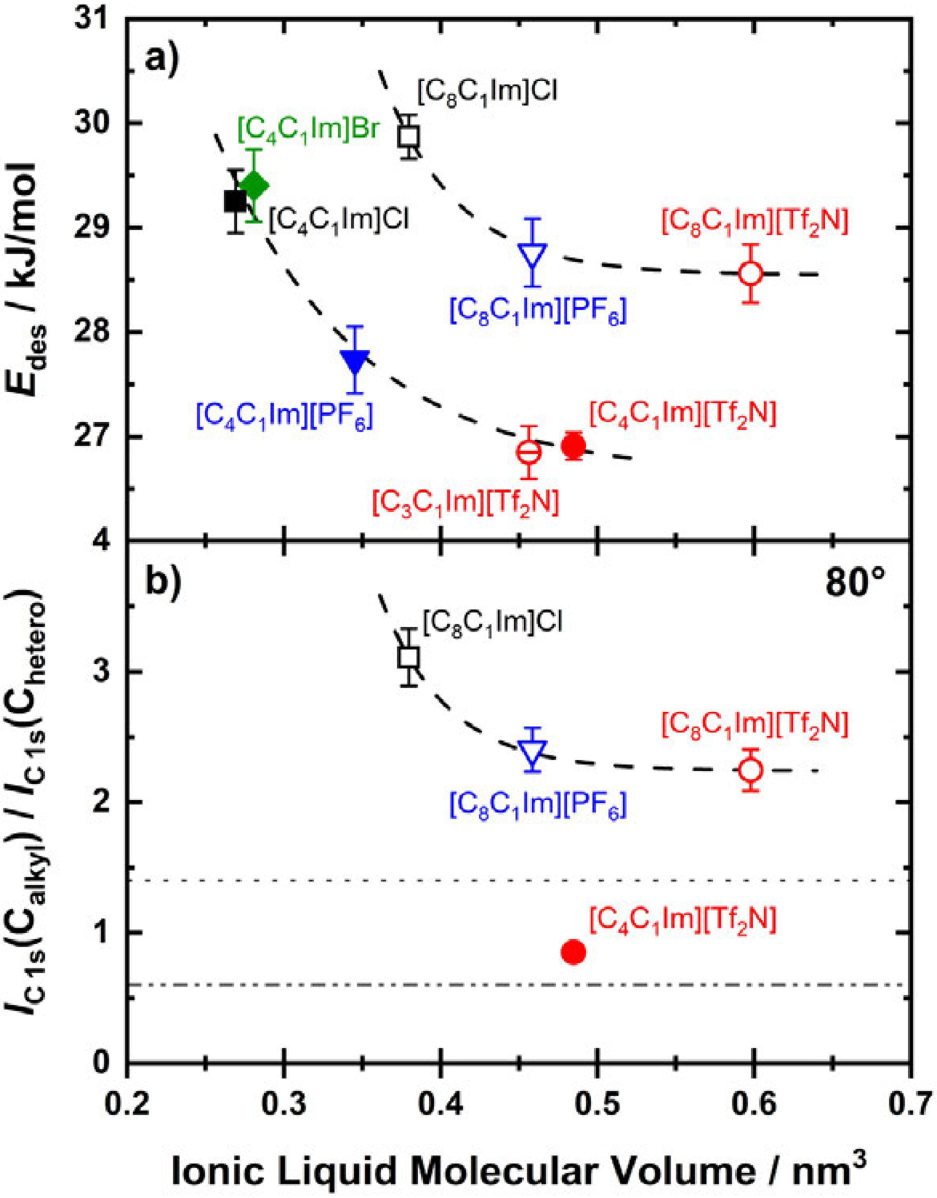

Figure 4.7: a) *n*-Butane desorption energy compared to **b)** the alkyl chain surface enrichment as measured by ARXPS. The data are plotted versus the IL molecular volume, which provides a measure for the anion sizes. The ILs are grouped using color codes and open/filled symbols, and the dashed lines are thought to serve as a guide for the eye. The IL densities at 298.15 K, 101.325 kPa (taking the average over the values published in the ILThermo database from NIST[131]) were used to calculate the IL molecular volume. The error bars estimate the uncertainty, assuming an identical prefactor for all ILs (for details see Chapter 4.2.2). The data from (b) were originally published in different studies of the Steinrück/Maier group.[132-133] The dotted and dash-dotted horizontal lines in (b) indicate the stoichiometrically expected $I_{C\ 1s}(C_{alkyl})$ / $I_{C\ 1s}(C_{hetero})$ ratios for [C$_8$C$_1$Im]X (= 1.4) and [C$_4$C$_1$Im]X (= 0.6), respectively. Adapted from Ref[127] under the license CC BY-NC-ND 4.0.

Figure 4.7 clearly demonstrates that the two quantities E_{des} and $I_{\mathrm{C\,1s}}(\mathrm{C_{alkyl}})$ / $I_{\mathrm{C\,1s}}(\mathrm{C_{hetero}})$ display the same trends – a steep decrease from $\mathrm{Cl^-}$ (black symbols) to $[\mathrm{PF_6}]^-$ (blue), a more shallow further decrease to $[\mathrm{Tf_2N}]^-$ (red) and a strong increase from $[\mathrm{C_4C_1Im}]\mathrm{X}$ (full symbols) to $[\mathrm{C_8C_1Im}]\mathrm{X}$ (open symbols). This implies that the interaction strength of *n*-butane with the IL surface depends strongly on the degree of alkyl chain enrichment. This interpretation fits the observation that the interaction of *n*-butane with ILs based on the $[\mathrm{C_2C_1Im}]^+$ or $[\mathrm{C_1C_1Im}]^+$ cations is very weak (see Chapter 4.1.1). Consequently, the interactions of *n*-butane with surfaces of imidazolium-based ILs are dominated by interactions with the alkyl chains.

4.4 C4-Hydrocarbon Sticking on the $[C_1C_1Im][Tf_2N]/Pt(111)$ surface [P4]

In the last results chapter, the focus moves away from the trapping dynamics of saturated C4-hydrocarbon physisorption at the outer surface of pure ILs at around 100 K to the chemisorption dynamics of C4-olefins on IL-modified Pt(111). Chapter 4.4.1 will address the adsorption dynamics of 1,3-butadiene and 1-butene on clean Pt(111). Chapter 4.4.2 will present how the adsorption changes, if the Pt(111) surface is modified with ultrathin films of the imidazolium-based IL $[C_1C_1Im][Tf_2N]$. Finally, in Chapter 4.4.3 the effects of preadsorbed hydrogen will be discussed. Studying the selectivity of 1,3-butadiene versus 1-butene adsorption on $[C_1C_1Im][Tf_2N]$-modified Pt(111) surfaces is crucial in the context of SCILL catalysis for the selective hydrogenation of 1,3-butadiene (see also Chapter 1).

4.4.1 Adsorption Dynamics on Pt(111)

Figure 4.8a shows the time-dependent sticking coefficient for the adsorption of 1,3-butadiene (green curve) and 1-butene (red curve) on clean Pt(111) at 180 K. As was already mentioned in Chapter 2.1.2, it is more intuitive to discuss the coverage-dependent sticking coefficient $S(\theta_{\mathrm{olefin}})$ using the uncalibrated coverage determined from integrating $S(t)$ (compare also with Equation (2.6)):

$$\theta_{olefin} = \int_0^t S(t)\,dt \tag{4.11}$$

Following this approach, the green line in Figure 4.8b shows the $S(\theta_{\mathrm{butadiene}})$ curve for the sticking of 1,3-butadiene on clean Pt(111) at 180 K. For low coverages, $S(\theta_{\mathrm{butadiene}})$ stays constant at ≈ 0.87, until it eventually decreases and rapidly approaches zero at $\theta_{\mathrm{butadiene}} \approx 8$ (note that the uncalibrated coverage defined by Equation (4.11) bears the unit “seconds”; to avoid any confusion, θ_{olefin} values are given without unit in the text, and in the figures “arbitrary units” are indicated at the coverage axis). Such an $S(\theta)$ trace is typical for precursor-mediated adsorption.[129, 138] In the precursor model, the impinging molecule is trapped into a loosely bound precursor state at first. From there final chemisorption can then occur. Because of the high mobility in the precursor state on top of already covered surface regions, the adsorption process stays efficient even if a considerable share of the adsorption sites are blocked.[129, 138-139] Note that in this case the decrease of $S(\theta)$ is attributed to site-blocking and not to an increasing desorption rate as it was previously the case in Chapter 4.2.1.

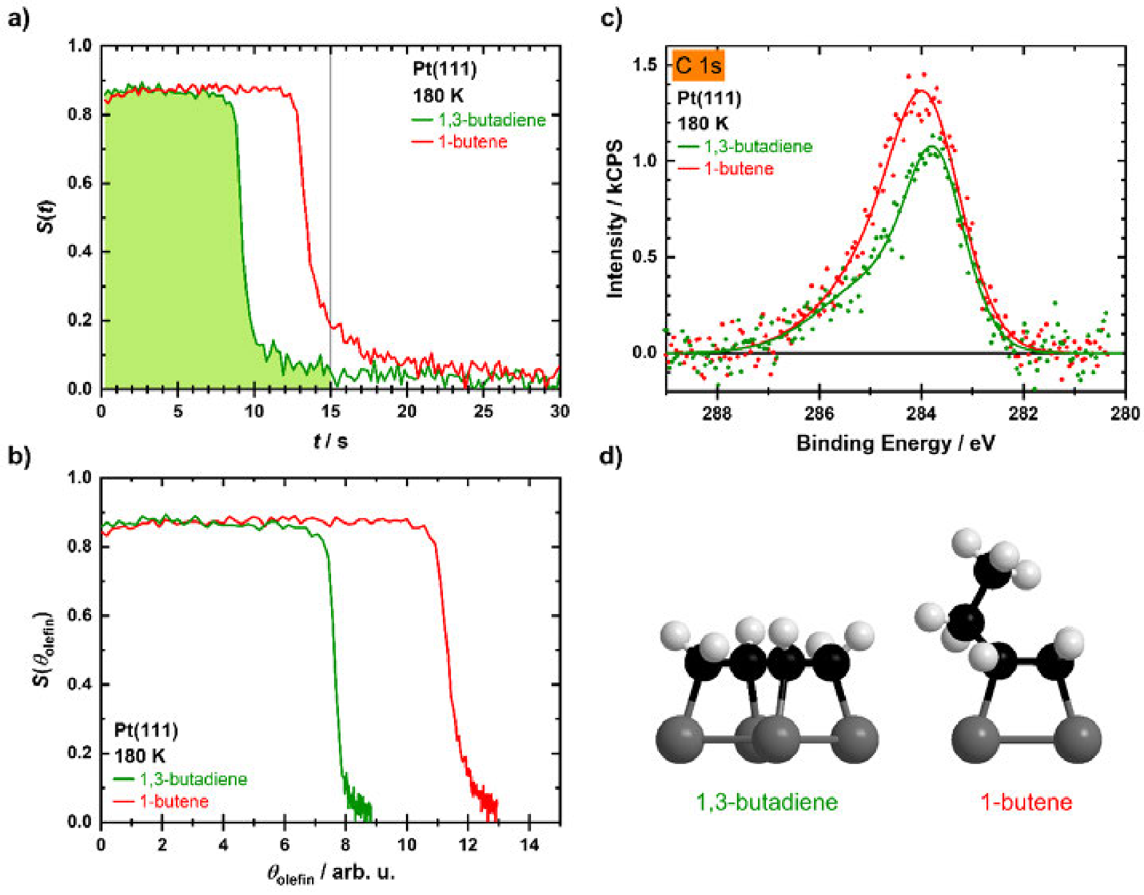

Figure 4.8: a) The time-dependent sticking coefficient $S(t)$ of 1-butene (red) and 1,3-butadiene (green) on clean Pt(111) at 180 K. The uncalibrated olefin coverage θ_{olefin} can be obtained from the area below the $S(t)$ curve. **b)** The olefin coverage-dependent sticking coefficient $S(\theta_{\text{olefin}})$ derived from the plots in a). **c)** XP spectra of the C 1s region measured after the adsorption experiments shown in a) and b). **d)** Sketches of the most stable adsorption structures of 1,3-butadiene – a *trans*-1,2,3,4-tetra-σ complex – and 1-butene – a 1,2-di-σ complex – on Pt(111). Adapted from Ref[140] under the license CC BY-NC-ND 4.0.

Also for the red curve in Figure 4.8b, which shows the adsorption of 1-butene on clean Pt(111) at 180 K, $S(\theta_{\text{butene}})$ remains constant at ≈ 0.87, until it quickly decreases to zero at $\theta_{\text{butene}} \approx 11$. This shows that 1-butene follows precursor dynamics, too, but in this case, $S(\theta_{\text{butene}})$ only starts to drop at higher coverages. The difference can be explained by a factor ≈ 1.4 higher saturation coverage of the 1-butene monolayer compared to the 1,3-butadiene monolayer on Pt(111) at 180 K. The XP spectra (see Figure 4.8c) measured after the adsorption experiments support this interpretation, because the C 1s intensity of the saturated 1-butene layer is by a factor of ≈ 1.3 higher than the one of the 1,3-butadiene layer. This finding can be related to the different footprints of the two olefins due to the different adsorption geometries (see Figure 4.8d).

4.4.2 Adsorption Dynamics on [C_1C_1Im][Tf_2N]/Pt(111)

The effect of the IL film on the adsorption dynamics of 1,3-butadiene and 1-butene on Pt(111) was studied by measuring $S(t)$ and $S(\theta_{\mathrm{olefin}})$ for different IL pre-coverages θ_{IL} (see Figure 4.9). The IL film preparation was done at 180 K, and the olefins were also adsorbed at 180 K.

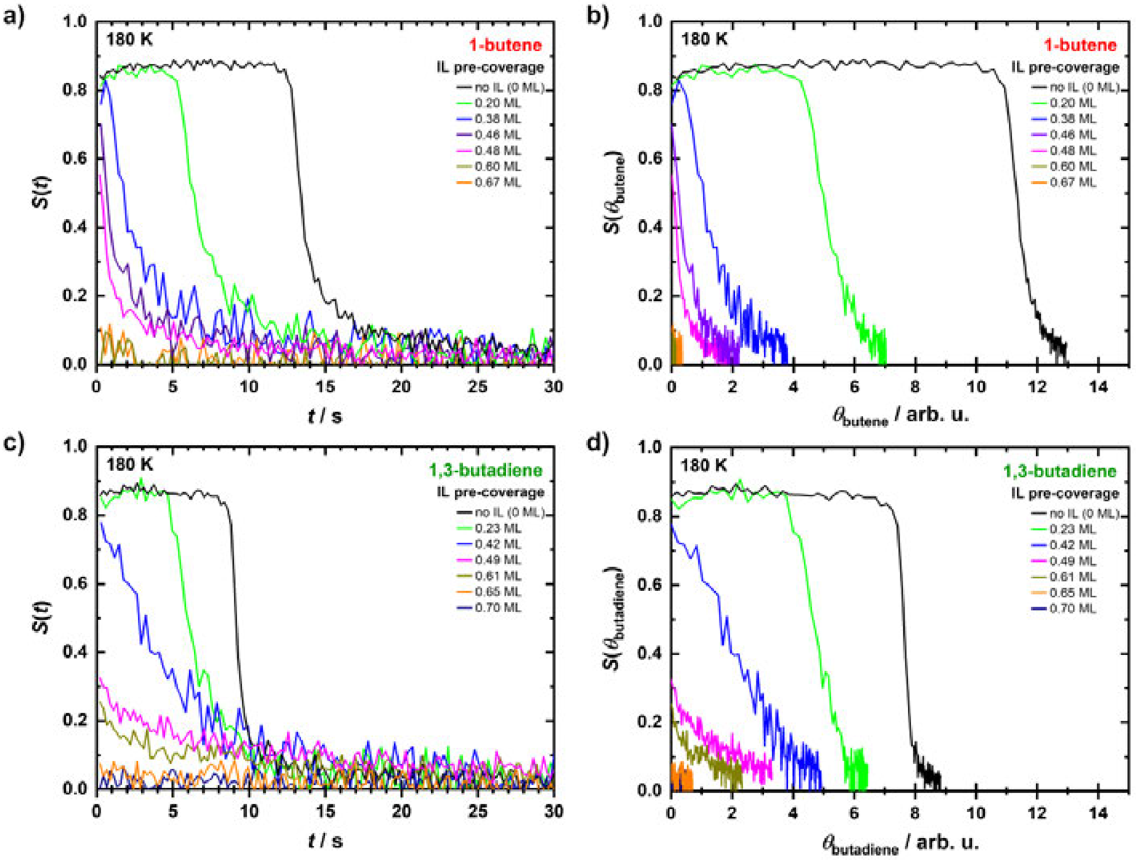

Figure 4.9: **a)** Time-dependent sticking coefficient $S(t)$ and **b)** coverage-dependent sticking coefficient $S(\theta_{\mathrm{butene}})$ of 1-butene on Pt(111) for different IL pre-coverages θ_{IL} at 180 K. **c)** Time-dependent sticking coefficient $S(t)$ and **d)** coverage-dependent sticking coefficient $S(\theta_{\mathrm{butadiene}})$ of 1,3-butadiene on Pt(111) for different IL pre-coverages θ_{IL} at 180 K. Adapted from Ref[140] under the license CC BY-NC-ND 4.0.

At a low IL pre-coverage of $\theta_{\mathrm{IL}} = 0.20$ ML, 1-butene has the same initial sticking coefficient S_0 as on clean Pt(111) (see green curves in Figure 4.9a and b). Similar to the clean Pt(111) surface, $S(\theta_{\mathrm{butene}})$ stays at the same constant value of ≈ 0.87, until at $\theta_{\mathrm{butene}} \approx 5$ it steeply decreases to zero, which is earlier than $\theta_{\mathrm{butene}} \approx 11$ found on clean Pt(111) (black curve). Further increasing θ_{IL}, shifts the drop of the $S(\theta_{\mathrm{butene}})$ curve to lower 1-butene coverages (blue curve). For $\theta_{\mathrm{IL}} > 0.40$ ML, also S_0 begins to decrease (purple and magenta curves). In the IL pre-coverage regime above $\theta_{\mathrm{IL}} = 0.55$ ML, no significant 1-butene adsorption is detectable anymore (dark yellow and orange curves).

While the overall behavior of 1,3-butadiene adsorption (see Figure 4.9c and d) appears to be similar to the one of 1-butene, there are remarkable differences: In the IL pre-coverage regime of $\theta_{\mathrm{IL}} \approx 0.4$ to 0.5 ML, the $S(\theta_{\mathrm{butadiene}})$ traces decrease much more shallow with increasing olefin coverage, so that a higher $S(\theta_{\mathrm{olefin}})$ is observed for a given olefin coverage (e.g. $\theta_{\mathrm{olefin}} = 2$) as compared to 1-butene (compare blue and magenta curves in Figure 4.9b and d). Most obvious is this effect at $\theta_{\mathrm{IL}} \approx 0.6$ ML (dark yellow curves), where 1,3-butadiene has an initial sticking coefficient $S_0 \approx 0.2$, while 1-butene shows no sticking.

In Figure 4.10a, the 1-butene saturation coverage $\theta_{\mathrm{butene,SAT}}$ is plotted versus the IL pre-coverage θ_{IL} for IL films prepared at 180 K (full squares, colors matching the experiments in Figure 4.9a). $\theta_{\mathrm{butene,SAT}}$ decreases linearly until $\theta_{\mathrm{IL}} = 0.55$ ML, where the linear fit intercepts the abscissa. This trend indicates that the IL increasingly blocks 1-butene adsorption sites, until at $\theta_{\mathrm{IL}} = 0.55$ ML all sites are blocked. Similarly as for 1-butene, $\theta_{\mathrm{butadiene,SAT}}$ also decreases linearly with increasing θ_{IL} (see Figure 4.10b, full squares), but the interception of the linear fit with the θ_{IL}-axis is found at a higher IL coverage of $\theta_{\mathrm{IL}} = 0.75$ ML. Consequently, substantial 1,3-butadiene adsorption is still feasible at IL pre-coverages approaching a closed IL layer, while 1-butene adsorption does not occur in this coverage regime.

The observed difference between 1,3-butadiene and 1-butene can be explained in the following way: 1,3-Butadiene is bound by approximately 70 kJ/mol stronger to Pt(111) as 1-butene (-143 versus -72 kJ/mol[141], or -156 versus -83 kJ/mol[142]), which represents a larger driving force for squeezing in additional 1,3-butadiene molecules into an already densely packed IL layer. The experimental results show that the required rearrangement of the IL film is more feasible in the case of 1,3-butadiene adsorption as for 1-butene, which could also be due to the different adsorption geometries (see Figure 4.8d).

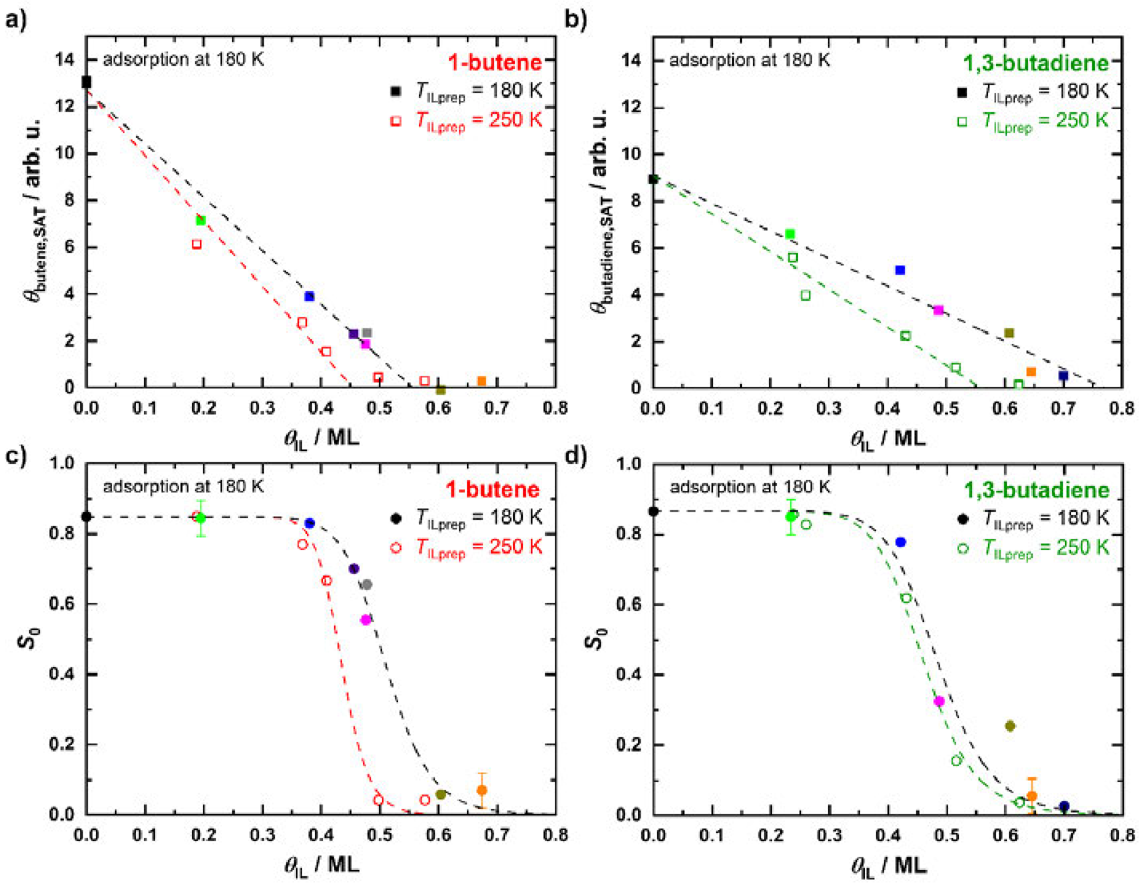

Figure 4.10: a) $\theta_{\mathrm{butene,SAT}}$, the 1-butene saturation coverage as determined from the area below the $S(t)$ curve, is plotted versus the IL pre-coverage θ_{IL}. **b)** The 1,3-butadiene saturation coverage $\theta_{\mathrm{butadiene,SAT}}$ plotted against the IL pre-coverage θ_{IL}. **c), d)** The initial sticking coefficients S_0 of 1-butene and 1,3-butadiene, respectively, in dependence of the IL pre-coverage θ_{IL}. The IL films prepared at 250 K are represented by open symbols, the films prepared at 180 K by closed symbols, whose colors match the colors of the curves in Figure 4.9. The dashed lines in a) and b) are linear fits to the data (not taking the data points with $\theta_{\mathrm{olefin}} \approx 0$ into account), the dashed lines in c) and d) are only a guide to the eye. In c) and d), exemplary error bars indicate the estimated uncertainty of ±0.05. Adapted from Ref[140] under the license CC BY-NC-ND 4.0.

To get further insights, the effective adsorption energies $E_{\mathrm{ads}}^{\mathrm{eff}}$ of both olefins on IL-modified Pt(111) were determined with QM/MM (quantum mechanics/ molecular mechanics) simulations that were performed by the group of Prof. Dirk Zahn in a collaboration.[140] At low θ_{IL}, $E_{\mathrm{ads}}^{\mathrm{eff}}$ is equal to the binding energy of the respective olefin on clean Pt(111). With increasing θ_{IL}, $E_{\mathrm{ads}}^{\mathrm{eff}}$ becomes less negative, i.e., the olefins are more weakly bound. For 1-butene, E_{ads}^{eff} finally becomes positive at ≈ 0.64 ML preventing a stable 1-butene coadsorption with IL films exceeding that coverage. In contrast, the tipping point of E_{ads}^{eff} becoming positive is found at ≈ 0.79 ML for 1,3-butadiene,[140] which fits to the experimental observation that a higher θ_{IL} is required to block 1,3-butadiene adsorption.

The experimental and theoretical results suggest that in an IL pre-coverage regime of around 0.5 to 0.7 ML, 1,3-butadiene adsorption is significantly preferred over 1-butene adsorption. Consequently, a Pt surface with such an IL layer is expected to be a highly selective catalyst for 1,3-butadiene hydrogenation. This result can be seen in the context of the test catalytic studies of the Jess group,[49-50] which showed that a SCILL catalyst with an IL loading corresponding to approximately a closed layer of IL ion pairs has an optimum selectivity.

As was already mentioned earlier, the initial sticking coefficient S_0 of 1-butene on IL-covered surfaces with $\theta_{IL} < 0.4$ ML is identical to that on clean Pt(111). Only at higher θ_{IL} (≈ 0.5 ML), S_0 drops to a value close to zero (see Figure 4.10c). Based on the precursor dynamics found for 1-butene on clean Pt(111), the following explanation is suggested: The mobile precursor state does not only exist on 1-butene adsorbates but also on IL-covered areas. In other words, 1-butene molecules are weakly bound as a precursor and can also diffuse on the IL islands and even cross boundaries of 1-butene- and IL-covered regions to finally arrive and adsorb at an empty adsorption site. For 1,3-butadiene, the overall behavior is comparable: S_0 stays initially constant with increasing θ_{IL} and then decreases for $\theta_{IL} > 0.3$ ML (see Figure 4.10d), so the precursor-mediated mechanism also applies for 1,3-butadiene on top of IL islands.

A very recent XPS and scanning tunneling microscopy (STM) study by the Steinrück group addresses the adsorption and thermal evolution of $[C_1C_1Im][Tf_2N]$ on Pt(111).[70] It shows that the IL is adsorbed intact below 200 K, but a reaction of the IL ions with Pt(111) occurs between 200 and 400 K. Thereby, a considerable amount of $[Tf_2N]^-$ anion decomposes and the resulting products desorb with the degree of decomposition and desorption depending on temperature. Despite the fact that the XPS signals of the $[C_1C_1Im]^+$ cations do not show major changes with increasing temperature, it is very likely that for charge neutrality reasons a similar amount of cations also reacts with the Pt(111) surface with the resulting (charge-neutral) decomposition products remaining adsorbed on the Pt(111) surface. The XPS measurements have been reproduced in this thesis (but are not shown).

To investigate how the onset of decomposition changes the adsorption properties of 1-butene and 1,3-butadiene, additional experiments were performed with IL films prepared at 250 K. As for the film prepared at 180 K, $\theta_{\mathrm{butene,SAT}}$ shows a linear decrease with increasing θ_{IL} (red open squares in Figure 4.10a). However, the intercept of the fit with the abscissa is shifted to a lower IL coverage of $\theta_{\mathrm{IL}} = 0.45$ ML for the IL layer prepared at 250 K, compared to the value of 0.55 ML for the IL layer prepared at 180 K. This lower saturation coverage can be explained in the following way: After decomposition, carbon and nitrogen-containing products (stemming from the cation) remain on the surface. They probably cover the surface forming a very flat thin film; therefore, a smaller amount of material is needed to block all adsorption sites as compared to an IL film also containing the quite voluminous intact $[Tf_2N]^-$ anion. Note that at 250 K, intact anions and cations are expected to be coadsorbed with decomposition products, i.e., the effect will only occur on a fraction of the surface. 1,3-Butadiene shows a similar trend (see green open squares in Figure 4.10b): $\theta_{\mathrm{butadiene,SAT}}$ shows a linear decrease until intersecting the IL coverage axis at $\theta_{\mathrm{IL}} = 0.55$ ML (for the IL layer prepared at 180 K, this occurred at 0.75 ML). The initial sticking coefficients S_0 (see Figure 4.10c and d) also change for IL films prepared at 250 K as compared to the 180 K IL film. The decrease of S_0 is shifted to lower IL pre-coverage, but overall still the same trend is observed. This observation shows that the partial IL decomposition does not affect the precursor dynamics.

4.4.3 Adsorption Dynamics on $[C_1C_1Im][Tf_2N]$/H/Pt(111)

For the hydrogenation reaction of 1,3-butadiene to 1-butene, the interplay of coadsorbed hydrogen and the olefins also plays an important role. To this end, the adsorption dynamics of 1,3-butadiene was studied on Pt(111) saturated with hydrogen, which adsorbs dissociatively on Pt(111).[143-144]

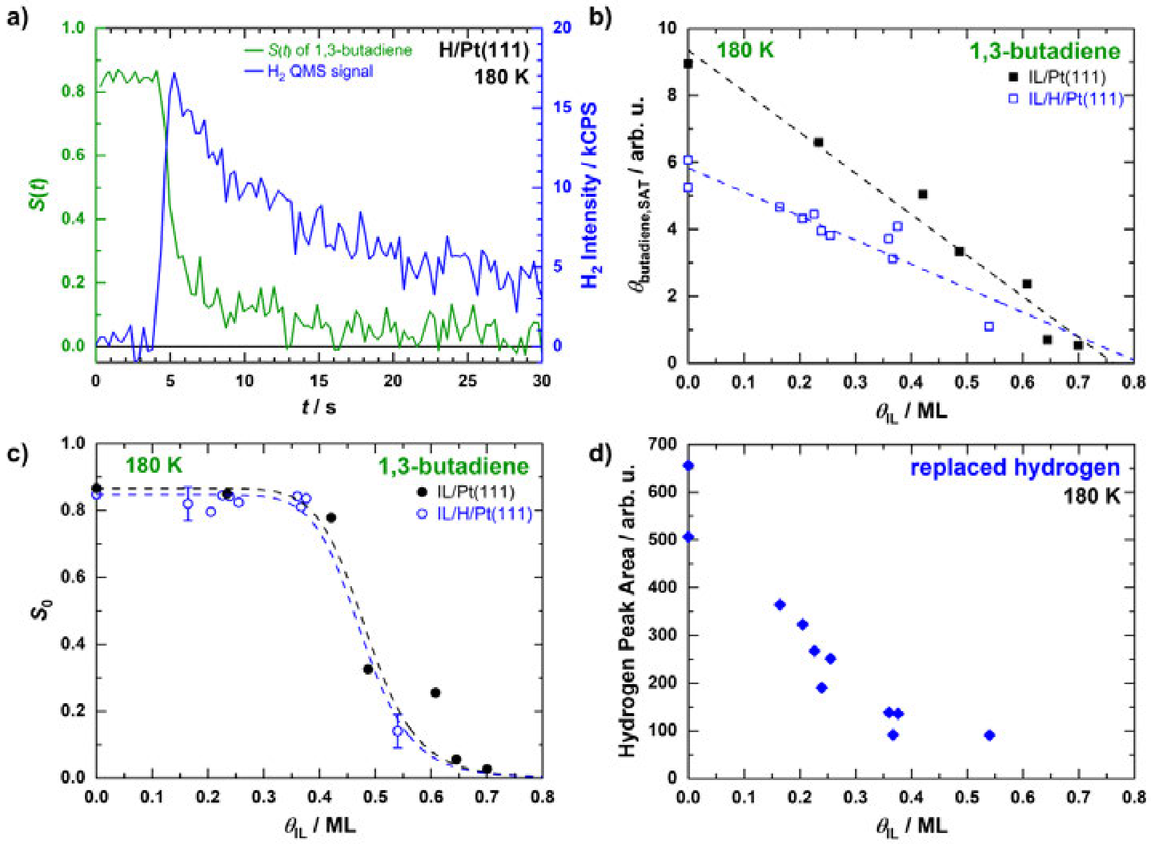

Figure 4.11: a) Time-dependent sticking coefficient $S(t)$ of 1,3-butadiene on Pt(111) saturated with hydrogen, together with the $m/z = 2$ signal, which is representative for the amount of desorbing H_2. **b)** 1,3-Butadiene saturation coverage $\theta_{\text{butadiene,SAT}}$ plotted against the IL pre-coverage θ_{IL} for a hydrogen-saturated Pt(111) surface (open blue squares) compared to the measurements on the hydrogen-free Pt(111) already shown in Figures 4.9 and 4.10 (filled black squares). Linear fits to the data are given by dashed lines. **c)** The initial sticking coefficient S_0 of 1,3-butadiene depending on the IL pre-coverage θ_{IL} for the hydrogen-free surface (filled black circles) and the hydrogen-saturated surface (open blue circles). The dashed lines are guides to the eye and the exemplary error bars represent the estimated uncertainty of ± 0.05. **d)** Amount of desorbing hydrogen from the hydrogen-saturated surface during 1,3-butadiene adsorption determined from peak integration. Adapted from Ref[140] under the license CC BY-NC-ND 4.0.

Figure 4.11a shows the $S(t)$ curve of 1,3-butadiene and the resulting desorption signal of hydrogen on the Pt(111) surface. As on clean Pt(111), 1,3-butadiene initially also has a sticking coefficient of ≈ 0.87, but already after ≈ 4 s, $S(t)$ drops rapidly to reach a value of ≈ 0.10 after 10 s (see green curve). The observed behavior can be compared to the clean Pt(111) surface, where the decrease of $S(t)$ only started after 10 s (see Figure 4.9c, black curve). This observation shows that precovering the surface with hydrogen eventually hampers the adsorption of 1,3-butadiene on the Pt(111) surface. Simultaneously to the decrease of $S(t)$, a pronounced increase of hydrogen desorption from the sample is observed (blue curve). These observations imply that initially a comparably low 1,3-butadiene coverage can be coadsorbed with the hydrogen layer and when this 1,3-butadiene coverage reaches a certain value, hydrogen is replaced from the surface. Notably, the 1,3-butadiene coverage reaches only about 63% of $\theta_{\mathrm{butadiene,SAT}}$ on clean Pt(111) (see Figure 4.11b), implying that the hydrogen is not replaced completely.

The measurements on clean Pt(111) yielded H_2 initial sticking coefficients between 0.02 and 0.08. If IL was preadsorbed (lowest tested coverage 0.19 ML), no H_2 sticking ($S_0 < 0.01$) was observed. An investigation from Auras et al. showed that the initial sticking coefficient of H_2 scales with the step density on Pt surfaces, reaching an almost vanishing value of approximately 0.025 for the Pt(111) facet.[145] The finding of a sticking coefficient below the detection limit on the [C_1C_1Im][Tf_2N]/Pt(111) surface could be explained in the following way: All remaining steps and defect sites on the Pt crystal are decorated by IL ion pairs and therefore, H_2 adsorption is prohibited even for low θ_{IL}.

Nevertheless, the adsorption dynamics of 1,3-butadiene on Pt(111) with coadsorbed hydrogen and [C_1C_1Im][Tf_2N] can be studied by reversing the deposition sequence: Firstly, the Pt(111) surface is saturated with hydrogen, secondly, [C_1C_1Im][Tf_2N] is evaporated onto this H/Pt(111) surface at 180 K, and finally, 1,3-butadiene is provided via the molecular beam. Figure 4.11c shows that the coadsorbed hydrogen does not significantly influence the S_0 of 1,3-butadiene. However, the adsorbed hydrogen decreases $\theta_{\mathrm{butadiene,SAT}}$ by about 37% compared to the hydrogen-free surface (see Figure 4.11b, open blue squares versus filled black squares). Similar to the hydrogen-free surface, $\theta_{\mathrm{butadiene,SAT}}$ still decreases linearly, and all adsorption sites are blocked at $\theta_{\mathrm{IL}} = 0.75$ ML. Figure 4.11d shows that the amount of hydrogen replaced from the surface by incoming 1,3-butadiene, as can be determined by integration of the $m/z = 2$ signal, decreases with increasing θ_{IL}.

5 Summary

Ionic Liquids (ILs) are applied in supported IL thin film catalysis with great success. The complementary Supported Ionic Liquid Phase (SILP) and Solid Catalyst with Ionic Liquid Layer (SCILL) approaches even have already found commercial applications. Since they are typically used in hydroformylation and hydrogenation reactions, knowledge about the adsorption dynamics and interactions of hydrocarbons at the relevant gas/IL/catalyst interfaces is crucial to gain a detailed understanding of these catalytic systems, which can serve as a basis for further improvement and new developments.

This thesis addresses the adsorption dynamics of a set of model C4-hydrocarbons – *n*-butane, *iso*-butane, 1-butene and 1,3-butadiene – at the gas/IL and the gas/IL/metal interface. Trapping probabilities and sticking coefficients are measured with the direct method of King and Wells using a supersonic molecular beam setup (see Chapter 2.1). The apparatus used in this thesis is a unique, newly developed ultra-high vacuum chamber consisting of a fast-entry load lock, a preparation chamber with an IL evaporator, and an analysis chamber with an XPS setup, a mass spectrometer, and a three-stage supersonic molecular beam. This setup and its characterization is described in detail in Chapter 3, and some additional material is provided in Appendix 8.5.

A first set of experiments deals with the physisorption of C4-hydrocarbons – *n*-butane, *iso*-butane and 1-butene – on the surface of frozen macroscopic films of 1-alkyl-3-methylimidazolium-based ILs $[C_nC_1Im]X$, where $n = 1, 2, 3, 4$ and 8 and $X^- = Cl^-, Br^-, [PF_6]^-$ and $[Tf_2N]^-$. On ILs with $n \geq 3$, *n*-butane adsorbs with an initial trapping probability of ≈ 0.9 at 90 K. In contrast, no *n*-butane trapping is found for ILs with $n \leq 2$, which is attributed to a too short residence time on the IL surface to form condensation nuclei even at 90 K. This finding shows that the binding energy is dominated by the interaction of *n*-butane with the alkyl chains of the IL cations, whereas the cationic headgroups and the anions contribute only weakly (see Chapter 4.1).

Two complementary methods were developed within this thesis, in order to obtain the desorption energies, which equal the adsorption energies, of hydrocarbons on IL surfaces. The first one uses the coverage- and temperature-dependent trapping probability to deduce the desorption energy and the associated pre-exponential factor in an Arrhenius-type approach. The second method is based on the temperature-dependent initial trapping probability. It needs fewer prerequisites, and therefore is successfully applied to the complete set of ILs with $n \geq 3$ (see Chapter 4.2).

Comparing ILs with different alkyl chains at the IL cation, the desorption energy of *n*-butane increases with increasing length of the alkyl chain. For ILs with different anions, the desorption energy increases with decreasing size of the anion. This effect is not attributed to different interaction strengths with the anions, but to a different degree of alkyl chain surface enrichment induced by different anions (see Chapter 4.3). Notably, the desorption energy also depends on the adsorbing molecule: It decreases in the order *n*-butane > 1-butene > *iso*-butane, which is attributed to dispersion interactions of different strengths.

The second set of experiments deals with the adsorption dynamics on an IL-modified metal surface, that is, Pt(111) with ultrathin layers of $[C_1C_1Im][Tf_2N]$. This system serves as a model system for a SCILL catalyst, which can be used to enhance the selectivity of hydrogenation reactions, like the selective hydrogenation of 1,3-butadiene to 1-butene. Both olefins adsorb on clean Pt(111) and on the IL-modified surface following a precursor-mediated mechanism. With increasing IL coverage, an increasing number of adsorption sites are blocked for the incoming olefins; notably, hydrogen does not affect the precursor and site-blocking effects for 1,3-butadiene in a major way.

Interestingly, less IL is required to prevent 1-butene adsorption as compared to 1,3-butadiene adsorption, which is proposed to be directly related to the IL’s influence on selective hydrogenation in SCILL catalysis. Molecular dynamics simulations from the Zahn group suggest IL film densification/relaxation as the key mechanism to allowing/excluding olefin adsorption on the metal. Being a function of IL coverage, the energy of film penetration controls the effective olefin adsorption energy – and therefore creates an operation regime for allowing 1,3-butadiene adsorption and potential hydrogenation to 1-butene, while adsorption of the latter – and thus, hydrogenation to *n*-butane – is suppressed.

6 Kurzfassung der Arbeit

Ionische Flüssigkeiten (engl. Ionic Liquids, ILs) werden erfolgreich in der geträgerten IL-Dünnschichtkatalyse eingesetzt. Die komplementären Katalysekonzepte Supported Ionic Liquid Phase (SILP) und Solid Catalyst with Ionic Liquid Layer (SCILL) werden sogar bereits in kommerziellen Anwendungen genutzt, typischerweise für Hydroformylierungs- und Hydrierungsreaktionen. Detaillierte Kenntnisse über die Adsorptionsdynamik und die Wechselwirkung von Kohlenwasserstoffen mit den Gas/IL/Katalysator-Grenzflächen sind daher von entscheidender Bedeutung für ein detailliertes Verständnis dieser Katalysatoren. Dieses ist wiederum Grundlage für weitere Verbesserungen und neue Entwicklungen.

In dieser Dissertation wird die Adsorptionsdynamik einer Reihe von Modell-C4-Kohlenwasserstoffen – *n*-Butan, *iso*-Butan, 1-Buten und 1,3-Butadien – an der Gas/IL- und der Gas/IL/Metall-Grenzfläche untersucht. Die dafür erforderlichen Messungen der Haftfaktoren wurden mit der direkten Methode von King und Wells unter Verwendung eines Überschallmolekularstrahls durchgeführt (siehe Kapitel 2.1). Dabei kam eine neu entwickelte Ultrahochvakuumkammer zum Einsatz, bestehend aus einer Einschleuskammer, einer Präparationskammer mit einem IL-Verdampfer und einer Analysenkammer mit einem Röntgenphotoelektronenspektrometer, einem Massenspektrometer und einem dreistufigen Überschallmolekularstrahl. Die Vakuumkammer und ihre Charakterisierung werden in Kapitel 3 beschrieben, und in Anhang 8.5 finden sich weitere detaillierte Pläne und Angaben.

Der erste Ergebnisteil befasst sich mit der Physisorption von C4-Kohlenwasserstoffen – *n*-Butan, *iso*-Butan und 1-Buten – auf der Oberfläche gefrorener makroskopischer Filme von 1-Alkyl-3-Methylimidazolium-basierten ILs $[C_nC_1Im]X$, mit $n = 1, 2, 3, 4$ und 8 und $X^- = Cl^-, Br^-, [PF_6]^-$ und $[Tf_2N]^-$. Auf ILs mit $n \geq 3$ adsorbiert *n*-Butan bei 90 K mit einem Anfangshaftfaktor von ≈ 0,9. Im Gegensatz dazu tritt für ILs mit $n \leq 2$ keine *n*-Butan-Adsorption auf, was auf eine zu kurze Verweilzeit auf der IL-Oberfläche zurückgeführt wird, die selbst bei 90 K nicht zur Bildung von Kondensationskeimen ausreicht. Dieses Ergebnis zeigt, dass die Bindungsenergie von der Wechselwirkung des *n*-Butans mit den Alkylketten der Kationen dominiert wird, während die kationischen Kopfgruppen und die Anionen kaum dazu beitragen (siehe Kapitel 4.1).

Im Rahmen dieser Arbeit wurden zwei komplementäre Methoden zur Bestimmung der Desorptionsenergie – und damit der Adsorptionsenergie dieser physisorbierten Adsorbate – von Kohlenwasserstoffen auf IL-Oberflächen entwickelt. Die erste basiert auf dem bedeckungs- und temperaturabhängigen Haftfaktor, und erlaubt mit einem Arrhenius-Ansatz die Ermittlung der Desorptionsenergie und den zugehörigen Präexponentialfaktor. Die zweite stützt sich auf den temperaturabhängigen Anfangshaftfaktor. Sie benötigt weniger Vorbedingungen, so dass sie erfolgreich auf den kompletten Satz von ILs mit $n \geq 3$ angewendet werden konnte (siehe Kapitel 4.2).

Die systematische Untersuchung der Desorptionsenergie von *n*-Butan auf ILs mit verschiedenen Alkylketten des IL-Kations zeigt eine systematische Zunahme mit zunehmender Länge der Alkylkette. Für ILs mit unterschiedlichen Anionen nimmt die Desorptionsenergie mit abnehmender Größe des Anions zu. Letzterer Effekt resultiert nicht aus unterschiedlich starken Wechselwirkungen von *n*-Butan mit den Anionen, sondern aus einem unterschiedlichen Grad an Alkylkettenanreicherung an der IL-Oberfläche, welcher seinerseits durch die verschiedenen Anionen induziert wird (siehe Kapitel 4.3). Die Desorptionsenergie wird auch durch das auftreffende Molekül beeinflusst: Sie nimmt in der Reihenfolge *n*-Butan > 1-Buten > *iso*-Butan ab, was auf unterschiedlich starke Dispersionswechselwirkungen zurückgeführt wird.

Der zweite Ergebnisteil befasst sich mit der Adsorptionsdynamik auf einer IL-bedeckten Pt(111) Oberfläche, die mit ultradünnen $[C_1C_1Im][Tf_2N]$-Filmen beschichtet wurde. Dieses System dient als Modellsystem für SCILL-Katalysatoren, welche zur Verbesserung der Selektivität von Hydrierungsreaktionen, wie z. B. der selektiven Hydrierung von 1,3-Butadien zu 1-Buten, eingesetzt werden können. Beide Olefine adsorbieren auf sauberem und IL-bedeckten Pt(111) über einen Precursor-Mechanismus. Mit zunehmender IL-Bedeckung werden mehr und mehr Adsorptionsplätze für die auftreffenden Olefine blockiert. Voradsorbierter Wasserstoff beeinflusst den Precursor-Mechanismus und die Adsorptionsplatzblockierungseffekte für 1,3-Butadien kaum.

Erstaunlicherweise ergibt sich zwischen den beiden Olefinen ein wesentlicher Unterschied: Um die Adsorption von 1-Buten zu verhindern, ist im Vergleich zu 1,3-Butadien eine geringere IL-Bedeckung vonnöten. Daraus folgt, dass eine Pt(111)-Oberfläche, die vollständig mit einer Schicht von IL-Ionen bedeckt ist, eine hohe Selektivität für die

Adsorption von 1,3-Butadien gegenüber 1-Buten aufweist. Molekulardynamiksimulationen der Arbeitsgruppe Zahn bestätigen, dass das Wechselspiel aus Olefin-Bindungsenergie und lokaler Verdichtung des IL-Films durch die Olefine der Schlüsselmechanismus ist, der die Adsorption von Olefinen auf dem Metall ermöglicht bzw. ausschließt. Dies dürfte direkt mit dem Einfluss der IL auf die selektive Hydrierung bei der SCILL-Katalyse zusammenhängen (siehe Kapitel 4.4).

7 References

1. Wasserscheid, P.; Welton, T., *Ionic Liquids in Synthesis*; Wiley-VCH: Weinheim, 2003.
2. MacFarlane, D. R.; Kar, M.; Pringle, J. M., *Fundamentals of Ionic Liquids*; Wiley-VCH: Weinheim, 2017.
3. Walden, P., Ueber die Molekulargrösse und Elektrische Leitfähigkeit einiger geschmolzenen Salze. *Bull. Acad. Imp. Sci. Saint-Pétersbourg* **1914**, 405-422.
4. Wilkes, J. S.; Zaworotko, M. J., Air and Water Stable 1-Ethyl-3-Methylimidazolium Based Ionic Liquids. *J. Chem. Soc., Chem. Commun.* **1992**, 965-967.
5. Welton, T., Ionic Liquids: A Brief History. *Biophys. Rev.* **2018**, *10*, 691-706.
6. Seddon, K. R., Ionic Liquids for Clean Technology. *J. Chem. Technol. Biotechnol.* **1997**, *68*, 351-356.
7. Huddleston, J. G.; Willauer, H. D.; Swatloski, R. P.; Visser, A. E.; Rogers, R. D., Room Temperature Ionic Liquids as Novel Media for 'Clean' Liquid-Liquid Extraction. *Chem. Commun.* **1998**, 1765-1766.
8. Earle, M. J.; Seddon, K. R., Ionic Liquids. Green Solvents for the Future. *Pure Appl. Chem.* **2000**, *72*, 1391-1398.
9. Welton, T., Room-Temperature Ionic Liquids. Solvents for Synthesis and Catalysis. *Chem. Rev.* **1999**, *99*, 2071-2084.
10. Rogers, R. D.; Seddon, K. R., Ionic Liquids – Solvents of the Future? *Science* **2003**, *302*, 792-793.
11. Hallett, J. P.; Welton, T., Room-Temperature Ionic Liquids: Solvents for Synthesis and Catalysis. 2. *Chem. Rev.* **2011**, *111*, 3508-3576.
12. Galiński, M.; Lewandowski, A.; Stępniak, I., Ionic Liquids as Electrolytes. *Electrochim. Acta* **2006**, *51*, 5567-5580.
13. Hapiot, P.; Lagrost, C., Electrochemical Reactivity in Room-Temperature Ionic Liquids. *Chem. Rev.* **2008**, *108*, 2238-2264.
14. Watanabe, M.; Thomas, M. L.; Zhang, S.; Ueno, K.; Yasuda, T.; Dokko, K., Application of Ionic Liquids to Energy Storage and Conversion Materials and Devices. *Chem. Rev.* **2017**, *117*, 7190-7239.
15. Forsyth, M.; Porcarelli, L.; Wang, X.; Goujon, N.; Mecerreyes, D., Innovative Electrolytes Based on Ionic Liquids and Polymers for Next-Generation Solid-State Batteries. *Acc. Chem. Res.* **2019**, *52*, 686-694.
16. Minami, I., Ionic Liquids in Tribology. *Molecules* **2009**, *14*, 2286-2305.
17. Cai, M.; Yu, Q.; Liu, W.; Zhou, F., Ionic Liquid Lubricants: When Chemistry Meets Tribology. *Chem. Soc. Rev.* **2020**, *49*, 7753-7818.
18. Maase, M.; Massonne, K., Biphasic Acid Scavenging Utilizing Ionic Liquids: The First Commercial Process with Ionic Liquids. In *Ionic Liquids IIIb: Fundamentals, Progress, Challenges, and Opportunities: Transformations and Processes*, Rogers, R. D.; Seddon, K. R., Eds. American Chemical Society: 2005; Vol. 902, pp 126-132.
19. Ramdin, M.; de Loos, T. W.; Vlugt, T. J. H., State-of-the-Art of CO_2 Capture with Ionic Liquids. *Ind. Eng. Chem. Res.* **2012**, *51*, 8149-8177.
20. Zeng, S.; Zhang, X.; Bai, L.; Zhang, X.; Wang, H.; Wang, J.; Bao, D.; Li, M.; Liu, X.; Zhang, S., Ionic-Liquid-Based CO_2 Capture Systems: Structure, Interaction and Process. *Chem. Rev.* **2017**, *117*, 9625-9673.
21. Silvester, D. S., Recent Advances in the Use of Ionic Liquids for Electrochemical Sensing. *Analyst* **2011**, *136*, 4871-4882.
22. Silvester, D. S.; Jamil, R.; Doblinger, S.; Zhang, Y.; Atkin, R.; Li, H., Electrical Double Layer Structure in Ionic Liquids and its Importance for Supercapacitor, Battery, Sensing, and Lubrication Applications. *J. Phys. Chem. C* **2021**, *125*, 13707-13720.
23. Zhou, Y.; Qu, J., Ionic Liquids as Lubricant Additives: A Review. *ACS Appl. Mater. Interfaces* **2017**, *9*, 3209-3222.

24. Marrucho, I. M.; Branco, L. C.; Rebelo, L. P. N., Ionic Liquids in Pharmaceutical Applications. *Annu. Rev. Chem. Biomol. Eng.* **2014**, *5*, 527-546.
25. Egorova, K. S.; Gordeev, E. G.; Ananikov, V. P., Biological Activity of Ionic Liquids and their Application in Pharmaceutics and Medicine. *Chem. Rev.* **2017**, *117*, 7132-7189.
26. Curreri, A. M.; Mitragotri, S.; Tanner, E. E. L., Recent Advances in Ionic Liquids in Biomedicine. *Adv. Sci.* **2021**, *8*, 2004819.
27. Qiao, Y.; Ma, W.; Theyssen, N.; Chen, C.; Hou, Z., Temperature-Responsive Ionic Liquids: Fundamental Behaviors and Catalytic Applications. *Chem. Rev.* **2017**, *117*, 6881-6928.
28. Dai, C.; Zhang, J.; Huang, C.; Lei, Z., Ionic Liquids in Selective Oxidation: Catalysts and Solvents. *Chem. Rev.* **2017**, *117*, 6929-6983.
29. Karimi, B.; Tavakolian, M.; Akbari, M.; Mansouri, F., Ionic Liquids in Asymmetric Synthesis: An Overall View from Reaction Media to Supported Ionic Liquid Catalysis. *ChemCatChem* **2018**, *10*, 3173-3205.
30. Steinrück, H.-P.; Wasserscheid, P., Ionic Liquids in Catalysis. *Catal. Lett.* **2015**, *145*, 380-397.
31. Bartlewicz, O.; Dąbek, I.; Szymańska, A.; Maciejewski, H., Heterogeneous Catalysis with the Participation of Ionic Liquids. *Catalysts* **2020**, *10*, 1227.
32. Neofotistos, S. P.; Tzani, A.; Detsi, A., Ionic Liquids: Advances and Applications in Phase Transfer Catalysis. *Catalysts* **2023**, *13*, 474.
33. Frade, R. F. M.; Afonso, C. A. M., Impact of Ionic Liquids in Environment and Humans: An Overview. *Hum. Exp. Toxicol.* **2010**, *29*, 1038-1054.
34. Costa, S. P. F.; Azevedo, A. M. O.; Pinto, P. C. A. G.; Saraiva, M. L. M. F. S., Environmental Impact of Ionic Liquids: Recent Advances in (Eco)Toxicology and (Bio)Degradability. *ChemSusChem* **2017**, *10*, 2321-2347.
35. Clark, J. H.; Tavener, S. J., Alternative Solvents: Shades of Green. *Org. Process Res. Dev.* **2007**, *11*, 149-155.
36. Jessop, P. G., Searching for Green Solvents. *Green Chem.* **2011**, *13*, 1391-1398.
37. Cevasco, G.; Chiappe, C., Are Ionic Liquids a Proper Solution to Current Environmental Challenges? *Green Chem.* **2014**, *16*, 2375-2385.
38. Gomes, J. M.; Silva, S. S.; Reis, R. L., Biocompatible Ionic Liquids: Fundamental Behaviours and Applications. *Chem. Soc. Rev.* **2019**, *48*, 4317-4335.
39. Gaida, B.; Brzęczek-Szafran, A., Insights into the Properties and Potential Applications of Renewable Carbohydrate-Based Ionic Liquids: A Review. *Molecules* **2020**, *25*, 3285.
40. Steinrück, H.-P., Recent Developments in the Study of Ionic Liquid Interfaces Using X-Ray Photoelectron Spectroscopy and Potential Future Directions. *Phys. Chem. Chem. Phys.* **2012**, *14*, 5010-5029.
41. Greer, A. J.; Jacquemin, J.; Hardacre, C., Industrial Applications of Ionic Liquids. *Molecules* **2020**, *25*, 5207.
42. Cokoja, F.; Adams, D. S.; Cooper, D., Ultra-Selective Acetylene Hydrogenation Catalyst Developed to Boost Profitability in Ethylene Production. *The Catalyst Review* 2018, pp 8-9.
43. Mehnert, C. P.; Cook, R. A.; Dispenziere, N. C.; Afeworki, M., Supported Ionic Liquid Catalysis – a New Concept for Homogeneous Hydroformylation Catalysis. *J. Am. Chem. Soc.* **2002**, *124*, 12932-12933.
44. Schönweiz, A.; Franke, R., Supported Ionic Liquid Phase (SILP) Materials in Hydroformylation Catalysis. In *Supported Ionic Liquids*, Fehrmann, R.; Riisager, A.; Haumann, M., Eds. Wiley-VCH: Weinheim, 2014; pp 307-326.
45. Marinkovic, J. M.; Riisager, A.; Franke, R.; Wasserscheid, P.; Haumann, M., Fifteen Years of Supported Ionic Liquid Phase-Catalyzed Hydroformylation: Material and Process Developments. *Ind. Eng. Chem. Res.* **2019**, *58*, 2409-2420.
46. Kernchen, U.; Etzold, B.; Korth, W.; Jess, A., Solid Catalyst with Ionic Liquid Layer (SCILL) – a New Concept to Improve Selectivity Illustrated by Hydrogenation of Cyclooctadiene. *Chem. Eng. Technol.* **2007**, *30*, 985-994.

47. Korth, W.; Jess, A., Solid Catalyst with Ionic Liquid Layer (SCILL). In *Supported Ionic Liquids*, Fehrmann, R.; Riisager, A.; Haumann, M., Eds. Wiley-VCH: Weinheim, 2014; pp 279-306.
48. Naicker, L.; Schörner, M.; Kremitzl, D.; Friedrich, H. B.; Haumann, M.; Wasserscheid, P., Influencing the Product Distribution in Citral Hydrogenation Using Ionic Liquid Modified Cu Catalysts. *ChemCatChem* **2022**, *14*, e202200388.
49. Barth, T. Selektivhydrierung von 1,3-Butadien an mit Ionischen Fluiden beschichteten heterogenen Katalysatoren. PhD thesis, Universität Bayreuth, Bayreuth, 2016.
50. Barth, T.; Korth, W.; Jess, A., Selectivity-Enhancing Effect of a SCILL Catalyst in Butadiene Hydrogenation. *Chem. Eng. Technol.* **2017**, *40*, 395-404.
51. Jalal, A.; Uzun, A., An Exceptional Selectivity for Partial Hydrogenation on a Supported Nickel Catalyst Coated with [BMIm][BF_4]. *J. Catal.* **2017**, *350*, 86-96.
52. Jalal, A.; Uzun, A., An Ordinary Nickel Catalyst Becomes Completely Selective for Partial Hydrogenation of 1,3-Butadiene when Coated with Tributyl(methyl) Phosphonium Methyl Sulfate. *Appl. Catal. A* **2018**, *562*, 321-326.
53. Geilen, F. M. A.; Stochniol, G.; Peitz, S.; Schulte-Koerne, E., Butenes. In *Ullmann's Encyclopedia of Industrial Chemistry*, Wiley-VCH: Weinheim, 2014.
54. Zaera, F., The Surface Chemistry of Metal-Based Hydrogenation Catalysis. *ACS Catal.* **2017**, *7*, 4947-4967.
55. Zhang, L.; Zhou, M.; Wang, A.; Zhang, T., Selective Hydrogenation over Supported Metal Catalysts: From Nanoparticles to Single Atoms. *Chem. Rev.* **2020**, *120*, 683-733.
56. Selvakannan, P. R.; Hoang, L.; Kumar, V. V.; Dumbre, D.; Jampaiah, D.; Das, J.; Bhargava, S. K., Selective Hydrogenation of 1,3-Butadiene to 1-Butene: Review on Catalysts, Selectivity, Kinetics and Reaction Mechanism. In *Catalysis for Clean Energy and Environmental Stability – Petrochemicals and Refining Processes*, Pant, K. K.; Gupta, S. K.; Ahmad, E., Eds. Springer Nature Switzerland: Cham, 2021; Vol. 2, pp 205-228.
57. Sobota, M.; Happel, M.; Amende, M.; Paape, N.; Wasserscheid, P.; Laurin, M.; Libuda, J., Ligand Effects in SCILL Model Systems: Site-Specific Interactions with Pt and Pd Nanoparticles. *Adv. Mater.* **2011**, *23*, 2617-2621.
58. Arras, J.; Paki, E.; Roth, C.; Radnik, J.; Lucas, M.; Claus, P., How a Supported Metal is Influenced by an Ionic Liquid: In-Depth Characterization of SCILL-Type Palladium Catalysts and their Hydrogen Adsorption. *J. Phys. Chem. C* **2010**, *114*, 10520-10526.
59. Lexow, M.; Maier, F.; Steinrück, H.-P., Ultrathin Ionic Liquid Films on Metal Surfaces: Adsorption, Growth, Stability and Exchange Phenomena. *Adv. Phys. X* **2020**, *5*, 1761266.
60. Meusel, M.; Lexow, M.; Gezmis, A.; Bayer, A.; Maier, F.; Steinrück, H.-P., Growth of Multilayers of Ionic Liquids on Au(111) Investigated by Atomic Force Microscopy in Ultrahigh Vacuum. *Langmuir* **2020**, *36*, 13670-13681.
61. Bühlmeyer, H.; Hauner, J.; Eschenbacher, R.; Steffen, J.; Trzeciak, S.; Taccardi, N.; Görling, A.; Zahn, D.; Wasserscheid, P.; Libuda, J., Structure Formation in an Ionic Liquid Wetting Layer: A Combined STM, IRAS, DFT and MD Study of [C_2C_1Im][OTf] on Au(111). *Chem. Eur. J.* **2023**, *29*, e202301328.
62. Meusel, M.; Gezmis, A.; Jaekel, S.; Lexow, M.; Bayer, A.; Maier, F.; Steinrück, H.-P., Time- and Temperature-Dependent Growth Behavior of Ionic Liquids on Au(111) Studied by Atomic Force Microscopy in Ultrahigh Vacuum. *J. Phys. Chem. C* **2021**, *125*, 20439-20449.
63. Rietzler, F.; May, B.; Steinrück, H.-P.; Maier, F., Switching Adsorption and Growth Behavior of Ultrathin [C_2C_1Im][OTf] Films on Au(111) by Pd Deposition. *Phys. Chem. Chem. Phys.* **2016**, *18*, 25143-25150.
64. Syres, K. L.; Jones, R. G., Adsorption, Desorption, and Reaction of 1-Octyl-3-Methylimidazolium Tetrafluoroborate, [C_8C_1Im][BF_4], Ionic Liquid Multilayers on Cu(111). *Langmuir* **2015**, *31*, 9799-9808.
65. Massicot, S.; Sasaki, T.; Lexow, M.; Maier, F.; Kuwabata, S.; Steinrück, H.-P., On-Surface Metathesis of an Ionic Liquid on Ag(111). *Chem. Eur. J.* **2022**, *28*, e202200167.

66. Lexow, M.; Heller, B. S. J.; Maier, F.; Steinrück, H.-P., Anion Exchange at the Liquid/Solid Interface of Ultrathin Ionic Liquid Films on Ag(111). *ChemPhysChem* **2018**, *19*, 2978-2984.
67. Lexow, M.; Heller, B. S. J.; Partl, G.; Bhuin, R. G.; Maier, F.; Steinrück, H.-P., Cation Exchange at the Interfaces of Ultrathin Films of Fluorous Ionic Liquids on Ag(111). *Langmuir* **2019**, *35*, 398-405.
68. Adhikari, R.; Massicot, S.; Fromm, L.; Talwar, T.; Gezmis, A.; Meusel M.; Bayer, A.; Jaekel S.; Maier, F.; Görling, A.; Steinrück, H.-P., Structure and Reactivity of the Ionic Liquid [C_1C_1Im][Tf_2N] on Cu(111). *Top. Catal.* **2023**, *66*, 1178-1195.
69. Massicot, S.; Sasaki, T.; Lexow, M.; Shin, S.; Maier, F.; Kuwabata, S.; Steinrück, H.-P., Adsorption, Wetting, Growth, and Thermal Stability of the Protic Ionic Liquid Diethylmethylammonium Trifluoromethanesulfonate on Ag(111) and Au(111). *Langmuir* **2021**, *37*, 11552-11560.
70. Massicot, S.; Gezmis, A.; Talwar, T.; Meusel, M.; Jaekel, S.; Adhikari, R.; Winter, L.; Fernández, C. C.; Bayer, A.; Maier, F.; Steinrück, H.-P., Adsorption and Thermal Evolution of [C_1C_1Im][Tf_2N] on Pt(111). *Phys. Chem. Chem. Phys.* **2023**, DOI: 10.1039/d3cp02743k.
71. Forster-Tonigold, K.; Buchner, F.; Bansmann, J.; Behm, R. J.; Groß, A., A Combined XPS and Computational Study of the Chemical Reduction of BMP-TFSI by Lithium. *Batteries Supercaps* **2022**, *5*, e202200307.
72. Carmichael, A. J.; Hardacre, C.; Holbrey, J. D.; Seddon, K. R.; Nieuwenhuyzen, M., Structure and Bonding in Ionic Liquids. *Proc. Vol. 1999* **1999**, *41*, 209-221.
73. Haddad, J.; Pontoni, D.; Murphy, B. M.; Festersen, S.; Runge, B.; Magnussen, O. M.; Steinrück, H.-G.; Reichert, H.; Ocko, B. M.; Deutsch, M., Surface Structure Evolution in a Homologous Series of Ionic Liquids. *Proc. Natl. Acad. Sci. USA* **2018**, *115*, E1100-E1107.
74. Gannon, T. J.; Law, G.; Watson, P. R.; Carmichael, A. J.; Seddon, K. R., First Observation of Molecular Composition and Orientation at the Surface of a Room-Temperature Ionic Liquid. *Langmuir* **1999**, *15*, 8429-8434.
75. Nakajima, K.; Lísal, M.; Kimura, K., Surfaces of Ionic Liquids. In *Surface and Interface Science*, Wandelt, K., Ed. Wiley-VCH: Weinheim, 2020; Vol. 7, pp 351-389.
76. Nakajima, K.; Ohno, A.; Suzuki, M.; Kimura, K., Observation of Molecular Ordering at the Surface of Trimethylpropylammonium Bis(trifluoromethanesulfonyl)imide Using High-Resolution Rutherford Backscattering Spectroscopy. *Langmuir* **2008**, *24*, 4482-4484.
77. Caporali, S.; Bardi, U.; Lavacchi, A., X-Ray Photoelectron Spectroscopy and Low Energy Ion Scattering Studies on 1-Butyl-3-Methyl-Imidazolium Bis(trifluoromethane) Sulfonimide. *J. Electron Spectrosc.* **2006**, *151*, 4-8.
78. Villar-Garcia, I. J.; Fearn, S.; De Gregorio, G. F.; Ismail, N. L.; Gschwend, F. J. V.; McIntosh, A. J. S.; Lovelock, K. R. J., The Ionic Liquid-Vacuum Outer Atomic Surface: A Low-Energy Ion Scattering Study. *Chem. Sci.* **2014**, *5*, 4404-4418.
79. Wu, B.; Zhang, J.; Minton, T. K.; McKendrick, K. G.; Slattery, J. M.; Yockel, S.; Schatz, G. C., Scattering Dynamics of Hyperthermal Oxygen Atoms on Ionic Liquid Surfaces: [EMIm][NTf_2] and [C_{12}MIm][NTf_2]. *J. Phys. Chem. C* **2010**, *114*, 4015-4027.
80. Purcell, S. M.; Lane, P. D.; D'Andrea, L.; Elstone, N. S.; Bruce, D. W.; Slattery, J. M.; Smoll, E. J.; Greaves, S. J.; Costen, M. L.; Minton, T. K.; McKendrick, K. G., Surface Structure of Alkyl/Fluoroalkylimidazolium Ionic-Liquid Mixtures. *J. Phys. Chem. B* **2022**, *126*, 1962-1979.
81. Baldelli, S., Influence of Water on the Orientation of Cations at the Surface of a Room-Temperature Ionic Liquid: A Sum Frequency Generation Vibrational Spectroscopic Study. *J. Phys. Chem. B* **2003**, *107*, 6148-6152.
82. Iwahashi, T.; Ishiyama, T.; Sakai, Y.; Morita, A.; Kim, D.; Ouchi, Y., Bi-Layering at Ionic Liquid Surfaces: A Sum-Frequency Generation Vibrational Spectroscopy- and Molecular Dynamics Simulation-Based Study. *Phys. Chem. Chem. Phys.* **2020**, *22*, 12565-12576.
83. Smith, E. F.; Rutten, F. J. M.; Villar-Garcia, I. J.; Briggs, D.; Licence, P., Ionic Liquids in Vacuo: Analysis of Liquid Surfaces Using Ultra-High-Vacuum Techniques. *Langmuir* **2006**, *22*, 9386-9392.

84. Lovelock, K. R. J.; Villar-Garcia, I. J.; Maier, F.; Steinrück, H.-P.; Licence, P., Photoelectron Spectroscopy of Ionic Liquid-Based Interfaces. *Chem. Rev.* **2010**, *110*, 5158-5190.
85. Kolbeck, C.; Niedermaier, I.; Deyko, A.; Lovelock, K. R. J.; Taccardi, N.; Wei, W.; Wasserscheid, P.; Maier, F.; Steinrück, H.-P., Influence of Substituents and Functional Groups on the Surface Composition of Ionic Liquids. *Chem. Eur. J.* **2014**, *20*, 3954-3965.
86. Men, S.; Mitchell, D. S.; Lovelock, K. R. J.; Licence, P., X-Ray Photoelectron Spectroscopy of Pyridinium-Based Ionic Liquids: Comparison to Imidazolium- and Pyrrolidinium-Based Analogues. *ChemPhysChem* **2015**, *16*, 2211-2218.
87. Heller, B. S. J.; Lexow, M.; Greco, F.; Shin, S.; Partl, G.; Maier, F.; Steinrück, H.-P., Temperature-Dependent Surface Enrichment Effects in Binary Mixtures of Fluorinated and Non-Fluorinated Ionic Liquids. *Chem. Eur. J.* **2020**, *26*, 1117-1126.
88. Paap, U.; Seidl, V.; Meyer, K.; Maier, F.; Steinrück, H.-P., Direct Correlation of Surface Tension and Surface Composition of Ionic Liquid Mixtures – a Combined Vacuum Pendant Drop and Angle-Resolved X-Ray Photoelectron Spectroscopy Study. *Molecules* **2022**, *27*, 8561.
89. Hemmeter, D.; Kremitzl, D.; Schulz, P. S.; Wasserscheid, P.; Maier, F.; Steinrück, H.-P., The Buoy Effect: Surface Enrichment of a Pt Complex in IL Solution by Ligand Design. *Chem. Eur. J.* **2023**, e202203325.
90. Lynden-Bell, R. M., Gas-Liquid Interfaces of Room Temperature Ionic Liquids. *Mol. Phys.* **2003**, *101*, 2625-2633.
91. Shimizu, K.; Tariq, M.; Freitas, A. A.; Pádua, A. A. H.; Canongia Lopes, J. N., Self-Organization in Ionic Liquids: From Bulk to Interfaces and Films. *J. Brazil. Chem. Soc.* **2016**, *27*, 349-362.
92. Shimizu, K.; Heller, B. S. J.; Maier, F.; Steinrück, H.-P.; Canongia Lopes, J. N., Probing the Surface Tension of Ionic Liquids Using the Langmuir Principle. *Langmuir* **2018**, *34*, 4408-4416.
93. Roscioli, J. R.; Nesbitt, D. J., State-Resolved Scattering at Room-Temperature Ionic Liquid-Vacuum Interfaces: Anion Dependence and the Role of Dynamic versus Equilibrium Effects. *J. Phys. Chem. Lett.* **2010**, *1*, 674-678.
94. Roscioli, J. R.; Nesbitt, D. J., Quantum State Resolved Scattering from Room-Temperature Ionic Liquids: The Role of Cation versus Anion Structure at the Interface. *J. Phys. Chem. A* **2011**, *115*, 9764-9773.
95. Ziemkiewicz, M. P.; Zutz, A.; Nesbitt, D. J., Inelastic Scattering of Radicals at the Gas-Ionic Liquid Interface: Probing Surface Dynamics of BMIm-Cl, BMIm-BF_4, and BMIm-Tf_2N by Rovibronic Scattering of NO [$^2\pi_{1/2}(0.5)$]. *J. Phys. Chem. C* **2012**, *116*, 14284-14294.
96. Zutz, A.; Nesbitt, D. J., Quantum State-Resolved Molecular Scattering of NO ($^2\pi_{1/2}$) at the Gas-[C_nMIm][Tf_2N] Room Temperature Ionic Liquid Interface: Dependence on Alkyl Chain Length, Collision Energy, and Temperature. *AIP Adv.* **2016**, *6*, 105207.
97. Tesa-Serrate, M. A.; Marshall, B. C.; Smoll, E. J.; Purcell, S. M.; Costen, M. L.; Slattery, J. M.; Minton, T. K.; McKendrick, K. G., Ionic Liquid-Vacuum Interfaces Probed by Reactive Atom Scattering: Influence of Alkyl Chain Length and Anion Volume. *J. Phys. Chem. C* **2015**, *119*, 5491-5505.
98. Marshall, B. C.; Smoll, E. J.; Purcell, S. M.; Costen, M. L.; McKendrick, K. G.; Minton, T. K., Scattering Dynamics of Oxygen Atoms on Imidazolium Tetrafluoroborate Ionic Liquid Surfaces: Dependence on Alkyl Chain Length. *J. Phys. Chem. C* **2016**, *120*, 12472-12483.
99. Tesa-Serrate, M. A.; Smoll, E. J.; D'Andrea, L.; Purcell, S. M.; Costen, M. L.; Bruce, D. W.; Slattery, J. M.; Minton, T. K.; McKendrick, K. G., Hiding the Headgroup? Remarkable Similarity in Alkyl Coverage of the Surfaces of Pyrrolidinium- and Imidazolium-Based Ionic Liquids. *J. Phys. Chem. C* **2016**, *120*, 27369-27379.
100. Deyko, A.; Jones, R. G., Adsorption, Absorption and Desorption of Gases at Liquid Surfaces: Water on [C_8C_1Im][BF_4] and [C_2C_1Im][Tf_2N]. *Faraday Discuss.* **2012**, *154*, 265-288.
101. Dunoyer, L., Sur la réalisation d'un rayonnement matériel d'origine purement thermique. Cinétique expérimentale. *Le Radium* **1911**, *8*, 142-146.

102. Gerlach, W.; Stern, O., Der experimentelle Nachweis der Richtungsquantelung im Magnetfeld. *Z. Phys.* **1922**, *9*, 349-352.
103. van de Meerakker, S. Y. T.; Bethlem, H. L.; Vanhaecke, N.; Meijer, G., Manipulation and Control of Molecular Beams. *Chem. Rev.* **2012**, *112*, 4828-4878.
104. Libuda, J.; Freund, H.-J., Molecular Beam Experiments on Model Catalysts. *Surf. Sci. Rep.* **2005**, *57*, 157-298.
105. Zaera, F., Use of Molecular Beams for Kinetic Measurements of Chemical Reactions on Solid Surfaces. *Surf. Sci. Rep.* **2017**, *72*, 59-104.
106. Lucas, C. B., *Atomic and Molecular Beams: Production and Collimation*; CRC Press/Taylor & Francis Group: Boca Raton, FL, 2014.
107. Scoles, G. (Ed.), *Atomic and Molecular Beam Methods*; Oxford University Press: New York, NY, 1988; Vol. 1.
108. Sanna, G.; Tomassetti, G., *Introduction to Molecular Beams Gas Dynamics*; Imperial College Press: London, 2005.
109. Dunning, F. B.; Hulet, R. G. (Eds.), *Atomic, Molecular, and Optical Physics: Atoms and Molecules*; Academic Press: San Diego, CA, 1996.
110. Jankunas, J.; Osterwalder, A., Cold and Controlled Molecular Beams: Production and Applications. *Annu. Rev. Phys. Chem.* **2015**, *66*, 241-262.
111. Kleyn, A. W., Molecular Beams and Chemical Dynamics at Surfaces. *Chem. Soc. Rev.* **2003**, *32*, 87-95.
112. Weaver, J. F.; Carlsson, A. F.; Madix, R. J., The Adsorption and Reaction of Low Molecular Weight Alkanes on Metallic Single Crystal Surfaces. *Surf. Sci. Rep.* **2003**, *50*, 107-199.
113. King, D. A.; Wells, M. G., Molecular Beam Investigation of Adsorption Kinetics on Bulk Metal Targets – Nitrogen on Tungsten. *Surf. Sci.* **1972**, *29*, 454-482.
114. Winter, L.; Bhuin, R. G.; Lexow, M.; Maier, F.; Steinrück, H.-P., On the Adsorption of *n*-Butane on Alkyl Imidazolium Ionic Liquids with Different Anions Using a New Molecular Beam Setup. *J. Chem. Phys.* **2020**, *153*, 214706.
115. Kneitz, S. Adsorptions- und Streumessungen von CO an ultradünnen Metallschichtsystemen mittels eines Überschalldüsen-Molekularstrahls. Bayerische Julius-Maximilians-Universität, Würzburg, 1998.
116. Briggs, D.; Seah, M. P. (Eds.), *Practical Surface Analysis: Auger and X-Ray Photoelectron Spectroscopy*, 2nd ed., repr. ed.; Wiley: Chichester, New York, NY, 1994; Vol. 1.
117. Hüfner, S., *Photoelectron Spectroscopy: Principles and Applications*, 3rd ed.; Springer: Berlin, New York, NY, 2003.
118. van der Heide, P., *X-Ray Photoelectron Spectroscopy: An Introduction to Principles and Practices*; Wiley: Hoboken, NJ, 2012.
119. Maier, F.; Cremer, T.; Kolbeck, C.; Lovelock, K. R. J.; Paape, N.; Schulz, P. S.; Wasserscheid, P.; Steinrück, H.-P., Insights into the Surface Composition and Enrichment Effects of Ionic Liquids and Ionic Liquid Mixtures. *Phys. Chem. Chem. Phys.* **2010**, *12*, 1905-1915.
120. Cremer, T.; Stark, M.; Deyko, A.; Steinrück, H.-P.; Maier, F., Liquid/Solid Interface of Ultrathin Ionic Liquid Films: [C_1C_1Im][Tf_2N] and [C_8C_1Im][Tf_2N] on Au(111). *Langmuir* **2011**, *27*, 3662-3671.
121. Cremer, T.; Killian, M.; Gottfried, J. M.; Paape, N.; Wasserscheid, P.; Maier, F.; Steinrück, H.-P., Physical Vapor Deposition of [EMIm][Tf_2N]: A New Approach to the Modification of Surface Properties with Ultrathin Ionic Liquid Films. *ChemPhysChem* **2008**, *9*, 2185-2190.
122. Rietzler, F.; Nagengast, J.; Steinrück, H.-P.; Maier, F., Interface of Ionic Liquids and Carbon: Ultrathin [C_1C_1Im][Tf_2N] Films on Graphite and Graphene. *J. Phys. Chem. C* **2015**, *119*, 28068-28076.
123. Cremer, T.; Wibmer, L.; Krick Calderón, S.; Deyko, A.; Maier, F.; Steinrück, H.-P., Interfaces of Ionic Liquids and Transition Metal Surfaces – Adsorption, Growth, and Thermal Reactions of Ultrathin [C_1C_1Im][Tf_2N] Films on Metallic and Oxidised Ni(111) Surfaces. *Phys. Chem. Chem. Phys.* **2012**, *14*, 5153-5163.

124. Lexow, M.; Talwar, T.; Heller, B. S. J.; May, B.; Bhuin, R. G.; Maier, F.; Steinrück, H.-P., Time-Dependent Changes in the Growth of Ultrathin Ionic Liquid Films on Ag(111). *Phys. Chem. Chem. Phys.* **2018**, *20*, 12929-12938.
125. Meusel, M.; Lexow, M.; Gezmis, A.; Schötz, S.; Wagner, M.; Bayer, A.; Maier, F.; Steinrück, H.-P., Atomic Force and Scanning Tunneling Microscopy of Ordered Ionic Liquid Wetting Layers from 110 K up to Room Temperature. *ACS Nano* **2020**, *14*, 9000-9010.
126. Bhuin, R. G.; Winter, L.; Lexow, M.; Maier, F.; Steinrück, H.-P., On the Dynamic Interaction of *n*-Butane with Imidazolium-Based Ionic Liquids. *Angew. Chem. Int. Ed.* **2020**, *59*, 14429-14433.
127. Winter, L.; Bhuin, R. G.; Maier, F.; Steinrück, H.-P., *n*-Butane, *iso*-Butane and 1-Butene Adsorption on Imidazolium-Based Ionic Liquids Studied with Molecular Beam Techniques. *Chem. Eur. J.* **2021**, *27*, 17059-17065.
128. Majer, V.; Svoboda, V., *Enthalpies of Vaporization of Organic Compounds: A Critical Review and Data Compilation*; Blackwell Scientific Publications: Oxford, 1985.
129. Kolasinski, K. W., *Surface Science – Foundations of Catalysis and Nanoscience*, 3rd ed.; John Wiley & Sons Ltd: Chichester, 2012.
130. Lee, K.; Morikawa, Y.; Langreth, D. C., Adsorption of *n*-Butane on Cu(100), Cu(111), Au(111), and Pt(111): Van der Waals Density-Functional Study. *Phys. Rev. B* **2010**, *82*, 155461.
131. Dong, Q.; Muzny, C. D.; Kazakov, A.; Diky, V.; Magee, J. W.; Widegren, J. A.; Chirico, R. D.; Marsh, K. N.; Frenkel, M., ILThermo: A Free-Access Web Database for Thermodynamic Properties of Ionic Liquids. *J. Chem. Eng. Data* **2007**, *52*, 1151-1159.
132. Lovelock, K. R. J.; Kolbeck, C.; Cremer, T.; Paape, N.; Schulz, P. S.; Wasserscheid, P.; Maier, F.; Steinrück, H.-P., Influence of Different Substituents on the Surface Composition of Ionic Liquids Studied Using ARXPS. *J. Phys. Chem. B* **2009**, *113*, 2854-2864.
133. Kolbeck, C.; Cremer, T.; Lovelock, K. R. J.; Paape, N.; Schulz, P. S.; Wasserscheid, P.; Maier, F.; Steinrück, H.-P., Influence of Different Anions on the Surface Composition of Ionic Liquids Studied Using ARXPS. *J. Phys. Chem. B* **2009**, *113*, 8682-8688.
134. Lynden-Bell, R. M.; Del Pópolo, M., Simulation of the Surface Structure of Butylmethylimidazolium Ionic Liquids. *Phys. Chem. Chem. Phys.* **2006**, *8*, 949-954.
135. Ohno, A.; Hashimoto, H.; Nakajima, K.; Suzuki, M.; Kimura, K., Observation of Surface Structure of 1-Butyl-3-Methylimidazolium Hexafluorophosphate Using High-Resolution Rutherford Backscattering Spectroscopy. *J. Chem. Phys.* **2009**, *130*, 204705.
136. Lockett, V.; Sedev, R.; Bassell, C.; Ralston, J., Angle-Resolved X-Ray Photoelectron Spectroscopy of the Surface of Imidazolium Ionic Liquids. *Phys. Chem. Chem. Phys.* **2008**, *10*, 1330-1335.
137. Men, S.; Hurisso, B. B.; Lovelock, K. R. J.; Licence, P., Does the Influence of Substituents Impact upon the Surface Composition of Pyrrolidinium-Based Ionic Liquids? An Angle Resolved XPS Study. *Phys. Chem. Chem. Phys.* **2012**, *14*, 5229-5238.
138. Kisliuk, P., The Sticking Probabilities of Gases Chemisorbed on the Surfaces of Solids. *J. Phys. Chem. Solids* **1957**, *3*, 95-101.
139. Taylor, J. B.; Langmuir, I., The Evaporation of Atoms, Ions and Electrons from Caesium Films on Tungsten. *Phys. Rev.* **1933**, *44*, 423-458.
140. Winter, L.; Trzeciak, S.; Fernández, C. C.; Massicot, S.; Talwar, T.; Maier, F.; Zahn, D.; Steinrück, H.-P., Tailoring the Selectivity of 1,3-Butadiene versus 1-Butene Adsorption on Pt(111) by Ultrathin Ionic Liquid Films. *ACS Catal.* **2023**, *13*, 10866-10877.
141. Mittendorfer, F.; Thomazeau, C.; Raybaud, P.; Toulhoat, H., Adsorption of Unsaturated Hydrocarbons on Pd(111) and Pt(111): A DFT Study. *J. Phys. Chem. B* **2003**, *107*, 12287-12295.
142. Valcárcel, A.; Clotet, A.; Ricart, J. M.; Delbecq, F.; Sautet, P., Comparative DFT Study of the Adsorption of 1,3-Butadiene, 1-Butene and 2-*cis*/*trans*-Butenes on the Pt(111) and Pd(111) Surfaces. *Surf. Sci.* **2004**, *549*, 121-133.

143. Christmann, K.; Ertl, G.; Pignet, T., Adsorption of Hydrogen on a Pt(111) Surface. *Surf. Sci.* **1976**, *54*, 365-392.
144. Christmann, K., Interaction of Hydrogen with Solid Surfaces. *Surf. Sci. Rep.* **1988**, *9*, 1-163.
145. Auras, S. V.; van Lent, R.; Bashlakov, D.; Piñeiros Bastidas, J. M.; Roorda, T.; Spierenburg, R.; Juurlink, L. B. F., Scaling Platinum-Catalyzed Hydrogen Dissociation on Corrugated Surfaces. *Angew. Chem. Int. Ed.* **2020**, *59*, 20973-20979.

8 Appendix

On the following pages, the publications [1-4] are reproduced under the licenses CC BY-NC-ND 4.0 ([P1, P3, P4]) and CC BY 4.0 ([P2]).

[P1] **On the Dynamic Interaction of *n*-Butane with Imidazolium-Based Ionic Liquids**
R. G. Bhuin, L. Winter, M. Lexow, F. Maier, H.-P. Steinrück
Angew. Chem. Int. Ed. **2020**, *59*, 14429-14433

Die Dynamische Wechselwirkung von *n*-Butan mit Imidazolium-Basierten Ionischen Flüssigkeiten
R. G. Bhuin, L. Winter, M. Lexow, F. Maier, H.-P. Steinrück
Angew. Chem., **2020**, *132*, 14536-14541

[P2] **On the Adsorption of *n*-Butane on Alkyl Imidazolium Ionic Liquids with Different Anions Using a New Molecular Beam Setup**
L. Winter, R. G. Bhuin, M. Lexow, F. Maier, H.-P. Steinrück
J. Chem. Phys., **2020**, *153*, 214706

[P3] ***n*-Butane, *iso*-Butane and 1-Butene Adsorption on Imidazolium-Based Ionic Liquids Studied with Molecular Beam Techniques**
L. Winter, R. G. Bhuin, F. Maier, H.-P. Steinrück
Chem. Eur. J., **2021**, *27*, 17059-17065

[P4] **Tailoring the Selectivity of 1,3-Butadiene versus 1-Butene Adsorption on Pt(111) by Ultrathin Ionic Liquid Films**
L. Winter, S. Trzeciak, C. C. Fernández, S. Massicot, T. Talwar, F. Maier, D. Zahn, H.-P. Steinrück
ACS Catal., **2023**, *13*, 10866-10877

In the last part of the appendix, technical drawings and tables of the ILID chamber are provided.

GDCh **Communications** Angewandte International Edition

Ionic Liquids **Hot Paper**

How to cite: *Angew. Chem. Int. Ed.* **2020**, *59*, 14429–14433
International Edition: doi.org/10.1002/anie.202005991
German Edition: doi.org/10.1002/ange.202005991

On the Dynamic Interaction of *n*-Butane with Imidazolium-Based Ionic Liquids

*Radha G. Bhuin, Leonhard Winter, Matthias Lexow, Florian Maier, and Hans-Peter Steinrück**

Abstract: *The impact of a reactant from the gas phase on the surface of a liquid and its transfer through this gas/liquid interface are crucial for various concepts applying ionic liquids (ILs) in catalysis. We investigated the first step of the adsorption dynamics of n-butane on a series of 1-alkyl-3-methylimidazolium bis(trifluoromethanesulfonyl)imide ILs ($[C_nC_1Im][Tf_2N]$; $n = 1, 2, 3, 8$). Using a supersonic molecular beam in ultra-high vacuum, the trapping of n-butane on the frozen ILs was determined as a function of surface temperature, between 90 and 125 K. On the C_8- and C_3-ILs, n-butane adsorbs at 90 K with an initial trapping probability of ≈ 0.89. The adsorption energy increases with increasing length of the IL alkyl chain, whereas the ionic headgroups seem to interact only weakly with n-butane. The absence of adsorption on the C_1- and C_2-ILs is attributed to a too short residence time on the IL surface to form nuclei for condensation even at 90 K.*

The catalytic conversion of hydrocarbons is a key process of the chemical industry, for example, for the production of commodity chemicals or polymers. In this context, two important catalytic concepts have been introduced.[1] Both utilize ionic liquids (ILs), which are salts typically with melting points below 100 °C[2] and often an extremely low vapor pressure.[3] ILs can be tailored over a wide range, and thus are an important class of liquid materials for many applications.[1c,4] The two catalytic concepts are supported ionic liquid phase (SILP)[1a,d] catalysis and solid catalyst with ionic liquid layer (SCILL).[1b] In both, a thin IL layer coats the catalyst support. The reactants enter from the gas phase through the gas/liquid interface, react with the dissolved catalyst complex in SILP or with the IL-modified solid catalyst in SCILL, and the formed products are released again through the gas/liquid interface. Thus, the transfer of gas molecules through this interface is crucial in both concepts. Despite the importance of ILs in catalysis, the dynamics of the adsorption of reactants at the gas/IL interface and its dependence on the interface properties have hardly been studied in detail so far. Previous studies concern the adsorption/desorption and state-resolved scattering experiments of small molecules.[5]

Upon impact of a gas molecule onto an IL, it exchanges energy and momentum with the moieties in the topmost IL layer. This situation corresponds to the interaction of molecules with solid surfaces, which has been studied using supersonic molecular beams under ultra-high vacuum (UHV) conditions in detail in the past. Using this approach, the trapping of physisorbed species (or the sticking of chemisorbed species) have been determined on a variety of metal surfaces.[6] The trapping (or sticking) probability, S, is defined as ratio of the adsorption rate R_{ads} and the impingement rate R_{imp} of molecules on the surface, $S = R_{ads}/R_{imp}$.[6a,e] S depends on the properties of the surface (temperature, composition, adsorbate coverage) and of the incoming molecules (kinetic and internal energy, angle of incidence, orientation).[6a]

In this study, we address the interaction of *n*-butane with a series of 1-alkyl-3-methylimidazolium bis(trifluoromethanesulfonyl)imide ILs, $[C_nC_1Im][Tf_2N]$ ($C_n = C_1, C_2, C_3, C_8$), which we denote as C_n-ILs in the following. *n*-Butane is considered as a model system for a number of important catalytic processes, for example, refinery alkylation reactions,[7] hydroformylations[1a] and hydrogenations of alkenes.[1b] In addition, investigations on single crystal metal surfaces can serve as reference systems. By studying ILs with different lengths of the alkyl chain, we aim in particular for an understanding of the role of the alkyl chain as compared to the ionic groups.

The dynamic interaction of an incoming molecule with an IL depends on the interaction potential. For hydrocarbons, the interaction potential is a sum of weak attractive van-der-Waals forces and strong short-range Pauli repulsion. The resulting well-depth is only shallow, such that no stable adsorption occurs at room temperature (RT).[6a] In order to obtain information on trapping probabilities and adsorption energies, we thus have to work at conditions, where stable adsorption of *n*-butane on the IL occurs. This cannot be achieved at RT, but requires temperatures below 100 K. Notably, at this temperature, ILs are not in their liquid state, but are frozen. Nevertheless, we expect that the surface structures in the liquid and in the frozen states are quite similar, since many ILs form amorphous solids upon cooling. For the C_8-IL, we verified this for thin IL films by temperature-dependent angle-resolved X-ray photoelectron spectroscopy (ARXPS, see Figure S1 and S2 of the Supporting Information). We are therefore confident that we can transfer our conclusions also to the liquid state at or above RT.

---

[*] Dr. R. G. Bhuin, L. Winter, Dr. M. Lexow, Dr. F. Maier, Prof. Dr. H.-P. Steinrück
Lehrstuhl für Physikalische Chemie 2, Friedrich-Alexander-Universität Erlangen-Nürnberg
Egerlandstr. 3, 91058 Erlangen (Germany)
E-mail: hans-peter.steinrueck@fau.de

Supporting information and the ORCID identification number(s) for the author(s) of this article can be found under: https://doi.org/10.1002/anie.202005991.

To determine the trapping probabilities of n-butane on the different ILs, we used a newly built three-stage supersonic molecular beam setup with a quadrupole mass spectrometer (QMS), which is combined with an X-ray photoelectron spectrometer (XPS). In contrast to common supersonic beam setups with a horizontal beam, our beam impinges on the surface vertically from the top, to be able to study horizontally mounted liquid samples. The ultraclean ILs (as checked by XPS) were spread on a polycrystalline Ni support ($12 \times 12\ \mathrm{mm}^2$, Goodfellow), which can be cooled with liquid N_2 down to 88 K. The temperature is measured by a K-type thermocouple, which is inserted into a small hole at the side of the Ni support. The thickness of the IL films was ≈ 1 mm.

The trapping probabilities were determined using the well-established direct method by King and Wells,[8] which uses two flags to control the molecular beam: The beam flag inside the molecular beam setup allows us to switch the beam on and off. The sample flag in the analysis chamber can be positioned such that the molecular beam can impinge or not impinge on the sample.

In Figure 1, two series of trapping probability measurements of n-butane on the C_8- and C_3-IL are depicted, for temperatures from 90 to 118 K. To explain the King and Wells method,[8] we discuss the data at 90 and 102 K for the C_8-IL. The Figure shows the partial pressure of n-butane ($m/z = 43$) in the chamber, as measured by QMS, versus time. At $t = -40$ s, the beam flag and the sample flag are closed, which yields a zero n-butane signal (after background subtraction). At $t = -20$ s, the beam flag is opened, leading to a sudden signal increase, Δp_{beam}, in the analysis chamber. The closed sample flag prevents the beam from hitting the sample at this time. At $t = 0$ s, the sample flag is removed so that the beam hits the sample, which induces a pronounced signal drop, Δp_{ads}, by $\approx 90\,\%$. This drop is due to the fact that molecules adsorb on the sample and thus are not detected by the QMS (if all molecules would adsorb, the n-butane signal would go back to zero, that is, the sample would act like a perfect pump). From this initial drop, we determine the initial trapping probability S_0 (at zero n-butane coverage on the IL) as the ratio of the signal drop at $t = 0$ s devided by the

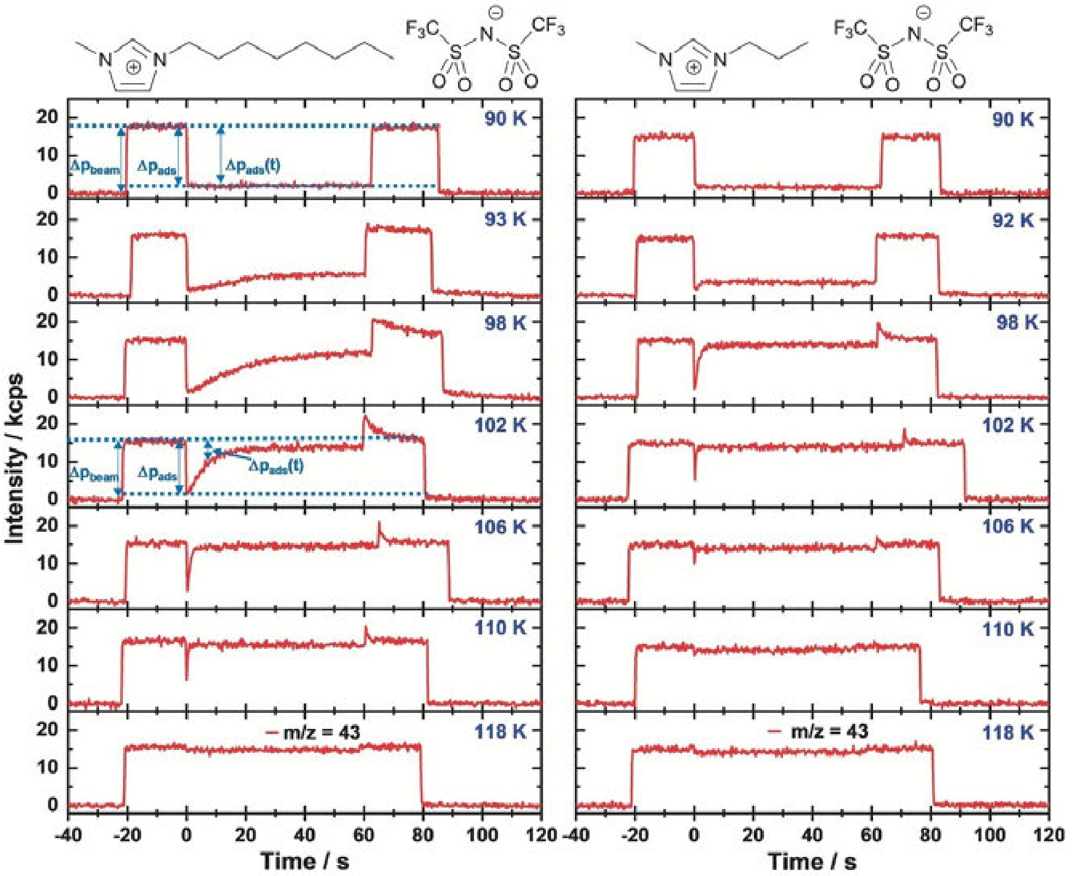

Figure 1. Trapping probability measurements of n-butane on $[C_8C_1Im][Tf_2N]$ (left) and $[C_3C_1Im][Tf_2N]$ (right) at selected temperatures. The n-butane partial pressure was monitored using $m/z = 43$, which is the most intense fragment. A linear background was subtracted from all curves. The kinetic energy of the unseeded n-butane beam with the nozzle at RT is estimated to be 13 kJ mol^{-1}, by comparison to ref. [12].

signal increase at $t=-20$ s, that is, $S_0=R_{ads}/R_{imp}=\Delta p_{ads}/\Delta p_{beam}$.

With increasing time, the signal stays constant (90 K) or increases again (102 K), which reflects the time-dependent trapping probability $S(t)=\Delta p_{ads}(t)/\Delta p_{beam}$. The time dependence follows from the fact that with time n-butane accumulates on the IL surface, which can influence the trapping behavior. With the knowledge of the beam flux, the time dependence can be converted into a coverage dependence (see below).

At $t\approx 60$ s (depending on the individual experiment), the sample flag is closed. At 90 K, the pressure increases back to the value before opening the sample flag, as one would expect. At 102 K, the increase is even larger, and after the sudden increase the signal decreases exponentially to the value before opening the sample flag; this effect will be addressed below. Finally at ≈ 80 s, the beam flag is also closed and the n-butane signal drops back to zero.

We first address the initial trapping probability S_0 (at zero coverage) on the C_8-IL as a function of IL temperature, as plotted in Figure 2 (red circles). At 90 K, we observe a value of 0.89 ± 0.03. S_0 stays constant up to ≈ 102 K and then drops to zero. At the characteristic temperature $T_{50\%}$ $(C_8)=110$ K, S_0 has dropped to 50% of its initial value. We attribute this decrease of S_0 above ≈ 102 K not to a change of the probability of getting adsorbed on the surface, but to the concomitant onset of desorption from the adsorbed layer. If desorption is fast compared to the measurement time of the first data point (0.30 s), one obtains an apparently smaller value of S_0. Thus, $T_{50\%}$ contains valuable information on the desorption energy (see below).

For the C_3-IL, we observe a very similar behavior in Figure 2 (blue triangles), albeit shifted to lower temperature by 6 K: The initial S_0 value of 0.88 ± 0.03 is constant until ≈ 96 K and then drops to zero with $T_{50\%}$ $(C_3)=104$ K. Interestingly, for the C_1- and C_2-ILs (green diamonds and purple triangles in Figure 2) no trapping is observed even at the lowest temperature of 88 K. For comparison, we also plotted a measurement series on clean Ni(111), that is, without an IL (black squares). While the initial trapping probability is identical, 0.88 ± 0.04 at 90 K, it stays constant up to ≈ 135 K, and decreases thereafter with $T_{50\%}$ (Ni) = 150 K. Our data clearly show that the interaction with n-butane depends on the length of the alkyl chain of the IL. The $T_{50\%}$ values are 110 K for the C_8-IL, 104 K for the C_3-IL, and values to small to be measured for the C_2- and C_1-ILs. Using the $T_{50\%}$ values, we can determine information on the differences in desorption energy of n-butane on the different ILs (see below).

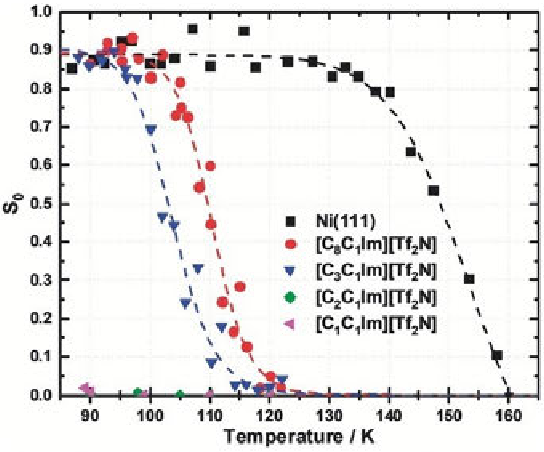

Figure 2. Temperature-dependent initial trapping probability of n-butane on $[C_nC_1Im][Tf_2N]$ ILs with varying chain length compared to the initial trapping probability on Ni(111). The dashed lines are guides to the eye.

Next, we discuss the time dependence of the trapping probabilities $S(t)$ in Figure 1. For the C_8-IL, the n-butane signal at 90 K remains unchanged after the initial drop at $t=0$ s, until the sample flag is closed at $t\approx 60$ s. This indicates negligible desorption, and that after saturation of the first layer, n-butane multilayers continue to adsorb with the same trapping probability. At higher temperatures, the signal increases after the initial drop at $t=0$ s, and this increase becomes more pronounced with increasing temperature. This is due to the fact that the desorption rate now is not negligible any more, but rather is proportional to the coverage, which increases until the first layer is filled. It levels off either when the (higher) desorption rate of the multilayer at this temperature is reached (from 93 to 98 K) or when the pressure value before opening the sample flag is reached, which indicates identical desorption and adsorption rates (that is, zero "net" trapping). After switching off the beam at $t\approx 60$ s, the pressure increases to values above those before opening the sample flag. This behavior is due to the fact that now the adsorption flux is turned off, but desorption still occurs. This differential signal decays exponentially.

In Figure 3a, we show the "net" trapping probability, $S^*(\theta)$, on the C_8-IL as a function of coverage for temperatures up to 106 K. While $S(\theta)$ solely describes the trapping probability into the adsorbed state, $S^*(\theta)$ also accounts for possible desorption, at given coverage θ. For all temperatures above 90 K, we initially observe a linear decrease of $S^*(\theta)$, which in a simple picture can be understood in the following way: We assume that $S(\theta)$ is independent of coverage (which is the case at 90 K; see Figure 3a). Then the adsorption rate is $R_{ads}=S(\theta)\cdot R_{imp}=S_0\cdot R_{imp}$ (with $R_{imp}=2.0\times10^{13}$ molecules $cm^{-2}s^{-1}$). With time, the coverage $\theta=\int(R_{ads}-R_{des})\,dt$ builds up on the surface. While the desorption rate is zero at 90 K, at higher temperatures significant desorption starts counteracting adsorption, with a rate $R_{des}=\theta\cdot\nu\cdot\exp(-E_{des}/RT)$, leading to a decrease of $S^*(\theta)$. If the desorption energy E_{des} does not depend on coverage, the desorption rate increases linearly with coverage, which explains the linear decrease of $S^*(\theta)$ in Figure 3a. In a next step, the slopes of this decrease for different temperatures are analyzed in an Arrhenius plot in Figure 3b. From a linear fit, we obtain a desorption energy of 29 ± 3 kJ mol^{-1} and a prefactor of $1.4\times10^{14\pm2}$ s^{-1}.

For the C_3-IL, we observe an overall similar behavior as for the C_8-IL, albeit shifted to lower temperatures (compare data at 106 K for the C_8-IL and 98 K for the C_3-IL in Figure 1). In Figure S3 of the Supporting Information, we show the

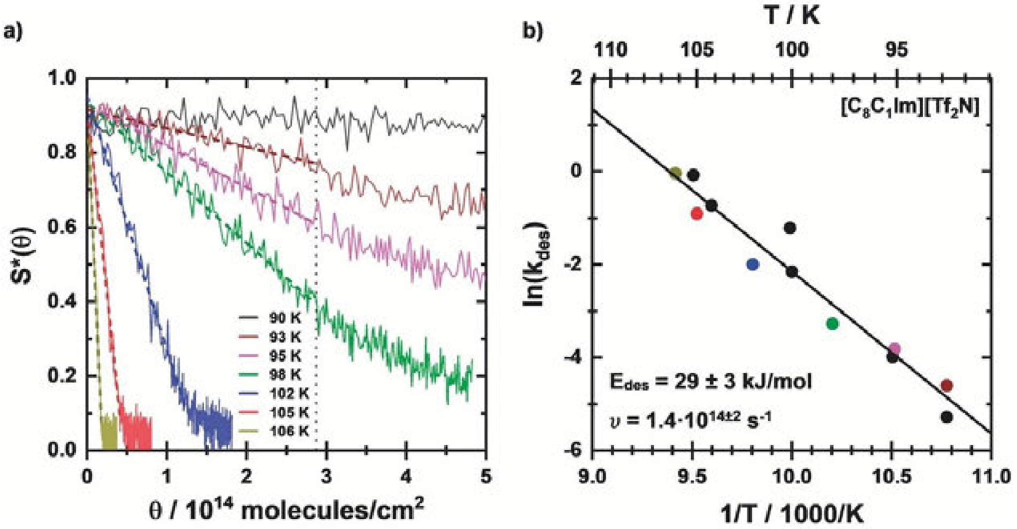

Figure 3. (a) Net trapping probability of *n*-butane on [C_8C_1Im][Tf_2N] as a function of coverage for various temperatures. The behavior is fitted linearly (dashed lines). (b) Arrhenius analysis of the rate constants k_{des} obtained from (a). From the linear fit, the desorption energy and the pre-exponential factor are derived; colored symbols in (b) correspond to the colored curves in (a). The coverage of a closed monolayer is indicated by a vertical dotted line in (a). It was determined assuming that the saturation coverage on Ni(111) at 102 K corresponds to that of a freestanding layer of flat-lying *n*-butane, that is, 2.87×10^{14} molecules cm^{-2}, as taken from ref. [13].

"net" trapping probability, $S^*(\theta)$, also for the C_3-IL as a function of coverage. In this case, however, the accessible temperature range is too small for an Arrhenius analysis. However, we can use the shift of $T_{50\%}$ in Figure 2 by 6 K to lower temperatures to estimate the difference in desorption energy compared to the C_8-IL. Using the same prefactor, a decrease of the desorption energy by ≈6% explains the observed shift.

To understand the absence of any trapping on the C_2- and C_1-ILs, we have to consider that *n*-butane multilayers on the C_8- and C_3-ILs start to desorb with an onset just above 90 K. The fact that we observe constant S_0 values of ≈0.89 up to 102 and 95 K on the C_8- and C_3-IL, respectively, indicates that *n*-butane molecules are stronger bound to these two ILs than in the multilayer; otherwise desorption would immediately occur. For the C_2- and C_1-ILs, the adsorption energy is smaller than the condensation energy, and individual molecules immediately desorb after adsorption, such that we measure a zero value for S_0.

In a simplified picture, the surface of the investigated ILs is composed of the $[Tf_2N]^-$ anion with the CF_3 groups pointing outwards,[9] the imidazolium headgroup, and the non-polar alkyl chains of the cation.[10] The absence of trapping on the C_1- and C_2-ILs at 88 K (that is, where *n*-butane condenses in multilayers on other surfaces) indicates that the attractive van-der-Waals forces between *n*-butane and the polar head groups and also with the C_1- and C_2-chains are too weak. Only upon increasing the alkyl chain length, we observe trapping, which indicates that starting from the C_3-IL, the attractive interaction between *n*-butane and the alkyl chain is strong enough for permanent adsorption on the surface. For the C_8-IL, the interaction is even stronger; here, also the well-known alkyl surface enrichment for chains with $n \geq 4$ will contribute.[9,11]

An interesting point to be addressed is the reason why we observe multilayer formation of *n*-butane on the C_8- and C_3-ILs up to 95 K, but not on the C_2- and C_1-ILs. We attribute this observation to the fact that nuclei are required for multilayer growth. The formation of stable nuclei needs, however, a certain coverage on the surface, so that statistically enough molecules encounter each other. Due to the weak interaction with the C_2- and C_1-ILs, the residence time of *n*-butane on these surfaces is too short to form such stable nuclei. We tried to increase the beam flux by a factor of 10, and also extended the exposure time to 900 s, but did not observe any adsorption.

Interestingly, a similar effect was observed in thermal desorption studies for water adsorbed on frozen [C_8C_1Im][BF_4] and [C_2C_1Im][Tf_2N], where the desorption energies of the monolayers were found to be smaller than for the multilayer, along with a vanishing initial trapping probability below the multilayer desorption temperature.[5f] This is in line with the behavior observed here for *n*-butane on C_1- and C_2-ILs, where no trapping was observed either. For water on the two ILs, an observed increase of the trapping probability with coverage was attributed to dominating adsorbate-adsorbate interactions.[5f] This effect was not observed here, which is assigned to the too short residence time for the formation of a nucleus. It is also noteworthy to mention that state-resolved scattering experiments on the same ILs as studied here showed that the sticking probabilities of NO are not influenced by the alkyl chain length for low kinetic energies, in line with our results for *n*-butane.[5a]

In conclusion, we studied the trapping of *n*-butane on different $[C_nC_1Im][Tf_2N]$ ILs ($n = 1, 2, 3, 8$) using a supersonic molecular beam at low temperatures. From the initial trapping probability at zero *n*-butane coverage, we deduce that the adsorption energy on the ILs increases with increasing chain length. On the C_8- and C_3-ILs, we find pronounced trapping while on the C_2- and C_1-ILs no trapping occurs. We thus conclude that the adsorption energy of *n*-butane on the IL surface is dominated by the interaction with the alkyl chain, while the interaction with the ionic head groups seems much weaker. One interesting observation is that at 88 K on the C_2- and C_1-ILs multilayer formation is suppressed, despite the fact that it occurs on the C_8- and C_3-ILs and also on Ni(111) even at significantly higher temperatures. This is attributed to the absence of nucleus formation due to a too short residence time. We believe that the conclusions derived from our UHV experiments at low temperature on frozen amorphous ILs can be transferred to ILs in their liquid phase at room temperature or above, because the first impact of a molecule from the gas phase determines the energy and momentum transfer with the liquid. Since the interaction strength increases with increasing chain length, using ILs with longer alkyl chains should increase the efficiency of this first step. The well-known surface enrichment of longer alkyl chains could even enhance this effect.

Acknowledgements

R.B., L.W., M.L. and H.-P.S. thank the European Research Council (ERC) under the European Union's Horizon 2020 research and innovation programme for financial support, in the context of the Advanced Investigator Grant "ILID" to H.-P.S. (Grant Agreement No. 693398-ILID). We acknowledge the support by Bernd Kreß, Hans-Peter Bäumler and the mechanical workshop, when planning and assembling the new UHV setup.

Conflict of interest

The authors declare no conflict of interest.

Keywords: gas-surface dynamics · ionic liquids · molecular beam · *n*-butane · trapping and adsorption

---

[1] a) C. P. Mehnert, R. A. Cook, N. C. Dispenziere, M. Afeworki, *J. Am. Chem. Soc.* **2002**, *124*, 12932–12933; b) U. Kernchen, B. Etzold, W. Korth, A. Jess, *Chem. Eng. Technol.* **2007**, *30*, 985–994; c) H.-P. Steinrück, P. Wasserscheid, *Catal. Lett.* **2015**, *145*, 380–397; d) A. Riisager, R. Fehrmann, M. Haumann, B. S. K. Gorle, P. Wasserscheid, *Ind. Eng. Chem. Res.* **2005**, *44*, 9853–9859; e) S. Walter, M. Haumann, P. Wasserscheid, H. Hahn, R. Franke, *AIChE J.* **2015**, *61*, 893–897; f) T. Barth, W. Korth, A. Jess, *Chem. Eng. Technol.* **2017**, *40*, 395–404.

[2] "Ionic Liquids in Synthesis": *Ionic Liq. Synth.*, 2nd ed. (Eds.: P. Wasserscheid, T. Welton), Wiley-VCH, Weinheim, **2008**.

[3] a) P. Wasserscheid, *Nature* **2006**, *439*, 797; b) M. J. Earle, J. M. S. S. Esperança, M. A. Gilea, J. N. Canongia Lopes, L. P. N. Rebelo, J. W. Magee, K. R. Seddon, J. A. Widegren, *Nature* **2006**, *439*, 831–834.

[4] N. V. Plechkova, K. R. Seddon, *Chem. Soc. Rev.* **2008**, *37*, 123–150.

[5] a) A. Zutz, D. J. Nesbitt, *AIP Adv.* **2016**, *6*, 105207; b) X. Li, G. C. Schatz, D. J. Nesbitt, *J. Phys. Chem. B* **2012**, *116*, 3587–3602; c) J. R. Roscioli, D. J. Nesbitt, *J. Phys. Chem. Lett.* **2010**, *1*, 674–678; d) M. Buckley, K. L. Syres, R. G. Jones, *Faraday Discuss.* **2018**, *206*, 475–495; e) S. G. Hessey, R. G. Jones, *Chem. Sci.* **2013**, *4*, 2519–2529; f) A. Deyko, R. G. Jones, *Faraday Discuss.* **2012**, *154*, 265–288.

[6] a) J. F. Weaver, A. F. Carlsson, R. J. Madix, *Surf. Sci. Rep.* **2003**, *50*, 107–199; b) C.-L. Kao, R. J. Madix, *Surf. Sci.* **2004**, *557*, 215–230; c) C. R. Henry, *Surf. Sci. Rep.* **1998**, *31*, 231–325; d) S. L. Bernasek, *Adv. Chem. Phys.* **1980**, *41*, 477–516; e) J. A. Barker, D. J. Auerbach, *Surf. Sci. Rep.* **1984**, *4*, 1–99; f) C. R. Arumainayagam, R. J. Madix, *Prog. Surf. Sci.* **1991**, *38*, 1–102.

[7] C.-P. Huang, Z.-C. Liu, C.-M. Xu, B.-H. Chen, Y.-F. Liu, *Appl. Catal. A* **2004**, *277*, 41–43.

[8] D. A. King, M. G. Wells, *Surf. Sci.* **1972**, *29*, 454–482.

[9] K. R. J. Lovelock, C. Kolbeck, T. Cremer, N. Paape, P. S. Schulz, P. Wasserscheid, F. Maier, H.-P. Steinrück, *J. Phys. Chem. B* **2009**, *113*, 2854–2864.

[10] a) C. Waring, P. A. J. Bagot, J. M. Slattery, M. L. Costen, K. G. McKendrick, *J. Phys. Chem. A* **2010**, *114*, 4896–4904; b) M. A. Tesa-Serrate, B. C. Marshall, E. J. Smoll, S. M. Purcell, M. L. Costen, J. M. Slattery, T. K. Minton, K. G. McKendrick, *J. Phys. Chem. C* **2015**, *119*, 5491–5505.

[11] K. Shimizu, B. S. J. Heller, F. Maier, H.-P. Steinrück, J. N. Canongia Lopes, *Langmuir* **2018**, *34*, 4408–4416.

[12] A. V. Hamza, H.-P. Steinrück, R. J. Madix, *J. Chem. Phys.* **1986**, *85*, 7494–7495.

[13] K. Lee, Y. Morikawa, D. C. Langreth, *Phys. Rev. B* **2010**, *82*, 155461.

Manuscript received: April 25, 2020
Revised manuscript received: May 18, 2020
Accepted manuscript online: May 19, 2020
Version of record online: July 1, 2020

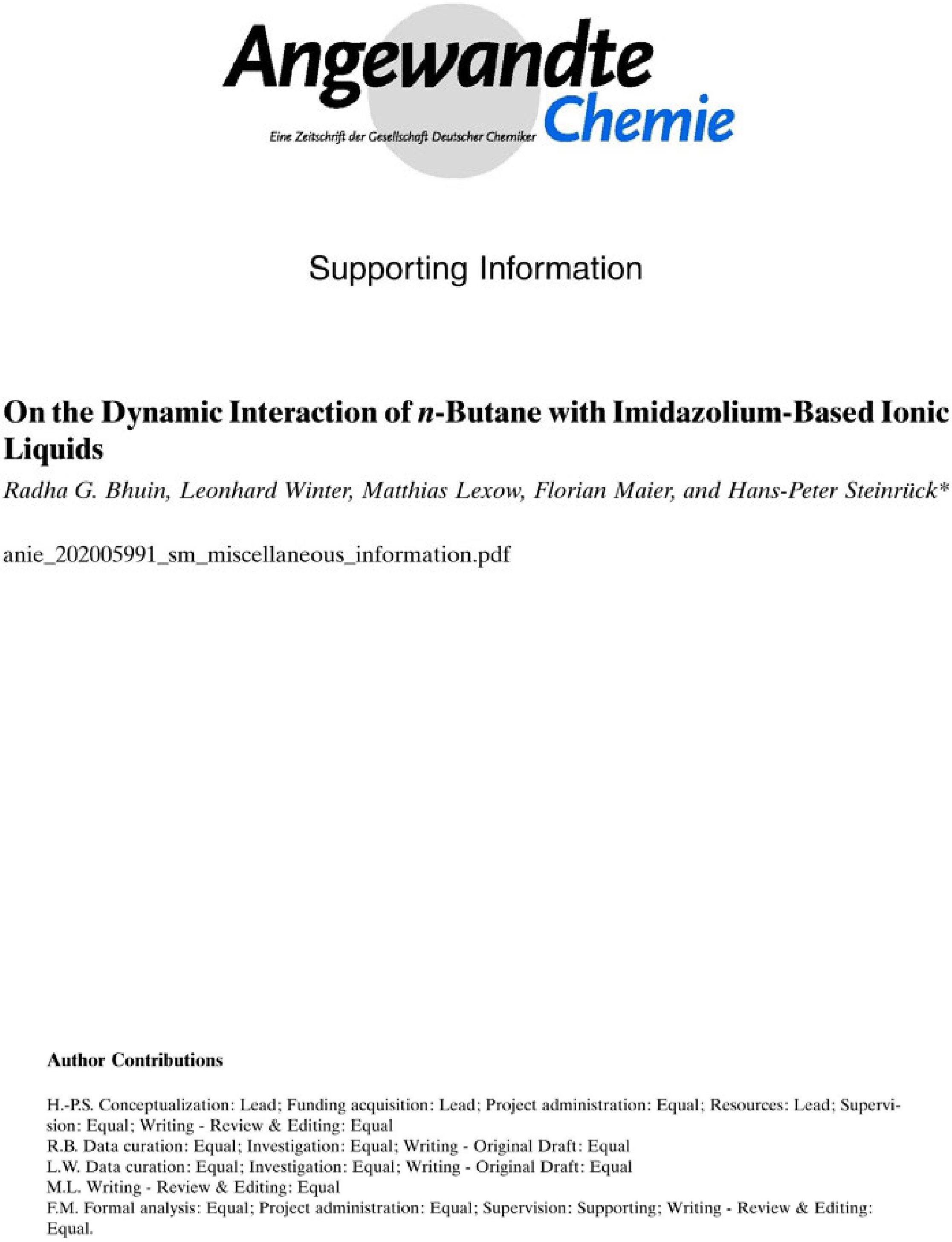

Angewandte Chemie
Eine Zeitschrift der Gesellschaft Deutscher Chemiker

Supporting Information

On the Dynamic Interaction of *n*-Butane with Imidazolium-Based Ionic Liquids

*Radha G. Bhuin, Leonhard Winter, Matthias Lexow, Florian Maier, and Hans-Peter Steinrück**

anie_202005991_sm_miscellaneous_information.pdf

Author Contributions

H.-P.S. Conceptualization: Lead; Funding acquisition: Lead; Project administration: Equal; Resources: Lead; Supervision: Equal; Writing - Review & Editing: Equal
R.B. Data curation: Equal; Investigation: Equal; Writing - Original Draft: Equal
L.W. Data curation: Equal; Investigation: Equal; Writing - Original Draft: Equal
M.L. Writing - Review & Editing: Equal
F.M. Formal analysis: Equal; Project administration: Equal; Supervision: Supporting; Writing - Review & Editing: Equal.

Surface composition of ILs in the liquid and the frozen state

Surfaces of $[C_nC_1Im][Tf_2N]$ ILs (C_n-ILs) in the liquid state have already been characterized in detail by angle-resolved X-ray photoelectron spectroscopy (ARXPS) in our group.[1] In these ARXPS measurements, spectra at 0° emission are considered bulk-sensitive (with an information depth, ID, of 7-9 nm), while spectra at 80° are considered surface-sensitive (ID 1-1.5 nm), as they probe only the topmost IL layer(s). In order to rule out pronounced changes in surface composition during the phase transition from the liquid into the solid state, we performed ARXPS throughout cooling the C_8-IL. From the four C_n-ILs of this work, we deliberately chose this IL, because of the pronounced surface enrichment of the octyl chain, which is clearly seen in ARXPS (in contrast to the C_1-, C_2- and C_3-ILs with their shorter chains).[1] Thus, potential changes during phase transition are expected to be also most pronounced for this IL.

For macroscopic thick IL films, meaningful ARXPS measurements can only be conducted well above the glass transition temperature ($T_g \approx 185$ to 193 K[2] for the C_8-IL), because severe charging occurs at lower temperatures, yielding signal shifts and broadening.[3] This issue can be circumvented using ultrathin films consisting of several IL monolayers as prepared by physical vapor deposition (PVD): If the films are sufficiently thick (> 2 nm), the structure and composition at the vacuum/IL interface is identical to macroscopically thick films, as was shown by ARXPS.[4] The advantage is that these few nm thick PVD films do not charge in XPS in the solid state, even down to liquid nitrogen temperature. Figure S1 shows the comparison of C 1s spectra at 0° and 80° of a 2.5 nm C_8-IL film (2.5 nm corresponds to ~4 IL ion pair layers) prepared on Ag(111), acquired at 240 and 130 K, that is, above and below the glass transition temperature of the C_8-IL, respectively. The C 1s spectra show three signals, which stem from the anion and the cation of the C_8-IL. The C_{anion} signal corresponds to the two C atoms of the $[Tf_2N]^-$ anion, the C_{hetero} peak to the five C atoms neighboring the two N atoms of the cation, and the C_{alkyl} peak comprises the remaining seven C atoms of the octyl chain. The spectra at 240 and 130 K show no differences within the accuracy of our measurement, which allows us to assume identical composition of the IL surface, even though the IL was cooled well below the glass transition temperature in between the experiments.

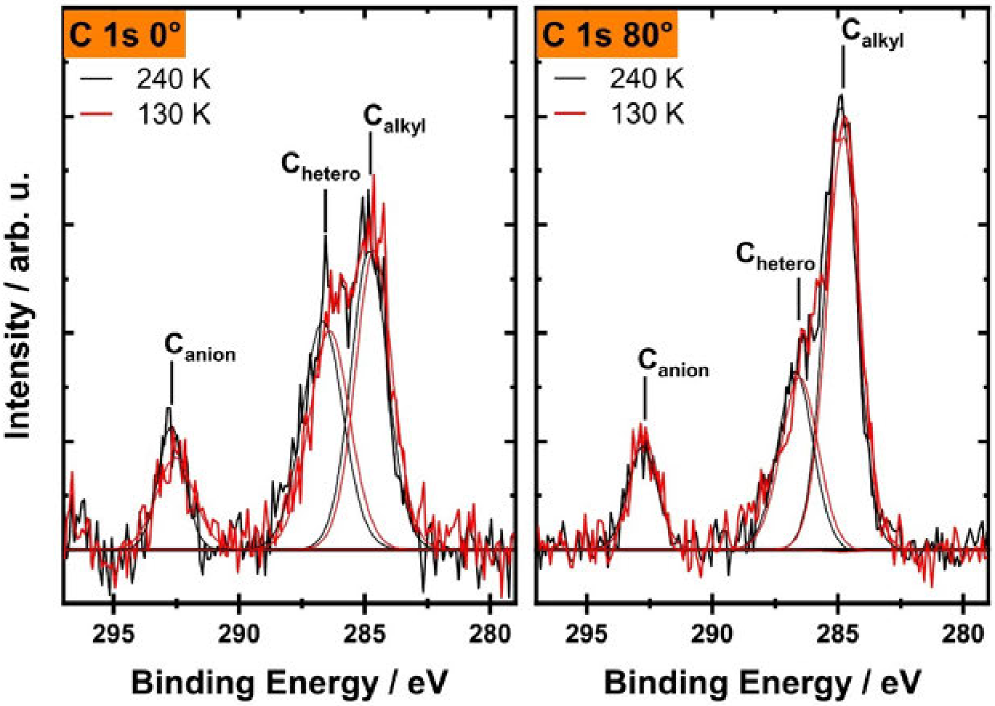

Figure S1: C 1s spectra of a 2.5 nm thick film of [C_8C_1Im][Tf_2N] on Ag(111) in 0° (left) and 80° (right) emission at 240 (black) and 130 K (red).

To assess the surface composition over a wide temperature window, we monitored the ratio of the C_{alkyl} and C_{hetero} peak areas for the 0° and 80° measurements (nominal intensity ratio 7:5 = 1.4). Figure S2 shows the C_{alkyl}:C_{hetero} ratio in the temperature range between RT and 110 K for thin (2.2 to 3.4 nm) PVD films, and between RT and the onset of charging (210 K) for macroscopic films. The spectra of the macroscopic films were already partly published,[3] but reanalyzed for this work using a refined analysis[5]. The higher ratio at 80° (red symbols) as compared to 0° (black) of all samples reflects the surface enrichment of the octyl chain, which does not change between 300 and 110 K. This temperature-independent behavior holds not only true for the C 1s spectra but also for the other C_8-IL signals demonstrating that virtually no changes in surface composition are observed during the phase transition in ARXPS.

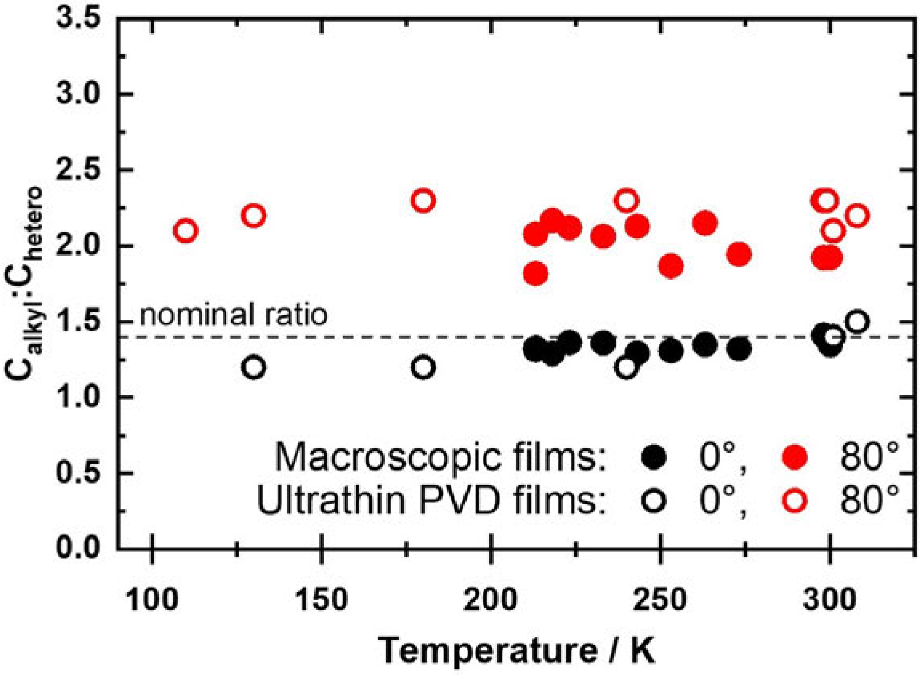

Figure S2: C_{alkyl}:C_{hetero} ratios measured at 0 (black) and 80° (red) emission for macroscopically thick C_8-IL films (closed symbols, derived from Ref. [3]) between RT and the onset of charging (~210 K), and for C_8-IL PVD films on Ag(111) (thickness between 2.2 and 3.4 nm, open symbols) between RT and 110 K.

Coverage-dependence of S^* for the C_8- and C_3-ILs

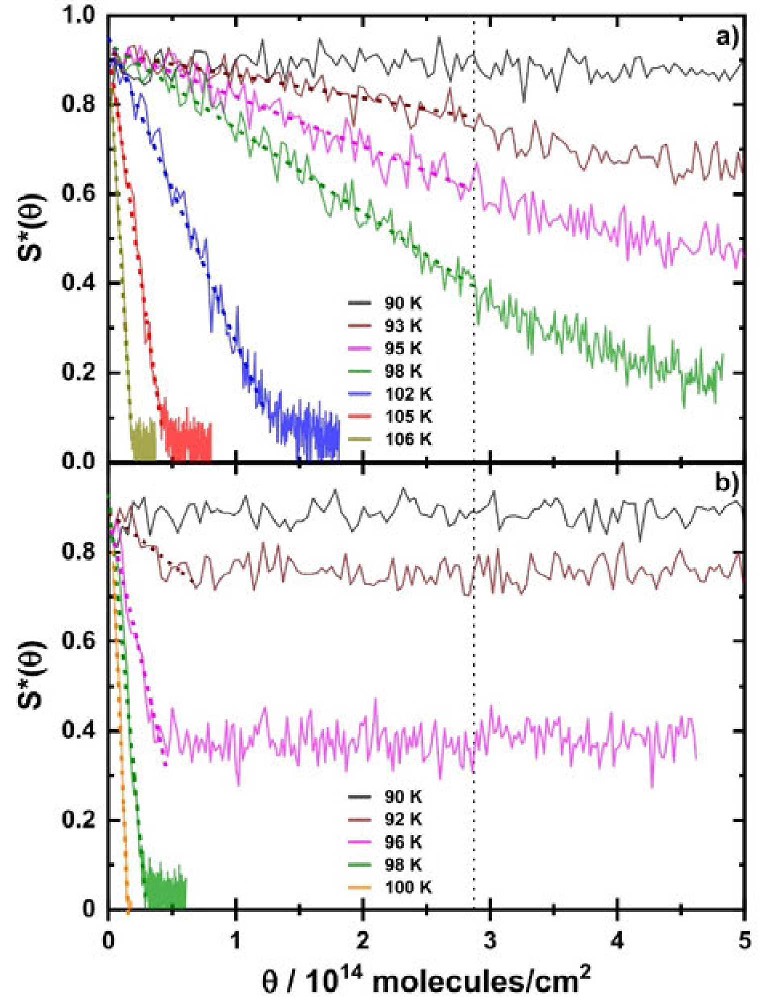

Figure S3: Net trapping probability S^* of *n*-butane on $[C_8C_1Im][Tf_2N]$ (a) and $[C_3C_1Im][Tf_2N]$ (b) as a function of coverage for various temperatures. The behavior is fitted linearly (dashed lines). The coverage of a closed monolayer is indicated by a vertical dotted line according to Figure 3 of the main manuscript.

References

[1] K. R. J. Lovelock, C. Kolbeck, T. Cremer, N. Paape, P. S. Schulz, P. Wasserscheid, F. Maier, H.-P. Steinrück, *J. Phys. Chem. B* **2009**, *113*, 2854-2864.

[2] a) Y. U. Paulechka, A. V. Blokhin, G. J. Kabo, A. A. Strechan, *J. Chem. Thermodyn.* **2007**, *39*, 866-877; b) N. Papaiconomou, N. Yakelis, J. Salminen, R. Bergman, J. M. Prausnitz, *J. Chem. Eng. Data* **2006**, *51*, 1389-1393; c) P. S. Kulkarni, L. C. Branco, J. G. Crespo, M. C. Nunes, A. Raymundo, C. A. M. Afonso, *Chem. Eur. J.* **2007**, *13*, 8478-8488; d) S. V. Dzyuba, R. A. Bartsch, *ChemPhysChem* **2002**, *3*, 161-166; e) H. Tokuda, K. Hayamizu, K. Ishii, M. A. B. H. Susan, M. Watanabe, *J. Phys. Chem. B* **2005**, *109*, 6103-6110.

[3] I. Niedermaier, C. Kolbeck, H.-P. Steinrück, F. Maier, *Rev. Sci. Instrum.* **2016**, *87*, 045105.

[4] M. Lexow, T. Talwar, B. S. J. Heller, B. May, R. G. Bhuin, F. Maier, H.-P. Steinrück, *Phys. Chem. Chem. Phys.* **2018**, *20*, 12929-12938.

[5] K. Shimizu, B. S. J. Heller, F. Maier, H.-P. Steinrück, J. N. Canongia Lopes, *Langmuir* **2018**, *34*, 4408-4416.

Ionische Flüssigkeiten **Hot Paper**

Zitierweise: *Angew. Chem. Int. Ed.* **2020**, *59*, 14429–14433
Internationale Ausgabe: doi.org/10.1002/anie.202005991
Deutsche Ausgabe: doi.org/10.1002/ange.202005991

Die dynamische Wechselwirkung von *n*-Butan mit Imidazolium-basierten ionischen Flüssigkeiten

*Radha G. Bhuin, Leonhard Winter, Matthias Lexow, Florian Maier und Hans-Peter Steinrück**

Abstract: *Das Auftreffen eines Reaktanten aus der Gasphase auf die Oberfläche einer Flüssigkeit und dessen Transfer durch die Gas/Flüssig-Grenzfläche sind äußerst wichtig für verschiedene Konzepte in der Katalyse, bei denen ionische Flüssigkeiten (engl. ionic liquids, ILs) verwendet werden. Wir haben daher die Adsorptionsdynamik von n-Butan auf einer Reihe von 1-Alkyl-3-methyl-imidazolium-bis(trifluoromethansulfonyl)imid-ILs ($[C_nC_1Im][Tf_2N]$; $n = 1, 2, 3, 8$) mithilfe eines Überschallmolekularstrahls im Ultrahochvakuum auf gefrorenen IL-Oberflächen in Abhängigkeit der Oberflächentemperatur zwischen 90 und 125 K bestimmt. Auf den C_8- und C_3-ILs adsorbiert n-Butan bei 90 K mit einem Anfangshaftfaktor von ≈ 0.89. Die Adsorptionsenergie steigt mit zunehmender Länge der Alkylseitenkette im Kation, während die ionischen Kopfgruppen anscheinend nur schwach mit n-Butan wechselwirken. Im Gegensatz dazu findet auf den C_1- und C_2-ILs keine Adsorption statt. Dies führen wir auf eine zu kurze Verweilzeit auf der IL-Oberfläche zurück, weshalb selbst bei 90 K keine Kondensationskeime gebildet werden können.*

Die katalytische Umwandlung von Kohlenwasserstoffen, z. B. zur Herstellung von Grundchemikalien oder Polymeren ist ein Schlüsselprozess in der chemischen Industrie. In diesem Kontext wurden zwei wichtige katalytische Konzepte entwickelt, die beide auf der Nutzung ionischer Flüssigkeiten (engl. ionic liquids, ILs) beruhen.[1] ILs sind Salze mit Schmelzpunkten typischerweise unterhalb von 100 °C[2] und in der Regel extrem niedrigen Dampfdrücken.[3] Ihre Eigenschaften können gezielt modifiziert werden. Wegen dieser hohen Flexibilität finden ILs in verschiedensten Bereichen Anwendung, was sie zu einer wichtigen Stoffklasse unter flüssigen Materialien macht.[1c,4]

Die beiden katalytischen Konzepte sind „Supported Ionic Liquid Phase" (SILP)[1a,d] und „Solid Catalyst with Ionic Liquid Layer" (SCILL).[1b] In beiden Fällen ist das Trägermaterial mit einem dünnen IL-Film bedeckt. Der Übergang der Reaktanten aus der Gasphase in den IL-Film geschieht durch die Gas/IL-Grenzfläche, gefolgt von der Reaktion mit einem gelösten Katalysatorkomplex (SILP) bzw. einem IL-modifizierten festen Katalysator (SCILL). Die gebildeten Produkte werden nach Diffusion zur Gas/IL-Grenzfläche wieder freigesetzt. Folglich ist der Transfer der Gasmoleküle durch diese Grenzfläche für beide Konzepte von entscheidender Bedeutung. Trotz der großen Bedeutung von ILs in der Katalyse wurde die Adsorptionsdynamik der Reaktanten an der Gas/IL-Grenzfläche und ihre Abhängigkeit von den Grenzflächeneigenschaften bisher kaum im Detail untersucht. Bisherige Arbeiten behandelten die Adsorption/Desorption und zustandsaufgelöste Streuexperimente kleiner Moleküle.[5]

Beim Auftreffen eines Gasmoleküls auf der Oberfläche einer IL erfolgen Energie- und Impulsaustausch mit den Gruppen der obersten IL-Schicht. Diese Situation entspricht der Wechselwirkung von Molekülen mit Festkörperoberflächen, die unter Ultrahochvakuumbedingungen (UHV) mithilfe von Überschallmolekularstrahlen bereits detailliert charakterisiert wurde. Mit diesem Ansatz wurde die Adsorption von Atomen und Molekülen auf einer Vielzahl von Metalloberflächen untersucht.[6] Der Haftfaktor S beschreibt die Wahrscheinlichkeit für die Adsorption in einen physisorbierten Zustand („Trapping") bzw. chemisorbierten Zustand („Sticking"). Er ist als das Verhältnis der Adsorptionsrate R_{ads} zur Auftreffrate R_{imp} von Atomen oder Molekülen auf der Oberfläche definiert, $S = R_{ads}/R_{imp}$.[6a,c] S hängt von den Eigenschaften der Oberfläche (Temperatur, Zusammensetzung, Adsorbatbedeckung) und der auftreffenden Moleküle (kinetische und innere Energie, Einfallswinkel, Orientierung) ab.[6a]

Diese Arbeit befasst sich mit der Wechselwirkung von *n*-Butan mit einer Reihe von 1-Alkyl-3-methyl-imidazolium-bis(trifluoromethansulfonyl)imid-ILs, $[C_nC_1Im][Tf_2N]$ ($C_n = C_1, C_2, C_3, C_8$), die im Folgenden als C_n-ILs bezeichnet werden. *n*-Butan dient dabei als Modellsystem für eine Reihe wichtiger Katalyseprozesse, z. B. Raffineriealkylierungsreaktionen,[7] Alkenhydroformylierungen[1a] und -hydrierungen.[1b] Zudem können Untersuchungen zu *n*-Butan auf einkristallinen Metalloberflächen als Referenzsysteme herangezogen werden. ILs mit unterschiedlich langen Alkylsubstituenten werden untersucht, um ein Verständnis für die Bedeutung der Alkylkette für den Adsorptionsprozess, im Vergleich zu den ionischen (Kopf-)Gruppen, zu erreichen.

Die dynamische Wechselwirkung eines auf eine IL Oberfläche auftreffenden Moleküls hängt vom Wechselwirkungspotential zwischen IL und Molekül ab. Für Kohlen-

---

[*] Dr. R. G. Bhuin, L. Winter, Dr. M. Lexow, Dr. F. Maier, Prof. Dr. H.-P. Steinrück
Lehrstuhl für Physikalische Chemie 2
Friedrich-Alexander-Universität Erlangen-Nürnberg
Egerlandstr. 3, 91058 Erlangen (Deutschland)
E-Mail: hans-peter.steinrueck@fau.de

Hintergrundinformationen und die Identifikationsnummern (ORCID) der Autoren sind unter: https://doi.org/10.1002/ange.202005991 zu finden.

wasserstoffe ergibt sich dieses als die Summe schwacher attraktiver Van-der-Waals-Kräfte und kurzreichweitiger Pauli-Abstoßung. Es resultiert eine flache Potentialmulde, so dass bei Raumtemperatur (RT) keine dauerhafte Adsorption auftritt.[6a] Um Informationen zu Haftfaktoren und Adsorptionsenergien zu erhalten, muss daher unter Bedingungen gearbeitet werden, bei denen *n*-Butan stabil auf der IL adsorbiert, d.h. bei Temperaturen unter 100 K. Bei diesen Temperaturen sind die untersuchten ILs allerdings nicht mehr flüssig, sondern gefroren. Wir erwarten aber, dass die Struktur der Oberfläche im flüssigen und gefrorenen Zustand sehr ähnlich ist, da viele ILs beim Abkühlen amorphe Feststoffe bilden. Im Fall der C_8-IL haben wir dies für dünne IL-Filme mittels temperaturabhängiger winkelaufgelöster Röntgenphotoelektronenspektroskopie (engl. Angle-Resolved X-Ray Photoelectron Spectroscopy, ARXPS) überprüft (siehe Abbildungen S1 und S2 in den Hintergrundinformationen). Wir sind daher überzeugt, dass sich die Ergebnisse unserer Untersuchungen auch auf den flüssigen Zustand bei oder oberhalb RT übertragen lassen.

Die Haftfaktoren von *n*-Butan auf den Oberflächen der verschiedenen ILs wurden mithilfe einer speziell für solche Messungen neu aufgebauten Apparatur untersucht, die aus einem dreistufigen Überschallmolekularstrahl, einem Quadrupol-Massenspektrometer (QMS) und einem Röntgenphotoelektronenspektrometer besteht. Im Gegensatz zu herkömmlichen Apparaturen ist der Molekularstrahlaufbau vertikal montiert, was die Untersuchung horizontal positionierter flüssiger Proben bei normalem Einfall des Molekularstrahls ermöglicht. Die ILs, deren hohe Reinheit mittels XPS sichergestellt wurde, wurden auf einem polykristallinen Nickel-Substrat (12×12 mm², Goodfellow) aufgebracht, der mit flüssigem Stickstoff auf bis zu 88 K heruntergekühlt werden kann. Die Temperaturmessung erfolgte mit einem Thermoelement (K-Typ), das in einem kleinen Loch an der Seite des Nickel-Trägers angebracht wurde. Die Dicke der IL-Filme betrug ≈ 1 mm.

Die Haftfaktoren wurden mithilfe der direkten Methode von King und Wells bestimmt.[8] Dabei werden zwei Flags zur Steuerung des Molekularstrahls verwendet: Die Strahl-Flag im Molekularstrahlaufbau wird zum Ein- und Ausschalten des Strahls benutzt. Die Proben-Flag in der Analysenkammer kann so positioniert werden, dass der Molekularstrahl auf die Probe auftreffen kann oder nicht.

Abbildung 1 zeigt zwei Messreihen für den Haftfaktor von *n*-Butan auf den C_8- und C_3-ILs, für Temperaturen von 90 bis 118 K. Die King-und-Wells-Methode[8] wird im Folgenden anhand der Messungen für die C_8-IL bei 90 und 102 K erklärt. In den entsprechenden Messkurven ist der Partialdruck von *n*-Butan ($m/z = 43$) in der Analysenkammer gegen die Zeit aufgetragen. Bei $t = -40$ s sind die Strahl-Flag und die Proben-Flag geschlossen, was (nach Korrektur des Untergrunds) ein *n*-Butansignal von null ergibt. Nach Öffnen der Strahl-Flag bei $t = -20$ s steigt das Signal in der Analysenkammer unmittelbar um Δp_{beam} an. Zu diesem Zeitpunkt verhindert die geschlossene Proben-Flag, dass der Strahl auf die Probe trifft. Bei $t = 0$ s wird die Proben-Flag geöffnet, so dass der Strahl auf die Probe treffen kann. Dies führt zu einem ausgeprägten Signalabfall, Δp_{ads}, um ≈ 90 %. Dieser Abfall ist darauf zurückzuführen, dass die Moleküle auf der Probenoberfläche adsorbieren und somit nicht vom QMS erfasst werden (würden alle Moleküle adsorbieren, ginge das Signal auf null zurück, d.h. die Probe verhielte sich wie eine perfekte Pumpe). Aus der anfänglichen Abnahme wird der Anfangshaftfaktor S_0 bestimmt (bei einer *n*-Butan-Bedeckung von null auf der IL). S_0 folgt aus dem Verhältnis von Signalabfall bei $t = 0$ s und Signalanstieg bei $t = -20$ s, d.h. $S_0 = R_{\mathrm{ads}}/R_{\mathrm{imp}} = \Delta p_{\mathrm{ads}}/\Delta p_{\mathrm{beam}}$.

Mit fortschreitender Zeit bleibt das Signal konstant (90 K) bzw. steigt wieder an (102 K), was den zeitabhängigen Haftfaktor $S(t) = \Delta p_{\mathrm{ads}}(t)/\Delta p_{\mathrm{beam}}$ widerspiegelt. Die Zeitabhängigkeit folgt aus der Tatsache, dass sich mit der Zeit eine zunehmende *n*-Butan-Bedeckung auf der IL-Oberfläche aufbaut, was wiederum das Trapping-Verhalten beeinflussen kann. Mit Kenntnis des Strahlflusses kann die Zeitabhängigkeit in eine Bedeckungsabhängigkeit umgewandelt werden (siehe unten).

Bei $t \approx 60$ s (abhängig vom jeweiligen Experiment) wird die Proben-Flag geschlossen. In der 90 K-Messung steigt der Druck wieder auf den Wert an, den er vor dem Öffnen der Proben-Flag besaß. Bei 102 K ist der Anstieg sogar noch größer und nach dem unmittelbaren Anstieg fällt das Signal exponentiell auf den Wert ab, den es hatte bevor die Proben-Flag geöffnet wurde. Dieser Effekt wird weiter unten noch einmal angesprochen. Schließlich wird bei ≈ 80 s auch die Strahl-Flag geschlossen und das *n*-Butansignal geht auf null zurück.

Zunächst diskutieren wir den Anfangshaftfaktor S_0 (bei Bedeckung gleich null) auf der C_8-IL als Funktion der IL-Temperatur (siehe Abbildung 2, rote Kreise). Bei 90 K ergibt sich ein Wert von 0.89 ± 0.03. S_0 bleibt bis ≈ 102 K konstant und fällt dann bei höheren Temperaturen auf null ab. Bei der charakteristischen Temperatur $T_{50\%}$ (C_8) = 110 K hat S_0 auf 50 % des Anfangswertes abgenommen. Diese Abnahme von S_0 oberhalb von ≈ 102 K wird nicht auf eine Änderung in der Adsorptionswahrscheinlichkeit auf der Oberfläche zurückgeführt, sondern auf den gleichzeitigen Beginn der Desorption aus der bereits adsorbierten Schicht. Wenn die Desorption im Vergleich zur Messzeit für den ersten Datenpunkt (0.30 s) schnell erfolgt, wird ein scheinbar kleinerer Wert für S_0 erhalten. Somit enthält $T_{50\%}$ wertvolle Informationen bezüglich der Desorptionsenergie (siehe unten).

Für die C_3-IL wird in Abbildung 2 (blaue Dreiecke) ein sehr ähnliches Verhalten beobachtet, wenn auch um 6 K in Richtung niedrigerer Temperaturen verschoben: Der anfängliche Wert für S_0 von 0.88 ± 0.03 bleibt bis ≈ 96 K konstant und fällt dann auf null ab, mit $T_{50\%}$ (C_3) = 104 K. Interessanterweise lässt sich für die C_1- und C_2-ILs (grüne Rauten und violette Dreiecke in Abbildung 2) auch bei der niedrigsten Temperatur von 88 K keine Adsorption beobachten. Als Referenz wurde zusätzlich eine Messreihe mit einer Ni(111) Oberfläche durchgeführt, d.h. ohne IL (schwarze Quadrate). Während auf Nickel der Anfangshaftfaktor bei 90 K mit 0.88 ± 0.04 vergleichbar zu jenem auf den ILs ist, bleibt er bis zu einer deutlich höheren Temperatur von ≈ 135 K konstant und nimmt erst danach ab, mit $T_{50\%}$ (Ni) = 150 K. Unsere Daten für die Adsorption auf den ILs zeigen eindeutig, dass die Länge der IL-Alkylkette die Wechselwir-

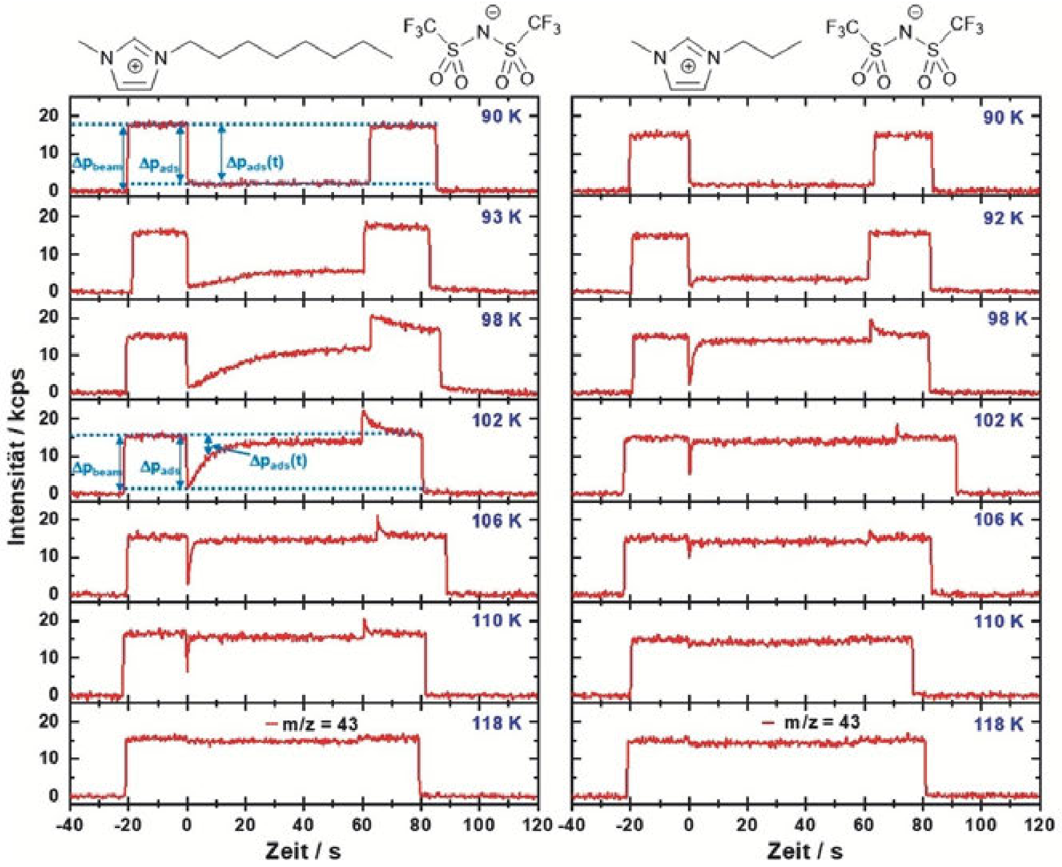

Abbildung 1. Haftfaktormessungen für *n*-Butan auf [C_8C_1Im][Tf_2N] (links) und [C_3C_1Im][Tf_2N] (rechts) für ausgewählte Temperaturen. Der *n*-Butan-Partialdruck wurde mittels $m/z = 43$ verfolgt, welches das signalstärkste Fragment *n*-Butans ist. Von allen Kurven wurde ein linearer Untergrund abgezogen. Aus dem Literaturvergleich[12] wird die kinetische Energie des *n*-Butanstrahls auf 13 kJ mol^{-1} geschätzt (der Strahl wurde mit den gleichen Bedingungen erzeugt, nämlich der Düse bei RT und ohne Seeding).

kung mit *n*-Butan beeinflusst. Die Werte für $T_{50\%}$ betragen 110 K für die C_8-IL, 104 K für die C_3-IL und unmessbar kleine Werte für die C_2- und C_1-ILs. Anhand der $T_{50\%}$-Werte können wir Informationen über Unterschiede in der Desorptionsenergie von *n*-Butan auf den verschiedenen IL-Oberflächen erhalten (siehe unten).

Als nächstes wird die Zeitabhängigkeit der Haftfaktoren $S(t)$ in Abbildung 1 diskutiert. Im Fall der C_8-IL bleibt das Signal für *n*-Butan bei 90 K nach dem anfänglichen Abfall bei $t = 0$ s unverändert, bis die Proben-Flag bei $t \approx 60$ s geschlossen wird. Dies zeigt, dass die Desorptionsrate vernachlässigbar klein ist und dass nach der Sättigung der ersten Lage *n*-Butan mit dem gleichen Haftfaktor in Form von Multilagen weiter adsorbiert. Bei höheren Temperaturen steigt das Signal nach dem anfänglichen Abfall bei $t = 0$ s wieder an, wobei dieser Anstieg mit steigender Temperatur stärker wird. Dies liegt daran, dass die Desorptionsrate nun nicht mehr vernachlässigbar ist, sondern proportional zur zunehmenden Bedeckung zunimmt, bis schließlich die erste Lage gefüllt ist. Das Signal flacht ab, wenn die (höhere) Desorptionsrate der Multilagen bei dieser Temperatur erreicht ist (Daten für 93 bis 98 K), oder wenn der Druck wieder den Wert von vor dem Öffnen der Proben-Flag erreicht. Dies bedeutet, dass die Desorptionsrate identisch zur Adsorptionsrate ist (d. h. es gibt kein „Netto-Trapping“). Nach dem Ausschalten des Strahls bei $t \approx 60$ s steigt der Druck auf Werte oberhalb des Drucks vor dem Öffnen der Proben-Flag an, da nun keine Adsorption, aber immer noch Desorption auftritt. Dieses Differenzsignal fällt anschließend exponentiell ab.

Abbildung 3a zeigt den „Netto-Haftfaktor“ $S^*(\theta)$ auf der C_8-IL als Funktion der Bedeckung für Temperaturen bis zu 106 K. Während $S(\theta)$ nur die Wahrscheinlichkeit für Trapping in den adsorbierten Zustand beschreibt, berücksichtigt $S^*(\theta)$ auch die eventuell auftretende Desorption bei gegebener Bedeckung θ. Für Temperaturen oberhalb von 90 K wird zunächst eine lineare Abnahme von $S^*(\theta)$ beobachtet, die in einem einfachen Modell wie folgt interpretiert werden kann: Unter der Annahme, dass $S(\theta)$ unabhängig von der Bede-

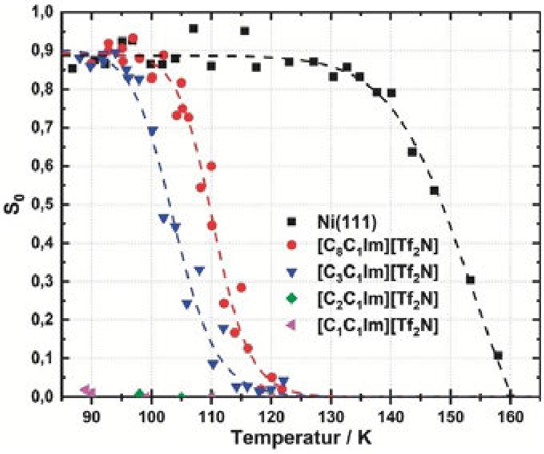

Abbildung 2. Temperaturabhängige Anfangshaftfaktoren von *n*-Butan auf [C_nC_1Im][Tf_2N]-ILs mit variierender Kettenlänge, im Vergleich zum Anfangshaftfaktor auf Ni(111). Die gestrichelten Linien verdeutlichen den Verlauf der Kurven.

ckung ist (was bei 90 K der Fall ist; siehe Abbildung 3 a), ergibt sich die Adsorptionsrate als $R_{ads} = S(\theta)\cdot R_{imp} = S_0\cdot R_{imp}$ (mit $R_{imp} = 2.0\times10^{13}$ Moleküle cm^{-2} s^{-1}). Mit der Zeit baut sich auf der Oberfläche eine Bedeckung $\theta = \int(R_{ads}-R_{des})\,dt$ auf. Während die Desorptionsrate bei 90 K gleich null ist, beginnt bei höheren Temperaturen eine signifikante Desorption der Adsorption entgegenzuwirken, wobei die entsprechende Rate $R_{des} = \theta\cdot\nu\cdot\exp(-E_{des}/RT)$ zu einer Abnahme von $S^*(\theta)$ führt. Wenn die Desorptionsenergie E_{des} unabhängig von der Bedeckung ist, steigt die Desorptionsrate linear mit der Bedeckung an, was wiederum die lineare Abnahme von $S^*(\theta)$ in Abbildung 3 a erklärt. Die Steigungen dieser Kurven für verschiedene Temperaturen werden in einem Arrhenius-Diagramm in Abbildung 3 b analysiert. Aus dem linearen Fit ergeben sich eine Desorptionsenergie von 29 ± 3 kJ mol^{-1} und ein präexponentieller Faktor ν von $1.4\times10^{14\pm2}$ s^{-1}.

Die C_3-IL zeigt insgesamt ein ähnliches Verhalten wie die C_8-IL, wenn auch in Richtung niedrigerer Temperaturen verschoben (vergleiche in Abbildung 1 die Daten bei 106 K für die C_8-IL und bei 98 K für die C_3-IL). Der „Netto-Haftfaktor" $S^*(\theta)$ als Funktion der Bedeckung für die C_3-IL ist in Abbildung S3 der Hintergrundinformationen dargestellt. In diesem Fall ist der nutzbare Temperaturbereich jedoch zu klein für eine Arrhenius-Analyse. Allerdings lässt sich zur Abschätzung der Differenz der Desorptionsenergien von C_3- und C_8-IL der Unterschied in den $T_{50\%}$-Werten aus Abbildung 2 verwenden, der 6 K beträgt. Bei Verwendung des gleichen präexponentiellen Faktors würde eine um ≈6 % geringere Desorptionsenergie den unterschiedlichen Kurvenverlauf erklären.

Um zu verstehen, warum auf den C_2- und C_1-ILs kein Trapping auftritt, muss berücksichtigt werden, dass auf den C_8- und C_3-ILs die Desorption von *n*-Butan aus Multilagen bereits wenig oberhalb von 90 K beginnt. Da für die C_8- und C_3-ILs konstante S_0-Werte von ≈0.89 bis 102 K bzw. bis 95 K beobachtet werden, nehmen wir an, dass einzelne *n*-Butan-

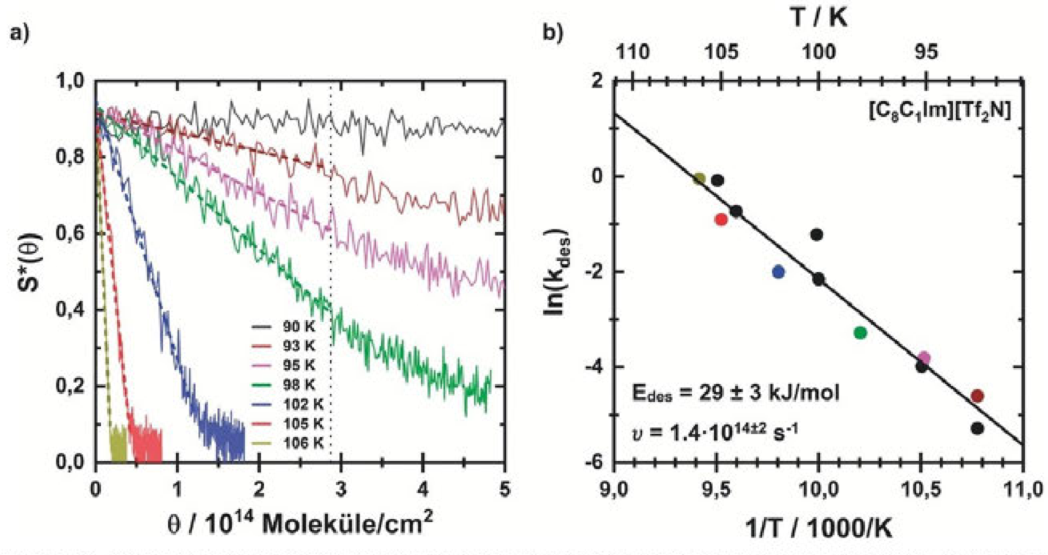

Abbildung 3. (a) „Netto-Haftfaktor" von *n*-Butan auf [C_8C_1Im][Tf_2N] als Funktion der Bedeckung für verschiedene Temperaturen. Ein linearer Fit (gestrichelte Linien) wurde an die jeweiligen Kurven angepasst. (b) Arrhenius-Analyse der aus (a) erhaltenen Geschwindigkeitskonstanten k_{des}. Die lineare Anpassung liefert die Desorptionsenergie und den präexponentiellen Faktor; die farbigen Symbole in (b) entsprechen den farbigen Kurven in (a). Die Bedeckung einer geschlossenen Monolage ist in (a) durch eine vertikale gepunktete Linie angegeben. Hierbei wurde angenommen, dass die Sättigungsbedeckung auf Ni(111) bei 102 K einer freistehenden Schicht aus flach liegendem *n*-Butan entspricht, d. h. $2{,}87\times10^{14}$ Moleküle cm^{-2}, wie aus Literatur[13] entnommen.

Moleküle auf diesen beiden ILs stärker gebunden sind als in der *n*-Butan-Multilage. Andernfalls würde die Desorption sofort erfolgen. Im Fall der C_2- und C_1-ILs ist die Adsorptionsenergie geringer als die Kondensationsenergie; daher desorbieren einzelne Moleküle unmittelbar nach der Adsorption, so dass für S_0 ein Wert von null gemessen wird.

Die Oberfläche der untersuchten ILs besteht aus den $[Tf_2N]^-$-Anionen mit nach außen zeigenden CF_3-Gruppen,[9] sowie den Imidazolium-Kopfgruppen und den unpolaren Alkylketten der Kationen.[10] Die Tatsache, dass auf den C_1- und C_2-ILs bei 88 K (d.h. bei einer Temperatur, bei der auf anderen Oberflächen *n*-Butan in Multilagen kondensiert) kein Trapping beobachtet wird, zeigt, dass die attraktiven Van-der-Waals-Kräfte zwischen *n*-Butan und den polaren Kopfgruppen, auch mit den C_1- und C_2-Ketten, zu schwach für eine stabile Bindung sind. Erst im Fall längerer Alkylketten findet Trapping statt. Dies deutet darauf hin, dass ab einer Kettenlänge von $n=3$, d.h. ab der C_3-IL, die attraktive Wechselwirkung zwischen *n*-Butan und den Alkylketten stark genug für eine dauerhafte Adsorption auf der Oberfläche ist. Im Fall der C_8-IL ist die Wechselwirkung noch stärker. Dazu sollte auch die Oberflächenanreicherung von Alkylketten mit $n \geq 4$ beitragen.[9,11]

Ein weiterer interessanter Punkt ist die Frage, warum Multilagenwachstum von *n*-Butan auf den C_8- und C_3-ILs bis zu 95 K beobachtet wird, nicht jedoch auf den C_2- und C_1-ILs. Wir führen diese Beobachtung auf die Tatsache zurück, dass für das Multilagenwachstum Kondensationskeime erforderlich sind. Die Bildung stabiler Keime erfordert jedoch eine gewisse Bedeckung der Oberfläche, damit statistisch gesehen genügend Moleküle aufeinander treffen können. Aufgrund der schwachen Wechselwirkung mit den C_2- und C_1-ILs ist die Verweilzeit von *n*-Butan auf diesen Oberflächen zu kurz, um solche stabilen Keime zu bilden. Auch bei einer Erhöhung des Strahlflusses um den Faktor 10 und einer Verlängerung der Messzeit auf 900 s, wird auf diesen beiden ILs keine Adsorption beobachtet.

Interessanterweise wurde in thermischen Desorptionsstudien zur Adsorption von Wasser auf gefrorenen $[C_8C_1Im][BF_4]$- und $[C_2C_1Im][Tf_2N]$-ILs ein ähnlicher Effekt beobachtet. Dabei wurde festgestellt, dass die Desorptionsenergien der Monolagen geringer sind als die der Multilagen und dass der Anfangshaftfaktor unterhalb der Multilagendesorptionstemperatur gegen null geht.[5f] Dies steht im Einklang mit dem hier beobachteten Verhalten für *n*-Butan auf den C_1- und C_2-ILs, wobei ebenfalls kein Trapping beobachtet wird. Dominierende Adsorbat-Adsorbat-Wechselwirkungen wurden im Fall der Wasseradsorption auf den ILs als Grund für den Anstieg des Haftfaktors mit steigender Bedeckung angegeben.[5f] Ein entsprechender Effekt wird hier nicht beobachtet, was auf die für Keimbildung zu kurze Verweilzeit zurückzuführen ist. Weiterhin bemerkenswert ist der Vergleich mit zustandsaufgelösten Streuexperimenten mit NO auf denselben ILs, wie den hier untersuchten. Diese zeigten, dass für niedrige kinetische Energien die Haftfaktoren nicht von der Länge der Alkylsubstituenten beeinflusst werden, in Einklang mit unseren Ergebnissen für *n*-Butan.[5a]

Zusammenfassend lässt sich sagen, dass durch Messungen mit einem Überschallmolekularstrahl interessante Einblicke in das Trapping von *n*-Butan auf verschiedenen $[C_nC_1Im][Tf_2N]$-ILs ($n=1, 2, 3, 8$) bei niedrigen Temperaturen gewonnen werden konnten. Aus den Anfangshaftfaktoren lässt sich schließen, dass die Adsorptionsenergie auf den ILs mit steigender Kettenlänge zunimmt. Auf den C_8- und C_3-ILs wird ausgeprägtes Trapping gefunden, während auf den C_2- und C_1-ILs kein Trapping auftritt. Daraus lässt sich schließen, dass die Adsorptionsenergie von *n*-Butan auf der IL-Oberfläche von der Wechselwirkung mit der Alkylkette der ILs dominiert wird, während die Wechselwirkung mit den ionischen Kopfgruppen eine untergeordnete Rolle spielt. Interessanterweise wird bei 88 K das Multilagenwachstum auf den C_2- und C_1-ILs unterdrückt, obwohl es auf den C_8- und C_3-ILs und auch auf Ni(111) noch bei höheren Temperaturen auftritt. Dies wird auf unzureichende Keimbildung aufgrund zu kurzer Verweilzeiten zurückgeführt. Wir glauben, dass die Schlussfolgerungen aus unseren UHV-Experimenten auf gefrorenen amorphen ILs bei niedrigen Temperaturen auch auf ILs in ihrer flüssigen Phase bei Raumtemperatur oder darüber übertragen werden können, weil das erste Auftreffen eines Moleküls aus der Gasphase die Energie- und Impulsübertragung mit der Flüssigkeit bestimmt. Da die Stärke der Wechselwirkung mit zunehmender Kettenlänge steigt, sollte die Verwendung von ILs mit längeren Alkylketten die Effizienz dieses ersten Schritts erhöhen. Die bekannte Oberflächenanreicherung längerer Alkylketten könnte diesen Effekt sogar verstärken.

Danksagung

R.B., L.W., M.L. und H.-P.S. danken dem Europäischen Forschungsrat (engl. European Research Council, ERC) für die finanzielle Unterstützung durch den Advanced Investigator Grant „ILID“ an H.-P.S. (Projekt: 693398-ILID) im Rahmen des Forschungs- und Innovationsprogramms Horizont 2020 der Europäischen Union. Wir danken Bernd Kreß, Hans-Peter Bäumler und der mechanischen Werkstatt für die Unterstützung bei der Planung und Montage der neuen UHV-Apparatur.

Interessenkonflikt

Die Autoren erklären, dass keine Interessenkonflikte vorliegen.

Stichwörter: Adsorption · Gas-Oberflächen-Dynamik · Ionische Flüssigkeiten · Molekularstrahl · *n*-Butan

---

[1] a) C. P. Mehnert, R. A. Cook, N. C. Dispenziere, M. Afeworki, *J. Am. Chem. Soc.* **2002**, *124*, 12932–12933; b) U. Kernchen, B. Etzold, W. Korth, A. Jess, *Chem. Eng. Technol.* **2007**, *30*, 985–994; c) H.-P. Steinrück, P. Wasserscheid, *Catal. Lett.* **2015**, *145*, 380–397; d) A. Riisager, R. Fehrmann, M. Haumann, B. S. K. Gorle, P. Wasserscheid, *Ind. Eng. Chem. Res.* **2005**, *44*, 9853–9859; e) S. Walter, M. Haumann, P. Wasserscheid, H. Hahn, R. Franke, *AIChE J.* **2015**, *61*, 893–897; f) T. Barth, W. Korth, A. Jess, *Chem. Eng. Technol.* **2017**, *40*, 395–404.

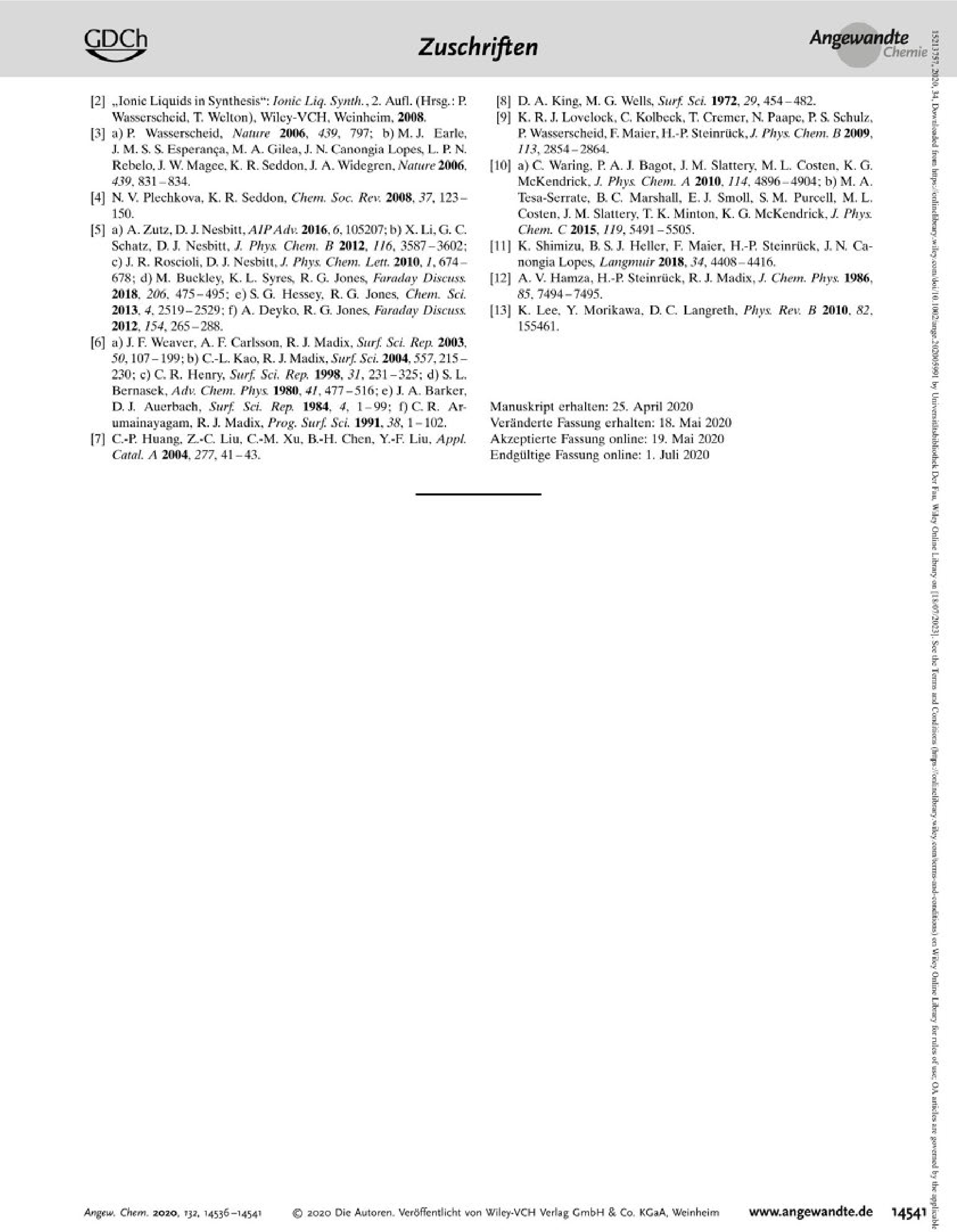

[2] „Ionic Liquids in Synthesis“: *Ionic Liq. Synth.*, 2. Aufl. (Hrsg.: P. Wasserscheid, T. Welton), Wiley-VCH, Weinheim, **2008**.

[3] a) P. Wasserscheid, *Nature* **2006**, *439*, 797; b) M. J. Earle, J. M. S. S. Esperança, M. A. Gilea, J. N. Canongia Lopes, L. P. N. Rebelo, J. W. Magee, K. R. Seddon, J. A. Widegren, *Nature* **2006**, *439*, 831–834.

[4] N. V. Plechkova, K. R. Seddon, *Chem. Soc. Rev.* **2008**, *37*, 123–150.

[5] a) A. Zutz, D. J. Nesbitt, *AIP Adv.* **2016**, *6*, 105207; b) X. Li, G. C. Schatz, D. J. Nesbitt, *J. Phys. Chem. B* **2012**, *116*, 3587–3602; c) J. R. Roscioli, D. J. Nesbitt, *J. Phys. Chem. Lett.* **2010**, *1*, 674–678; d) M. Buckley, K. L. Syres, R. G. Jones, *Faraday Discuss.* **2018**, *206*, 475–495; e) S. G. Hessey, R. G. Jones, *Chem. Sci.* **2013**, *4*, 2519–2529; f) A. Deyko, R. G. Jones, *Faraday Discuss.* **2012**, *154*, 265–288.

[6] a) J. F. Weaver, A. F. Carlsson, R. J. Madix, *Surf. Sci. Rep.* **2003**, *50*, 107–199; b) C.-L. Kao, R. J. Madix, *Surf. Sci.* **2004**, *557*, 215–230; c) C. R. Henry, *Surf. Sci. Rep.* **1998**, *31*, 231–325; d) S. L. Bernasek, *Adv. Chem. Phys.* **1980**, *41*, 477–516; e) J. A. Barker, D. J. Auerbach, *Surf. Sci. Rep.* **1984**, *4*, 1–99; f) C. R. Arumainayagam, R. J. Madix, *Prog. Surf. Sci.* **1991**, *38*, 1–102.

[7] C.-P. Huang, Z.-C. Liu, C.-M. Xu, B.-H. Chen, Y.-F. Liu, *Appl. Catal. A* **2004**, *277*, 41–43.

[8] D. A. King, M. G. Wells, *Surf. Sci.* **1972**, *29*, 454–482.

[9] K. R. J. Lovelock, C. Kolbeck, T. Cremer, N. Paape, P. S. Schulz, P. Wasserscheid, F. Maier, H.-P. Steinrück, *J. Phys. Chem. B* **2009**, *113*, 2854–2864.

[10] a) C. Waring, P. A. J. Bagot, J. M. Slattery, M. L. Costen, K. G. McKendrick, *J. Phys. Chem. A* **2010**, *114*, 4896–4904; b) M. A. Tesa-Serrate, B. C. Marshall, E. J. Smoll, S. M. Purcell, M. L. Costen, J. M. Slattery, T. K. Minton, K. G. McKendrick, *J. Phys. Chem. C* **2015**, *119*, 5491–5505.

[11] K. Shimizu, B. S. J. Heller, F. Maier, H.-P. Steinrück, J. N. Canongia Lopes, *Langmuir* **2018**, *34*, 4408–4416.

[12] A. V. Hamza, H.-P. Steinrück, R. J. Madix, *J. Chem. Phys.* **1986**, *85*, 7494–7495.

[13] K. Lee, Y. Morikawa, D. C. Langreth, *Phys. Rev. B* **2010**, *82*, 155461.

Manuskript erhalten: 25. April 2020
Veränderte Fassung erhalten: 18. Mai 2020
Akzeptierte Fassung online: 19. Mai 2020
Endgültige Fassung online: 1. Juli 2020

8.1 PUBLICATION 1

The Journal of Chemical Physics
ARTICLE
scitation.org/journal/jcp

On the adsorption of *n*-butane on alkyl imidazolium ionic liquids with different anions using a new molecular beam setup

Cite as: J. Chem. Phys. 153, 214706 (2020); doi: 10.1063/5.0028156
Submitted: 3 September 2020 • Accepted: 6 November 2020 •

View Online Export Citation CrossMark

Leonhard Winter, Radha G. Bhuin,[a] Matthias Lexow, Florian Maier, and Hans-Peter Steinrück[a]

AFFILIATIONS

Lehrstuhl für Physikalische Chemie 2, Friedrich-Alexander-Universität Erlangen-Nürnberg, Egerlandstr. 3, 91058 Erlangen, Germany

[a] **Authors to whom correspondence should be addressed:** radha.g.bhuin@fau.de and hans-peter.steinrueck@fau.de

ABSTRACT

The adsorption of reactants is an elementary step in the interaction of molecules with liquid or solid surfaces. We recently reported on the trapping of *n*-butane on the frozen surfaces of ionic liquids (ILs), namely, 1-alkyl-3-methylimidazolium bis(trifluoromethanesulfonyl)imide ILs ($[C_nC_1Im][Tf_2N]$; $n = 1, 2, 3$, and 8). To study the influence of the anion, we now present results concerning the trapping of *n*-butane on 1-alkyl-3-methylimidazolium hexafluorophosphate ILs ($[C_nC_1Im][PF_6]$; $n = 2, 4$, and 8), that is, ILs with a smaller anion. The adsorption energies close to zero coverage are determined from the temperature dependence of the initial trapping probability using a novel approach. For both groups of ILs, the binding energy is dominated by the interaction of *n*-butane with the alkyl chain of the cation, whereas the ionic headgroups contribute only weakly. Comparing ILs with different alkyl chains at the IL cation, we find that the adsorption strength of *n*-butane increases with increasing length of the alkyl chain. In addition, detailed information on the new setup and the data analysis is provided.

I. INTRODUCTION

The dynamic adsorption process of a gas molecule on a surface followed by possible physical and chemical transformations is of fundamental interest. Corresponding investigations of the relevant gas/surface interactions have typically been performed using supersonic molecular beams in ultra-high vacuum (UHV) for various molecules and solid surfaces in the past.[1–8] Detailed information on the adsorption/desorption process, preferred orientation and bonding of the molecules to the surface, surface diffusion, bond activation, and chemical reactions has been obtained.[1–19] Understanding these processes at the fundamental level is imperative for several applications such as heterogeneous catalysis, thin film growth, or separation technology.[11,20–22]

The investigation of dynamic processes at the surfaces and interfaces of liquids is equally important as for solids. However, sophisticated instrumentation is necessary to apply UHV-based molecular beam methods to explore the dynamics at the surfaces of conventional aqueous or organic liquids that are volatile under these conditions.[23,24] In these studies, the evaporating liquids are often supplied as a microjet or spread on a rotating wheel, which ensures their continuous replacement.[25–27] As an alternative to conventional liquids, a special class of liquid materials, that is, ionic liquids (ILs), can be chosen as model systems for this purpose: Due to their extremely rich structural diversity combined with a negligible vapor pressure,[28,29] ILs are ideal candidates for studying liquid surfaces under UHV conditions using the powerful surface science analytical toolbox (see, e.g., Refs. 30–36 and references therein).

ILs are per definition liquid below 100 °C, some of them even at room temperature. They comprise only anions and cations, such as conventional salts.[37–39] Due to their tunable physicochemical properties, they have been adapted to specific applications, ranging from solvents,[40,41] lubricants,[42] electrolytes,[43,44] acid scavengers,[45] and green chemistry[46] to catalysis.[47–49] Since 2005/2006, ILs are in the focus of surface science studies, and this new field of "ionic liquid surface science"[50] has developed a detailed understanding of the steady state or static properties of the vacuum/IL interface, such as surface composition, surface enrichment, and orientation effects.[30,31,33–36,51,52] For specific systems, even chemical reactions in ionic liquids have been studied (see Ref. 53 and references therein). The preparation of ultrathin IL films by physical vapor deposition made it possible to also study the fundamental properties of the IL/support interface,[54–56] which play a pivotal role in IL-based catalysis.

Based on ILs, two new concepts have been introduced in the area of catalysis, that is, supported ionic liquid phase (SILP)[57–60] and solid catalyst with ionic liquid layer (SCILL).[61,62] In these concepts, a thin IL layer coats the catalyst support, which enhances the selectivity, product distribution, and yields. In both, one crucial step is the transfer of gas molecules through the gas/IL interface. Despite this importance, only a few reports on the gas/IL interface dynamics exist. These concern adsorption/desorption and quantum-state-resolved scattering processes of small molecules.[63–68] Due to the small number of studies, the understanding of gas adsorption on IL surfaces and the subsequent interaction, diffusion, and transport is rather limited. This motivated us to build a novel UHV chamber combining a supersonic molecular beam, a rotatable mass spectrometer, and facilities for *in situ* X-ray photoelectron spectroscopy (XPS) to investigate the interaction of gases with non-volatile liquids. The liquid sample is positioned horizontally to avoid dripping off the support. To enable normal beam incidence, the molecular beam is mounted vertically, in contrast to most existing setups with a horizontal molecular beam. Recently, we published the first results on the dynamic interaction of n-butane with imidazolium-based bis(trifluoromethanesulfonyl)imide ILs with a varying alkyl chain length at the cation.[69]

Herein, we focus on the interaction of n-butane with related ILs, that is, 1-alkyl-3-methylimidazolium hexafluorophosphate, $[C_nC_1Im][PF_6]$ ($n = 2, 4$, and 8). We compare the data to those from our previous study on $[C_nC_1Im][Tf_2N]$ to further elucidate the role of the anion in the interaction process. In addition, we will introduce a novel approach to determine the desorption energy of n-butane from its temperature-dependent trapping probability in the zero-coverage limit. Moreover, we provide details on the instrumental setup and its characterization.

II. EXPERIMENTAL SECTION

The experiments were performed in a newly developed molecular beam setup, which was designed and assembled in-house. An overview of the instrument is presented in Fig. 1. The instrument's name ILID (ionic liquid interface dynamics) refers to its dedication to ionic liquid surface science. The compact instrument consists of (i) the preparation chamber for sample introduction, cleaning and *in situ* sample preparation, (ii) the analysis chamber where most of the measurements are done, and (iii) the three-stage molecular beam setup generating the supersonic molecular beam. All chambers (custom-built by VAb, Vakuum-Anlagenbau GmbH) are pumped by turbomolecular pumps (TP); notably, the first differential pumping stage of the molecular beam is pumped by two TPs. Each TP is backed by a rotary pump. The analysis and preparation

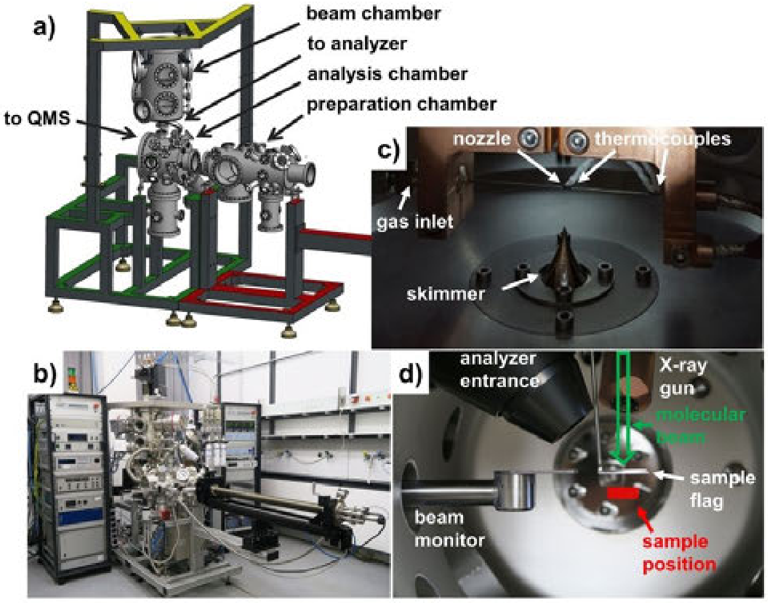

FIG. 1. An overview of the new molecular beam setup with a vertically mounted supersonic beam. (a) Three main parts of the ILID chamber: the preparation chamber (red), analysis chamber (green), and molecular beam setup (yellow). Ports for the analyzer and QMS are labeled in the analysis chamber. (b) A photograph of the complete setup. (c) A picture of the interior of the first pumping stage of the beam chamber. A Mo tube is mounted between two Cu brackets used for heating/cooling, the nozzle is located next to the central thermocouple, and below the nozzle sits the skimmer. (d) A picture of the interior of the analysis chamber. In the background, the (closed) gate valve to the preparation chamber is visible. The picture was taken through the open rotatable flange after dismounting the QMS, which is therefore not visible in this picture. The sample position and the impinging molecular beam are indicated.

chambers are additionally equipped with a combined ion getter and titanium sublimation pump each (see also Fig. S1 and Table S1 of the supplementary material).

A. Preparation chamber and manipulator

The preparation chamber is equipped with a sputter gun (SPECS IQE 11/35), together with a leak valve for Ar dosing and a four-grid LEED (low energy electron diffraction) setup (SPECS ErLEED 150) to determine the long-range order of single-crystal surfaces or possible adsorbate superstructures. For pressure measurement, a hot-filament ionization gauge is attached to the chamber.

The manipulator (VAb PM 25-800) enables motorized movement along the z-axis by 800 mm and manual movement along the x- and y-axes by ±25 mm (see also Fig. S2 of the supplementary material). Manual rotation around the z-axis is possible using a differentially pumped rotary feedthrough, which is pumped by a small ion getter pump. The sample is cooled using liquid N_2. The temperatures of the manipulator head and of the sample are measured by type K (chromel/alumel) thermocouples. Using a filament below the sample plate, the sample can be heated up to ≈450 K by indirect radiation heating. Alternatively, the sample can be heated up to ≈1200 K by electron bombardment from the back side with the filament biased with ≈−1 kV so that emitted electrons are accelerated toward the grounded sample.

The IL samples are introduced into the UHV chamber using a load-lock system. For that purpose, a transferable sample holder system with very reliable temperature readings was adopted for the instrument [see Fig. S2 (bottom) of the supplementary material]. The IL support, a polycrystalline Ni block ($12 \times 12 \times 4$ mm^3; Goodfellow), is fixed with a U-shaped Mo clamp onto a Ta ground plate ($18 \times 15 \times 1$ mm^3), which can be grabbed by the wobble stick. The type K thermocouple is inserted into the small hole (0.4 mm diameter and 3 mm depth) of the support, and the two wires are connected to thermocouple contacts, which are electrically insulated from the rest of the sample holder by ceramic spacers. The thermocouple contacts touch the corresponding type K thermocouple contacts of the sample stage in the manipulator head. With this setup, a very accurate and reliable relative measurement of the sample temperature (±1 K) is achieved (note that absolute temperature accuracy is estimated to be around ±3 K). Using liquid N_2, the sample can be cooled down to 88 K.

B. Analysis chamber

The analysis chamber is equipped with a hemispherical electron analyzer (SPECS PHOIBOS 100 1D-DLD) and a dual-anode X-ray gun (SPECS XR 50) for XPS. For molecular beam experiments, a quadrupole mass spectrometer (QMS) with a cross beam ionization source and a secondary electron multiplier as detector (Hiden Analytical 3F RC 301 PIC) is mounted on a rotatable flange, which allows for rotation by ≈270° around the sample (distance sample—QMS ionization source: 96 mm). Another feature of the analysis chamber is the beam monitor, which is mounted on a small xyz-manipulator. This device consists of a small volume separated from the analysis chamber by an orifice with a diameter of 1.0 mm.[70] Inside the beam monitor sits a hot-filament ionization gauge, which allows for the measurement of the stagnation pressure building up if the molecular beam covers the orifice completely. In this way, we can determine the flux of the incoming molecular beam. The chamber is also equipped with a sample flag, which can be used to deflect the molecular beam before it hits the sample surface. This type of sample flag is required for trapping (sticking) probability measurements by the King and Wells method.[71]

C. Molecular beam

The molecular beam setup comprises three differentially pumped chambers, referred to as stages 1, 2, and 3. The nozzle in stage 1 [Fig. 1(c)] is a round hole with a 100 μm diameter in a Mo stagnation tube with an inner diameter of 0.7 mm. The tube is mounted between two mechanical Cu brackets and can be moved by an xyz-manipulator to adjust the position of the nozzle. The nozzle can be resistively heated with the two Cu brackets as electrical contacts. The Cu brackets can be cooled with water so that the surroundings do not overheat if high nozzle temperatures (up to 1300 K) are used. The temperature of the stagnation tube can be measured by two type K thermocouples, one located close to the nozzle and the other one located close to the cooling/heating system. One side of the tube is a dead-end and the other one is connected to the gas inlet system, which can be fed through three mass flow controllers (Bronkhorst EL-FLOW Prestige). Thus, mixtures of up to three gases in any composition can be used in the molecular beam. The gas inlet system comprises a by-pass, which leads directly into stage 1. The by-pass can be used to pump down and purge the gas inlet system (through the nozzle only a limited amount of gas can flow).

The skimmer (Ni; opening diameter: 0.5 mm; Beam Dynamics, Inc.) sits directly below the nozzle and separates stages 1 and 2. It has a sharp edge and a conical form so that the flow of the supersonic jet is obstructed only minimally. Since a sufficiently low pressure in stage 1 is needed, to ensure that the gas reaches the supersonic velocity, stage 1 is pumped by two TPs.

The beam flag, a simple rotatable shutter in stage 2, can be used for rapidly switching the beam on and off. If the beam is blocked, the gas molecules are scattered and almost completely pumped away in stage 2, and only a small pressure rise is observed in stage 3 and the analysis chamber. Stages 2 and 3 are separated by four changeable apertures with diameters of 1.1 mm, 1.9 mm, 2.6 mm, and 3.7 mm. They are used to adjust the beam diameter and the position of the beam spot on the sample (see Fig. S3 of the supplementary material). A gate valve separates stage 3 and the analysis chamber. If this valve is closed, stages 1, 2, and 3 are completely sealed from the rest of the instrument. Thus, sample preparation and setting up of the molecular beam can be done at the same time.

The n-butane beam used in the present study is produced with the nozzle at room temperature and a gas flow of 1.0 SCCM using the smallest aperture (1.1 mm). The kinetic energy of the unseeded molecular beam was estimated to be 13 kJ/mol, in comparison to Ref. 59, and the resulting n-butane flux was $2.0 \cdot 10^{13}$ molecules/(cm^2 s).[69] The cleanliness of the n-butane gas is controlled by QMS. The largest signal in the n-butane mass spectrum at $m/z = 43$ was used in all time-dependent QMS measurements of n-butane.

The ILs studied here were purchased from IoLiTec Ionic Liquids Technologies GmbH ($[C_3C_1Im][Tf_2N]$, $[C_2C_1Im][PF_6]$,

$[C_4C_1Im][PF_6]$, and $[C_8C_1Im][PF_6]$; purity >99.5%), or synthesized according to previously published procedures ($[C_2C_1Im][Tf_2N]$ and $[C_8C_1Im][Tf_2N]$).[72] The purity and surface cleanliness of all ILs was further confirmed by XPS. A macroscopic film (≈1.0 mm thickness) of each IL was prepared on the polycrystalline Ni sample plate by spreading the IL with a Pasteur pipette. To ensure homogeneous spreading of the room temperature solid $[C_2C_1Im][PF_6]$, the sample plate was gently heated.

III. BEAM CHARACTERIZATION AND FLUX MEASUREMENT

The beam flux can be measured with the beam monitor mounted in the analysis chamber (as described in Sec. II). This device works similar to a pitot tube (stagnation tube), which is, e.g., used for velocity measurements in aviation. When the molecular beam hits the orifice of the beam monitor (diameter: 1.00 mm), the pressure in the beam monitor rises and slowly reaches equilibrium (pressure values are typically taken after 20 min waiting time to ensure equilibrium), which means no net flux through the orifice, that is, the incoming gas flux R_{in} equals the outcoming flux R_{out},

$$R_{in} = R_{out}. \tag{1}$$

R_{in} is the sum of two components, one originating from the background pressure, R_{bp}, of the analysis chamber and one from the directed incoming molecular beam, R_{MB},

$$R_{MB} + R_{bp} = R_{out}. \tag{2}$$

Under the reasonable simplification that the background gas in the analysis chamber and the gas accumulated in the beam monitor consists solely of the same molecules (with mass m) as used in the molecular beam and that the temperature in both chambers is the same and constant, we obtain

$$R_{MB} = R_{out} - R_{bp} = \frac{p_{MB} - p_{bgr}}{\sqrt{2\pi m k_B T}} = \frac{\Delta p}{\sqrt{2\pi m k_B T}}. \tag{3}$$

p_{bgr} is the pressure measured in the beam monitor with the molecular beam blocked by the closed sample flag in front of the beam monitor orifice and p_{MB} is the beam monitor pressure measured with the open sample flag, that is, the central part of the molecular beam passes the orifice.

The beam monitor allows for determining the beam flux impinging on the sample surface as a function of the gas flux through the nozzle, as set by the gas flow controller (see Fig. S4 of the supplementary material). Moreover, we used the beam monitor to create a lateral profile map of the beam intensity on the sample (see Fig. 2). As a typical example with the n-butane beam (gas flow 1.0 SCCM and the beam aperture between stage 2 and 3 of 1.1 mm in diameter), the Δp values were recorded along a grid of positions adjusted at the beam monitor manipulator. These settings were also used for the King and Wells measurements in Sec. IV. To decrease the measurement time, the valve to the additional pumping in the beam monitor was left open, and thus, equilibrium was reached faster (1.5 min equilibration time instead of 20 min with a closed valve). The Δp values from this experiment can therefore not directly be converted into the flux but allow for determining the profile. As one would expect, the shape of the beam in Fig. 2 appears to be round and symmetrical, and there is only very little intensity variation in the center of the beam. In the graph, the beam is broadened because of the finite diameter of the beam monitor orifice (1.00 mm). The black solid lines in the insets of Fig. 2 show the convolution of a 3.4 mm wide rectangular beam profile (indicated by dashed lines) and the broadening function of the beam monitor orifice. The excellent agreement indicates that we have a sharp rectangular beam profile, as indicated by the dashed lines. The determined beam diameter of 3.4 mm is in perfect agreement with the expectations from the geometrical parameters of the molecular beam, considering the distances of the beam monitor and the chosen beam aperture (diameter of 1.1 mm) to the skimmer, that is, 487 mm and 159 mm, respectively. This corresponds to an opening angle of the circular beam of 0.2°.

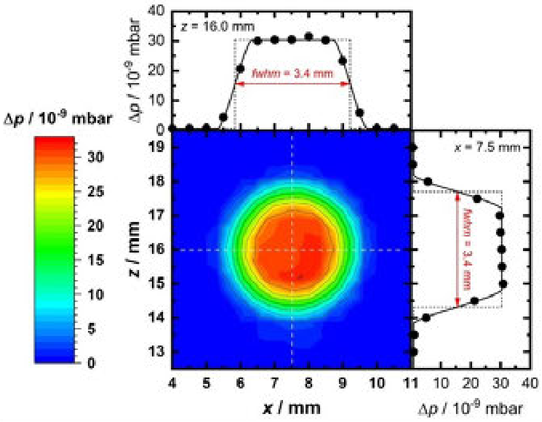

FIG. 2. Contour plot of the intensity of the n-butane molecular beam (gas flow 1.0 SCCM, smallest beam defining orifice with a diameter of 1.1 mm) measured with the beam monitor. The beam monitor was moved along a grid of points with 0.5 mm spacing, and the system has been given a time of 1.5 min to equilibrate at each grid position. Due to additional differential pumping, the obtained Δp values cannot be converted into the n-butane flux (see the text). The inset at the top shows the beam profile in the x-direction at z = 16.0 mm and the inset on the right shows the one in the z-direction at x = 7.5 mm; the locations of the beam profiles are indicated in the contour plot by white dashed lines. The black solid lines in the insets show the convolution of a rectangular beam profile (dashed lines) and the theoretically expected broadening function of the beam monitor orifice.

IV. RESULTS AND DISCUSSION

In the following, we will apply our new beam setup to study the temperature-dependent trapping of n-butane on frozen ILs, namely, $[C_8C_1Im][PF_6]$, $[C_4C_1Im][PF_6]$, and $[C_2C_1Im][PF_6]$, in the temperature range from 85 K to 125 K. As discussed previously, the surface structures of the ILs in their solid state are expected to be very similar to the ones in the liquid state.[69] First, we will address the time-dependent trapping probability $S(t)$, followed by the temperature-dependence of the trapping probability S_0 in the zero-coverage limit. From the obtained values, we will determine the desorption energies using a new analysis approach. The obtained results will then be compared to the earlier results on similar ILs with $[Tf_2N]^-$ instead of $[PF_6]^-$ as an anion.

A. Time-dependent trapping probability

The trapping probability S is defined as the probability for an incoming molecule to get trapped in a physisorbed state, which is given by the ratio of the adsorption rate R_{ads} to the impingement rate R_{MB},

$$S = \frac{R_{ads}}{R_{MB}}. \tag{4}$$

In the case of chemisorption, this ratio is called the sticking probability (or the sticking coefficient). The symbol S is common for both quantities, and occasionally, they are also used as synonyms in the literature. In this work, the trapping probability was determined by the direct method of King and Wells,[71] which is based on the time-dependent measurement of the partial pressure of gas molecules, typically with a QMS.

The trapping probability measurement follows a sequence of opening and closing of two flags (simple rotatable shutters) (see Fig. 3 for the adsorption of n-butane on $[C_8C_1Im][PF_6]$). The "beam flag" is placed behind the skimmer so that the beam can already be stopped before it reaches the analysis chamber, and the "sample flag" is located right in front of the sample so that it can block the beam before reaching the sample surface.

In the beginning of the experiment ($t \approx -40$ s), both flags are closed, and the beam cannot enter the analysis chamber. The QMS only measures a background signal, which can later be set as $p = 0$. At $t \approx -20$ s, the beam flag is opened; so, now, the molecular beam can enter the analysis chamber. The sample flag remains closed, and all incoming molecules are scattered on its inert surface, which leads to a pressure increase Δp_{MB} in the analysis chamber. At $t = 0$ s, the sample flag is also opened so that the gas molecules directly impinge on the sample surface. Adsorption on the sample surface leads to a sudden pressure drop Δp_0 because molecules adsorbing on the surface do not contribute to the signal measured by the QMS; if all impinging molecules would adsorb (that is, $S = 1$), the pressure would drop to zero. The ratio of Δp_0 and Δp_{MB} directly gives the trapping probability in the zero-coverage limit S_0,

$$S_0 = \frac{\Delta p_0}{\Delta p_{MB}}. \tag{5}$$

S can depend on coverage (and therefore also on time in a King and Wells experiment). Equivalently to (5), it can be written as

$$S(t) = \frac{\Delta p(t)}{\Delta p_{MB}}. \tag{6}$$

In our trapping probability measurements on ILs, we distinguish three characteristic behaviors A, B, and C: In case A [Fig. 3(a)], the trapping probability is coverage-independent (that is, identical adsorption occurs in the mono- and multilayer regime), which means that the pressure stays constant as long as the sample flag is open. Closing the sample flag ($t \approx 60$ s) brings the pressure back to its original level before opening the sample flag ($p = \Delta p_{MB}$) because then the molecular beam is again scattered on the inert sample flag.

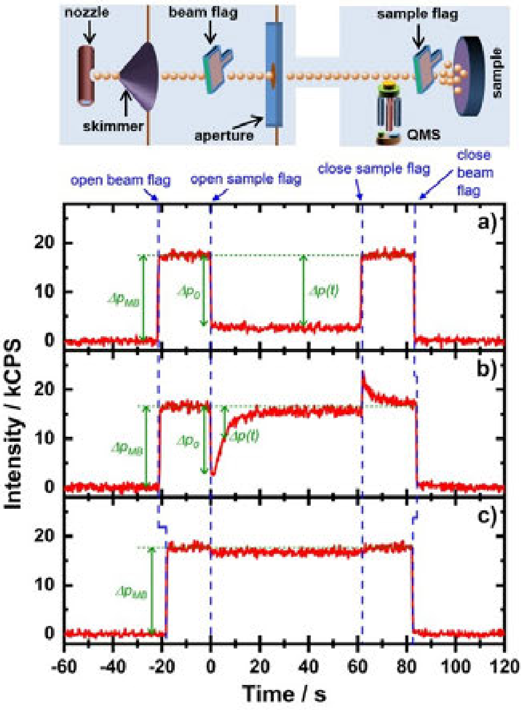

FIG. 3. Exemplary King and Wells measurements with n-butane on $[C_8C_1Im][PF_6]$ at (a) 85 K, (b) 102 K, and (c) 125 K representing cases A, B, and C (see the text). The most intense fragment ($m/z = 43$) of n-butane was used to monitor the partial pressure. A linear background was subtracted from all curves. The opening and closing of the two flags are marked in blue, and the characteristic pressure differences are marked in green (for details, see the main text). A schematic of the beam is shown at the top of the figure; the distances from the skimmer and the aperture to the sample are 487 mm and 159 mm, respectively.

In case B [Fig. 3(b)], the pressure drops initially (Δp_0) but rises afterward until it reaches the level it had before opening the sample flag ($p = \Delta p_{MB}$). For our systems, we attribute this effect to partial desorption from the sample surface, yielding a steady state between adsorbing and desorbing molecules. This becomes apparent by looking at the pressure response on closing the sample flag ($t \approx 60$ s): The pressure rises above the level it had before opening the sample flag ($p > \Delta p_{MB}$) because in addition to the molecules being scattered from the sample flag, the QMS also detects molecules desorbing from the sample surface while the adsorption rate has dropped to zero. In case *B*, the trapping probability determined by the King and Wells method is not the trapping probability in its narrow sense. We therefore denote it as net trapping probability, S^{net}, which will later be used to determine adsorption energies. In the time interval $t = 20$ s–60 s in Fig. 3(b), with $S^{net}(t) = 0$ and $p = \Delta p_{MB}$, the system is in a steady state: The rate of adsorption from the molecular beam to the sample surface is equal to the rate of desorption from the sample surface into the analysis chamber.

In case *C* [Fig. 3(c)], the trapping probability is zero [$S_0 = S(t) = 0$]. Consequently, no initial pressure drop Δp_0 is observable when the sample flag is opened ($t = 0$ s), and the pressure does also not increase in the moment of closing the sample flag ($t \approx 60$ s). However on close inspection of the measurement curve, a very small pressure change in $0.04 \cdot \Delta p_{MB}$ is always visible at $t = 0$ s and $t \approx 60$ s, which is independent of sample nature and temperature and only occurs with liquid nitrogen cooling of the manipulator. We thus attribute this small pressure change not to adsorption at the sample surface but to an experimental artifact. We always corrected for this effect in the following trapping probability analysis. After closing the beam flag at $t \approx 80$ s, the pressure returns to the initial background pressure.

In the measurement series for frozen [C_8C_1Im][PF_6] (Fig. 4, left) and [C_4C_1Im][PF_6] (Fig. 4, right), a gradual transition from case *A* to case *C* occurs with increasing temperature. At low temperature (89 K–91 K), the trapping probability $S = 0.86 \pm 0.02$ is independent of coverage. In the measurement at 95 K, the pressure increases after the initial pressure drop until the first layer is filled (indicated by an arrow). As soon as the first layer is filled, the desorption rate (and the pressure) stays constant. This observation is somehow equivalent to a zeroth order multilayer desorption in temperature-programmed desorption (TPD). Since the net trapping probability is still larger than zero, the multilayer continues to grow until the end of the experiment, albeit with a smaller trapping probability. Above 99 K, the transition to case *B* is completed for both ILs, which means, the steady state with $S^{net} = 0$ is reached before the first layer is filled completely. At higher temperatures, the increasing desorption rate already influences the initial trapping probability $S_0{}^{net}$ (as will be discussed later), which decreases with increasing temperature. At 120 K for [C_8C_1Im][PF_6] and 115 K for [C_4C_1Im][PF_6], the transition to case *C* is complete and no trapping is observed any more. While the behavior is similar for both ILs, the transition from one case to the other occurs at lower temperatures for [C_4C_1Im][PF_6] than for [C_8C_1Im][PF_6].

B. Temperature-dependence of S_0

The difference between the two ILs, [C_4C_1Im][PF_6] and [C_8C_1Im][PF_6], becomes more apparent if the initial trapping probability is plotted vs the sample temperature (Fig. 5). We also included data for [C_2C_1Im][PF_6] and for comparison, also our previously published data for three different [C_nC_1Im][Tf_2N] ILs with $n = 2$, 3, and 8.[69] The latter have [Tf_2N]$^-$ as an anion instead of [PF_6]$^-$. The overall behavior of the ILs with $n = 3$–8 is similar: At temperatures well below 100 K, a plateau with constant $S_0 = 0.88 \pm 0.05$ is observed for all ILs with $n \geq 3$. Above a certain temperature, which depends on the particular IL, S_0 starts to decrease until it reaches

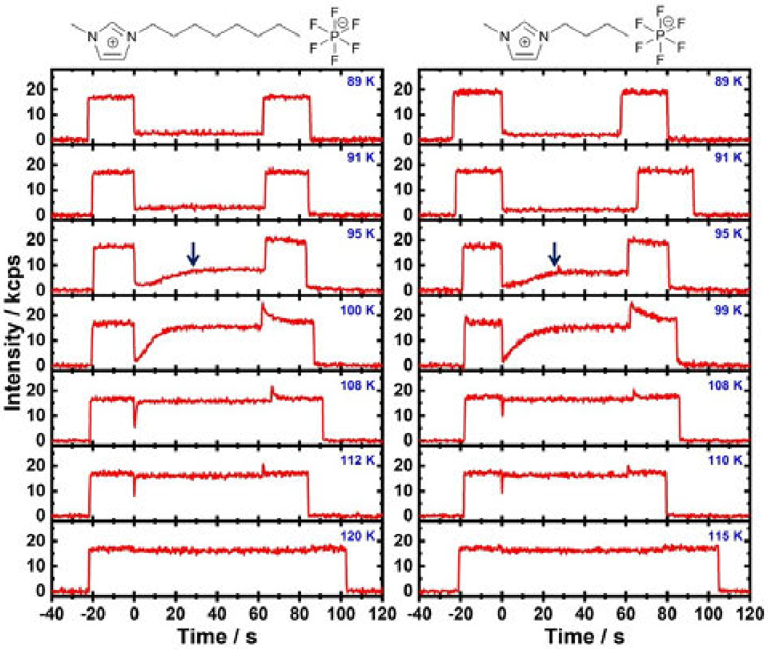

FIG. 4. Temperature dependent trapping probability measurements of *n*-butane on [C_8C_1Im][PF_6] (left) and [C_4C_1Im][PF_6] (right). The most intense fragment ($m/z = 43$) of *n*-butane was used to monitor the partial pressure. A linear background was subtracted from all curves.

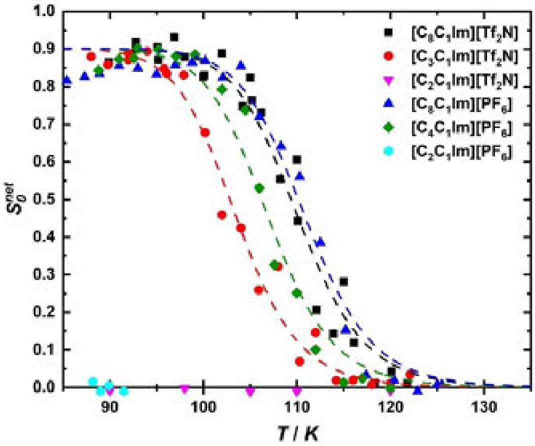

FIG. 5. Temperature-dependent initial trapping probability S_0^{net} of *n*-butane on various ILs after background subtraction (see the text). The dashed lines are fits to the data [according to Eq. (16) in Sec. IV C]. This fitting model was used to calculate the desorption energies for the ILs (Table I). The data for the [Tf$_2$N]-ILs were adapted from Ref. 69.

zero. As in our previous publication,[69] we describe this behavior using the characteristic temperature $T_{50\%}$ at which S_0 of a specific IL has dropped to 50% of its initial value (Table I). The two ILs with an octyl side chain — [C$_8$C$_1$Im][Tf$_2$N] and [C$_8$C$_1$Im][PF$_6$] — have very similar $T_{50\%}$ values, 110 K and 111 K, respectively (the difference falls within the margin of error of ±1 K). This shows that in this case, the adsorption/desorption dynamics are dominated by the van der Waals interactions of *n*-butane with the alkyl chains in the cation, while the nature of the anions does not appear to play a decisive role. For [C$_4$C$_1$Im][PF$_6$], $T_{50\%}$ is 107 K, which lies in between the values for [C$_8$C$_1$Im][Tf$_2$N] and [C$_3$C$_1$Im][Tf$_2$N]. The decrease in the characteristic temperature is attributed to weaker van der Waals interactions of *n*-butane with the shorter alkyl chains.

The two investigated ILs with $n = 2$ — [C$_2$C$_1$Im][PF$_6$] and [C$_2$C$_1$Im][Tf$_2$N] — show a completely different behavior, that is, no trapping is observed even in the temperature range of multilayer condensation (case *A*) on the other ILs. The two ILs have in common that the longest alkyl substituent is only an ethyl chain. In line with our previous study, we suggest that for both ILs, the interaction of *n*-butane with all IL constituents (ethyl chain, cationic head group, and anion) is weak, resulting in an insufficient residence time for the formation of condensation nuclei. Since [C$_2$C$_1$Im][PF$_6$] shows the same behavior as [C$_2$C$_1$Im][Tf$_2$N], we conclude that the polar character of the surface is responsible for the weak interaction.

TABLE I. Characteristic $T_{50\%}$ values and desorption energies E_{des} determined by the method described in Sec. IV C using the prefactor $\nu = 1.4 \cdot 10^{14}$ 1/s from Ref. 69 for the fitting process.

IL	$T_{50\%}$ (K)	E_{des} (kJ/mol)
[C$_3$C$_1$Im][Tf$_2$N]	104	26.8
[C$_4$C$_1$Im][PF$_6$]	107	27.7
[C$_8$C$_1$Im][Tf$_2$N]	110	28.6
[C$_8$C$_1$Im][PF$_6$]	111	28.8

C. Determination of the desorption energy

As mentioned earlier, the King and Wells method is widely used to determine sticking or trapping probabilities, that is, the probability for an incoming molecule to adsorb on the surface. Precisely, this is only true if desorption is negligible because desorbing molecules will contribute to the partial pressure of the molecule in the vacuum chamber. Hence, the quantity measured with the King and Wells method is also denoted as the net trapping probability, S^{net}, defined as

$$S^{net} = \frac{R_{ads} - R_{des}}{R_{MB}}, \tag{7}$$

where R_{ads} is the adsorption rate, R_{des} is the desorption rate, and R_{MB} is the impingement rate of the molecular beam (note that S^{net} was denoted as S^* in our previous publication[69]). At low temperatures (LT, $T \approx 90$ K), desorption is negligible in our experiments. Otherwise, an increase in the partial pressure would be observable after closing the sample flag, as it is the case for higher temperatures [compare also Figs. 3(a) and 3(b)]. The net trapping probability at LT, S^{LT}, is therefore equal to the trapping probability in its narrow sense,

$$S^{LT} = \frac{R_{ads}}{R_{MB}} \Leftrightarrow R_{ads} = S^{LT} \cdot R_{MB}. \tag{8}$$

Assuming that the adsorption rate is independent of temperature in the region of interest, we obtain

$$S^{net} = \frac{S^{LT} \cdot R_{MB} - R_{des}}{R_{MB}} = S^{LT} - \frac{R_{des}}{R_{MB}}. \tag{9}$$

If desorption follows first order kinetics, the desorption rate is given by

$$R_{des} = \theta \cdot \nu \cdot e^{-\frac{E_{des}}{RT}}, \tag{10}$$

where θ is the adsorbate coverage, ν is a preexponential frequency factor, R is the universal gas constant, T is the temperature, and E_{des} is the activation energy for desorption. For non-activated adsorption, as it is typically the case for physisorption, the latter is equal to the binding energy of the adsorbate.

In a more general approach, the change in coverage $d\theta$ during a time interval dt is given by the difference of the adsorption and desorption rates,

$$d\theta = R_{ads}dt - R_{des}dt = \left(S^{net} \cdot R_{MB}\right)dt. \tag{11}$$

Integration yields

$$\theta(t) = R_{MB} \cdot \int_0^t S^{net}\, \mathrm{d}t. \tag{12}$$

$t = 0$ is defined as the time when the sample flag is opened. In our previous publication,[69] we obtained values for $\theta(t)$ by numerical integration of the $S^{net}(t)$ curve until time t. If the desorption energy E_{des} does not depend on coverage, the desorption rate R_{des} increases linearly with coverage, and thus, S^{net} decreases linearly in an S^{net} vs θ plot. In this case, the (constant) slopes of the $S^{net}(\theta)$ decrease for different temperatures can be analyzed in an Arrhenius analysis. In our previous study, this approach worked quite well for *n*-butane adsorption on [C_8C_1Im][Tf_2N] in the temperature range between 106 K and 93 K, yielding a desorption energy of 29 ± 3 kJ/mol and a prefactor of $1.4 \cdot 10^{14\pm2}$ 1/s.[69] It should, however, be noted that this analysis only can be applied if (a) the trapping probability is coverage-independent over a large coverage range and (b) the desorption rate is large enough to be measurable but low enough to allow for the formation of a considerable adsorbate layer; this was the main reason why our previous analysis only worked for [C_8C_1Im][Tf_2N] but not for the ILs with shorter chains.[69]

In this work, we now want to focus on the low coverage limit to directly access the initial net trapping probability $S_0{}^{net}$ in the time interval [0; t_m] required to measure the first data point after opening the sample flag (t_m is the measurement time per data point, that is, 0.5 s). During this time interval, a small coverage θ_0 already builds up on the surface (even at the lowest temperature, θ_0 is only 3% of a closed *n*-butane layer), yielding a certain desorption rate $R_{des,0}$. θ_0 *and* $R_{des,0}$ will increase with progressing time. In a first approximation, both are best represented by their values in the center of the time interval, i.e., at $t_m/2$,

$$\begin{aligned} R_{des,0} &= R_{des}\left(t = \frac{t_m}{2}\right) = \theta\left(t = \frac{t_m}{2}\right) \cdot \nu \cdot e^{-\frac{E_{des}}{RT}} \\ &= R_{MB} \cdot \left(\int_0^{\frac{t_m}{2}} S_0^{net}\, \mathrm{d}t\right) \cdot \nu \cdot e^{-\frac{E_{des}}{RT}}. \end{aligned} \tag{13}$$

Under the approximation that $S_0{}^{net}$ remains constant in this short time interval, it can be written as follows:

$$R_{des,0} = R_{MB} \cdot S_0^{net} \cdot \frac{t_m}{2} \cdot \nu \cdot e^{-\frac{E_{des}}{RT}}. \tag{14}$$

For $S_0{}^{net}$, we then obtain

$$S_0^{net} = S^{LT} - \frac{R_{des,0}}{R_{MB}} = S^{LT} - S_0^{net} \cdot \frac{t_m}{2} \cdot \nu \cdot e^{-\frac{E_{des}}{RT}} \tag{15}$$

$$\Rightarrow S_0^{net} = \frac{S^{LT}}{1 + \frac{t_m}{2} \cdot \nu \cdot e^{-\frac{E_{des}}{RT}}}. \tag{16}$$

This expression provides a model description of the measurement data in Fig. 5. A value for S^{LT} can be extracted from the measurements at LT, and t_m is known from the experimental conditions to be 0.50 s. Therefore, only two unknowns remain, E_{des} and ν, which are (unfortunately) strongly coupled in this equation. Thus, it is necessary to make an assumption for one of them to obtain unambiguous fitting results. In our previous publication, we derived $\nu = 1.4 \cdot 10^{14\pm2}$ 1/s for [C_8C_1Im][Tf_2N] from an Arrhenius analysis, based on the assumption of a coverage-independent trapping probability.[69] For the analysis in this work, we assume that this prefactor is applicable for all of the ILs.

The fit curves according to Eq. (16) are shown in Fig. 5, and the resulting desorption energies are summarized in Table I. Although the absolute uncertainty in activation energies is estimated to be ±2 kJ/mol (due to the uncertainty of the prefactor and the absolute temperature scale), the uncertainty in differences of derived activation energy values is only about ±0.3 kJ/mol. Previously, we used an Arrhenius analysis to determine the desorption energy of [C_8C_1Im][Tf_2N] to be 29 ± 3 kJ/mol;[69] with our newly developed method for the zero-coverage limit, we obtain 28.6 ± 2 kJ/mol assuming the same prefactor. Considering the margin of error of the evaluations, the agreement of this result is very satisfactory.

Table I shows that E_{des} increases from 26.8 kJ/mol for [C_3C_1Im][Tf_2N] over 27.7 kJ/mol for [C_4C_1Im][PF_6] to 28.6 kJ/mol for [C_8C_1Im][Tf_2N] and 28.8 kJ/mol for [C_8C_1Im][PF_6]. The length of the alkyl substituent clearly correlates with the desorption energy: the longer the alkyl chain, the higher the desorption energy, and thus, the stronger the binding of *n*-butane on the IL surface. We assume that the corresponding interaction potentials also hold for the liquid state due to the similarity between frozen and liquid surfaces.[69] Our results clearly show that the interaction is dominated by van der Waals forces between *n*-butane and the chemically similar alkyl chains of the IL cations. The difference found for the two [C_8C_1Im]-ILs lies in the order of the margin of error. This finding corroborates our interpretation that the interaction of *n*-butane with the anion is irrelevant for the bonding mechanism. The very small difference between [C_8C_1Im][Tf_2N] and [C_8C_1Im][PF_6] could be rationalized by the slightly larger surface enrichment of the octyl chain in ILs with smaller anions such as $[PF_6]^-$ compared to ILs with larger anions such as $[Tf_2N]^-$.[33,73] Since the difference is smaller than the margin of error, this interpretation, however, has to be treated with great caution.

V. CONCLUSIONS

We present a novel multi-analysis UHV apparatus dedicated for the investigation of gas molecules interacting with vacuum-compatible liquid surfaces. The system comprises a vertically mounted supersonic molecular beam for the investigation of horizontally mounted liquid samples at normal beam incidence. The flux of the molecular beam can be determined with a beam monitor, which can also be used to measure the beam profile; in the here presented experiments using *n*-butane, a very sharp circular profile with a diameter of 3.4 mm in the sample plane is achieved. A rotatable mass spectrometer is installed, allowing for a variety of molecular beam scattering and adsorption studies. Additionally, an integrated XPS setup is used for chemical analysis and enables future combined experiments.

Using this new apparatus, we determined the trapping probabilities of n-butane on $[C_nC_1Im][PF_6]$ ILs (n = 2, 4, and 8) in the temperature range of 85 K–125 K by the so-called King and Wells method. On $[C_2C_1Im][PF_6]$, no trapping of n-butane is observed. The same behavior was previously also found for $[C_2C_1Im][Tf_2N]$ and explained by a too short n-butane residence time for the formation of condensation nuclei.[69] On $[C_4C_1Im][PF_6]$ and $[C_8C_1Im][PF_6]$, the adsorption characteristics are temperature-dependent: n-butane grows in multilayers at low temperatures (≈90 K), while at temperatures above 120 K, the desorption rate becomes too high to observe trapping on the IL surfaces.

For $[C_4C_1Im][PF_6]$, the initial net trapping probability starts to decrease at lower temperatures than for $[C_8C_1Im][PF_6]$. This finding shows that van der Waals interactions with the alkyl side chain of the cation dominate the adsorption process. The decrease in trapping probability with decreasing side chain length can be described by the characteristic temperature values $T_{50\%}$ at which the initial net trapping probability has dropped to 50% of its maximum value. We obtain values of $T_{50\%}$ = 107 K for $[C_4C_1Im][PF_6]$ and 110 K for $[C_8C_1Im][PF_6]$. The value for $[C_8C_1Im][PF_6]$ is almost identical to the value of 111 K found for $[C_8C_1Im][Tf_2N]$ in a previous study.[69] We thus conclude that the nature of the anion does not seem to play a significant role for the adsorption process, which is not surprising due to the pronounced surface enrichment of the octyl chains for both ILs.

Based on the assumption that the initial trapping probability in its narrow sense is temperature-independent in the investigated temperature range, we attribute the decrease in the observed net trapping probability with increasing temperature solely to the increasing desorption rate. From this temperature-dependence, we determine the desorption energy of n-butane in the low-coverage limit on the different ILs using a simple analysis procedure. The resulting desorption energies on the different ILs show the same trend as found for the $T_{50\%}$ values, that is, they increase with increasing alkyl chain length. For $[C_8C_1Im][Tf_2N]$, we previously determined the desorption energy in an Arrhenius analysis under the assumption that the trapping probability in its narrow sense is coverage-independent.[69] The results of the previous Arrhenius analysis and the new approach focusing on the low-coverage limit are in very good agreement.

SUPPLEMENTARY MATERIAL

See the supplementary material for the schematic drawing of the vacuum system (Fig. S1) with the specification of the components (Table S1); photo plus drawings of the manipulator and sample holder (Fig. S2); contour plots of the molecular beam profile (Fig. S3); and the n-butane beam flux measured with the beam monitor as a function of the gas flow in the mass flow controller (Fig. S4).

ACKNOWLEDGMENTS

L.W., R.G.B., M.L., and H.-P.S. thank the European Research Council (ERC) under the European Union's Horizon 2020 research and innovation programme for financial support, in the context of the Advanced Investigator Grant "ILID" to H.-P.S. (Grant Agreement No. 693398—ILID). We acknowledge the support by Bernd Kreß, Hans-Peter Bäumler, and the mechanical workshop when planning and assembling the new UHV setup.

DATA AVAILABILITY

The data that support the findings of this study are available from the corresponding authors upon reasonable request.

REFERENCES

[1] A. F. Carlsson and R. J. Madix, J. Phys. Chem. B **105**, 8155 (2001).
[2] C. R. Arumainayagam and R. J. Madix, Prog. Surf. Sci. **38**, 1 (1991).
[3] F. Zaera, Surf. Sci. Rep. **72**, 59 (2017).
[4] C.-L. Kao and R. J. Madix, Surf. Sci. **557**, 215 (2004).
[5] J. F. Weaver, A. F. Carlsson, and R. J. Madix, Surf. Sci. Rep. **50**, 107 (2003).
[6] C. T. Rettner *et al.*, J. Phys. Chem. **100**, 13021 (1996).
[7] J. A. Barker and D. J. Auerbach, Surf. Sci. Rep. **4**, 1 (1984).
[8] M. P. D'Evelyn and R. J. Madix, Surf. Sci. Rep. **3**, 413 (1984).
[9] R. S. Smith and B. D. Kay, J. Phys. Chem. B **122**, 587 (2018).
[10] M. Okada, Chem. Rec. **14**, 775 (2014).
[11] J. Libuda and H.-J. Freund, Surf. Sci. Rep. **57**, 157 (2005).
[12] J. F. Weaver, M. A. Krzyzowski, and R. J. Madix, J. Chem. Phys. **112**, 396 (2000).
[13] *Heterogeneous Reaction Dynamics*, edited by S. Bernasek (VCH, 1995).
[14] R. Gomer, Rep. Prog. Phys. **53**, 917 (1990).
[15] M. P. D'Evelyn *et al.*, Surf. Sci. **167**, 451 (1986).
[16] U. Köhler and H.-W. Wassmuth, Surf. Sci. **126**, 448 (1983).
[17] C. Papp and H.-P. Steinrück, Surf. Sci. Rep. **68**, 446 (2013).
[18] J. A. Fair and R. J. Madix, J. Chem. Phys. **73**, 3486 (1980).
[19] I. E. Wachs and R. J. Madix, Surf. Sci. **65**, 287 (1977).
[20] J. H. Larsen and I. Chorkendorff, Surf. Sci. Rep. **35**, 165 (1999).
[21] J. L. Anderson and D. W. Armstrong, Anal. Chem. **77**, 6453 (2005).
[22] G. A. Odugbesi *et al.*, J. Chromatogr. A **1604**, 460466 (2019).
[23] S.-C. Park, D. K. Burden, and G. M. Nathanson, Acc. Chem. Res. **42**, 379 (2009).
[24] G. M. Nathanson, Annu. Rev. Phys. Chem. **55**, 231 (2004).
[25] J. A. Faust and G. M. Nathanson, Chem. Soc. Rev. **45**, 3609 (2016).
[26] T. Lewis *et al.*, Angew. Chem., Int. Ed. **50**, 10178 (2011).
[27] B. G. Perkins, T. Häber, and D. J. Nesbitt, J. Phys. Chem. B **109**, 16396 (2005).
[28] P. Wasserscheid, Nature **439**, 797 (2006).
[29] M. J. Earle *et al.*, Nature **439**, 831 (2006).
[30] H.-P. Steinrück, Phys. Chem. Chem. Phys. **14**, 5010 (2012).
[31] K. R. J. Lovelock *et al.*, Chem. Rev. **110**, 5158 (2010).
[32] E. F. Smith *et al.*, Langmuir **22**, 9386 (2006).
[33] M. A. Tesa-Serrate *et al.*, J. Phys. Chem. C **119**, 5491 (2015).
[34] I. J. Villar-Garcia *et al.*, Chem. Sci. **5**, 4404 (2014).
[35] K. Nakajima *et al.*, Anal. Sci. **32**, 1089 (2016).
[36] C. S. Santos and S. Baldelli, Chem. Soc. Rev. **39**, 2136 (2010).
[37] M. V. Fedorov and A. A. Kornyshev, Chem. Rev. **114**, 2978 (2014).
[38] *Ionic Liquids in Synthesis*, 2nd ed., edited by P. Wasserscheid and T. Welton (Wiley-VCH Verlag GmbH & Co. KGaA, 2008).
[39] T. Welton, Chem. Rev. **99**, 2071 (1999).
[40] R. I. Canales and J. F. Brennecke, J. Chem. Eng. Data **61**, 1685 (2016).
[41] R. D. Rogers and K. R. Seddon, Science **302**, 792 (2003).
[42] I. Minami, Molecules **14**, 2286 (2009).
[43] M. Galiński, A. Lewandowski, and I. Stępniak, Electrochim. Acta **51**, 5567 (2006).

[44] W. Xu and C. A. Angell, Science **302**, 422 (2003).

[45] M. Maase and K. Massonne, in *Ionic Liquids IIIB: Fundamentals, Progress, Challenges, and Opportunities: Transformations and Processes*, edited by R. D. Rogers and K. R. Seddon (American Chemical Society, 2005), p. 126.

[46] T. Welton, Green Chem. **13**, 225 (2011).

[47] M. Sobota *et al.*, Adv. Mater. **23**, 2617 (2011).

[48] T. Welton, Coord. Chem. Rev. **248**, 2459 (2004).

[49] H.-P. Steinrück and P. Wasserscheid, Catal. Lett. **145**, 380 (2015).

[50] H.-P. Steinrück, Surf. Sci. **604**, 481 (2010).

[51] F. Maier *et al.*, Phys. Chem. Chem. Phys. **12**, 1905 (2010).

[52] S. Baldelli, Acc. Chem. Res. **41**, 421 (2008).

[53] F. Maier, I. Niedermaier, and H.-P. Steinrück, J. Chem. Phys. **146**, 170901 (2017).

[54] M. Lexow, F. Maier, and H.-P. Steinrück, Adv. Phys.: X **5**, 1761266 (2020).

[55] T. Cremer *et al.*, ChemPhysChem **9**, 2185 (2008).

[56] R. Souda, J. Phys. Chem. B **112**, 15349 (2008).

[57] C. P. Mehnert *et al.*, J. Am. Chem. Soc. **124**, 12932 (2002).

[58] A. Riisager *et al.*, Ind. Eng. Chem. Res. **44**, 9853 (2005).

[59] S. Walter *et al.*, AIChE J. **61**, 893 (2015).

[60] J. M. Marinkovic *et al.*, Ind. Eng. Chem. Res. **58**, 2409 (2019).

[61] U. Kernchen *et al.*, Chem. Eng. Technol. **30**, 985 (2007).

[62] T. Barth, W. Korth, and A. Jess, Chem. Eng. Technol. **40**, 395 (2017).

[63] A. Zutz and D. J. Nesbitt, AIP Adv. **6**, 105207 (2016).

[64] X. Li, G. C. Schatz, and D. J. Nesbitt, J. Phys. Chem. B **116**, 3587 (2012).

[65] J. R. Roscioli and D. J. Nesbitt, J. Phys. Chem. Lett. **1**, 674 (2010).

[66] S. G. Hessey and R. G. Jones, Chem. Sci. **4**, 2519 (2013).

[67] A. Deyko and R. G. Jones, Faraday Discuss. **154**, 265 (2012).

[68] M. Buckley, K. L. Syres, and R. G. Jones, Faraday Discuss. **206**, 475 (2018).

[69] R. G. Bhuin *et al.*, Angew. Chem., Int. Ed. **59**, 14429 (2020).

[70] G. Scoles, *Atomic and Molecular Beam Methods* (Oxford University Press, 1988).

[71] D. A. King and M. G. Wells, Surf. Sci. **29**, 454 (1972).

[72] K. R. J. Lovelock *et al.*, J. Phys. Chem. B **113**, 2854 (2009).

[73] C. Kolbeck *et al.*, J. Phys. Chem. B **113**, 8682 (2009).

Supporting Information

On the adsorption of *n*-butane on alkyl imidazolium ionic liquids with different anions using a new molecular beam setup

Leonhard Winter ORCID: 0000-0001-9733-1444, Radha G. Bhuin*, ORCID: 0000-0001-5914-1615,
Matthias Lexow ORCID: 0000-0002-1441-2909, Florian Maier ORCID: 0000-0001-9725-8961, and
Hans-Peter Steinrück*, ORCID: 0000-0003-1347-8962

Lehrstuhl für Physikalische Chemie 2, Friedrich-Alexander-Universität Erlangen-Nürnberg,
Egerlandstr. 3, 91058 Erlangen, Germany

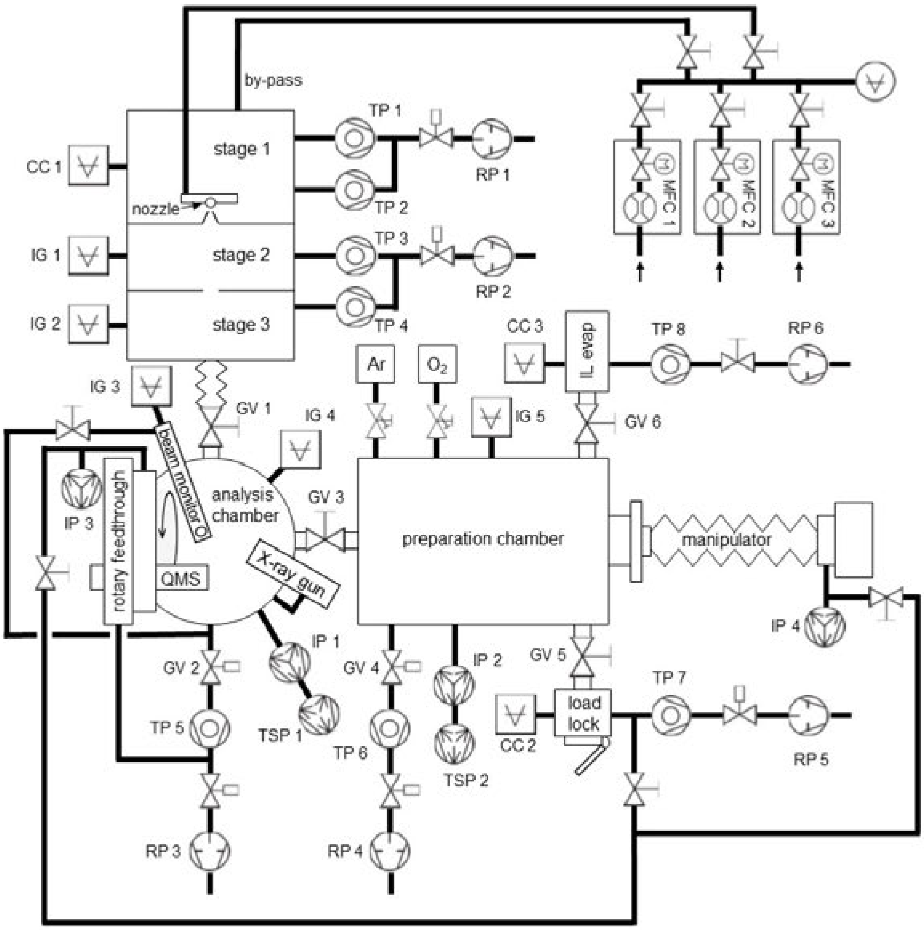

Figure S1: Schematic drawing of the vacuum system using the standard symbols of vacuum technology. The labeled components are specified in Table S1.

Table S1: Specification of the components abbreviated in Figure S1.

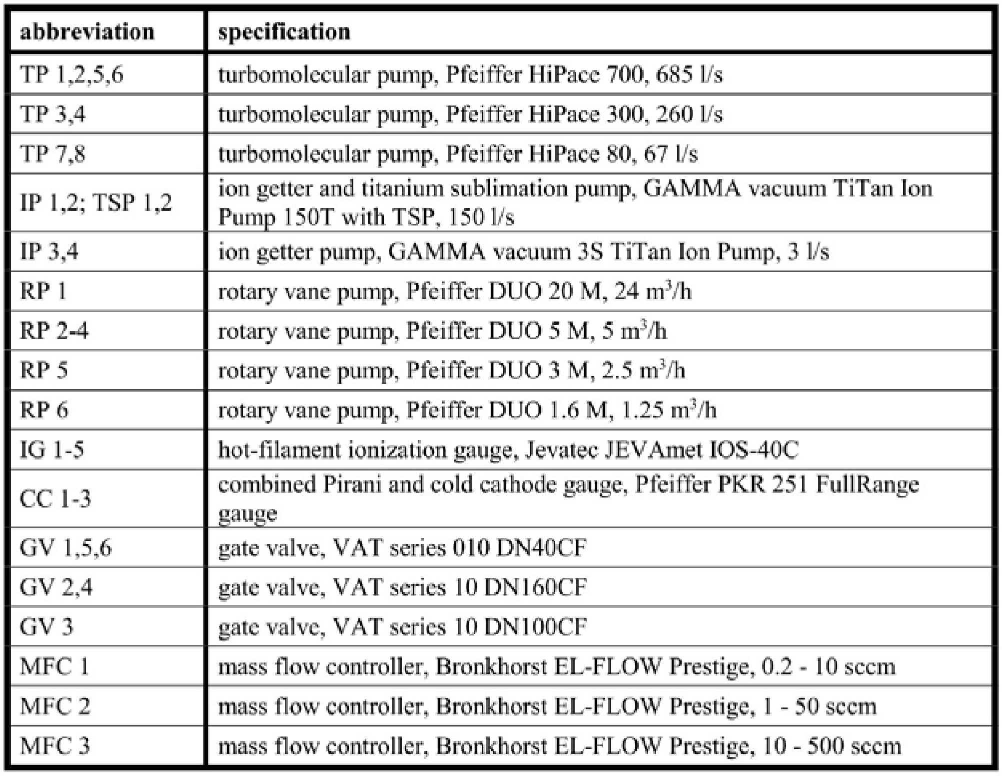

abbreviation	**specification**
TP 1,2,5,6	turbomolecular pump, Pfeiffer HiPace 700, 685 l/s
TP 3,4	turbomolecular pump, Pfeiffer HiPace 300, 260 l/s
TP 7,8	turbomolecular pump, Pfeiffer HiPace 80, 67 l/s
IP 1,2; TSP 1,2	ion getter and titanium sublimation pump, GAMMA vacuum TiTan Ion Pump 150T with TSP, 150 l/s
IP 3,4	ion getter pump, GAMMA vacuum 3S TiTan Ion Pump, 3 l/s
RP 1	rotary vane pump, Pfeiffer DUO 20 M, 24 m^3/h
RP 2-4	rotary vane pump, Pfeiffer DUO 5 M, 5 m^3/h
RP 5	rotary vane pump, Pfeiffer DUO 3 M, 2.5 m^3/h
RP 6	rotary vane pump, Pfeiffer DUO 1.6 M, 1.25 m^3/h
IG 1-5	hot-filament ionization gauge, Jevatec JEVAmet IOS-40C
CC 1-3	combined Pirani and cold cathode gauge, Pfeiffer PKR 251 FullRange gauge
GV 1,5,6	gate valve, VAT series 010 DN40CF
GV 2,4	gate valve, VAT series 10 DN160CF
GV 3	gate valve, VAT series 10 DN100CF
MFC 1	mass flow controller, Bronkhorst EL-FLOW Prestige, 0.2 - 10 sccm
MFC 2	mass flow controller, Bronkhorst EL-FLOW Prestige, 1 - 50 sccm
MFC 3	mass flow controller, Bronkhorst EL-FLOW Prestige, 10 - 500 sccm

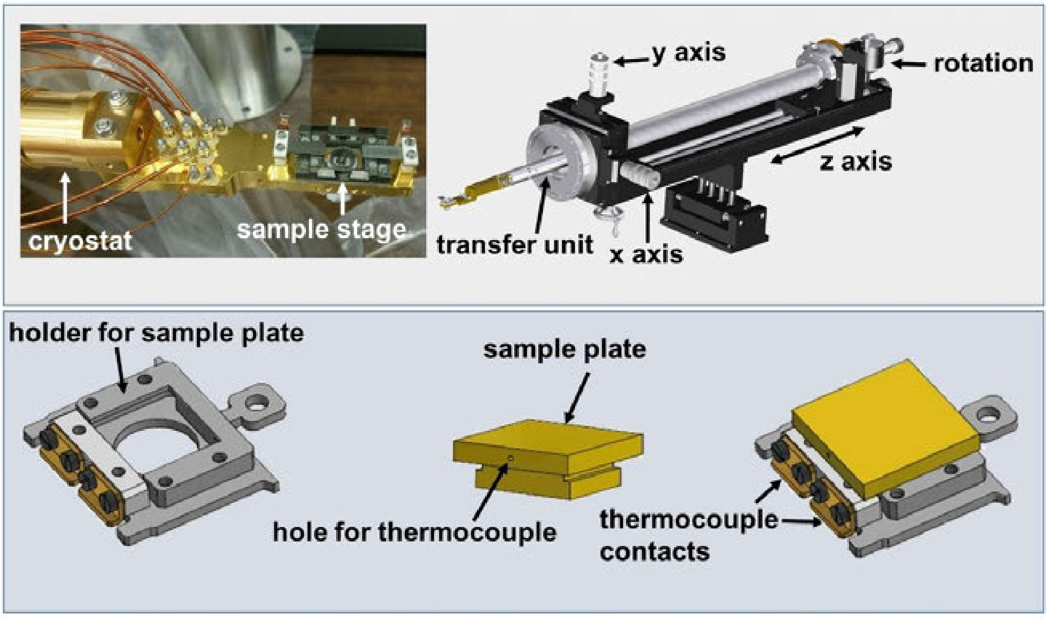

Figure S2: Top: Manipulator with sample stage of the ILID chamber, which allows movements in three directions, rotation around the *z*-axis, cooling, heating and temperature measurement of the sample. Bottom: Typical sample holder design with a 12 x 12 x 4 mm^3 sample plate with a tiny hole for a type K thermocouple. The thermocouple wires are fixed to electrically insulated thermocouple contacts, which can touch the thermocouple contacts of the sample stage.

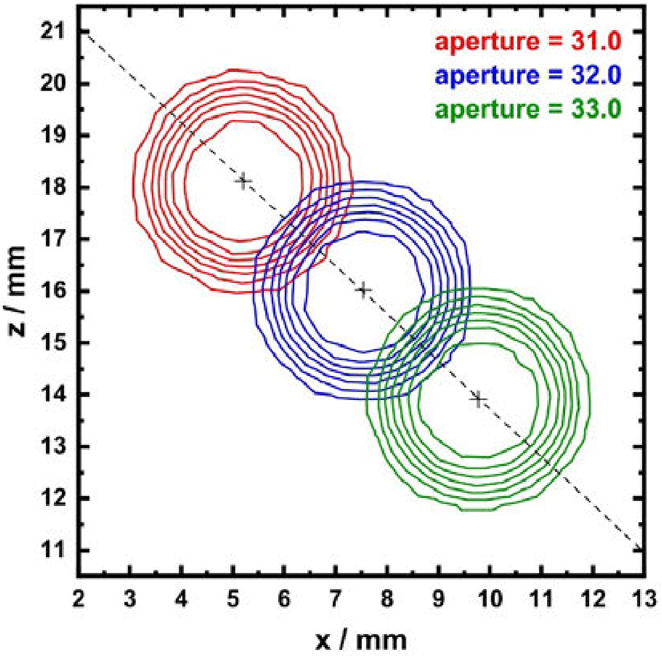

Figure S3: Contour plots of the intensity of an *n*-butane molecular beam (gas flow 1.0 sccm, smallest beam defining orifice with a diameter of 1.1 mm) measured with the beam monitor. The beam monitor was moved along a grid of points with 0.5 mm spacing. The system has been given a time of 1.5 min to equilibrate at each grid position. The figure shows that the position of the molecular beam in the coordinate system of the sample plane can be adjusted by changing the position of the beam-defining orifice.

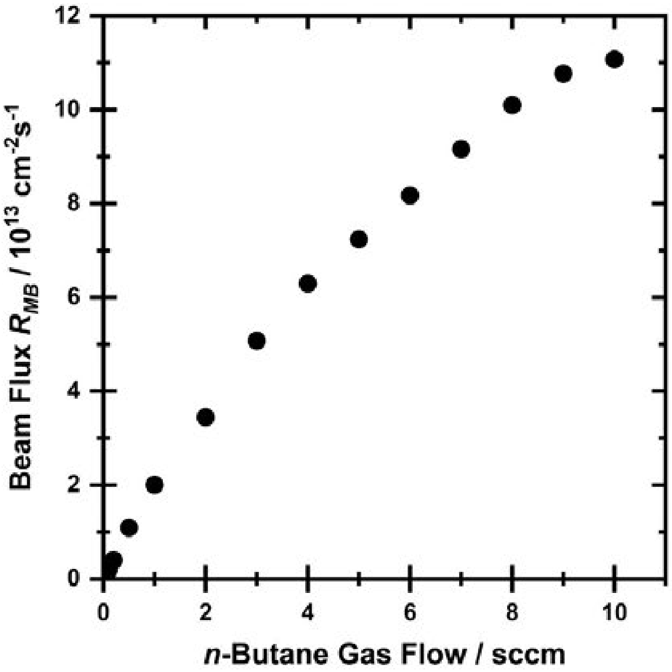

Figure S4: *n*-Butane beam flux measured with the beam monitor as a function of the gas flow in the mass flow controller.

Chemistry–A European Journal
Full Paper
doi.org/10.1002/chem.202102492

Chemistry Europe
European Chemical Societies Publishing

n-Butane, *iso*-Butane and 1-Butene Adsorption on Imidazolium-Based Ionic Liquids Studied with Molecular Beam Techniques

Leonhard Winter,[a] Radha G. Bhuin,[a] Florian Maier,[a] and Hans-Peter Steinrück*[a]

Abstract: The interaction of molecules, especially hydrocarbons, at the gas/ionic liquid (IL) surface plays a crucial role in supported IL catalysis. The dynamics of this process is investigated by measuring the trapping probabilities of *n*-butane, *iso*-butane and 1-butene on a set of frozen 1-alkyl-3-methylimidazolium-based ILs $[C_nC_1Im]X$, where $n=4$, 8 and $X^-=Cl^-$, Br^-, $[PF_6]^-$ and $[Tf_2N]^-$. The decrease of the initial trapping probability with increasing surface temperature is used to determine the desorption energy of the hydrocarbons at the IL surfaces. It increases with increasing alkyl chain length *n* and decreasing anion size for the ILs studied. We attribute these effects to different degrees of alkyl chain surface enrichment, while interactions between the adsorbate and the anion do not play a significant role. The adsorption energy also depends on the adsorbing molecule: It decreases in the order *n*-butane > 1-butene > *iso*-butane, which can be explained by different dispersion interactions.

Introduction

Substances consisting solely of ions and possessing a low melting point, often below room temperature, are classified as ionic liquids (ILs).[1] Although materials fulfilling this definition are known for a long time,[2] extensive research on ILs started only in the 1990s.[3] In the beginning, ILs were seen as "green" alternatives for conventional bulk chemicals,[4] like solvents,[5] electrolytes,[6] lubricants[7] or scavengers.[8] With the years, the "green" label for ILs came increasingly under debate, because of their unknown toxicity,[9] poor biodegradability[10] and cost- and waste-intensive synthesis.[11] In the last years, efforts were made to make ILs environmentally friendlier like using biorenewable raw materials and optimized synthetic routes.[12] An alternative (or additional) strategy to decrease the environmental footprint of ILs is the targeted use of small IL amounts for specific purposes, for example as lubricant additives,[13] pharmaceuticals[14] or in catalysis.[15]

In modern catalytic applications, ILs are often not used as bulk solvents in a biphasic approach, but rather in heterogeneous systems on porous supports.[15d,e] This is realized as Solid Catalysts with Ionic Liquid Layer (SCILL)[16] or Supported Ionic Liquid Phase (SILP) catalysts,[17] which have both found commercial applications.[18] In SCILL, the heterogeneous catalyst is modified by an ionic liquid thin film, which typically improves the catalyst's selectivity.[15d,e,19] In SILP, an originally homogenous catalytic process is "heterogenized" by immobilization of the IL phase containing the dissolved catalyst on an inert porous support, which facilitates product separation and increases the mobile phase/IL interface area.[15d,e,20] In both concepts, the mass transfer across the gas/IL interface plays a crucial role for the selectivity and activity of the catalytic system.

Therefore, the structure of the vacuum/IL interface has been in the center of surface science investigations using different techniques like molecular dynamics calculations,[21] X-ray reflectivity,[22] direct recoil spectrometry,[23] Rutherford backscattering,[23b,24] low energy ion scattering,[25] reactive atom scattering,[26] sum frequency generation vibrational spectroscopy[27] and X-ray photoelectron spectroscopy (XPS).[28] Thereby, a good understanding of the static properties of this interface has been obtained. However, the interaction dynamics of gas molecules at the gas/IL interface has only been investigated for few specific examples: CO_2 is scattered from imidazolium-based ionic liquid surfaces at room temperature by two distinctive pathways, trapping/desorption (TD) and inelastic scattering (IS). The share of the TD pathway increases with increasing alkyl chain length and decreasing anion size.[29] Similar trends were observed for NO scattering, additional to interesting rotational, vibrational and electronic effects occurring for this open-shell molecule.[30] O atoms are scattered inelastically and/or reactively forming OH and H_2O from imidazolium- and pyrrolidinium-based ionic liquids. For both cation classes, the reaction probability increases with increasing alkyl chain length and decreasing anion size.[26a,31] H_2O adsorbs on frozen $[C_2C_1Im][Tf_2N]$ and $[C_8C_1Im][BF_4]$ with an initial trapping probability close to zero, which then increases with coverage. The multilayer (=condensed phase) desorption energy was found to lie above the one of the monolayer (=

---

[a] L. Winter, Dr. R. G. Bhuin, Dr. F. Maier, Prof. Dr. H.-P. Steinrück
Lehrstuhl für Physikalische Chemie II
Friedrich-Alexander-Universität Erlangen-Nürnberg
Egerlandstr. 3, 91058 Erlangen (Germany)
E-mail: hans-peter.steinrueck@fau.de

Part of a Special Issue on Contemporary Challenges in Catalysis.

layer in direct contact with the substrate), which was attributed to strong adsorbate-adsorbate interactions.[32]

Our group has recently reported on the adsorption of *n*-butane from a supersonic molecular beam onto frozen imidazolium-based $[Tf_2N]^-$ and $[PF_6]^-$ ILs.[33] For $[C_1C_1Im]^+$ and $[C_2C_1Im]^+$ cations, no trapping occurs, even at 90 K, which is below the onset of measurable *n*-butane multilayer desorption at 93 K. For cations with at least three carbon atoms in the alkyl side chain, the initial trapping probability is ≈0.9 at 90 K. It decreases with increasing surface temperature, which was attributed to an increasing desorption rate. We developed a procedure to extract the *n*-butane desorption energy from our data, and found that it increases with increasing cation alkyl chain length. In this paper, we aim to extend our work to ILs with the much smaller halides as anions, and to other adsorbates, namely *iso*-butane and 1-butene. The anion dependence of the desorption energy will be rationalized by comparison to the static surface structure probed by angle-resolved X-ray photoelectron spectroscopy (ARXPS).

Experimental Section

The ILs were purchased from IoLiTec Ionic Liquid Technologies GmbH ($[C_8C_1Im][PF_6]$, $[C_4C_1Im][PF_6]$, $[C_4C_1Im]Br$, and $[C_4C_1Im]Cl$, purity >99%) or prepared according to previously published procedures[34] ($[C_8C_1Im][Tf_2N]$, $[C_4C_1Im][Tf_2N]$, and $[C_8C_1Im]Cl$). XPS proved the ILs to be satisfactorily (surface) clean. In particular, we detected none of the IL-typical contaminations, like Si (indicative of silicones) or hydrocarbon species.[35] The quantitative analysis showed that the measured XPS signals agreed with the nominal compositions to within 5%, which is the typical uncertainty of XPS.[34] Only the chloride ILs contained a small oxygen signal indicative of minor amounts of water (4–6 mol%), and a small additional N 1s peak at 400 eV (10% for $[C_8C_1Im]Cl$ and 19% for $[C_4C_1Im]Cl$, possibly due to beam damage). A macroscopic film (≈ 0.5 mm thickness) was spread with a Pasteur pipette on a polycrystalline Ni sample plate (12×12 mm²). In the case of the room temperature solids $[C_4C_1Im]Br$ and $[C_4C_1Im]Cl$, the sample plate was gently heated to melt the ILs to ensure homogenous spreading. The samples were introduced via a loadlock into the ultra-high vacuum system (base pressure $\approx 1\cdot10^{-10}$ mbar), which was already described in detail elsewhere.[33b] A type K thermocouple inserted into the sample plate was used to measure the sample temperature, which was controlled by liquid nitrogen cooling and radiation heating with a filament mounted at the back of the sample.

The continuous supersonic molecular beam was generated from a pure *n*-butane, *iso*-butane or 1-butene (purchased from Messer Griesheim, purity >99%) gas stream (1.0 sccm) expanding from a room-temperature nozzle (100 µm diameter). The beam passed a conical skimmer (opening diameter 0.5 mm) and an aperture (1.1 mm diameter) creating a circular beam spot of 3.4 mm diameter. The kinetic energy of the *n*-butane beam was estimated to be approximately 13 kJ/mol by comparison to a similarly generated beam from Ref. [36]. The beam flux was estimated to $2.0\cdot10^{13}$ cm^{-1} s^{-1}.[33a]

The partial pressure in the analysis chamber was measured with a quadrupole mass spectrometer (Hiden Analytical) by recording the time-dependent signal of m/z = 43 (*n*-butane and *iso*-butane) or m/z = 41 (1-butene), which are the most intense fragments generated from the corresponding molecules by electron ionization (70 eV). A linear background was subtracted from the raw data and an average over the first 0.50 s after opening the sample flag was used to determine the initial trapping probability (see also below). Between two measurements, the IL was heated to 180 K to remove remaining *n*-butane/*iso*-butane/1-butene and other adsorbates potentially contaminating the surface. Water, for example, desorbs from IL surfaces between 140 and 170 K.[32] Heating to higher temperatures was omitted to avoid melting and refreezing of the IL. At least three independently prepared samples were used for each gas/IL combination to ensure reproducibility.

Results and Discussion

The trapping probability *S* represents the probability for an incoming molecule to become trapped, that means adsorbed, on a surface. In our study, we apply the direct method of King and Wells[37] to determine the trapping probability. When applying this method, one uses a supersonic molecular beam with a set of mechanical shutters, also called flags, and measures the background partial pressure. As example, Figure 1 shows typical measurement curves for the adsorption of *n*-butane on two ILs with very different anions, $[C_8C_1Im]Cl$ and $[C_8C_1Im][Tf_2N]$, at ≈90 and 118 K (left side), and a sketch of our setup (right side). The measurement procedure follows a sequence of opening and closing two flags (marked by blue dashed lines in Figure 1), while simultaneously recording the partial pressure of the molecule in the analysis chamber with a quadrupole mass spectrometer (QMS).

In the beginning ($t=-40$ s), the molecular beam is blocked by the beam flag far away from the analysis chamber and the gas is pumped away by differential pumping stages, so that the partial pressure in the analysis chamber is zero. At $t=-20$ s, the beam flag is opened, which allows the molecular beam to enter the analysis chamber, where it is scattered from the inert sample flag. This leads to the pressure increase Δp_{MB}. At $t=0$ s the sample flag is opened and the molecular beam impinges on the sample surface. If the molecules adsorb on the sample surface, the pressure drops (Figure 1a–c). This initial pressure drop Δp_0 is used to determine the initial trapping probability S_0 (Equation (1)),

$$S_0 = \frac{\Delta p_0}{\Delta p_{MB}} \tag{1}$$

which corresponds to the trapping probability on the uncovered surface, that is, at zero coverage. If all molecules are scattered from the surface (that is, $S_0=0$), no change in pressure is observed (Figure 1d). Note that in this case in our experiment a small apparent pressure drop occurs, because of an experimental artifact caused by our sample cooling system, for which we apply a correction in our data evaluation procedure.[33b]

If the molecule adsorbs on the surface, a certain coverage builds up, which can influence the trapping probability. A change in the trapping probability will be proportional to a change in partial pressure, so that, analogously to S_0, a time-dependent trapping probability $S(t)$ can be determined from $\Delta p(t)$. In the example of Figure 1c, desorption from the adlayer

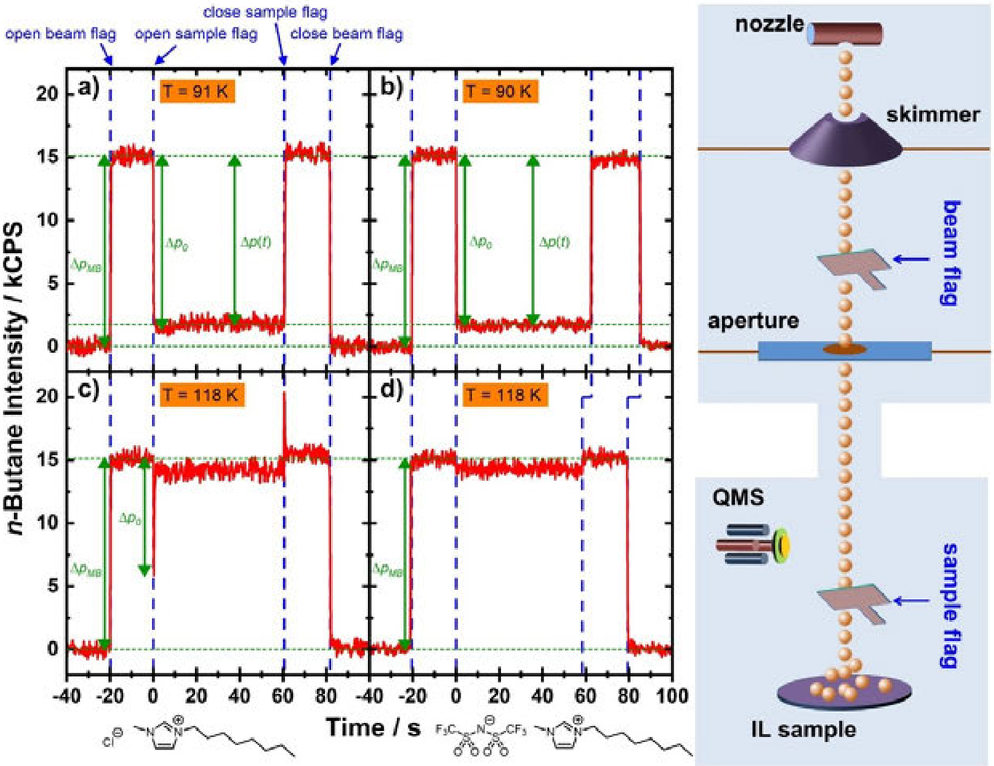

Figure 1. Typical measurement curves obtained with the King and Wells method (left) together with a sketch of the used molecular beam setup (right). The curves show the adsorption dynamics of *n*-butane on [C_8C_1Im]Cl (a, c) and on [C_8C_1Im][Tf_2N] at ≈90/91 and 118 K (b, d). For details see the text.

sets in very quickly, which leads to a very fast pressure increase. After only a few seconds, a steady state situation is reached, in which the adsorption and desorption rates are equal. Thus, the pressure comes back to the level it had before opening the sample flag, so that $S^{net}(t>3\text{ s})=0$. In cases, where the desorption rate is not zero, the trapping probabilities determined by the King and Wells method are often called "net" trapping probabilities, since they do not represent the probability for an individual molecule to become trapped or scattered, but rather refer to the overall balance between adsorption and desorption rate. In the example of Figures 1a and b, that is, at ≈90 K, the partial pressure remains at a low level, which means that the coverage continues to increase, ultimately leading to multilayer growth.

At $t=60$ s, the sample flag is closed, so that the molecular beam is again scattered by it. The partial pressure returns to the value, which it had during the equivalent situation from −20 to 0 s. In Figure 1c, at 118 K, a spike in the partial pressure curve is visible at $t=60$ s. It is caused by molecules desorbing rapidly from the still present adlayer once the molecular beam does not hit the surface any more. Finally, the beam flag is also closed at $t\approx 80$ s and the partial pressure returns to zero.

n-Butane on [C_nC_1Im]X – temperature dependence of S_0^{net}

In the next step, we want to discuss the temperature-dependent behavior of the initial net trapping probability S_0^{net} of *n*-butane on different imidazolium-based ILs. At this point, we will not further address the time-dependence of the trapping probabilities as shown in Figure 1, because the behavior is almost identical for all investigated ILs. Figure 2 shows plots of S_0^{net} vs. T for the set of investigated ILs; part of the results have already been published,[33] but we show them here again, since we are interested in identifying trends upon changing the size of the IL anion. All displayed ILs show a similar S-shaped decrease of S_0^{net} with increasing temperature. For example, for [C_8C_1Im]Cl (black squares in Figure 2a), S_0^{net} stays constant at 0.90 ± 0.05 up to ≈107 K, and thereafter decreases to 0.00 ± 0.05 at $T>126$ K.

At low temperature ($T\leq 90$ K), all trapped *n*-butane molecules remain adsorbed on the surface since desorption from the adlayer is negligible. At high temperature ($T\geq 127$ K), trapped (that is, thermally accommodated) *n*-butane molecules desorb again almost immediately. We expect that thermal accommodation is very efficient for the unseeded *n*-butane beam generated from our nozzle at room temperature. Firstly, its kinetic energy

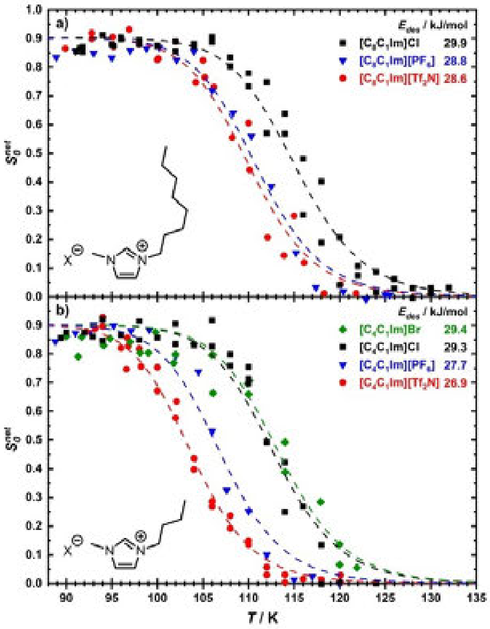

Figure 2. Temperature-dependent initial *n*-butane trapping probabilities of (a) $[C_8C_1Im]X$ (X^- = $[Tf_2N]^-$, $[PF_6]^-$ and Cl^-) and (b) $[C_4C_1Im]X$ (X^- = $[Tf_2N]^-$, $[PF_6]^-$, Cl^- and Br^-). The dashed lines represent fits to the data using Equation (2), in which $S_0^{LT} = 0.90$ and $\nu = 1.4 \cdot 10^{14}\ s^{-1}$ were used as constant parameters for all ILs. Part of the data is already published.[33]

is comparably low (≈13 kJ/mol) and secondly, *n*-butane is a quite heavy and flexible molecule compared to other typical gases like atoms or diatomic molecules. This makes energy transfer from translation to internal rotations and soft vibrations (torsion and bending) very efficient.[38] In the transition region, the residence time of the *n*-butane molecules is in the order of the measurement time required to determine S_0^{net}. We developed a model,[33b] based on the reasonable assumption that thermal accommodation occurs always with the same probability S_0^{LT}, which can be measured at low temperature, where desorption is negligible. S_0^{net} is then given by Equation (2)

$$S_0^{net} = \frac{S_0^{LT}}{1 + \frac{t_m}{2} \cdot \nu \cdot e^{-\frac{E_{des}}{RT}}} \quad (2)$$

where t_m is the measurement time (in our case 0.50 s), ν the pre-exponential factor, R the universal gas constant and E_{des} the desorption energy, which in case of non-activated adsorption is equal to the adsorption or binding energy. Figure 2 shows the results of fitting Equation (2) to the data as dashed lines. Note that S_0^{net} is indeed influenced by the chosen t_m, but E_{des} does not change if a different t_m is used for evaluation. Since ν and E_{des} are strongly coupled, it is necessary to constrain one of them to obtain unambiguous fitting results. In our evaluation, we used $\nu = 1.4 \cdot 10^{14}\ s^{-1}$; this value was found in an Arrhenius-type analysis of time-dependent *n*-butane trapping probabilities on $[C_8C_1Im][Tf_2N]$.[33a] Since the adsorbate remains the same and the binding motif is expected to be similar, that is, the interaction is dominated by the IL alkyl chains, we assume that this pre-exponential factor holds for all ILs. Overall, the relative accuracy of our approach is estimated to ±0.3 kJ/mol. Relative accuracy refers hereby to comparing data measured with the same experimental setup, which is the case here. However, the absolute accuracy is estimated to ±2 kJ/mol, which is due to the uncertainty of the pre-exponential factor and the absolute thermocouple reading at these low temperatures (±3 K).

n-Butane on $[C_nC_1Im]X$ – trends in the desorption energy

The data for the imidazolium-based ILs with different lengths of the alkyl chain (n = 4 and 8) and different anions (Cl^-, Br^-, $[PF_6]^-$ and $[Tf_2N]^-$) in Figure 2 shows two trends: Firstly, E_{des} increases with increasing alkyl chain length, so that the curves in Figure 2a for the $[C_8C_1Im]X$ series are shifted to higher temperature compared to the corresponding curves in Figure 2b for the $[C_4C_1Im]X$ series. Secondly, E_{des} increases with decreasing size of the anion, that is, in the order $[Tf_2N]^- < [PF_6]^- < Br^- \approx Cl^-$. For example, in the $[C_4C_1Im]X$ series E_{des} increases from 26.9 kJ/mol ($[Tf_2N]^-$) via 27.7 kJ/mol ($[PF_6]^-$) to 29.3 kJ/mol (Cl^-) and 29.4 kJ/mol (Br^-).

A readily available quantitative measure for the anion size is the molecular volume, which can be easily calculated from literature density data (obtained from the NIST ILThermo database[39]). Figure 3a shows the correlation of E_{des} with the molecular volume for the two investigated groups of ILs, $[C_8C_1Im]X$ as open symbols and $[C_4C_1Im]X$ as filled symbols. Apparently, the correlation is not linear, but a rather steep decrease of E_{des} is found from the halide anions to $[PF_6]^-$, followed by a more shallow decrease from $[PF_6]^-$ to $[Tf_2N]^-$.

While Figure 3a indicates a correlation between the observed initial adsorption behavior and the bulk molecular volume of the ILs, one rather expects a dependence on surface properties. Indeed, it has been demonstrated that the outer surface layer of ILs considerably differs from the average bulk composition. In particular, the size of the anion has a strong impact on the degree of surface enrichment of the imidazolium alkyl chains protruding into the vacuum. This behavior has been demonstrated by a number of theoretical studies and experimental investigations including molecular dynamics simulations,[21b,40] reactive atom scattering,[26a,31a] Rutherford backscattering[23b,41] and X-ray photoelectron spectroscopy.[34,42] Especially the last method provides a very convenient way to quantify the degree of alkyl chain enrichment: Imidazolium-based cations show two peaks in the C 1s region, one belonging to the carbon atoms bound to at least one nitrogen atom (called C_{hetero}) and one belonging to the carbon atoms bound only to carbon and hydrogen (called C_{alkyl}). The ratio of the peak areas $I_{C\,1s}(C_{alkyl})/I_{C\,1s}(C_{hetero})$ is expected to be 7:5 = 1.4 for $[C_8C_1Im]X$ and 3:5 = 0.6 for $[C_4C_1Im]X$ based on the stoichiometries of the ILs (see dotted horizontal lines in Figure 3b). These ratios were indeed found for XPS measure-

Chemistry–A European Journal | Full Paper
doi.org/10.1002/chem.202102492
Chemistry Europe
European Chemical Societies Publishing

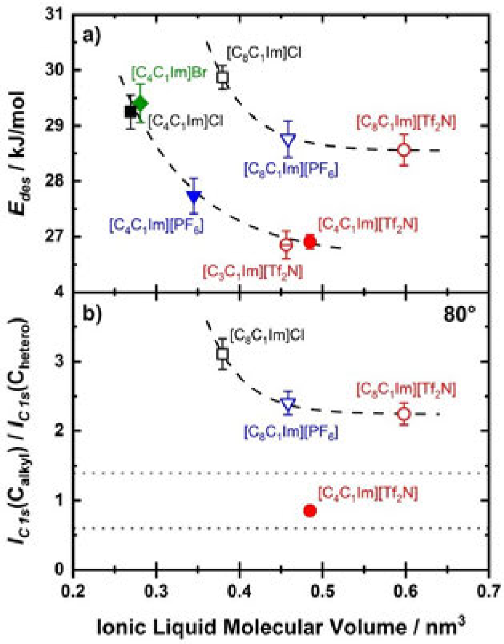

Figure 3. Comparison of (a) *n*-butane desorption energy and (b) alkyl chain surface enrichment. The datasets are plotted vs. the IL's molecular volume to visualize the effect of the anion size. Color codes and open/filled symbols are used to group the ILs by their anion and cation identity. The dashed lines serve as a guide for the eye. The molecular volumes were calculated from the IL densities at 298.15 K, 101.325 kPa, for which an average over the values published in the ILThermo database from NIST[39] were used. Some of the values for E_{des} are already published.[33b] The error bars indicate the estimated uncertainty, by assuming an identical prefactor for all ILs (for details see text). The data from (b) were adapted from previously published studies of our group.[34,42b] The dotted lines in (b) indicate the nominal C_{alkyl}/C_{hetero} ratios for $[C_8C_1Im]^+$ (=1.4) and $[C_4C_1Im]^+$ (=0.6).

ments in 0° emission angle (information depth ≈ 8.4 nm), but for measurements at a surface-sensitive emission angle of 80° (information depth ≈ 1.5 nm) ratios higher than the nominally expected ones were obtained.[34,42b,c] Comparing the peak ratios at 80° emission of different ILs showed that the degree of enrichment increases with increasing chain length[34] and with decreasing anion size.[42b] The latter can be explained by a denser packing of the imidazolium cations if they are incorporated into an ionic sublayer with smaller anions, which in turn also leads to a denser packing of the protruding alkyl chains. A selection of this literature data is shown in Figure 3b, where the C_{alkyl}/C_{herero} ratio is plotted for several ILs.

The two datasets compiled in Figure 3 demonstrate that the alkyl enrichment derived by XPS and the *n*-butane desorption energies derived by the King and Wells method show the same trends with increasing molecular volume. For both, a steep decrease from Cl^- (black symbols) to $[PF_6]^-$ (blue) is followed by a shallow further decrease to $[Tf_2N]^-$ (red). Furthermore, the values strongly increase from $[C_4C_1Im]^+$ (full symbols) to $[C_8C_1Im]^+$ (open symbols). Thus, we conclude that the interaction strength of *n*-butane with the IL surface critically depends on the alkyl chain enrichment. The interaction of *n*-butane with the alkyl chains is stronger than with the imidazolium headgroups and the anions, as is proven by the fact that *n*-butane does not adsorb on ILs with the $[C_2C_1Im]^+$ cation, which only possesses a very short alkyl chain.[33a] The changes in the desorption energy observed for different anions are not caused by interactions between *n*-butane and the anion, but by the different IL surface structure induced by the anion.

iso-Butane and 1-butene on $[C_8C_1Im][Tf_2N]$

So far, we used *n*-butane as a model system to study the adsorption of hydrocarbons on different IL surfaces. Since the adsorption dynamics, however, will also be influenced by the nature of the hydrocarbon, we studied the adsorption of two other C4 hydrocarbons on $[C_8C_1Im][Tf_2N]$, and compare the observed behavior with the already published results for *n*-butane.[33] *iso*-Butane is the isomer of *n*-butane and 1-butene is an unsaturated analogue of *n*-butane. The molecular structures and the temperature-dependent initial trapping probabilities are shown in Figure 4. At low temperature ($T \approx 90$ K), all three hydrocarbons show the same trapping probability $S_0^{LT} = 0.90 \pm 0.05$. This shows that thermal accommodation is equally efficient for all three hydrocarbons at our experimental conditions, although the different molecular structures could principally result in different energy transfer mechanisms to bending and torsion modes.

For *iso*-butane and 1-butene, S_0^{net} shows a similar S-shaped decrease, as it was found for *n*-butane. This allows us to determine the desorption energy by fitting Equation (2) to the data, assuming the same pre-exponential factor $\nu = 1.4 \cdot 10^{14}$ s^{-1} for all three hydrocarbons. We observe that the desorption energy decreases from 28.6 kJ/mol (*n*-butane) via 27.9 kJ/mol (1-butene) to 27.5 kJ/mol (*iso*-butane). Interestingly, this trend is

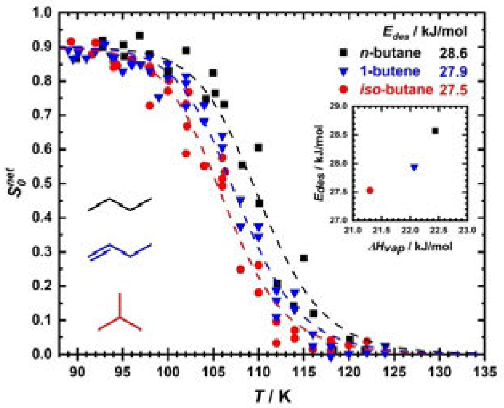

Figure 4. Temperature-dependent initial trapping probabilities of *iso*-butane, 1-butene and *n*-butane on $[C_8C_1Im][Tf_2N]$. The dashed lines represent fits to the datasets according to Equation (2). The inset shows the correlation between E_{des} and the enthalpies of vaporization.[43]

correlated with the enthalpies of vaporization[43] of the pure hydrocarbons, as is evident from the inset in Figure 4. The differences in the enthalpies of vaporization for the three compounds are caused by the dispersion forces between one molecule and its neighbors of the same kind. These forces decrease in the order *n*-butane > 1-butene > *iso*-butane, which is mainly caused by better intermolecular alignment of elongated compared to ball-like molecules. The situation at the IL surface is somewhat similar: Since the molecule/IL interaction is dominated by the interaction with the IL alkyl chains (on ILs with short chains no adsorption occurs), the hydrocarbon molecules will align with the IL alkyl chains, so that also in this case the interaction is the strongest for *n*-butane and the weakest for *iso*-butane with 1-butene lying somewhere in between.

Conclusion

We determined the trapping probabilities for *n*-butane on a series of imidazolium-based $[C_nC_1Im]X$ ($n=4$, 8; $X^-=Cl^-$, Br^-, $[PF_6]^-$, $[Tf_2N]^-$) ionic liquids by the direct method of King and Wells.[37] Furthermore, we compared the behavior for *n*-butane with that of *iso*-butane and 1-butene on $[C_8C_1Im][Tf_2N]$. *n*-Butane adsorbs at 90 K with an initial trapping probability of 0.90 ± 0.05 on all ILs investigated. With increasing surface temperature, the trapping probability decreases to zero forming an S-shaped curve. This characteristic decrease shifts to higher temperatures for longer alkyl chains and smaller anions, which can be attributed to an increase in desorption energy. The pronounced dependence on the alkyl chain length indicates that *n*-butane mainly interacts with the alkyl chains and the interaction with the anion and the cationic headgroup is only weak.[33a] The desorption energy also increases with decreasing anion size: While only a weak increase is seen from $[Tf_2N]^-$ to $[PF_6]^-$, a quite strong increase occurs when going to Cl^- and Br^-. The exact same trend was observed previously in X-ray photoelectron spectroscopy measurements of the alkyl chain enrichment.[42b] Therefore, we conclude that the observed differences are not due to *n*-butane adsorption on the anion moiety, but rather by an increasingly denser packing of the alkyl chains when decreasing the size of the anion.

iso-Butane and 1-butene also show an initial trapping probability of 0.90 ± 0.05 at 90 K and an S-shaped decrease with increasing surface temperature. This decrease is shifted to lower temperatures in the order *n*-butane > 1-butene > *iso*-butane, again attributed to a decrease in desorption energy in the same order. This finding can be explained by the intermolecular dispersion forces between the gas molecule and the IL surface, which are expected to be strongest for *n*-butane and weakest for *iso*-butane.

Our study shows that the interactions of molecules with IL surfaces are dominated by the specific groups (here alkyl chains) at the outermost surface as well as by the properties of the molecules. This knowledge is a first step for the rational design of gas/IL interfaces, which are of high relevance for the SILP and SCILL concepts, for both of which the interaction of the reactants with the IL surface is the first and possibly decisive step for their functionality. Another possible application is separation technology. For the here studied molecules, the differences in adsorption strength are quite small, however, so that a successful application in this area does not seem feasible to us. Further studies with different ILs and different molecules are required to obtain a more general picture.

Acknowledgements

L.W., R.G.B. and H.-P.S. thank the European Research Council (ERC) under the European Union's Horizon 2020 research and innovation programme for financial support, in the context of the Advanced Investigator Grant "ILID" to H.-P.S. (Grant Agreement No. 693398-ILID). We thank Dr. Matthias Lexow for fruitful discussions. Open Access funding enabled and organized by Projekt DEAL.

Conflict of Interest

The authors declare no conflict of interest.

Keywords: adsorption · catalysis · gas-surface dynamics · ionic liquids · molecular beam

[1] a) P. Wasserscheid, T. Welton, *Ionic liquids in synthesis*, Wiley-VCH, Weinheim **2003**; b) D. R. MacFarlane, M. Kar, J. M. Pringle, *Fundamentals of Ionic Liquids*, Wiley-VCH, Weinheim **2017**.

[2] P. Walden, *Bull. Acad. Imp. Sci. St.-Petersbourg* **1914**, 405–422.

[3] a) J. S. Wilkes, M. J. Zaworotko, *J. Chem. Soc. Chem. Commun.* **1992**, 965–967; b) T. Welton, *Biophys. Rev. Lett.* **2018**, *10*, 691–706.

[4] a) K. R. Seddon, *J. Chem. Technol. Biotechnol.* **1997**, *68*, 351–356; b) J. G. Huddleston, H. D. Willauer, R. P. Swatloski, A. E. Visser, R. D. Rogers, *Chem. Commun.* **1998**, 1765–1766; c) M. J. Earle, K. R. Seddon, *Pure Appl. Chem.* **2000**, *72*, 1391–1398.

[5] a) T. Welton, *Chem. Rev.* **1999**, *99*, 2071–2084; b) R. D. Rogers, K. R. Seddon, *Science* **2003**, *302*, 792–793; c) J. P. Hallett, T. Welton, *Chem. Rev.* **2011**, *111*, 3508–3576.

[6] a) M. Galiński, A. Lewandowski, I. Stępniak, *Electrochim. Acta* **2006**, *51*, 5567–5580; b) P. Hapiot, C. Lagrost, *Chem. Rev.* **2008**, *108*, 2238–2264; c) M. Watanabe, M. L. Thomas, S. Zhang, K. Ueno, T. Yasuda, K. Dokko, *Chem. Rev.* **2017**, *117*, 7190–7239; d) M. Forsyth, L. Porcarelli, X. Wang, N. Goujon, D. Mecerreyes, *Acc. Chem. Res.* **2019**, *52*, 686–694.

[7] a) I. Minami, *Molecules* **2009**, *14*, 2286–2305; b) M. Cai, Q. Yu, W. Liu, F. Zhou, *Chem. Soc. Rev.* **2020**, *49*, 7753–7818.

[8] a) M. Maase, K. Massonne, *Ionic Liquids IIIB: Fundamentals, Progress, Challenges, and Opportunities: Transformations and Processes*, Vol. 902 (Eds.: R. D. Rogers, K. R. Seddon), American Chemical Society **2005**, pp. 126–132; b) M. Ramdin, T. W. de Loos, T. J. H. Vlugt, *Ind. Eng. Chem. Res.* **2012**, *51*, 8149–8177; c) S. Zeng, X. Zhang, L. Bai, X. Zhang, H. Wang, J. Wang, D. Bao, M. Li, X. Liu, S. Zhang, *Chem. Rev.* **2017**, *117*, 9625–9673.

[9] R. F. M. Frade, C. A. M. Afonso, *Hum. Exp. Toxicol.* **2010**, *29*, 1038–1054.

[10] S. P. F. Costa, A. M. O. Azevedo, P. C. A. G. Pinto, M. L. M. F. S. Saraiva, *ChemSusChem* **2017**, *10*, 2321–2347.

[11] a) J. H. Clark, S. J. Tavener, *Org. Process Res. Dev.* **2007**, *11*, 149–155; b) P. G. Jessop, *Green Chem.* **2011**, *13*, 1391–1398; c) G. Cevasco, C. Chiappe, *Green Chem.* **2014**, *16*, 2375–2385.

[12] a) B. L. Gadilohar, G. S. Shankarling, *J. Mol. Liq.* **2017**, *227*, 234–261; b) J. M. Gomes, S. S. Silva, R. L. Reis, *Chem. Soc. Rev.* **2019**, *48*, 4317–4335; c) B. Gaida, A. Brzęczek-Szafran, *Molecules* **2020**, *25*, 3285.

[13] Y. Zhou, J. Qu, *ACS Appl. Mater. Interfaces* **2017**, *9*, 3209–3222.

[14] a) I. M. Marrucho, L. C. Branco, L. P. N. Rebelo, *Annu. Rev. Chem. Biomol. Eng.* **2014**, *5*, 527–546; b) K. S. Egorova, E. G. Gordeev, V. P. Ananikov, *Chem. Rev.* **2017**, *117*, 7132–7189.

[15] a) Y. Qiao, W. Ma, N. Theyssen, C. Chen, Z. Hou, *Chem. Rev.* **2017**, *117*, 6881–6928; b) C. Dai, J. Zhang, C. Huang, Z. Lei, *Chem. Rev.* **2017**, *117*, 6929–6983; c) B. Karimi, M. Tavakolian, M. Akbari, F. Mansouri, *ChemCatChem* **2018**, *10*, 3173–3205; d) H.-P. Steinrück, P. Wasserscheid, *Catal. Lett.* **2015**, *145*, 380–397; e) O. Bartlewicz, I. Dąbek, A. Szymańska, H. Maciejewski, *Catalysts* **2020**, *10*, 1227.

[16] U. Kernchen, B. Etzold, W. Korth, A. Jess, *Chem. Eng. Technol.* **2007**, *30*, 985–994.

[17] C. P. Mehnert, R. A. Cook, N. C. Dispenziere, M. Afeworki, *J. Am. Chem. Soc.* **2002**, *124*, 12932–12933.

[18] A. J. Greer, J. Jacquemin, C. Hardacre, *Molecules* **2020**, *25*, 5207.

[19] W. Korth, A. Jess, *Supported Ionic Liquids*, (Eds.: R. Fehrmann, A. Riisager, M. Haumann), Wiley-VCH, Weinheim **2014**, pp. 279–306.

[20] a) A. Schönweiz, R. Franke, *Supported Ionic Liquids* (Eds.: R. Fehrmann, A. Riisager, M. Haumann), Wiley-VCH, Weinheim **2014**, pp. 307–326; b) J. M. Marinkovic, A. Riisager, R. Franke, P. Wasserscheid, M. Haumann, *Ind. Eng. Chem. Res.* **2019**, *58*, 2409–2420.

[21] a) R. M. Lynden-Bell, *Mol. Phys.* **2003**, *101*, 2625–2633; b) K. Shimizu, B. S. J. Heller, F. Maier, H.-P. Steinrück, J. N. Canongia Lopes, *Langmuir* **2018**, *34*, 4408–4416.

[22] a) A. J. Carmichael, C. Hardacre, J. D. Holbrey, K. R. Seddon, M. Nieuwenhuyzen, *Proc. Vol. 1999* **1999**, *41*, 209–221; b) J. Haddad, D. Pontoni, B. M. Murphy, S. Festersen, B. Runge, O. M. Magnussen, H.-G. Steinrück, H. Reichert, B. M. Ocko, M. Deutsch, *Proc. Natl. Acad. Sci. USA* **2018**, *115*, E1100–E1107.

[23] a) T. J. Gannon, G. Law, P. R. Watson, A. J. Carmichael, K. R. Seddon, *Langmuir* **1999**, *15*, 8429–8434; b) K. Nakajima, M. Lísal, K. Kimura, *Surface and Interface Science*, Vol. 7 (Ed.: K. Wandelt), Wiley-VCH, Weinheim **2020**, pp. 351–389.

[24] K. Nakajima, A. Ohno, M. Suzuki, K. Kimura, *Langmuir* **2008**, *24*, 4482–4484.

[25] a) S. Caporali, U. Bardi, A. Lavacchi, *J. Electron Spectrosc.* **2006**, *151*, 4–8; b) I. J. Villar-Garcia, S. Fearn, G. F. De Gregorio, N. L. Ismail, F. J. V. Gschwend, A. J. S. McIntosh, K. R. J. Lovelock, *Chem. Sci.* **2014**, *5*, 4404–4418.

[26] a) B. Wu, J. Zhang, T. K. Minton, K. G. McKendrick, J. M. Slattery, S. Yockel, G. C. Schatz, *J. Phys. Chem. C* **2010**, *114*, 4015–4027; b) E. J. Smoll, S. M. Purcell, L. D'Andrea, J. M. Slattery, D. W. Bruce, M. L. Costen, K. G. McKendrick, T. K. Minton, *J. Phys. Chem. Lett.* **2019**, *10*, 156–163.

[27] a) S. Baldelli, *J. Phys. Chem. B* **2003**, *107*, 6148–6152; b) T. Iwahashi, T. Ishiyama, Y. Sakai, A. Morita, D. Kim, Y. Ouchi, *Phys. Chem. Chem. Phys.* **2020**, *22*, 12565–12576.

[28] a) E. F. Smith, F. J. M. Rutten, I. J. Villar-Garcia, D. Briggs, P. Licence, *Langmuir* **2006**, *22*, 9386–9392; b) K. R. J. Lovelock, I. J. Villar-Garcia, F. Maier, H.-P. Steinrück, P. Licence, *Chem. Rev.* **2010**, *110*, 5158–5190; c) H.-P. Steinrück, *Phys. Chem. Chem. Phys.* **2012**, *14*, 5010–5029; d) C. Kolbeck, I. Niedermaier, A. Deyko, K. R. J. Lovelock, N. Taccardi, W. Wei, P. Wasserscheid, F. Maier, H.-P. Steinrück, *Chem. Eur. J.* **2014**, *20*, 3954–3965; e) S. Men, D. S. Mitchell, K. R. J. Lovelock, P. Licence, *ChemPhysChem* **2015**, *16*, 2211–2218; f) B. S. J. Heller, M. Lexow, F. Greco, S. Shin, G. Partl, F. Maier, H.-P. Steinrück, *Chem. Eur. J.* **2020**, *26*, 1117–1126.

[29] a) J. R. Roscioli, D. J. Nesbitt, *J. Phys. Chem. Lett.* **2010**, *1*, 674–678; b) J. R. Roscioli, D. J. Nesbitt, *J. Phys. Chem. A* **2011**, *115*, 9764–9773.

[30] a) M. P. Ziemkiewicz, A. Zutz, D. J. Nesbitt, *J. Phys. Chem. C* **2012**, *116*, 14284–14294; b) A. Zutz, D. J. Nesbitt, *AIP Adv.* **2016**, *6*, 105207.

[31] a) M. A. Tesa-Serrate, B. C. Marshall, E. J. Smoll, S. M. Purcell, M. L. Costen, J. M. Slattery, T. K. Minton, K. G. McKendrick, *J. Phys. Chem. C* **2015**, *119*, 5491–5505; b) B. C. Marshall, E. J. Smoll, S. M. Purcell, M. L. Costen, K. G. McKendrick, T. K. Minton, *J. Phys. Chem. C* **2016**, *120*, 12472–12483; c) M. A. Tesa-Serrate, E. J. Smoll, L. D'Andrea, S. M. Purcell, M. L. Costen, D. W. Bruce, J. M. Slattery, T. K. Minton, K. G. McKendrick, *J. Phys. Chem. C* **2016**, *120*, 27369–27379.

[32] A. Deyko, R. G. Jones, *Faraday Discuss.* **2012**, *154*, 265–288.

[33] a) R. G. Bhuin, L. Winter, M. Lexow, F. Maier, H.-P. Steinrück, *Angew. Chem. Int. Ed.* **2020**, *59*, 14429–14433; *Angew. Chem.* **2020**, *132*, 14536–14541; b) L. Winter, R. G. Bhuin, M. Lexow, F. Maier, H.-P. Steinrück, *J. Chem. Phys.* **2020**, *153*, 214706.

[34] K. R. J. Lovelock, C. Kolbeck, T. Cremer, N. Paape, P. S. Schulz, P. Wasserscheid, F. Maier, H.-P. Steinrück, *J. Phys. Chem. B* **2009**, *113*, 2854–2864.

[35] J. M. Gottfried, F. Maier, J. Rossa, D. Gerhard, P. S. Schulz, P. Wasserscheid, H.-P. Steinrück, *Z. Phys. Chem.* **2006**, *220*, 1439–1453.

[36] A. V. Hamza, H.-P. Steinrück, R. J. Madix, *J. Chem. Phys.* **1986**, *85*, 7494–7495.

[37] D. A. King, M. G. Wells, *Surf. Sci.* **1972**, *29*, 454–482.

[38] J. F. Weaver, A. F. Carlsson, R. J. Madix, *Surf. Sci. Rep.* **2003**, *50*, 107–199.

[39] Q. Dong, C. D. Muzny, A. Kazakov, V. Diky, J. W. Magee, J. A. Widegren, R. D. Chirico, K. N. Marsh, M. Frenkel, *J. Chem. Eng. Data* **2007**, *52*, 1151–1159.

[40] R. M. Lynden-Bell, M. Del Pópolo, *Phys. Chem. Chem. Phys.* **2006**, *8*, 949–954.

[41] A. Ohno, H. Hashimoto, K. Nakajima, M. Suzuki, K. Kimura, *J. Chem. Phys.* **2009**, *130*, 204705.

[42] a) V. Lockett, R. Sedev, C. Bassell, J. Ralston, *Phys. Chem. Chem. Phys.* **2008**, *10*, 1330–1335; b) C. Kolbeck, T. Cremer, K. R. J. Lovelock, N. Paape, P. S. Schulz, P. Wasserscheid, F. Maier, H.-P. Steinrück, *J. Phys. Chem. B* **2009**, *113*, 8682–8688; c) F. Maier, T. Cremer, C. Kolbeck, K. R. J. Lovelock, N. Paape, P. S. Schulz, P. Wasserscheid, H.-P. Steinrück, *Phys. Chem. Chem. Phys.* **2010**, *12*, 1905–1915; d) S. Men, B. B. Hurisso, K. R. J. Lovelock, P. Licence, *Phys. Chem. Chem. Phys.* **2012**, *14*, 5229–5238.

[43] V. Majer, V. Svoboda, *Enthalpies of Vaporization of Organic Compounds: A Critical Review and Data Compilation*, Blackwell Scientific Publications, Oxford **1985.**

Manuscript received: July 9, 2021
Accepted manuscript online: September 9, 2021
Version of record online: September 29, 2021

8.3 PUBLICATION 3

ACS Catalysis

pubs.acs.org/acscatalysis

Research Article

Tailoring the Selectivity of 1,3-Butadiene versus 1-Butene Adsorption on Pt(111) by Ultrathin Ionic Liquid Films

Leonhard Winter, Simon Trzeciak, Cynthia C. Fernández,* Stephen Massicot, Timo Talwar, Florian Maier, Dirk Zahn, and Hans-Peter Steinrück*

Cite This: *ACS Catal.* 2023, 13, 10866−10877

Read Online

ACCESS | Metrics & More | Article Recommendations | Supporting Information

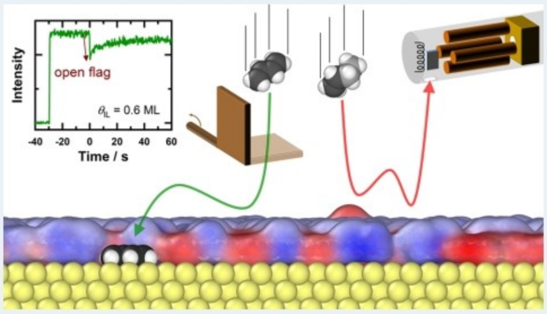

ABSTRACT: The solid catalyst with ionic liquid layer (SCILL) concept is a promising approach to enhance the selectivity of hydrogenation reactions, like the selective hydrogenation of 1,3-butadiene to 1-butene using transition-metal catalysts. In this context, the adsorption dynamics of 1,3-butadiene and 1-butene were studied on Pt(111) modified with ultrathin layers of the ionic liquid (IL) 1,3-dimethylimidazolium bis(trifluoromethanesulfonyl)imide ($[C_1C_1Im][Tf_2N]$). The sticking coefficients of the two hydrocarbons are measured using the direct method of King and Wells. Both olefins show pronounced precursor-mediated dynamics on clean Pt(111) and on the IL-modified surface. Increasing the IL coverage leads to an increased blocking of adsorption sites for the incoming olefins. Coadsorbed hydrogen does not significantly affect the precursor and site-blocking effects for 1,3-butadiene. Interestingly, a smaller IL amount is needed to prevent 1-butene adsorption compared to 1,3-butadiene adsorption, which is proposed to be directly related to the IL's influence on selective hydrogenation in SCILL catalysis. Indeed, molecular dynamics simulations show IL film densification/relaxation as the key mechanism to allowing/excluding olefin adsorption on the metal. Being a function of IL coverage, the energy of film penetration is used to control the effective olefin adsorption energy and thus creates an operation regime for suppressing 1-butene while permitting 1,3-butadiene adsorption.

KEYWORDS: *molecular beam, molecular dynamics, ionic liquids, SCILL, selectivity, adsorption, hydrogenation, gas-surface dynamics*

■ INTRODUCTION

In the hydrocarbon industry, 1-butene is used as a monomer for the polymerization to polybutenes and as a comonomer for the production of low-density polyethylenes.[1,2] Since catalysts used in these polymerizations are poisoned by 1,3-butadiene, a 1-butene stream containing <5 ppm 1,3-butadiene is required.[2,3] This purity level is not reached by removing 1,3-butadiene from the C4-fraction of steam crackers using extractive distillation. Consequently, an additional selectively catalyzed hydrogenation step is required (see Scheme 1).[1−4] The requirements for this catalyst are quite demanding: It needs to almost fully convert trace amounts of 1,3-butadiene to 1-butene while at the same time suppressing the hydrogenation of 1-butene to *n*-butane and also the isomerization of 1-butene to *cis*-2-butene and *trans*-2-butene. An additional challenge is catalyst deterioration by the accumulation of higher hydrocarbons, so-called green oil, which are the products of C−C coupling side reactions.[3,4]

Different heterogeneous transition-metal catalysts have been applied successfully in this reaction, most prominently Pd-based ones,[5−11] but also Pt,[12−15] Ni,[16] Co,[17] Rh,[18] Ir,[19,20] Fe,[21] Ru,[21] Cu,[22] and even Au[23,24] catalysts have shown activity.[2−4] The selectivity can be improved by various strategies, such as using tuned supports,[6,13,18,24] co-fed CO,[18] different metal alloys,[6−8,14,15,21,25] sulfide materials,[8,26] single-atom catalysts,[9,13,14,20] and since recently also the SCILL concept.[10,11,16] In a solid catalyst with ionic liquid layer (SCILL), supported nanoparticles are modified by adding a layer of ionic liquids (ILs).[27,28] ILs consist solely of cations and anions and possess a remarkably low melting point, often below room temperature.[29] Catalytic test experiments with a SCILL system showed very promising results, increasing the selectivity toward butenes from 0 to 99% at 99.5% 1,3-butadiene conversion compared to a commercial Pd catalyst.[11]

In the earlier literature, the SCILL effect was often attributed to solubility differences of the competing reactants in the IL film.[27] But this view has been challenged since in many cases, the selectivity of SCILL catalysts is larger than explainable by taking

Received: May 10, 2023
Revised: July 11, 2023
Published: August 2, 2023

https://doi.org/10.1021/acscatal.3c02126
ACS Catal. 2023, 13, 10866−10877

Scheme 1. Selective Hydrogenation of 1,3-Butadiene[a]

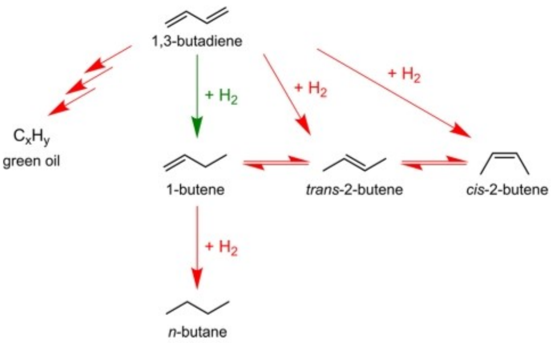

[a]The desired reaction is marked in green; the undesired side reactions, in red.

into account only solubility differences.[11] Additionally, the SCILL effect already sets in if only minor amounts of ILs are used in the catalyst preparation, far less than is needed for the formation of a three-dimensional IL phase.[11] In the recent literature, the SCILL effect is thus often attributed to site-blocking and/or ligand effects, but a thorough understanding is still lacking.[11,30] With this work, we aim to obtain insights into the adsorption dynamics of olefins on IL-modified metal surfaces. We base our model catalytic approach on a Pt(111) surface in ultrahigh vacuum (UHV). Onto this surface, we deposit controlled amounts of the IL 1,3-dimethylimidazolium bis(trifluoromethanesulfonyl)imide ($[C_1C_1Im][Tf_2N]$) by in situ physical vapor deposition (PVD).[31−33] The adsorption dynamics are addressed by measuring sticking coefficients of 1,3-butadiene and 1-butene using the method of King and Wells[34] with a supersonic molecular beam and by molecular dynamics simulations.

■ EXPERIMENTAL SECTION

The measurements were performed in a UHV apparatus with a base pressure of $\approx 1 \times 10^{-10}$ mbar, which was already described in detail elsewhere.[35] The Pt(111) crystal (MaTeck, 12 mm × 12 mm) was cleaned using Ar^+ sputtering (1 kV, 10 mA, 3.0×10^{-5} mbar, 30 min) and subsequent annealing to 1100 K for 3 min, followed by heating in 3.0×10^{-7} mbar O_2 at 800 K for 12 min, and a final annealing step to 900 K for 1 min to remove residual oxygen. The long-range order of the crystal surface was verified by low-energy electron diffraction (LEED, SPECS ErLEED 150), and the cleanliness was confirmed by X-ray photoelectron spectroscopy (XPS), using a non-monochromatic Al Kα X-ray source (1486.6 eV, SPECS XR 50, 12.0 kV, 350 W) and a hemispherical electron analyzer (SPECS PHOIBOS 100 1D-DLD). The IL 1,3-dimethylimidazolium bis(trifluoromethanesulfonyl)imide ($[C_1C_1Im][Tf_2N]$) was synthesized by a procedure adapted from the literature.[36] The ultrathin IL films were prepared by physical vapor deposition using a home-built IL evaporator.[37] The IL dose was controlled by varying the deposition time while keeping the evaporator crucible at a constant temperature of 405 K.

The IL coverage, θ_{IL}, was determined from the attenuation of the Pt 4f X-ray photoelectron spectroscopy (XPS) signal at normal emission. The intensity of the Pt 4f signal was obtained by numerical integration from 77.0 to 66.0 eV binding energy after subtraction of a constant background adjusted at low binding energy. This method proved to be more robust toward adsorbate-induced changes in the Pt 4f satellite structure than subtraction of a Shirley or linear background. The thickness of an ideal 2D IL layer d can be obtained by $d = -\lambda \cos(\vartheta)\ln\left(\frac{I_d}{I_0}\right)$,[31,38] where I_0 is the Pt 4f intensity of the clean surface, I_d is the Pt 4f intensity of the IL-covered surface, ϑ is the emission angle (in this case 0°), and λ is the inelastic mean free path of the Pt 4f photoelectrons ($E_{kin} \approx 1414$ eV) in the IL film. We used $\lambda = 3.1$ nm, obtained by extrapolation from previously reported data.[32,37−39] Following previous publications from our group,[38] we estimate the thickness, h, of one IL monolayer (ML) by $h = \sqrt[3]{V_m} = \sqrt[3]{\frac{M}{N_A \rho}}$, where V_m is the bulk molecular volume, N_A is the Avogadro constant, M is the molar mass, and ρ is the bulk density of the respective IL, which gives $h = 0.74$ nm for $[C_1C_1Im][Tf_2N]$. We define that $\theta_{IL} = 1$ ML is the amount of IL that corresponds to the substrate damping expected from an ideal 2D film with thickness $h = 0.74$ nm. In a simplified picture, this monolayer has the same density as the bulk IL and is composed of pairs of cations and anions, vertically arranged on top of each other. On many metal surfaces, the formation of a wetting layer, that is, a closed layer of cations and anions adsorbed next to each other on the surface in a checkerboard-like structure is observed, with an ideal coverage of 0.5 ML.[40] One should note, however, that the actual IL coverage required to form a closed wetting layer can deviate from this ideal value due to the specific ion/substrate interactions, the resulting adsorption geometry and long-range ordered structure, and a different density compared to the bulk.

1,3-Butadiene was purchased from Air Liquide (purity > 99.5%), 1-butene from Messer Griesheim (purity > 99%), and hydrogen from Linde (purity 99.999%). The gas phase mass spectra reproduce the literature data,[41] indicating a satisfactory purity of the compounds. Unseeded continuous supersonic molecular beams were generated by expanding a gas flow of the pure gases (nominally 1.0 sccm for 1,3-butadiene and 1-butene, 4.0 sccm for H_2) through a room-temperature nozzle (100 μm diameter). The molecular beam passed a conical skimmer (opening diameter 0.5 mm) and an aperture (2.6 mm diameter) creating a circular beam spot with 8.1 mm diameter on the sample. For preadsorption of hydrogen, a larger aperture with 3.7 mm diameter was used to create a larger beam spot with 11.5 mm diameter. We expect the kinetic energy of the 1-butene and 1,3-butadiene beams to be approximately 13 kJ/mol by comparison to a similarly generated *n*-butane beam.[42] The beam flux was followed with a beam monitor.[35]

A quadrupole mass spectrometer (Hiden Analytical) was used to follow the partial pressures of 1-butene, 1,3-butadiene, and hydrogen in the analysis chamber. The heights of the most intense peaks generated by electron ionization (70 eV), that is, $m/z = 41$ for 1-butene, $m/z = 39$ for 1,3-butadiene, and $m/z = 2$ for hydrogen, were recorded in time intervals of 0.22 s. The raw data was corrected for nonconstant pumping speeds adapting an iterative procedure (for details, see the Supporting Information).[43]

Molecular Dynamics Simulations. All molecular dynamics (MD) simulations were performed with the large-scale atomic/molecular massively parallel simulator (LAMMPS) with the code version from June 23, 2022. For all simulations, the integration step was set to 1.0 fs, and the systems were coupled to the Nose−Hoover thermostat with a relaxation constant of 0.5 ps to impose constant system temperature.[44] Atomic

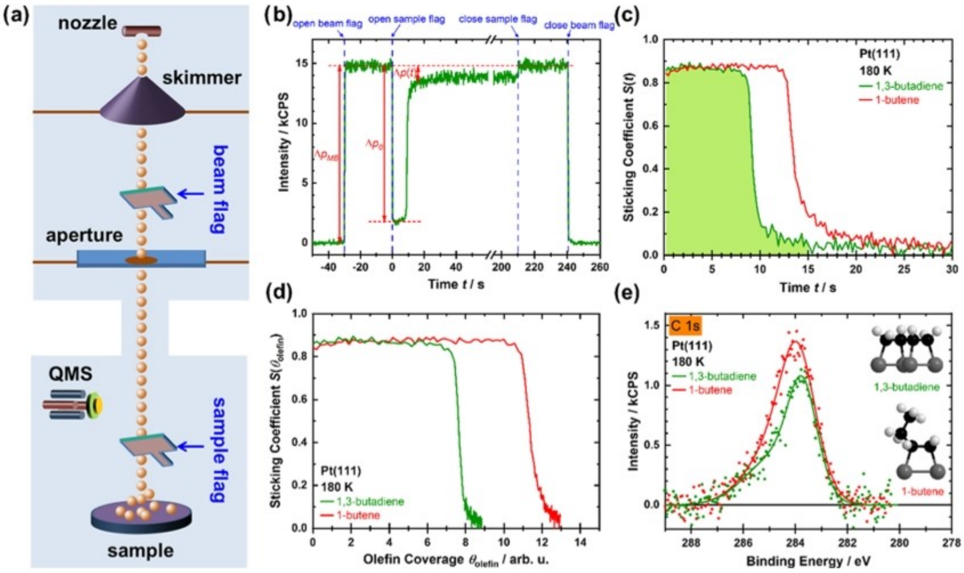

Figure 1. (a) Sketch of the employed molecular beam setup. (b) 1,3-Butadiene adsorption on clean Pt(111) shown as an exemplary measurement curve obtained by the method of King and Wells. The 1,3-butadiene partial pressure is recorded by following the corresponding mass spectrometer signal ($m/z = 39$). The first signal increase Δp_{MB} is the result of opening the beam flag; the initial decrease Δp_0 is caused by opening the sample flag. The initial sticking coefficient S_0 can then be determined by $S_0 = \Delta p_0/\Delta p_{MB}$. Further details are given in the main text. (c) Plots of the time-dependent sticking coefficient $S(t)$ of 1,3-butadiene (green) and 1-butene (red) on clean Pt(111) at 180 K. The area below the $S(t)$ curve can be used as a measure of the olefin coverage θ_{olefin}. (d) Plots of the olefin coverage-dependent sticking coefficient $S(\theta_{olefin})$ derived from the plots in panel (c). (e) C 1s XP spectra measured after the adsorption experiments shown in panels (c) and (d) together with a sketch of the most stable adsorption structures of 1,3-butadiene (a *trans*-1,2,3,4-tetra-σ complex) and 1-butene (a 1,2-di-σ complex) on Pt(111).

interactions were described by Lennard-Jones potentials using a cutoff delimiter of 12 Å. Long-range electrostatics were considered by the particle−particle particle−mesh approach[45] using a slab correction for 2D periodic systems to mimic Ewald summation.[46] Fixed partial charges of the ionic liquid molecules were determined using Gaussian 09, revision D.01 code, via the restricted electrostatic potential (RESP) method with the HF/6-31G* basis set and refined by an antechamber tool from the Amber22 package. A full list of all atom charges and interaction parameters is provided in Tables S1−S4 (see the Supporting Information). The General AMBER Force Field (GAFF) 2.11 suite, as released with the Amber22 package[47] was used for describing the interactions of the IL and the IL-olefin (1,3-butadiene and/or 1-butene), respectively. In turn, the Lennard-Jones parameters for Pt were taken from ref 48. The Pt(111) slab was chosen as a 9.99 nm × 10.1 nm × 1.8 nm block, featuring 2D periodic boundary conditions. Thus, the Pt(111) slab was modeled as 9 explicit atomic layers each comprising 1512 atoms arranged according to fixed positions based on a lattice constant of 0.3924 nm.[48]

The standard GAFF model was found to reproduce the 1,3-butadiene/1-butene adsorption on Pt only at unsatisfactory accuracy. For this reason, we directly adopted the geometries and binding energy terms from DFT calculations.[49] This leads to a QM/MM type approximation of the effective binding energy in the presence of an IL film via

$$E^{\mathrm{eff}}_{\mathrm{adsorption}} = E^{\mathrm{DFT}}_{\mathrm{adsorption}} - \Delta E^{\mathrm{MD}}_{\mathrm{IL-\ relaxation}} \tag{1}$$

To calculate the IL relaxation energy, the interaction energies IL−IL and IL−Pt must be added for the initial and final states. The relaxation energy is then the difference of the energies of these two states; see the equation below

$$\Delta E^{\mathrm{MD}}_{\mathrm{IL-\ relaxation}} = (E_{\mathrm{IL-IL}} + E_{\mathrm{IL-Pt}})_{\mathrm{initial\ state}} - (E_{\mathrm{IL-IL}} + E_{\mathrm{IL-Pt}})_{\mathrm{final\ state}} \tag{2}$$

Based on the minimum energy configurations adopted from the DFT calculations of ref 49, three 1,3-butadiene and three 1-butene molecules were placed on the Pt(111) surface. Next, parallel setups were created for adding 40, 60, 80, 100, 121, 141, 161, 181, and 202 ion pairs of $[C_1C_1Im][Tf_2N]$ mimicking surface coverages of 0.22, 0.33, 0.43, 0.54, 0.65, 0.76, 0.87, 0.98, and 1.08 ML, respectively. The IL coverages, θ_{IL}, were obtained assuming that the density of the film matches the bulk density

$$\theta_{\mathrm{IL}} = \frac{d}{h} = \frac{{V_{\mathrm{m}}}^{2/3}N}{A} \tag{3}$$

where d is the mean thickness of the film, h is the thickness of one IL monolayer, V_m is the bulk molecular volume, N is the number of ion pairs in the simulation slab, and A is the surface area of the simulation slab.

Each of the film models were subjected to simulated annealing studies to allow film formation free from bias by the (randomly generated) starting configurations. For this, the IL film was propagated for 3 ns at 1000 K (no vaporization was observed within this short time scale) to implement a highly mobile 2D-liquid. We then performed cooling to 180 K at a rate of 10 K/ns, followed by an additional 5 ns equilibration run at the target temperature. For the sampling of the interaction energies, a period of 10 ns was found appropriate (Gaussian-distributed occurrence profiles for all energy terms).

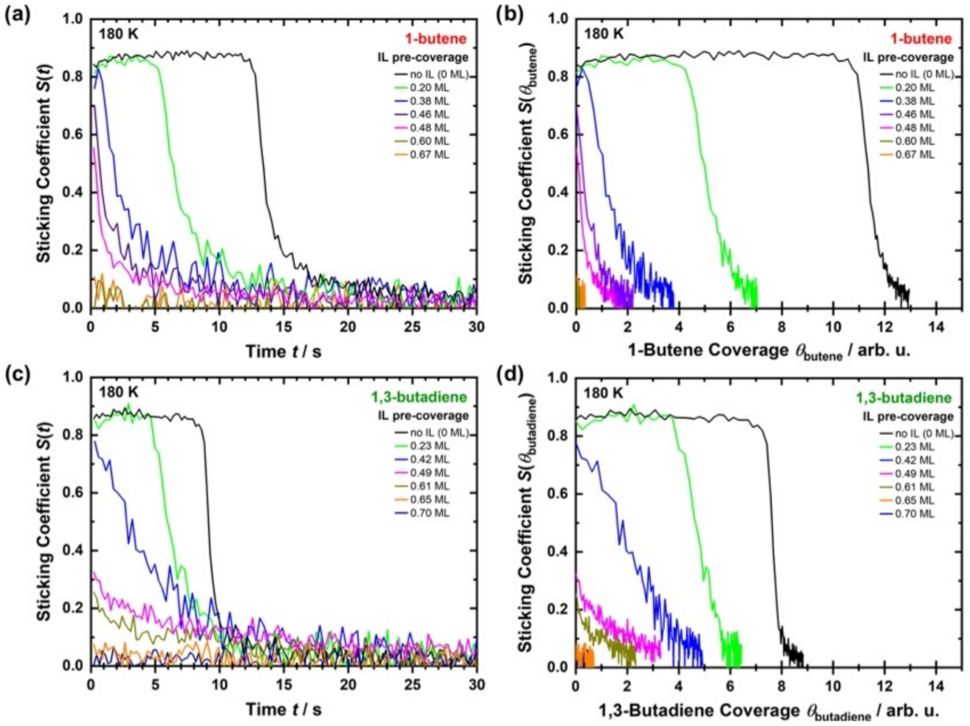

Figure 2. (a) Time-dependent sticking coefficient $S(t)$ and (b) coverage-dependent sticking coefficient $S(\theta_{\text{butene}})$ of 1-butene on Pt(111) with varying IL pre-coverages θ_{IL} at 180 K. (c) Time-dependent sticking coefficient $S(t)$ and (d) coverage-dependent sticking coefficient $S(\theta_{\text{butadiene}})$ of 1,3-butadiene on Pt(111) for different IL pre-coverages θ_{IL} at 180 K.

■ RESULTS AND DISCUSSION

The sticking coefficient, S, describes the probability for an incoming molecule to adsorb on (or stick to) a sample surface. In this work, we used the direct method of King and Wells[34] to measure S of 1-butene and 1,3-butadiene on ionic liquid-modified surfaces. This method is based on following the changes of a quadrupole mass spectrometer (QMS) signal, which is proportional to the partial pressure of the molecule of interest, during a sequence of opening and closing inert flags (also called shutters). Figure 1a shows a sketch of the vertical molecular beam setup together with a representative example for a measurement curve (Figure 1b). At the beginning of the measurement ($t = -40$ s), the beam flag is closed, which blocks the molecular beam in the differential pumping stage, leading to a partial pressure $p = 0$ (after background subtraction). At $t = -30$ s, the beam flag is opened, which allows the molecular beam to enter the analysis chamber. Once there, it is blocked by the inert sample flag, thus leading to a pressure increase Δp_{MB}, caused by the molecules scattered off the sample flag into the chamber background. At $t = 0$ s, the sample flag is also opened, so the molecular beam can hit the sample surface. Adsorption of the gas molecules on the sample surface results in a pressure drop Δp_0 because the molecular beam is no longer scattered back into the chamber background. The initial sticking coefficient is then given by $S_0 = \frac{\Delta p_0}{\Delta p_{\text{MB}}}$. With ongoing time, the coverage of the gas molecules on the sample surface increases, which leads to time-dependent changes in the pressure difference $\Delta p(t)$ and consequently to a time-dependent sticking coefficient $S(t) = \frac{\Delta p(t)}{\Delta p_{\text{MB}}}$. At $t = 210$ s, the sample flag is closed again, so the mass spectrometer signal returns to the level it had between $t = -30$ s and $t = 0$ s. Note that the minor intensity increase visible at $t = 210$ s is an experimental artifact caused by alterations of the cryo-pumping speed of the cooled manipulator, which we attempt to compensate by including a correction term (for details, see the Supporting Information). Finally, the beam flag is closed at $t = 240$ s and the partial pressure returns to zero.

The green curve in Figure 1c shows $S(t)$ for the adsorption of 1,3-butadiene on clean Pt(111) at 180 K, as derived from the measurement shown in Figure 1b. When investigating the adsorption dynamics, it is however more intuitive to analyze the coverage dependency of the sticking coefficient. The absolute coverage Θ_{abs} (given in units of molecules cm^{-2}) adsorbed after a certain time t is given by

$$\Theta_{\text{abs}} = j \int_0^t S(t)\, \mathrm{d}t \tag{4}$$

where j is the flux of the molecular beam (in molecules cm^{-2} s^{-1}). Since measuring absolute values for j with a high accuracy is challenging, we refrain from giving values for Θ_{abs}, but rather will refer to the uncalibrated relative coverage of the corresponding olefin, θ_{olefin}, which will be simply obtained by integrating $S(t)$

$$\theta_{\text{olefin}} = \frac{\Theta_{\text{abs}}}{j} = \int_0^t S(t)\mathrm{d}t \tag{5}$$

The green line in Figure 1d shows the corresponding $S(\theta_{\text{butadiene}})$ curve for the adsorption of 1,3-butadiene on clean Pt(111) at

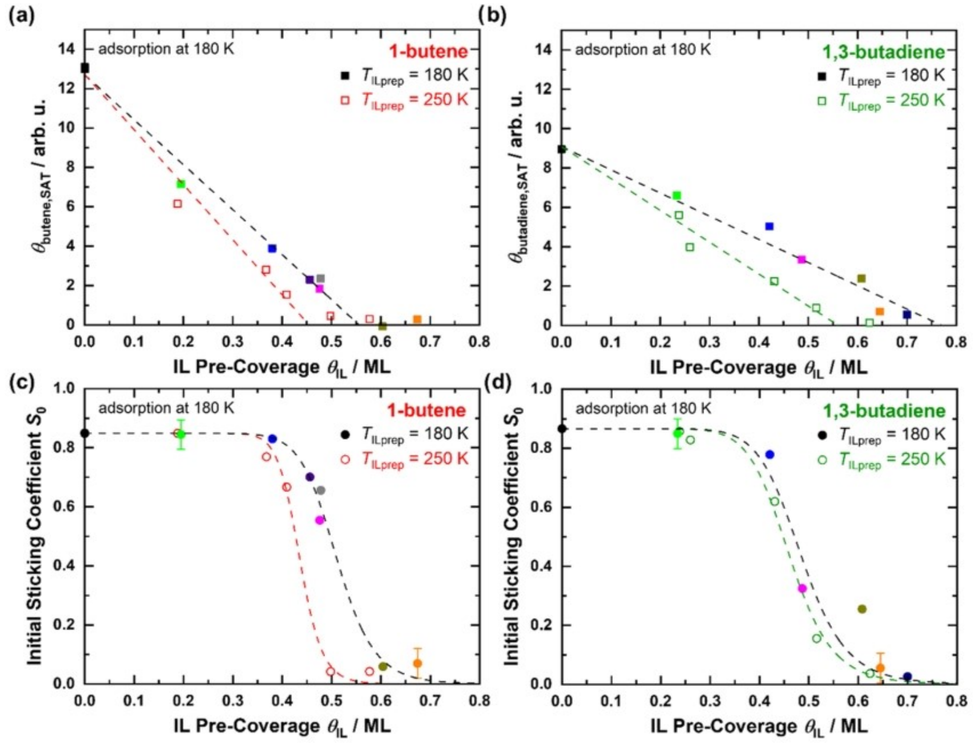

Figure 3. (a) 1-Butene saturation coverage $\theta_{\mathrm{butene,SAT}}$ (determined from the area below the $S(t)$ curve) versus the IL pre-coverage θ_{IL}. (b) 1,3-Butadiene saturation coverage $\theta_{\mathrm{butadiene,SAT}}$ plotted against the IL pre-coverage θ_{IL}. (c, d) The initial sticking coefficients S_0 of 1-butene and 1,3-butadiene versus the IL pre-coverage θ_{IL}. The open symbols refer to IL films prepared at 250 K and closed symbols refer to IL films prepared at 180 K, whose colors match the colors of the curves in Figure 2. In panels (a) and (b), the dashed lines are linear fits to the data (excluding the data points with $\theta_{\mathrm{olefin}} \approx 0$), and in panels (c) and (d), the dashed lines are only supposed to serve as a guide to the eye. In panels (c) and (d), exemplary error bars indicate the estimated uncertainty of ±0.05.

180 K. Initially, $S(\theta_{\mathrm{butadiene}})$ stays constant at ≈ 0.87 until at $\theta_{\mathrm{butadiene}} \approx 8$ it drops and rapidly approaches zero. This behavior is characteristic for adsorption following precursor dynamics.[50] In the precursor model, the incoming molecule is first trapped into a weakly bound precursor state, from which then final chemisorption occurs. With this type of dynamics, the adsorption process remains efficient even if a major fraction of the adsorption sites are occupied because the molecule is quite mobile in the precursor state allowing it to find a still empty site.[50,51]

The red curves in Figure 1c,d show $S(t)$ and $S(\theta_{\mathrm{butene}})$ for the adsorption of 1-butene on clean Pt(111) at 180 K. Also in this case, $S(\theta_{\mathrm{butene}})$ remains constant at ≈ 0.87 until it drops to zero at $\theta_{\mathrm{butene}} \approx 11$. Consequently, also 1-butene shows precursor-mediated adsorption. In contrast to 1,3-butadiene, $S(\theta_{\mathrm{butene}})$ starts to decrease at considerably higher coverages. Although we cannot fully rule out minor differences in the flux j of the 1-butene and 1,3-butadiene molecular beams, we propose that this difference is caused by a higher saturation coverage of the 1-butene monolayer (by a factor of ≈ 1.4) compared to the 1,3-butadiene monolayer on Pt(111) at 180 K. This interpretation is corroborated by our XP spectra recorded after the adsorption experiments (see Figure 1e). The C 1s intensity of the saturated 1-butene layer is by a factor of ≈ 1.3 higher than the one of the 1,3-butadiene layer.

These findings are in line with literature reports: Koel and coworkers[52,53] determined a coverage of 0.15 molecules per surface Pt atom for chemisorbed 1,3-butadiene[52] and a slightly larger value of 0.17 for chemisorbed 1-butene[53] based on calibrated temperature-programmed desorption (TPD) yields. A similar trend was found by Mittendorfer et al.[54] and Valcárcel et al.,[49] who predicted the thermodynamically most favorable adsorption structures depending on temperature and pressure by using density functional theory (DFT) calculations and a thermodynamical model: At 180 K, 1,3-butadiene should adsorb as a *trans*-1,2,3,4-tetra-σ complex in a $p(2 \times 3)$ superstructure, whereas 1-butene should form a 1,2-di-σ complex in the more compressed $p(2 \times 2)$ superstructure, which implies that the coverage of 1-butene is larger by a factor of 1.5 due to a different adsorption geometry requiring less space on the surface; the different adsorbate complexes are schematically indicated in Figure 1e.[49,54,55] The two DFT studies yield 1,3-butadiene adsorption energies of 143[54] and 156 kJ/mol[49] and 1-butene adsorption energies of 72[54] and 83 kJ/mol,[49] that is, 1,3-butadiene is bound by ≈ 70 kJ/mol stronger on Pt(111) than 1-butene.

In order to get insight into the effect of the IL film on the adsorption dynamics of 1,3-butadiene and 1-butene on Pt(111), we recorded $S(t)$ and $S(\theta_{\mathrm{olefin}})$ for different IL pre-coverages θ_{IL} (see Figure 2). The thin IL films were prepared at 180 K, and 1-butene and 1,3-butadiene were adsorbed also at 180 K. For 1-

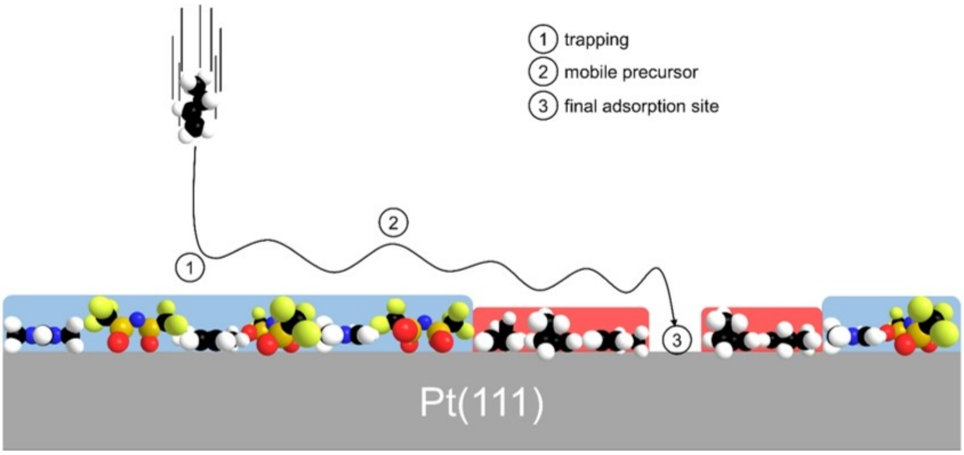

Figure 4. Schematic view of the adsorption process of 1-butene. A 1-butene molecule incoming from the molecular beam is first trapped (1) above the IL island (blue) into a mobile precursor (2). In the mobile precursor state, the molecule can then diffuse to the final adsorption site (3) between 1-butene islands (red).

butene, a low IL pre-coverage of $\theta_{IL} = 0.20$ ML does not change the initial sticking coefficient S_0 (see green curves in Figure 2a,b). Moreover, $S(\theta_{butene})$ stays at the same constant value of ≈ 0.87 until at $\theta_{butene} \approx 5$ it steeply decreases to zero. The overall behavior is very similar to that on clean Pt(111), where $S(\theta_{butene})$ stayed constant until it started to drop at $\theta_{butene} \approx 11$ (black curve in Figure 2b). Increasing θ_{IL} shifts the decrease of the $S(\theta_{butene})$ trace to lower 1-butene coverages (see blue curve), until at $\theta_{IL} > 0.40$ ML also S_0 starts to decrease (purple and magenta curves). For $\theta_{IL} > 0.55$ ML, no significant 1-butene sticking is detectable anymore (dark yellow and orange curves).

1,3-Butadiene adsorption (see Figure 2c,d) shows similar overall trends as 1-butene but also some important differences: At high IL pre-coverages, starting at $\theta_{IL} \approx 0.4$ ML (blue curve), the $S(\theta_{butadiene})$ curves of 1,3-butadiene show a much more shallow decrease with olefin coverage, which yield higher $S(\theta_{olefin})$ values at a given olefin coverage compared to 1-butene (compare blue and magenta curves in Figure 2b,d). The effect is most pronounced for $\theta_{IL} \approx 0.6$ ML (dark yellow curves), where no sticking occurs for 1-butene, but an initial sticking coefficient $S_0 \approx 0.2$ is observed for 1,3-butadiene, which only slowly decays with increasing olefin coverage.

In Figure 3a, the dependence of the 1-butene saturation coverage $\theta_{butene,SAT}$ on the IL pre-coverage θ_{IL} is shown for the IL films prepared at 180 K (full squares). The colors of the symbols directly refer to the $S(t)$ trace in Figure 2a, from which they were determined. $\theta_{butene,SAT}$ displays a linear decrease, until at $\theta_{IL} =$ 0.55 ML the linear fit intercepts the IL coverage axis. This behavior is interpreted as the blocking of 1-butene adsorption sites by the IL, until at $\theta_{IL} = 0.55$ ML the Pt(111) surface is completely covered by ILs. This finding is in line with previous studies from our group, which showed that (1) 1-butene adsorption is not expected at 180 K on pure IL surfaces[56] and (2) ~0.5 ML of IL is needed to wet a metal surface completely.[31] For 1,3-butadiene, a similar linear decrease of $\theta_{butadiene,SAT}$ is observed for increasing θ_{IL} (see Figure 3b, full squares). However in contrast to 1-butene, the linear fit intercepts the axis at higher IL coverages of $\theta_{IL} = 0.75$ ML. This behavior clearly reveals that at IL pre-coverages approaching a closed IL layer, significant adsorption of 1,3-butadiene is still possible, whereas 1-butene adsorption does not take place.

To understand the differences in the behavior observed for the two molecules, we have to consider again what is known about their adsorption properties on Pt(111): (1) due to the two double bonds, the interaction with Pt(111) is significantly stronger (by ≈ 70 kJ/mol) for 1,3-butadiene,[49,54] which represents a larger driving force for adsorption—see above; (2) due to this stronger interaction and the resulting adsorption geometry, the required space per molecule on the surface is larger for 1,3-butadiene than for 1-butene. On the one hand, this leads to the observed lower saturation coverage of the former on the clean surface (see above). On the other hand, at high IL pre-coverages, close to saturation, the larger driving force for adsorption of 1,3-butadiene allows for squeezing in additional molecules in an already densely packed IL layer. This could explain the more shallow decrease of the $S(\theta_{butadiene})$ curves of 1,3-butadiene at high IL pre-coverages in Figure 2d and the higher IL pre-coverages required to completely suppress 1,3-butadiene adsorption compared to 1-butene (Figure 3a versus b). The adsorption of 1,3-butadiene on/into a nominally closed IL layer (that is, for $\theta_{IL} \geq 0.5$ ML) requires rearrangements in the IL film structure, which are obviously less feasible for 1-butene. This is corroborated by our QM/MM results, see below. Very likely this occurs at IL domain boundaries or at dynamically formed vacancies in the IL layer, and could include changes in the adsorption geometry of the IL ions and/or even a replacement to the second layer. One should note here that IL films are comparably dynamic systems. This would also give an explanation for the still significant sticking observed at $\theta_{IL} \approx 0.55$ ML (dark yellow curve in Figure 2d).

Interestingly, the initial sticking coefficient S_0 of 1-butene on IL-covered surfaces is identical to that on the clean Pt(111) surface and stays constant with increasing IL pre-coverage until $\theta_{IL} \approx 0.4$ ML; only thereafter, S_0 decreases to reach a value close to zero at $\theta_{IL} \approx 0.5$ ML, as is evident from Figure 3c; the S-shaped dashed line serves as a guide to the eye. This finding can be understood in the context of the precursor dynamics observed for 1-butene adsorption on Pt(111): It indicates that a mobile precursor does not only exist on 1-butene-covered

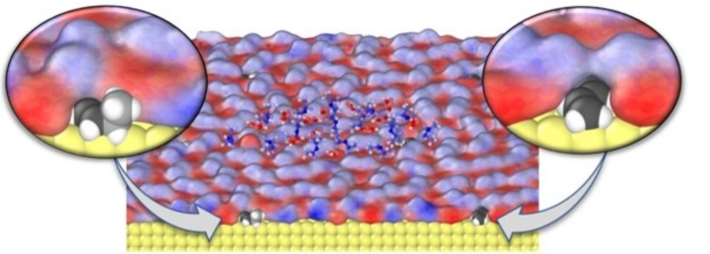

Figure 5. Snapshot from a molecular dynamics simulation with 1-butene and 1,3-butadiene adsorbed on a Pt(111) slab featuring an IL film with a coverage of $\theta_{\mathrm{IL}} = 0.87$ ML. IL ions in direct contact to Pt are shown in a molecular surface representation, while a ball-and-stick representation is used for ions located above the wetting layer. Cations and anions are indicated in red and blue, respectively. White indicates H, dark gray indicates C=C, light gray indicates C−C, and yellow indicates Pt.

areas but also on IL-covered areas. Thus, the weakly bound 1-butene molecules can also diffuse on the IL islands and even cross boundaries of 1-butene- and IL-covered regions to finally arrive and adsorb at an empty adsorption site (see Figure 4). Similarly as for 1-butene, S_0 of 1,3-butadiene also initially stays constant with increasing θ_{IL} (until $\theta_{\mathrm{IL}} \approx 0.3$ ML, see Figure 3d) and only thereafter decreases, which indicates that an equivalent precursor-mediated mechanism is active for 1,3-butadiene on top of IL islands.

To achieve atomic-level insights into the interplay of differently dense IL films and 1,3-butadiene versus 1-butene adsorption, we performed molecular dynamics simulations. Figure 5 illustrates one of the starting points, namely, the Pt slab decorated by three 1,3-butadiene and three 1-butene molecules and an IL film corresponding to a coverage of $\theta_{\mathrm{IL}} = 0.87$ ML. The snapshot clearly shows a compact layer of IL in direct contact to Pt atoms, while excess IL is forming a patch on top of the wetting layer. Upon removal of (a) all 1,3-butadiene or (b) all 1-butene molecules and subsequent relaxation of the IL film, we sampled the energy difference $\Delta E_{\text{IL-relaxation}}$ stemming from IL film rearrangements. This is taken as the negative of the energy cost of IL film penetration upon adsorption of olefin molecules on Pt(111)—see also eq 2.

As expected for low IL coverages, only very minor energy changes were observed for the relaxation of 0.22−0.54 ML films. At higher IL coverage, this picture changes as the energy cost of IL film penetration rises and finally exceeds the energy of the olefin−Pt interactions (see Figure 6 and also Table S5 in the Supporting Information). Strikingly, such tipping points are found at different IL coverages of $\theta_{\mathrm{IL}} \approx 0.64$ ML and $\theta_{\mathrm{IL}} \approx 0.79$ ML for 1-butene and 1,3-butadiene adsorption, respectively. In other terms, near $\theta_{\mathrm{IL}} \approx 0.6$ ML, our molecular dynamics simulations show that the mechanical work related to IL film densification accounts for a squeeze-out of 1-butene while still permitting 1,3-butadiene adsorption.

Since in real SCILL applications, reactions between the catalytically active metal and the IL often cannot be ruled out, we also performed an additional set of experiments, for which we prepared thin IL films at 250 K and measured S_0 and the saturation coverage $\theta_{\text{olefin,SAT}}$ for 1-butene and 1,3-butadiene at 180 K. These measurements were motivated by a very recent XPS and scanning tunneling microscopy (STM) investigation of the limited thermal stability of $[\mathrm{C_1C_1Im}][\mathrm{Tf_2N}]$ on Pt(111) by our group.[57] This study shows that below 200 K, the IL is adsorbed intact on the surface. However, between 200 and 400 K, a reaction of the IL ions in contact with Pt(111) occurs. Thereby, the $[\mathrm{Tf_2N}]^-$ anion partially decomposes and desorbs (with the degree of desorption depending on temperature), as is deduced from the decrease of anion XPS signals. In contrast, no major changes of cation-related signals occur in this temperature range. As charge neutrality has to be maintained, we assume that

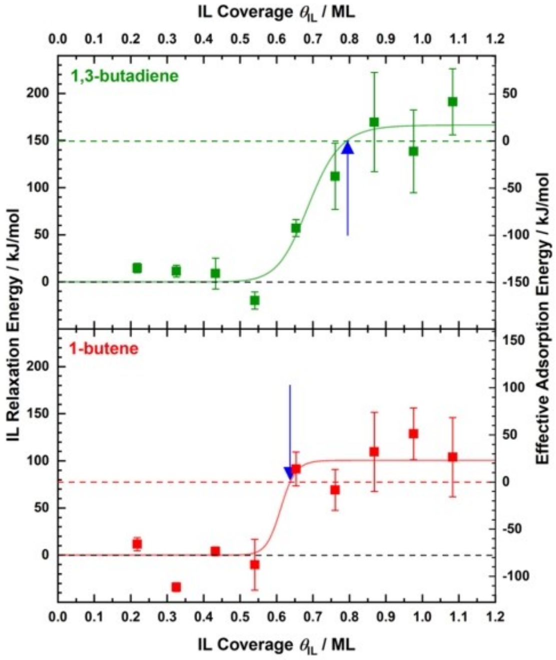

Figure 6. Relaxation energies (i.e., the negative of the film penetration energy) of the IL films upon release of 1,3-butadiene (top panel, green) and 1-butene (bottom panel, red) as functions of IL coverage. The adsorption energies stemming from the olefin−Pt(111) interactions are indicated by green and red dashed lines giving the zero point for the effective adsorption energy indicated on the right axis. Two independent runs were performed for each system, and the difference of the corresponding IL film relaxation energies are used as indicators for the error margins to our sampling procedure. The effective olefin adsorption energy is dominated by the olefin−Pt interactions at low IL coverage, whereas the film rearrangement is decisive at high IL coverage. The green and red solid curves are drawn as a guide to the eye. The blue arrows highlight the tipping points for which the mechanical work of IL film penetration exceeds the olefin−Pt interaction energies. Within the regime of ≈ 0.64−0.79 ML, we find 1-butene adsorption endothermic, whereas 1,3-butadiene adsorption is still exothermic.

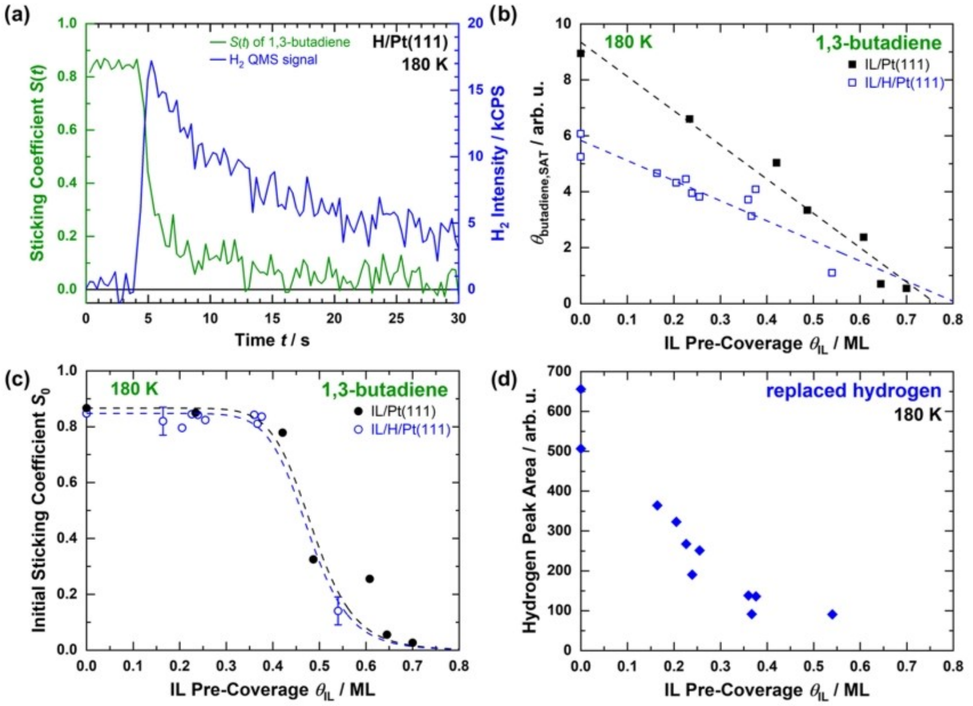

Figure 7. (a) Time-dependent sticking coefficient $S(t)$ of 1,3-butadiene on a hydrogen-saturated Pt(111) surface plotted together with the $m/z = 2$ signal corresponding to the amount of desorbing H_2. (b) 1,3-Butadiene saturation coverage $\theta_{\text{butadiene,SAT}}$ (determined from the area below the $S(t)$ curve) versus the IL pre-coverage θ_{IL} for a hydrogen-saturated Pt(111) surface (open blue squares) in comparison with the experiments on the hydrogen-free surface already shown in Figures 2 and 3 (filled black squares). The dashed lines are linear fits to the data. (c) Initial sticking coefficient S_0 of 1,3-butadiene plotted versus the IL pre-coverage θ_{IL} for the hydrogen-saturated surface (open blue circles) and the hydrogen-free surface (filled black circles). The dashed lines should serve as a guide to the eye, and the exemplary error bars illustrate the estimated uncertainty of ±0.05. (d) Amount of hydrogen replaced from the hydrogen-saturated surface during the 1,3-butadiene adsorption.

the cation also reacts with the Pt(111) surface forming charge neutral decomposition products that remain at the surface.

The saturation coverage of 1-butene adsorption on IL films prepared at 250 K shows a linear decrease with increasing θ_{IL} (red open squares in Figure 3a); however, the intercept of the fit with the IL coverage axis now is observed at a smaller IL pre-coverage of $\theta_{\text{IL}} = 0.45$ ML (instead of 0.55 ML found for the IL layer prepared at 180 K). For IL wetting layers at 250 K, XPS shows that the thermal decomposition reaction with the Pt(111) surface has started, as concluded from a decrease of the anion signals by 20% (as compared to 200 K), with the cation signals remaining unchanged.[57] Thus, a possible explanation for the observed lower saturation coverage is that the remaining decomposition products of the ongoing reaction require more space on the surface than the intact IL layer so that less material is needed to block all adsorption sites. A similar behavior is observed for 1,3-butadiene (green open squares in Figure 3b), for which $\theta_{\text{butadiene,SAT}}$ decreases linearly until reaching the intercept with the IL coverage axis at $\theta_{\text{IL}} = 0.55$ ML (instead of 0.75 ML found for the IL layer prepared at 180 K). A shift is also seen for the dependence of the initial sticking coefficients on IL pre-coverage in Figure 3c,d: For the IL films prepared at 250 K, S_0 decreases at lower IL pre-coverages than for the IL films prepared at 180 K but still follows the same overall trend. These observations indicate that the changes in the surface composition do not affect the precursor dynamics in a major way.

To mimic the reaction conditions of the hydrogenation reaction of 1,3-butadiene to 1-butene, we also studied the adsorption dynamics of 1,3-butadiene on a Pt(111) surface saturated with hydrogen, which adsorbs dissociatively on Pt(111).[58] In Figure 7a, the sticking coefficient $S(t)$ is plotted versus time along with the hydrogen evolution from the sample surface. Initially, the sticking coefficient of 1,3-butadiene stays constant at ≈ 0.87, very similar to the observation on clean Pt(111). After about 4 s, $S(t)$ starts to strongly decrease to reach a value of ≈ 0.10 after 10 s (green curve). Notably, on the clean Pt(111) surface, the decrease of $S(t)$ only started after 10 s (see Figure 2c, black curve). This behavior indicates that the hydrogen pre-coverage lowers the adsorption capacity of the Pt(111) surface. Most interestingly, simultaneously to the sharp decrease of the sticking coefficient, a sharp onset of hydrogen evolution into the gas phase is observed (Figure 7a, blue curve). This result suggests that initially a low 1,3-butadiene coverage can be coadsorbed with the saturated hydrogen layer. If this coverage exceeds a certain value, 1,3-butadiene replaces hydrogen from the surface. From the fact that the replacement does not start right away, we conclude that initially the adsorption of 1,3-butadiene only leads to a denser packing of the hydrogen atoms on the surface until the situation gets too crowded and the hydrogen atoms recombine to desorb as H_2 from the surface. Our measurement also indicates that the hydrogen is not replaced completely, because the final 1,3-butadiene coverage is only about 63% of the one on clean

Pt(111) (see Figure 7b). This might be due to the fact that the replacement effect becomes exceedingly slow at higher coverages.

In a next step, we addressed the adsorption dynamics of 1,3-butadiene on the $[C_1C_1Im][Tf_2N]/Pt(111)$ system with coadsorbed hydrogen. On clean Pt(111), H_2 showed an initial sticking coefficient between 0.02 and 0.08. Surprisingly, no H_2 sticking ($S_0 < 0.01$) was measurable on the $[C_1C_1Im][Tf_2N]/Pt(111)$ surface, even for the smallest tested IL coverage of 0.19 ML. On Pt surfaces, the initial sticking coefficient of H_2 was found to scale with the step density, reaching a very low value of ∼0.025 for the Pt(111) surface.[59] A possible explanation for the absence of a measurable sticking coefficient on the IL-modified Pt(111) surface is that the remaining steps and defect sites on the Pt(111) surface are all decorated by IL ion pairs and thereby passivated, even for low θ_{IL}.

To study the adsorption dynamics of 1,3-butadiene on the Pt(111) surface with coadsorbed IL and hydrogen, we thus reversed the deposition sequence: The Pt(111) surface is first saturated with hydrogen, then the IL is evaporated onto this H/Pt(111) surface at 180 K, and in a third step 1,3-butadiene is offered via the molecular beam. The coadsorbed hydrogen does not have a significant effect on S_0 of 1,3-butadiene, as is evident from Figure 7c, where the initial sticking coefficient is plotted versus IL pre-coverage for clean and H-pre-covered Pt(111). While the behavior of S_0 follows a very similar trend as on the hydrogen-free surface, the 1,3-butadiene saturation coverage $\theta_{\text{butadiene,SAT}}$ is decreased by about 37% by the preadsorbed hydrogen, as is evident from Figure 7b. Interestingly, it still shows an approximately linear decrease, and 0.75 ML of IL are required to block all adsorption sites, similar to the behavior on the hydrogen-free surface. By integration of the $m/z = 2$ signal, we can also determine the amount of hydrogen replaced by incoming 1,3-butadiene (see Figure 7d), which is found to decrease with increasing θ_{IL}.

■ CONCLUSIONS

The adsorption of 1,3-butadiene and 1-butene on Pt(111) at 180 K occurs in a precursor-mediated fashion with an initial sticking coefficient $S_0 \approx 0.87$. With increasing coverage, $S(\theta_{\text{olefin}})$ of both molecules remains unchanged until it drops rapidly to zero shortly before the saturation is reached. The larger saturation coverage of 1-butene compared to 1,3-butadiene is attributed to the weaker interaction of 1-butene via one double bond compared to 1,3-butadiene via two double bonds with the Pt(111) surface (difference in $E_{\text{ads}} \approx 70$ kJ/mol)[49,54] and the resulting more space-demanding adsorption geometry of the latter, in line with the literature.[49,52−54]

Preadsorbing the IL $[C_1C_1Im][Tf_2N]$ on the Pt(111) surface to mimic a SCILL catalyst changes the adsorption characteristics: The olefin saturation coverage $\theta_{\text{olefin,SAT}}$ decreases linearly with increasing θ_{IL}, which indicates that the IL blocks the olefin adsorption sites. The precursor dynamics are still prevailing on the IL-modified Pt(111) surface, that is, S_0 stays at ≈ 0.87 and only starts to drop when the Pt(111) surface is almost fully covered by IL.

For IL films prepared at 180 K, $\theta_{IL} > 0.55$ ML is required to prevent 1-butene adsorption, but $\theta_{IL} > 0.75$ ML is needed to prevent 1,3-butadiene adsorption. This behavior is attributed to the larger adsorption energy of 1,3-butadiene compared to 1-butene, which presents a larger driving force for adsorption of 1,3-butadiene, enabling to squeeze in additional 1,3-butadiene molecules in an already densely packed IL layer and/or reorient or replace them to the second layer. For IL films prepared at 250 K, partial decomposition occurs, with partial desorption of the anion fragments, while the cation fragments remain on the surface.[57] The resulting layers seem to block a larger fraction of the surface, as is concluded from smaller amounts of deposited ILs needed to block the surface for hydrocarbon adsorption.

1,3-Butadiene adsorption on H-pre-covered Pt(111) reveals partial replacement of hydrogen from the surface and results in a lower saturation coverage while still following precursor dynamics. Notably, the same IL pre-coverage as on the hydrogen-free surface is needed to block all adsorption sites. The pronounced precursor dynamics, which are in play on the IL-modified metal surface, provide a possible explanation how the reactants can reach the catalytically active sites, challenging the often assumed dissolution and diffusion of reactants inside of IL films.

One compelling observation is the preference for 1,3-butadiene adsorption at around 0.5−0.7 ML IL pre-coverage, where the IL layer is assumed to fully cover the surface. This behavior is deduced from the lower saturation coverage of 1-butene compared to 1,3-butadiene. It is explained by our QM/MM results, which show that in the higher IL coverage regime of 0.6−0.8 ML (around IL film saturation coverage), the mechanical work related to IL film densification still permits 1,3-butadiene adsorption while accounting for a squeeze-out of 1-butene. We believe that our model study on a single-crystal surface can be seen in the context of the test catalytic studies of selective 1,3-butadiene hydrogenation by the Jess group,[11] which showed that there is an ideal IL loading, which was interpreted to correspond to a closed layer of IL ion pairs. While our study focused on the Pt(111) surface, we expect that a similar effect may also be found on other transition-metal surfaces such as Pd(111), for which DFT calculations showed similar preference for 1,3-butadiene binding over 1-butene binding.[49,54]

■ ASSOCIATED CONTENT

Supporting Information

The Supporting Information is available free of charge at https://pubs.acs.org/doi/10.1021/acscatal.3c02126.

Additional details about necessary treatment procedures for the experimental data and the parametrization used for the molecular dynamics simulations (PDF)

■ AUTHOR INFORMATION

Corresponding Authors

Cynthia C. Fernández − *Lehrstuhl für Physikalische Chemie II, Friedrich-Alexander-Universität Erlangen-Nürnberg, 91058 Erlangen, Germany;* orcid.org/0000-0002-2722-5395; Email: cynthia.carolina.fernandez@fau.de

Hans-Peter Steinrück − *Lehrstuhl für Physikalische Chemie II, Friedrich-Alexander-Universität Erlangen-Nürnberg, 91058 Erlangen, Germany;* orcid.org/0000-0003-1347-8962; Email: hans-peter.steinrueck@fau.de

Authors

Leonhard Winter − *Lehrstuhl für Physikalische Chemie II, Friedrich-Alexander-Universität Erlangen-Nürnberg, 91058 Erlangen, Germany*

Simon Trzeciak − *Lehrstuhl für Theoretische Chemie, CCC, Friedrich-Alexander-Universität Erlangen-Nürnberg, 91052 Erlangen, Germany*

Stephen Massicot − *Lehrstuhl für Physikalische Chemie II, Friedrich-Alexander-Universität Erlangen-Nürnberg, 91058 Erlangen, Germany;* orcid.org/0000-0002-2530-8015
Timo Talwar − *Lehrstuhl für Physikalische Chemie II, Friedrich-Alexander-Universität Erlangen-Nürnberg, 91058 Erlangen, Germany*
Florian Maier − *Lehrstuhl für Physikalische Chemie II, Friedrich-Alexander-Universität Erlangen-Nürnberg, 91058 Erlangen, Germany;* orcid.org/0000-0001-9725-8961
Dirk Zahn − *Lehrstuhl für Theoretische Chemie, CCC, Friedrich-Alexander-Universität Erlangen-Nürnberg, 91052 Erlangen, Germany*

Complete contact information is available at:
https://pubs.acs.org/10.1021/acscatal.3c02126

Notes

The authors declare no competing financial interest.

■ ACKNOWLEDGMENTS

The authors thank Dr. Nicola Taccardi for providing us with an ultrapure sample of [C$_1$C$_1$Im][Tf$_2$N], Afra Gezmis, and Dr. Christian Papp for fruitful discussions. They acknowledge funding by the Deutsche Forschungsgemeinschaft (DFG, German Research Foundation) Project-ID 431791331−SFB 1452 (CLINT, Catalysis at Liquid Interfaces). C.C.F. thanks the Alexander von Humboldt foundation for a Humboldt Research Fellowship for Postdocs.

■ REFERENCES

(1) Geilen, F. M. A.; Stochniol, G.; Peitz, S.; Schulte-Koerne, E. Butenes. In *Ullmann's Encyclopedia of Industrial Chemistry*; Wiley-VCH, 2014 DOI: 10.1002/14356007.a04_483.pub3.

(2) Selvakannan, P. R.; Hoang, L.; Kumar, V. V.; Dumbre, D.; Jampaiah, D.; Das, J.; Bhargava, S. K. Selective Hydrogenation of 1,3-Butadiene to 1-Butene: Review on Catalysts, Selectivity, Kinetics and Reaction Mechanism. In *Catalysis for Clean Energy and Environmental Stability - Petrochemicals and Refining Processes*; Pant, K. K.; Gupta, S. K.; Ahmad, E., Eds.; Springer Nature Switzerland, 2021; Vol. 2, pp 205−228.

(3) Zhang, L.; Zhou, M.; Wang, A.; Zhang, T. Selective Hydrogenation over Supported Metal Catalysts: From Nanoparticles to Single Atoms. *Chem. Rev.* **2020**, *120*, 683−733.

(4) Zaera, F. The Surface Chemistry of Metal-Based Hydrogenation Catalysis. *ACS Catal.* **2017**, *7*, 4947−4967.

(5) Goetz, J.; Murzin, D. Y.; Touroude, R. A. Kinetic Aspects of Selectivity and Stereoselectivity for the Hydrogenation of Buta-1,3-diene over a Palladium Catalyst. *Ind. Eng. Chem. Res.* **1996**, *35*, 703−711.

(6) Castillejos-López, E.; Agostini, G.; Di Michel, M.; Iglesias-Juez, A.; Bachiller-Baeza, B. Synergy of Contact between ZnO Surface Planes and PdZn Nanostructures: Morphology and Chemical Property Effects in the Intermetallic Sites for Selective 1,3-Butadiene Hydrogenation. *ACS Catal.* **2017**, *7*, 796−811.

(7) (a) Furlong, B. K.; Hightower, J. W.; Chan, T. Y.-L.; Sarkany, A.; Guczi, L. 1,3-Butadiene Selective Hydrogenation over Pd/Alumina and CuPd/Alumina Catalysts. *Appl. Catal. A* **1994**, *117*, 41−51. (b) Yang, Q.; Hou, R.; Sun, K. Tuning Butene Selectivities by Cu Modification on Pd-Based Catalyst for the Selective Hydrogenation of 1,3-Butadiene. *J. Catal.* **2019**, *374*, 12−23.

(8) Cooper, A.; Bachiller-Baeza, B.; Anderson, J. A.; Rodríguez-Ramos, I.; Guerrero-Ruiz, A. Design of Surface Sites for the Selective Hydrogenation of 1,3-Butadiene on Pd Nanoparticles: Cu Bimetallic Formation and Sulfur Poisoning. *Catal. Sci. Technol.* **2014**, *4*, 1446−1455.

(9) Yan, H.; Cheng, H.; Yi, H.; Lin, Y.; Yao, T.; Wang, C.; Li, J.; Wei, S.; Lu, J. Single-Atom Pd$_1$/Graphene Catalyst Achieved by Atomic Layer Deposition: Remarkable Performance in Selective Hydrogenation of 1,3-Butadiene. *J. Am. Chem. Soc.* **2015**, *137*, 10484−10487.

(10) Barth, T. Selektivhydrierung von 1,3-Butadien an mit ionischen Fluiden beschichteten heterogenen Katalysatoren, PhD Thesis; Universität Bayreuth, 2016.

(11) Barth, T.; Korth, W.; Jess, A. Selectivity-Enhancing Effect of a SCILL Catalyst in Butadiene Hydrogenation. *Chem. Eng. Technol.* **2017**, *40*, 395−404.

(12) (a) Yoon, C.; Yang, M. X.; Somorjai, G. A. Hydrogenation of 1,3-Butadiene on Platinum Surfaces of Different Structures. *Catal. Lett.* **1997**, *46*, 37−41. (b) Hu, C.; Shao, M.; Xiang, M.; Li, S.; Xu, S. The Role of Hydrogen Coverage and Location in 1,3-Butadiene Hydrogenation over Pt/SiO$_2$. *React. Chem. Eng.* **2020**, *5*, 87−100.

(13) Wang, Y.; Wang, M.; Mou, X.; Wang, S.; Jiang, X.; Chen, Z.; Jiang, Z.; Lin, R.; Ding, Y. Host-Induced Alteration of the Neighbors of Single Platinum Atoms Enables Selective and Stable Hydrogenation of Butadiene. *Nanoscale* **2022**, *14*, 10506−10513.

(14) Lucci, F. R.; Liu, J.; Marcinkowski, M. D.; Yang, M.; Allard, L. F.; Flytzani-Stephanopoulos, M.; Sykes, E. C. H. Selective Hydrogenation of 1,3-Butadiene on Platinum-Copper Alloys at the Single-Atom Limit. *Nat. Commun.* **2015**, *6*, No. 8550.

(15) Jugnet, Y.; Sedrati, R.; Bertolini, J. C. Selective Hydrogenation of 1,3-Butadiene on Pt$_3$Sn(111) Alloys: Comparison to Pt(111). *J. Catal.* **2005**, *229*, 252−258.

(16) (a) Jalal, A.; Uzun, A. An Ordinary Nickel Catalyst Becomes Completely Selective for Partial Hydrogenation of 1,3-Butadiene when Coated with Tributyl(methyl) phosphonium methyl sulfate. *Appl. Catal. A* **2018**, *562*, 321−326. (b) Jalal, A.; Uzun, A. An Exceptional Selectivity for Partial Hydrogenation on a Supported Nickel Catalyst Coated with [BMIM][BF$_4$]. *J. Catal.* **2017**, *350*, 86−96.

(17) Chen, Z.; Guo, L.; Wang, Y.; Mou, X.; Chen, Z.; Lin, R.; Ding, Y. Carbonaceous Deposits on Cobalt Particles Reverse the Catalytic Patterns in Butadiene Hydrogenation. *Catal. Sci. Technol.* **2023**, *13*, 968−974.

(18) Yardimci, D.; Serna, P.; Gates, B. C. A Highly Selective Catalyst for Partial Hydrogenation of 1,3-Butadiene: MgO-Supported Rhodium Clusters Selectively Poisoned with CO. *ChemCatChem* **2012**, *4*, 1547−1550.

(19) Wang, M.; Yue, Y.; Wang, Y.; Mou, X.; Chang, R.; Chen, Z.; Lin, R.; Zhao, J.; Ding, Y. Selective Hydrogenation of 1,3-Butadiene on Iridium Nanostructures: Structure Sensitivity, Host Effect, and Deactivation Mechanism. *J. Energy Chem.* **2022**, *69*, 541−554.

(20) Liu, W.; Morfin, F.; Provost, K.; Bahri, M.; Baaziz, W.; Ersen, O.; Piccolo, L.; Zlotea, C. Unveiling the Ir Single Atoms as Selective Active Species for the Partial Hydrogenation of Butadiene by *operando* XAS. *Nanoscale* **2022**, *14*, 7641−7649.

(21) Piccolo, L.; Chatelier, C.; De Weerd, M.-C.; Morfin, F.; Ledieu, J.; Fournée, V.; Gille, P.; Gaudry, E. Catalytic Properties of Al$_{13}$TM$_4$ Complex Intermetallics: Influence of the Transition Metal and the Surface Orientation on Butadiene Hydrogenation. *Sci. Technol. Adv. Mater.* **2019**, *20*, 557−567.

(22) Totarella, G.; Beerthuis, R.; Masoud, N.; Louis, C.; Delannoy, L.; de Jongh, P. E. Supported Cu Nanoparticles as Selective and Stable Catalysts for the Gas Phase Hydrogenation of 1,3-Butadiene in Alkene-Rich Feeds. *J. Phys. Chem. C* **2021**, *125*, 366−375.

(23) Hugon, A.; Delannoy, L.; Louis, C. Supported Gold Catalysts for Selective Hydrogenation of 1,3-Butadiene in the Presence of an Excess of Alkenes. *Gold Bull.* **2008**, *41*, 127−138.

(24) Zhang, X.; Shi, H.; Xu, B.-Q. Catalysis by Gold: Isolated Surface Au^{3+} Ions are Active Sites for Selective Hydrogenation of 1,3-Butadiene over Au/ZrO$_2$ Catalysts. *Angew. Chem., Int. Ed.* **2005**, *44*, 7132−7135.

(25) Kolli, N. E.; Delannoy, L.; Louis, C. Bimetallic Au-Pd Catalysts for Selective Hydrogenation of Butadiene: Influence of the Preparation Method on Catalytic Properties. *J. Catal.* **2013**, *297*, 79−92.

(26) Bachiller-Baeza, B.; Iglesias-Juez, A.; Castillejos-López, E.; Guerrero-Ruiz, A.; Di Michiel, M.; Fernández-García, M.; Rodríguez-Ramos, I. Detecting the Genesis of a High-Performance Carbon-Supported Pd Sulfide Nanophase and its Evolution in the Hydrogenation of Butadiene. *ACS Catal.* **2015**, *5*, 5235−5241.

(27) Kernchen, U.; Etzold, B.; Korth, W.; Jess, A. Solid Catalyst with Ionic Liquid Layer (SCILL) - A New Concept to Improve Selectivity Illustrated by Hydrogenation of Cyclooctadiene. *Chem. Eng. Technol.* **2007**, *30*, 985−994.

(28) (a) Korth, W.; Jess, A. Solid Catalyst with Ionic Liquid Layer (SCILL). In *Supported Ionic Liquids*; Fehrmann, R.; Riisager, A.; Haumann, M., Eds.; Wiley-VCH, 2014; pp 279−306. (b) Steinrück, H.-P.; Wasserscheid, P. Ionic Liquids in Catalysis. *Catal. Lett.* **2015**, *145*, 380−397. (c) Bartlewicz, O.; Dąbek, I.; Szymańska, A.; Maciejewski, H. Heterogeneous Catalysis with the Participation of Ionic Liquids. *Catalysts* **2020**, *10*, 1227.

(29) (a) Wasserscheid, P.; Welton, T. *Ionic Liquids in Synthesis*; Wiley-VCH, 2003. (b) MacFarlane, D. R.; Kar, M.; Pringle, J. M. *Fundamentals of Ionic Liquids*; Wiley-VCH, 2017.

(30) (a) Sobota, M.; Happel, M.; Amende, M.; Paape, N.; Wasserscheid, P.; Laurin, M.; Libuda, J. Ligand Effects in SCILL Model Systems: Site-Specific Interactions with Pt and Pd Nanoparticles. *Adv. Mater.* **2011**, *23*, 2617−2621. (b) Arras, J.; Paki, E.; Roth, C.; Radnik, J.; Lucas, M.; Claus, P. How a Supported Metal Is Influenced by an Ionic Liquid: In-Depth Characterization of SCILL-Type Palladium Catalysts and Their Hydrogen Adsorption. *J. Phys. Chem. C* **2010**, *114*, 10520−10526. (c) Naicker, L.; Schörner, M.; Kremitzl, D.; Friedrich, H. B.; Haumann, M.; Wasserscheid, P. Influencing the Product Distribution in Citral Hydrogenation Using Ionic Liquid Modified Cu Catalysts. *ChemCatChem* **2022**, *14*, No. e202200388.

(31) Lexow, M.; Maier, F.; Steinrück, H.-P. Ultrathin Ionic Liquid Films on Metal Surfaces: Adsorption, Growth, Stability and Exchange Phenomena. *Adv. Phys. X* **2020**, *5*, No. 1761266.

(32) Cremer, T.; Killian, M.; Gottfried, J. M.; Paape, N.; Wasserscheid, P.; Maier, F.; Steinrück, H.-P. Physical Vapor Deposition of [EMIM][Tf_2N]: A New Approach to the Modification of Surface Properties with Ultrathin Ionic Liquid Films. *ChemPhysChem* **2008**, *9*, 2185−2190.

(33) Souda, R. Glass-Liquid Transition, Crystallization, and Melting of a Room Temperature Ionic Liquid: Thin Films of 1-Ethyl-3-methylimidazolium Bis[trifluoromethanesulfonyl]imide Studied with TOF-SIMS. *J. Phys. Chem. B* **2008**, *112*, 15349−15354.

(34) King, D. A.; Wells, M. G. Molecular Beam Investigation of Adsorption Kinetics on Bulk Metal Targets - Nitrogen on Tungsten. *Surf. Sci.* **1972**, *29*, 454−482.

(35) Winter, L.; Bhuin, R. G.; Lexow, M.; Maier, F.; Steinrück, H.-P. On the Adsorption of *n*-Butane on Alkyl Imidazolium Ionic Liquids with Different Anions using a New Molecular Beam Setup. *J. Chem. Phys.* **2020**, *153*, No. 214706.

(36) Lovelock, K. R. J.; Kolbeck, C.; Cremer, T.; Paape, N.; Schulz, P. S.; Wasserscheid, P.; Maier, F.; Steinrück, H.-P. Influence of Different Substituents on the Surface Composition of Ionic Liquids Studied using ARXPS. *J. Phys. Chem. B* **2009**, *113*, 2854−2864.

(37) Lexow, M.; Heller, B. S. J.; Maier, F.; Steinrück, H.-P. Anion Exchange at the Liquid/Solid Interface of Ultrathin Ionic Liquid Films on Ag(111). *ChemPhysChem* **2018**, *19*, 2978−2984.

(38) Cremer, T.; Stark, M.; Deyko, A.; Steinrück, H.-P.; Maier, F. Liquid/Solid Interface of Ultrathin Ionic Liquid Films: [C_1C_1lm]-[Tf_2N] and [C_8C_1Im][Tf_2N] on Au(111). *Langmuir* **2011**, *27*, 3662−3671.

(39) (a) Rietzler, F.; Nagengast, J.; Steinrück, H.-P.; Maier, F. Interface of Ionic Liquids and Carbon: Ultrathin [C_1C_1Im][Tf_2N] Films on Graphite and Graphene. *J. Phys. Chem. C* **2015**, *119*, 28068−28076. (b) Cremer, T.; Wibmer, L.; Krick Calderón, S.; Deyko, A.; Maier, F.; Steinrück, H.-P. Interfaces of Ionic Liquids and Transition Metal Surfaces - Adsorption, Growth, and Thermal Reactions of Ultrathin [C_1C_1Im][Tf_2N] Films on Metallic and Oxidised Ni(111) Surfaces. *Phys. Chem. Chem. Phys.* **2012**, *14*, 5153−5163. (c) Lexow, M.; Talwar, T.; Heller, B. S. J.; May, B.; Bhuin, R. G.; Maier, F.; Steinrück, H.-P. Time-dependent Changes in the Growth of Ultrathin Ionic Liquid Films on Ag(111). *Phys. Chem. Chem. Phys.* **2018**, *20*, 12929−12938.

(40) Meusel, M.; Lexow, M.; Gezmis, A.; Schötz, S.; Wagner, M.; Bayer, A.; Maier, F.; Steinrück, H.-P. Atomic Force and Scanning Tunneling Microscopy of Ordered Ionic Liquid Wetting Layers from 110 K up to Room Temperature. *ACS Nano* **2020**, *14*, 9000−9010.

(41) Linstrom, P. J.; Mallard, W. G.; NIST Mass Spectrometry Data Center. W. E. Wallace, director. Mass Spectra *NIST Chemistry WebBook, NIST Standard Reference Database Number 69*, National Institute of Standards and Technology 2023 https://webbook.nist.gov/cgi/cbook.cgi?ID=C106990&Units=SI&Mask=200#Mass-Spec.

(42) Hamza, A. V.; Steinrück, H.-P.; Madix, R. J. Activation of *n*-Butane with Translational Energy on Ir(110)-(1×2). *J. Chem. Phys.* **1986**, *85*, 7494−7495.

(43) Kneitz, S. Adsorptions- und Streumessungen von CO an ultradünnen Metallschichtsystemen mittels eines Überschalldüsen-Molekularstrahls, PhD Thesis; Bayerische Julius-Maximilians-Universität: Würzburg, 1998.

(44) Thompson, A. P.; Aktulga, H. M.; Berger, R.; Bolintineanu, D. S.; Brown, W. M.; Crozier, P. S.; in't Veld, P. J.; Kohlmeyer, A.; Moore, S. G.; Nguyen, T. D.; Shan, R.; Stevens, M. J.; Tranchida, J.; Trott, C.; Plimpton, S. J. LAMMPS - a Flexible Simulation Tool for Particle-Based Materials Modeling at the Atomic, Meso, and Continuum Scales. *Comput. Phys. Commun.* **2022**, *271*, No. 108171.

(45) Hockney, R. W.; Eastwood, J. W. *Computer Simulation Using Particles*; CRC Press, 1988.

(46) Hu, Z. Infinite Boundary Terms of Ewald Sums and Pairwise Interactions for Electrostatics in Bulk and at Interfaces. *J. Chem. Theory Comput.* **2014**, *10*, 5254−5264.

(47) Case, D. A.; Aktulga, H. M.; Belfon, K.; Ben-Shalom, I. Y.; Berryman, J. T.; Brozell, S. R.; Cerutti, D. S.; Cheatham, T. E., III; Cisneros, G. A.; Cruzeiro, V. W. D.; Darden, T. A.; Forouzesh, N.; Giambaşu, G.; Giese, T.; Gilson, M. K.; Gohlke, H.; Götz, A. W.; Harris, J.; Izadi, S.; Izmailov, S. A.; Kasavajhala, K.; Kaymak, M. C.; King, E.; Kovalenko, A.; Kurtzman, T.; Lee, T. S.; Li, P.; Lin, C.; Liu, J.; Luchko, T.; Luo, R.; Machado, M.; Man, V.; Manathunga, M.; Merz, K. M.; Miao, Y.; Mikhailovskii, O.; Monard, G.; Nguyen, H.; O'Hearn, K. A.; Onufriev, A.; Pan, F.; Pantano, S.; Qi, R.; Rahnamoun, A.; Roe, D. R.; Roitberg, A.; Sagui, C.; Schott-Verdugo, S.; Shajan, A.; Shen, J.; Simmerling, C. L.; Skrynnikov, N. R.; Smith, J.; Swails, J.; Walker, R. C.; Wang, J.; Wang, J.; Wei, H.; Wu, X.; Wu, Y.; Xiong, Y.; Xue, Y.; York, D. M.; Zhao, S.; Zhu, Q.; Kollman, P. A. *Amber 2023*; University of California: San Francisco, 2023.

(48) Heinz, H.; Vaia, R. A.; Farmer, B. L.; Naik, R. R. Accurate Simulation of Surfaces and Interfaces of Face-Centered Cubic Metals Using 12-6 and 9-6 Lennard-Jones Potentials. *J. Phys. Chem. C* **2008**, *112*, 17281−17290.

(49) Valcárcel, A.; Clotet, A.; Ricart, J. M.; Delbecq, F.; Sautet, P. Comparative DFT Study of the Adsorption of 1,3-Butadiene, 1-Butene and 2-cis/trans-Butenes on the Pt(111) and Pd(111) Surfaces. *Surf. Sci.* **2004**, *549*, 121−133.

(50) (a) Kolasinski, K. W. *Surface Science - Foundations of Catalysis and Nanoscience*; John Wiley & Sons Ltd, 2012; pp 207−210. (b) Kisliuk, P. The Sticking Probabilities of Gases Chemisorbed on the Surfaces of Solids. *J. Phys. Chem. Solids* **1957**, *3*, 95−101.

(51) Taylor, J. B.; Langmuir, I. The Evaporation of Atoms, Ions and Electrons from Caesium Films on Tungsten. *Phys. Rev.* **1933**, *44*, 423−458.

(52) Zhao, H.; Koel, B. E. Adsorption and Reaction of 1,3-Butadiene on Pt(111) and Sn/Pt(111) Surface Alloys. *Surf. Sci.* **2004**, *572*, 261−268.

(53) Tsai, Y.-L.; Koel, B. E. Temperature-Programmed Desorption Investigation of the Adsorption and Reaction of Butene Isomers on Pt(111) and Ordered Pt-Sn Surface Alloys. *J. Phys. Chem. B* **1997**, *101*, 2895−2906.

(54) Mittendorfer, F.; Thomazeau, C.; Raybaud, P.; Toulhoat, H. Adsorption of Unsaturated Hydrocarbons on Pd(111) and Pt(111): A DFT Study. *J. Phys. Chem. B* **2003**, *107*, 12287−12295.

(55) Gautier, S.; Steinmann, S. N.; Michel, C.; Fleurat-Lessard, P.; Sautet, P. Molecular Adsorption at Pt(111). How Accurate are DFT Functionals? *Phys. Chem. Chem. Phys.* **2015**, *17*, 28921−28930.

(56) Winter, L.; Bhuin, R. G.; Maier, F.; Steinrück, H.-P. *n*-Butane, *iso*-Butane and 1-Butene Adsorption on Imidazolium-Based Ionic Liquids Studied with Molecular Beam Techniques. *Chem.− Eur. J.* **2021**, *27*, 17059−17065.

(57) Massicot, S.; Gezmis, A.; Talwar, T.; Meusel, M.; Jaekel, S.; Adhikari, R.; Winter, L.; Fernández, C. C.; Bayer, A.; Maier, F.; Steinrück, H.-P. Adsorption and Thermal Evolution of [C_1C_1Im]-[Tf_2N] on Pt(111) *Phys. Chem. Chem. Phys.* 2023.

(58) (a) Christmann, K.; Ertl, G.; Pignet, T. Adsorption of Hydrogen on a Pt(111) Surface. *Surf. Sci.* **1976**, *54*, 365−392. (b) Christmann, K. Interaction of Hydrogen with Solid Surfaces. *Surf. Sci. Rep.* **1988**, *9*, 1−163.

(59) Auras, S. V.; van Lent, R.; Bashlakov, D.; Piñeiros Bastidas, J. M.; Roorda, T.; Spierenburg, R.; Juurlink, L. B. F. Scaling Platinum-Catalyzed Hydrogen Dissociation on Corrugated Surfaces. *Angew. Chem., Int. Ed.* **2020**, *59*, 20973−20979.

Supporting Information

Tailoring the Selectivity of 1,3-Butadiene versus 1-Butene Adsorption on Pt(111) by Ultrathin Ionic Liquid Films

Leonhard Winter[1, ORCID: 0000-0001-9733-1444], *Simon Trzeciak*[2, ORCID: 0000-0001-8883-3362],
Cynthia C. Fernández[1, *, ORCID: 0000-0002-2722-5395], *Stephen Massicot*[1, ORCID: 0000-0002-2530-8015],
Timo Talwar[1, ORCID: 0009-0002-1373-6108], *Florian Maier*[1, ORCID: 0000-0001-9725-8961],
Dirk Zahn[2, ORCID: 0000-0002-4303-3422], *and Hans-Peter Steinrück*[1, *, ORCID: 0000-0003-1347-8962]

[1] *Lehrstuhl für Physikalische Chemie II, Friedrich-Alexander-Universität Erlangen-Nürnberg,*
Egerlandstraße 3, 91058 Erlangen, Germany

[2] *Lehrstuhl für Theoretische Chemie, CCC, Friedrich-Alexander-Universität Erlangen-Nürnberg,*
Nägelsbachstraße 25, 91052 Erlangen, Germany

*cynthia.carolina.fernandez@fau.de, *hans-peter.steinrueck@fau.de

Correction for non-constant pumping speed

The method of King and Wells is based on the assumption that the partial pressure in the chamber background is proportional to the flux of molecules scattered from the sample flag or the sample itself. This assumption requires a constant pumping speed for the molecule of interest, which is not exactly fulfilled due to the tendency of 1,3-butadiene and 1-butene to adsorb on the chamber walls and especially on cooled parts of the cryostat. For that reason, we adapted a correction procedure originally proposed by Stefan Kneitz,[1] which is described in the following.

The inside of the chamber is modelled by a set of surfaces *s*, on which adsorption and from which desorption of the olefins can occur. Each of the surfaces *s* is associated with a specific desorption probability $\lambda_{D,s}$, maximum adsorption probability $\lambda_{A,s,max}$ and a saturation coverage $B_{s,max}$. In a time interval *i* (= one datapoint of the mass spectrometer signal), $H_{s,i}$ represents the coverage of molecules on the surface *s*. So the amount of molecules $D_{s,i}$ desorbing from the surface *s* in the time interval *i* is given by:

$$D_{s,i} = H_{s,i} \cdot \lambda_{D,s}$$

The adsorption probability $\lambda_{A,s,i}$ of the surface s in the time interval i drops with increasing $H_{s,i}$:

$$\lambda_{A,s,i} = \lambda_{A,s,max}\left(1 - \frac{H_{s,i}}{B_{s,max}}\right)$$

The amount of adsorbing molecules $A_{s,i}$ depends on the partial pressure in the chamber background given by the mass spectrometer signal M_i:

$$A_{s,i} = M_i \cdot \lambda_{A,s,i} = M_i \cdot \lambda_{A,s,max}\left(1 - \frac{H_{s,i}}{B_{s,max}}\right)$$

In the next time interval i+1 a new coverage $H_{s,i+1}$ has built up on the surface:

$$H_{s,i+1} = H_{s,i} - D_{s,i} + A_{s,i} = H_{s,i}\left(1 - \lambda_{D,s} - \frac{M_i \cdot \lambda_{A,s,max}}{B_{s,max}}\right) + M_i \cdot \lambda_{A,s,max}$$

With this equation the coverage on the surface can be iteratively determined knowing the coverage in the previous time interval, the measured mass spectrometer signal and the characteristic parameters of the surface.

Empirically, it was found that three surfaces s are needed to model the interior of the UHV chamber. The total adsorption to the chamber walls A_i in the interval i is then given by:

$$A_i = A_{1,i} + A_{2,i} + A_{3,i}$$

and the total desorption from the chamber walls D_i by:

$$D_i = D_{1,i} + D_{2,i} + D_{3,i}$$

With this, the mass spectrometer signal M_i measured in the time interval i can be corrected. The corrected signal C_i shows only the effects of scattering and adsorption on the sample surface, excluding excess adsorption and desorption effects on the chamber walls:

$$C_i = M_i + A_{1,i} + A_{2,i} + A_{3,i} - D_{1,i} - D_{2,i} - D_{3,i}$$

$$C_i = M_i\left(1 + \sum_{s=1}^{3} \lambda_{A,s,max}\left(1 - \frac{H_{s,i}}{B_{s,max}}\right)\right) - \sum_{s=1}^{3} H_{s,i} \cdot \lambda_{D,s}$$

The nine parameters $\lambda_{D,s}$, $\lambda_{A,s,max}$ and $B_{s,max}$ have to be found empirically for each measurement. To simplify the procedure, we constrained $\lambda_{D,1} = 0$, $\lambda_{D,2} = 0.0001$ and $\lambda_{D,3} = 0.01$. For the other six variables, suitable parameters have to be found for each individual measurement, depending on the type of gas used and the chamber history. The main criteria are that the corrected signal should have the same constant value when the beam flag is closed ($t < -30$ s and $t > 240$ s) and another constant value during the time the sample flag is closed ($t = -30$ to 0 s, $t = 120$ to 150 s and $t = 210$ to 240 s). Figure S1 shows the original measured data in comparison with the corrected data.

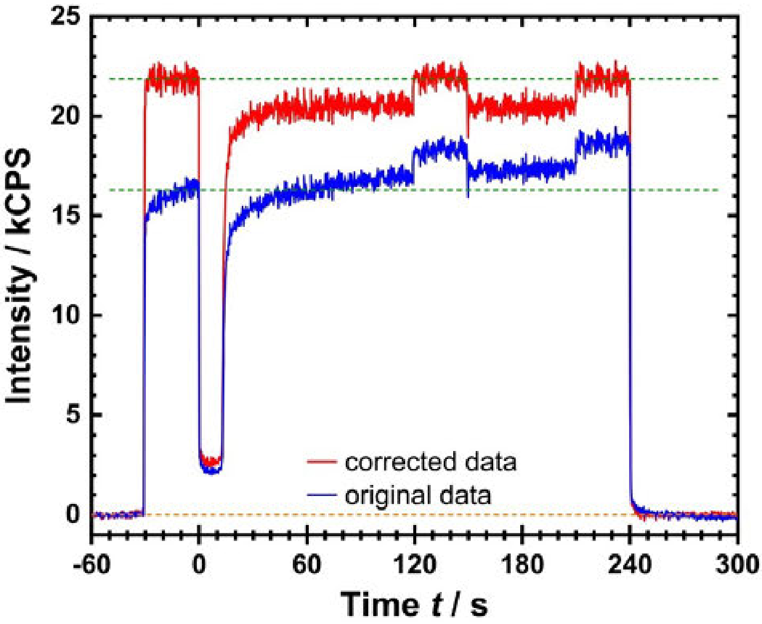

Figure S1: Comparison of the original (blue) and the corrected (red) data. The green (orange) dashed line indicates the criteria of a common constant signal during all times the sample flag (the beam flag) is closed, to which the parameter set was empirically optimized. The presented example shows the adsorption of 1-butene on clean Pt(111) at 180 K.

Empirically, we found that opening and closing of the sample flag also leads to alterations in the cryo pumping speed of the manipulator. These instantaneous change in the pumping speed causes an experimental artifact, which corresponds to an apparent sticking coefficient of approximately 0.05. Therefore, we correct the apparent sticking coefficients determined from the ratio of $\Delta p(t)$ and Δp_{MB}, using the same procedure as in previous publications:[2]

$$S(t)_{corr} = \frac{S(t)_{apparent} - 0.05}{0.95} = \frac{\Delta p(t) - 0.05\,\Delta p_{MB}}{0.95\,\Delta p_{MB}}$$

Molecular Dynamics Simulations

$[Tf_2N]^-$ model

The underlying Lennard-Jones parameters and partial charges are given in Table S1.

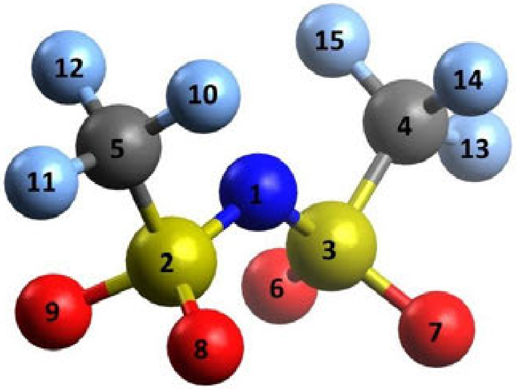

Table S1: Interaction parameters and partial charges of $[Tf_2N]^-$:

Atom Number	Element	Partial Charge / e	ε / kcal/mol	σ /Å
1	N	-0.75894	0.094	3.384
2	S	+1.14184	0.282	3.532
3	S	+1.14184	0.282	3.532
4	C	+0.35524	0.108	3.398
5	C	+0.35524	0.108	3.398
6	O	-0.58754	0.146	3.048
7	O	-0.58754	0.146	3.048
8	O	-0.58754	0.146	3.048
9	O	-0.58754	0.146	3.048
10	F	-0.14751	0.083	3.034
11	F	-0.14751	0.083	3.034
12	F	-0.14751	0.083	3.034
13	F	-0.14751	0.083	3.034
14	F	-0.14751	0.083	3.034
15	F	-0.14751	0.083	3.034

$[C_1C_1Im]^+$ model

The underlying Lennard-Jones parameters and partial charges are given in Table S2.

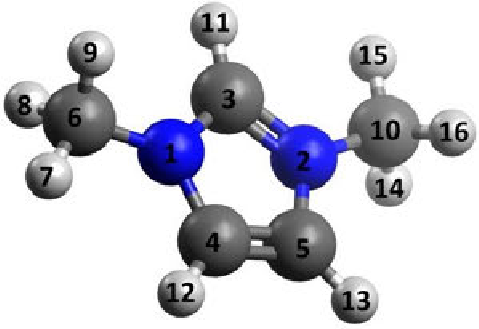

Table S2: Interaction parameters and partial charges of $[C_1C_1Im]^+$:

Atom Number	Element	Partial Charge / e	ε / kcal/mol	σ / Å
1	N	+0.173	0.204	3.206
2	N	+0.173	0.204	3.206
3	C	-0.066	0.099	3.315
4	C	-0.207	0.099	3.315
5	C	-0.207	0.099	3.315
6	C	-0.347	0.108	3.398
7	H	0.175	0.021	2.422
8	H	0.175	0.021	2.422
9	H	0.175	0.021	2.422
10	C	-0.347	0.108	3.398
11	H	0.250	0.016	2.447
12	H	0.263	0.016	2.536
13	H	0.263	0.016	2.536
14	H	0.175	0.021	2.422
15	H	0.175	0.021	2.422
16	H	0.175	0.021	2.422

1,3-Butadiene model

The underlying Lennard-Jones parameters and partial charges are given in Table S3.

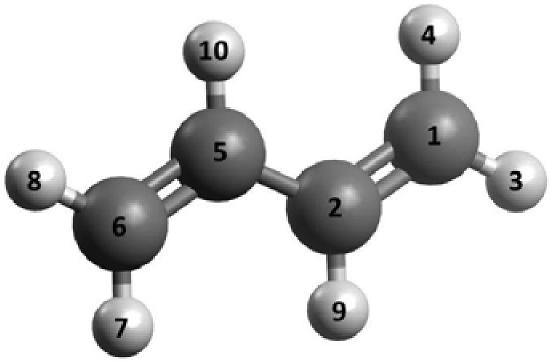

Table S3: Interaction parameters and partial charges of 1,3-butadiene:

Atom Number	Element	Partial Charge / e	ε / kcal/mol	σ / Å
1	C	-0.483	0.099	3.315
2	C	-0.046	0.099	3.315
3	H	+0.195	0.016	2.625
4	H	+0.195	0.016	2.625
5	C	-0.046	0.099	3.315
6	C	-0.483	0.099	3.315
7	H	+0.195	0.016	2.625
8	H	+0.195	0.016	2.625
9	H	+0.139	0.016	2.625
10	H	+0.139	0.016	2.625

1-Butene model

The underlying Lennard-Jones parameters and partial charges are given in Table S4.

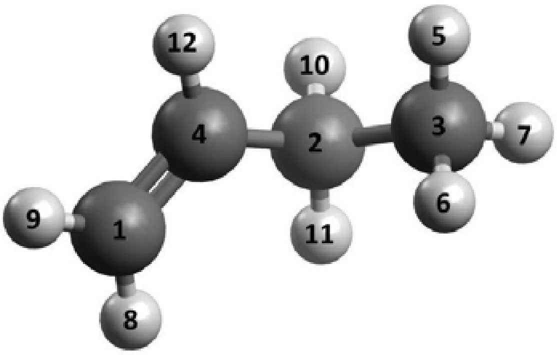

Table S4: Interaction parameters and partial charges of 1-butene:

Atom Number	Element	Partial Charge / e	ε / kcal/mol	σ / Å
1	C	-0.489	0.099	3.315
2	C	+0.205	0.108	3.398
3	C	-0.199	0.108	3.398
4	C	-0.172	0.099	3.315
5	H	+0.047	0.021	2.600
6	H	+0.047	0.021	2.600
7	H	+0.047	0.021	2.600
8	H	+0.198	0.016	2.625
9	H	+0.198	0.016	2.625
10	H	-0.012	0.021	2.600
11	H	-0.012	0.021	2.600
12	H	+0.140	0.016	2.625

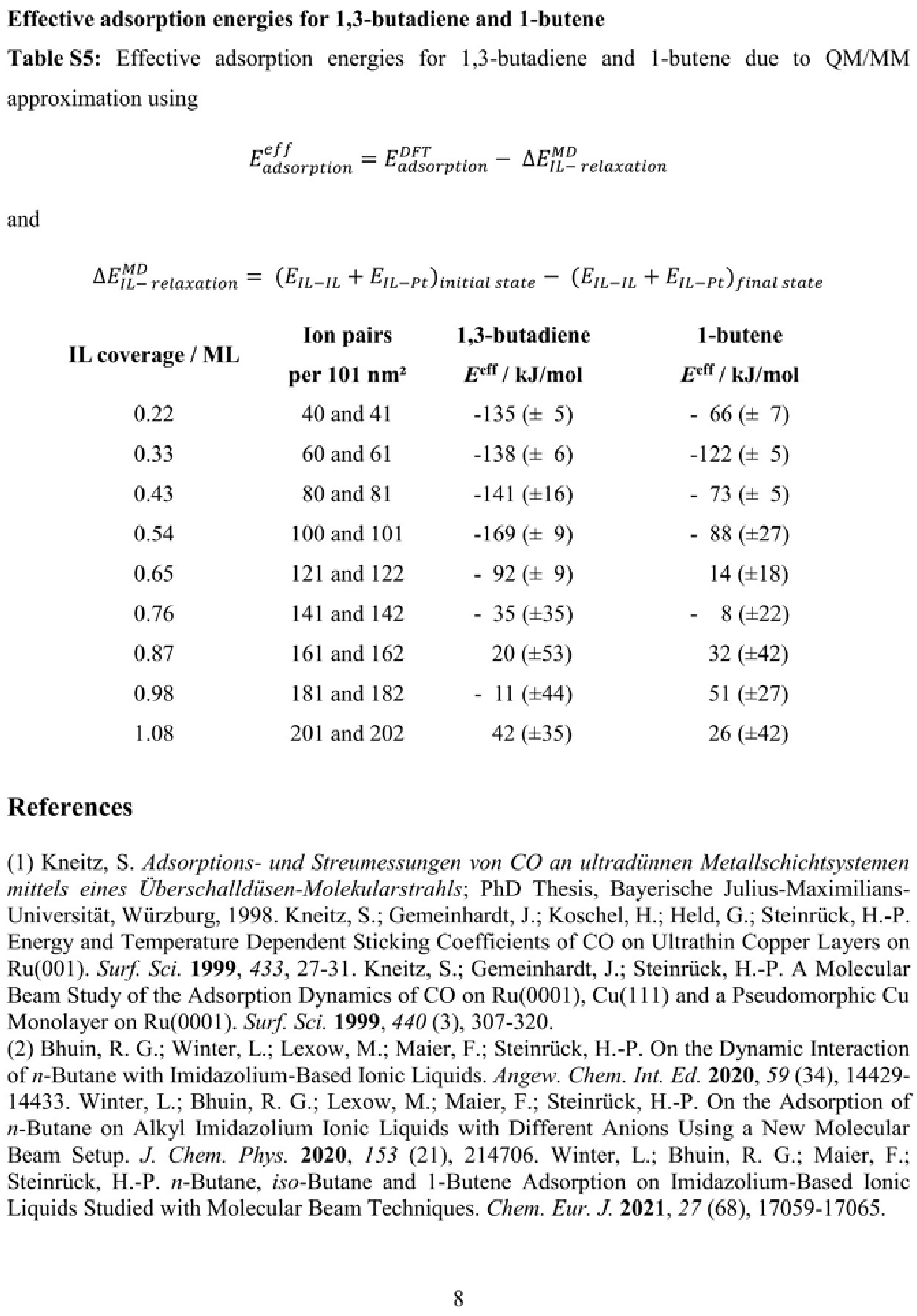

Effective adsorption energies for 1,3-butadiene and 1-butene

Table S5: Effective adsorption energies for 1,3-butadiene and 1-butene due to QM/MM approximation using

$$E^{eff}_{adsorption} = E^{DFT}_{adsorption} - \Delta E^{MD}_{IL-relaxation}$$

and

$$\Delta E^{MD}_{IL-relaxation} = (E_{IL-IL} + E_{IL-Pt})_{initial\,state} - (E_{IL-IL} + E_{IL-Pt})_{final\,state}$$

IL coverage / ML	Ion pairs per 101 nm²	1,3-butadiene E^{eff} / kJ/mol	1-butene E^{eff} / kJ/mol
0.22	40 and 41	-135 (± 5)	- 66 (± 7)
0.33	60 and 61	-138 (± 6)	-122 (± 5)
0.43	80 and 81	-141 (±16)	- 73 (± 5)
0.54	100 and 101	-169 (± 9)	- 88 (±27)
0.65	121 and 122	- 92 (± 9)	14 (±18)
0.76	141 and 142	- 35 (±35)	- 8 (±22)
0.87	161 and 162	20 (±53)	32 (±42)
0.98	181 and 182	- 11 (±44)	51 (±27)
1.08	201 and 202	42 (±35)	26 (±42)

References

(1) Kneitz, S. *Adsorptions- und Streumessungen von CO an ultradünnen Metallschichtsystemen mittels eines Überschalldüsen-Molekularstrahls*; PhD Thesis, Bayerische Julius-Maximilians-Universität, Würzburg, 1998. Kneitz, S.; Gemeinhardt, J.; Koschel, H.; Held, G.; Steinrück, H.-P. Energy and Temperature Dependent Sticking Coefficients of CO on Ultrathin Copper Layers on Ru(001). *Surf. Sci.* **1999**, *433*, 27-31. Kneitz, S.; Gemeinhardt, J.; Steinrück, H.-P. A Molecular Beam Study of the Adsorption Dynamics of CO on Ru(0001), Cu(111) and a Pseudomorphic Cu Monolayer on Ru(0001). *Surf. Sci.* **1999**, *440* (3), 307-320.

(2) Bhuin, R. G.; Winter, L.; Lexow, M.; Maier, F.; Steinrück, H.-P. On the Dynamic Interaction of *n*-Butane with Imidazolium-Based Ionic Liquids. *Angew. Chem. Int. Ed.* **2020**, *59* (34), 14429-14433. Winter, L.; Bhuin, R. G.; Lexow, M.; Maier, F.; Steinrück, H.-P. On the Adsorption of *n*-Butane on Alkyl Imidazolium Ionic Liquids with Different Anions Using a New Molecular Beam Setup. *J. Chem. Phys.* **2020**, *153* (21), 214706. Winter, L.; Bhuin, R. G.; Maier, F.; Steinrück, H.-P. *n*-Butane, *iso*-Butane and 1-Butene Adsorption on Imidazolium-Based Ionic Liquids Studied with Molecular Beam Techniques. *Chem. Eur. J.* **2021**, *27* (68), 17059-17065.

8.5 Technical Drawings and Tables of the ILID Chamber

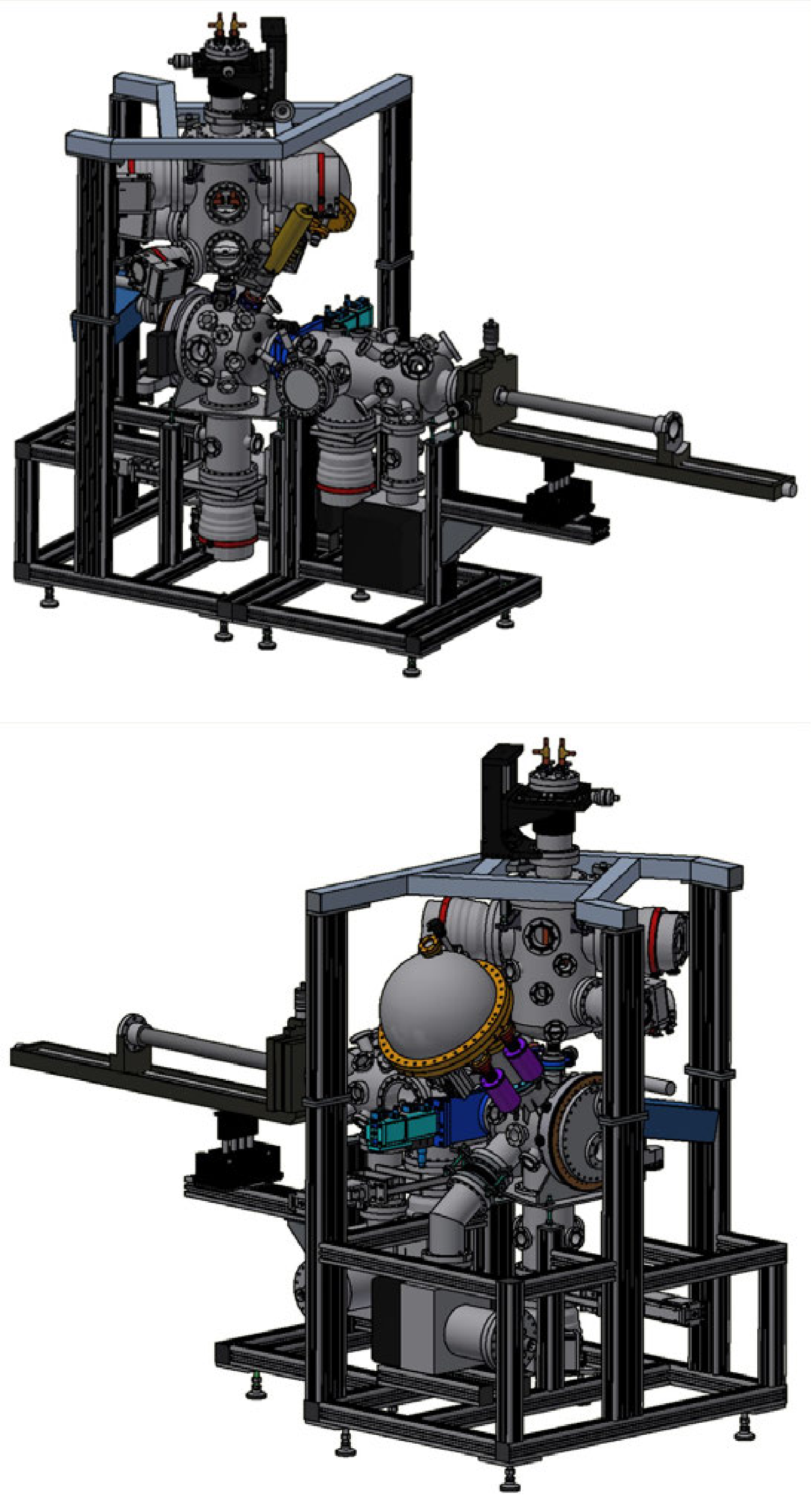

Figure 8.1: Drawing of the complete apparatus, view from two sides. Drawing by Bernd Kreß.

8.5.1 Preparation Chamber

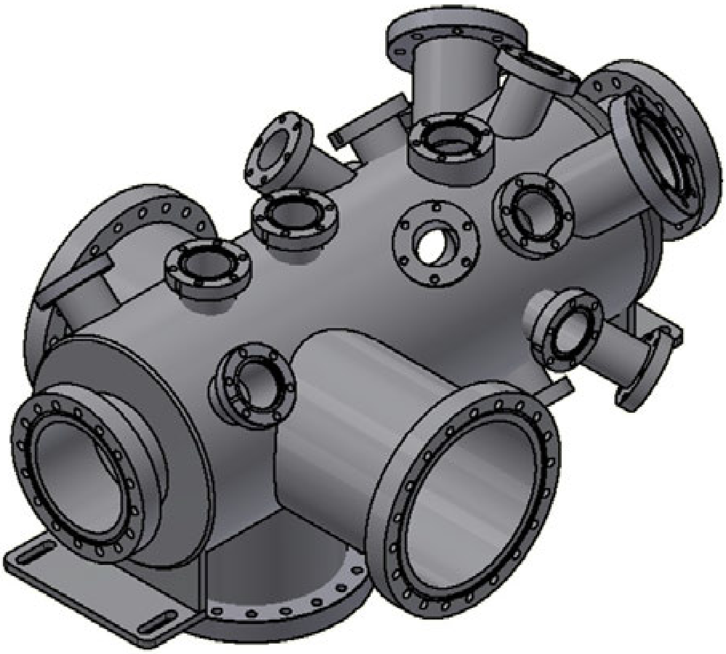

Figure 8.2: 3D drawing of the preparation chamber. Drawing by Bernd Kreß.

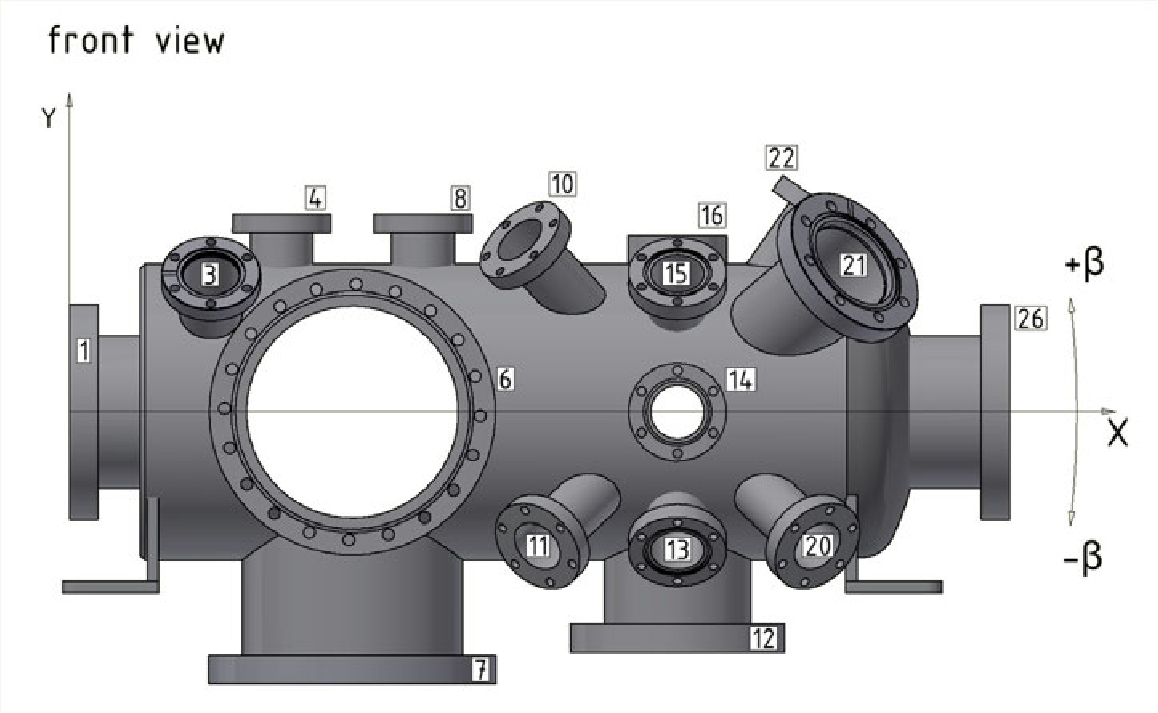

Figure 8.3: Front view of the preparation chamber. The numbers in the white boxes indicate the IDs of the flanges (see Table 8.1). Drawing by Bernd Kreß.

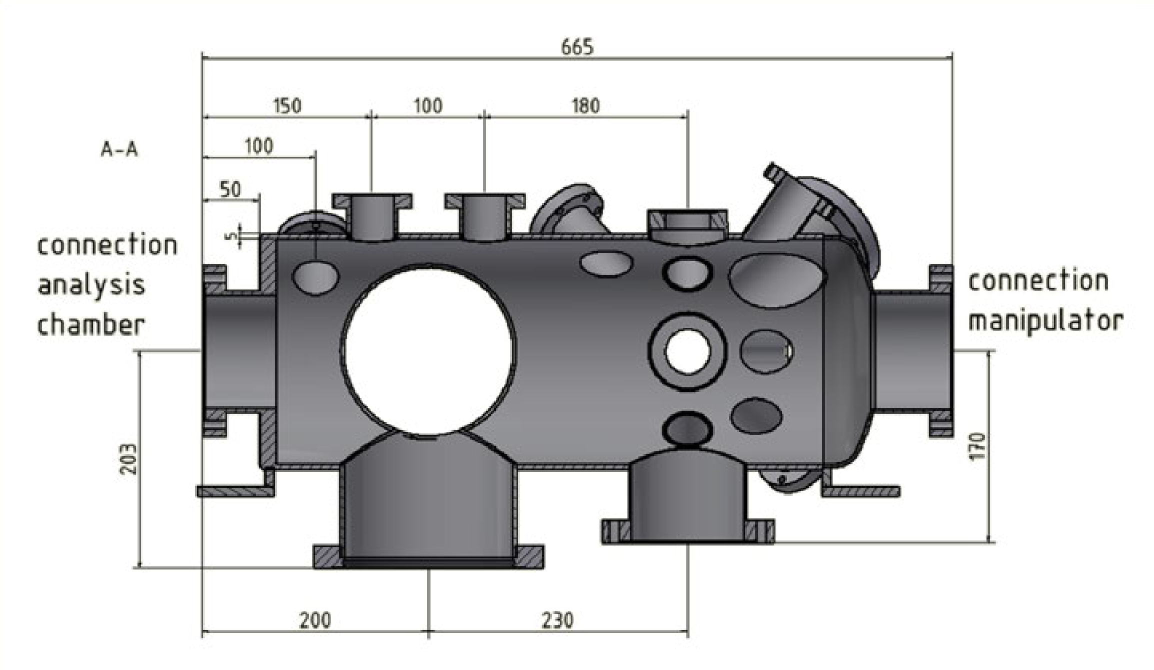

Figure 8.4: Sectional view of the preparation chamber. Dimensions are given in millimeters. Drawing by Bernd Kreß.

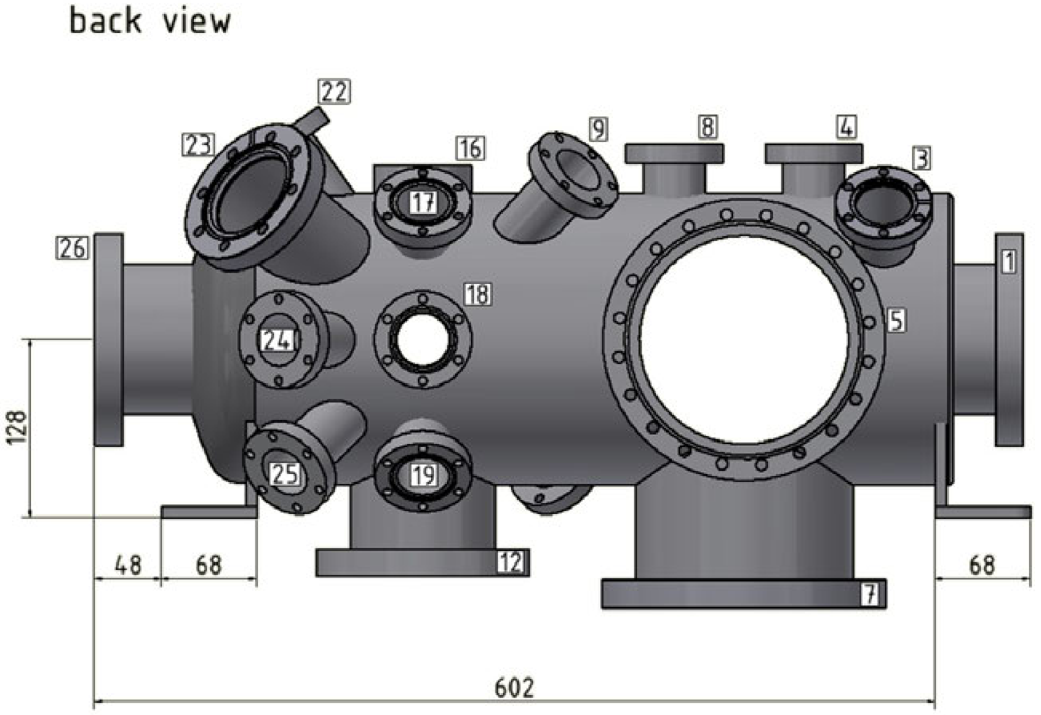

Figure 8.5: Back view of the preparation chamber. The numbers in the white boxes indicate the IDs of the flanges (see Table 8.1). Dimensions are given in millimeters. Drawing by Bernd Kreß.

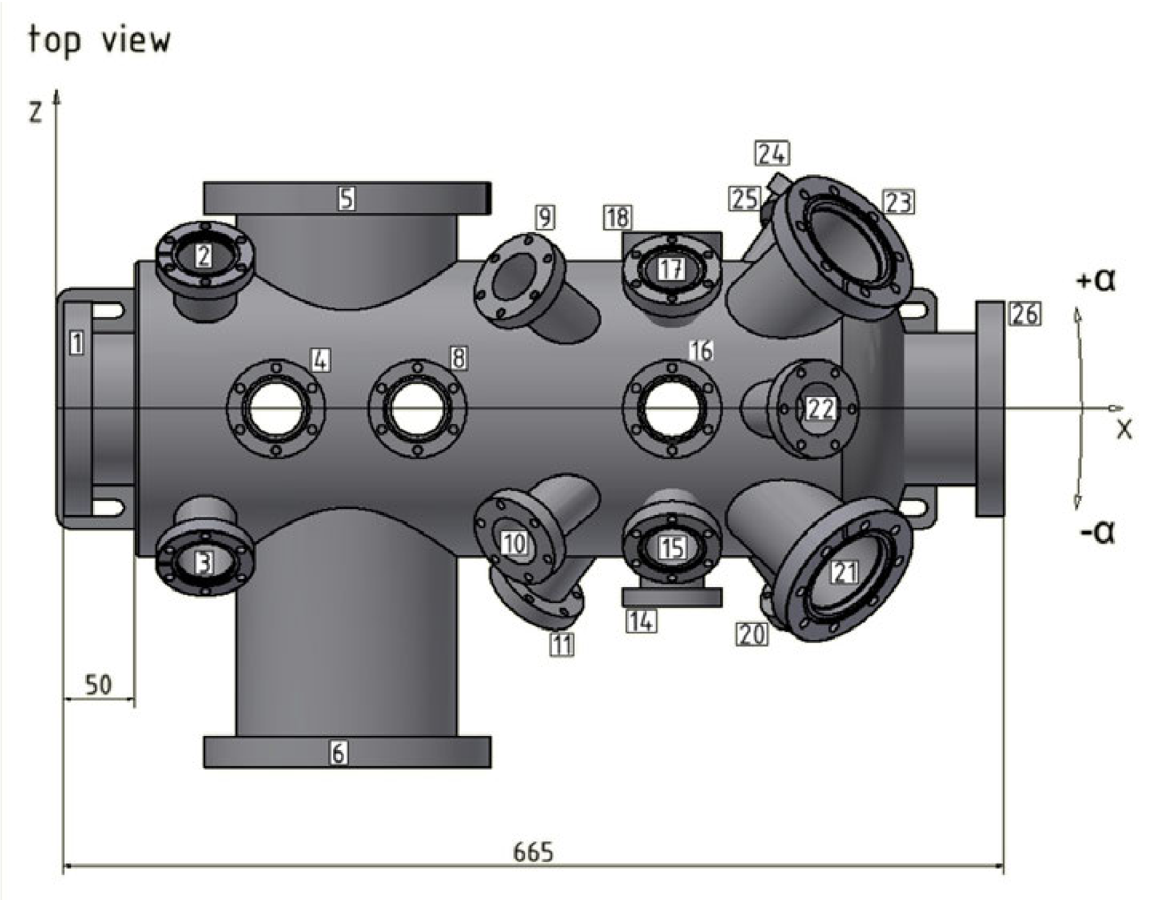

Figure 8.6: Top view of the preparation chamber. The numbers in the white boxes indicate the IDs of the flanges (see Table 8.1). Dimensions are given in millimeters. Drawing by Bernd Kreß.

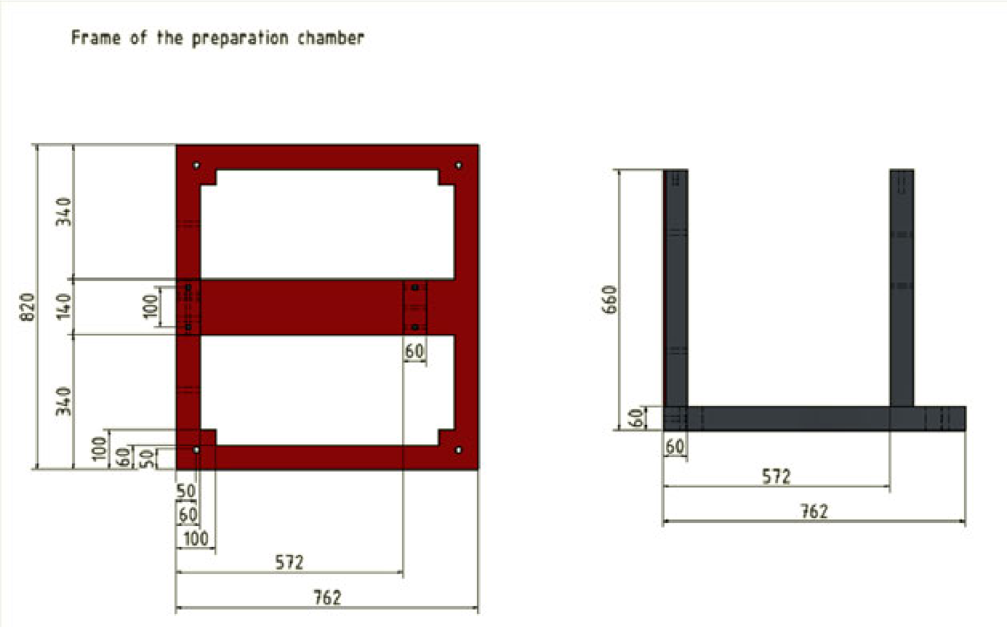

Figure 8.7: Drawing of the preparation chamber frame. Dimensions are given in millimeters. Drawing by Bernd Kreß.

Table 8.1: Flange overview for the preparation chamber. The flange IDs are indicated in Figures 8.3, 8.5 and 8.6. The angles and axes are defined in Figures 8.3 and 8.6.

ID	size static/rot.	flange length / mm	distance / mm	angle α / °	angle β / °	use
1	DN100 CF-R	0	0			connection analysis chamber
2	DN40 CF-S	140 to axis	X+100	90	45	ionization gauge
3	DN40 CF-S	140 to axis	X+100	-90	45	reserve
4	DN40 CF-R	140 to axis	X+150	0	90	sputter gun
5	DN160 CF-S	160 to axis	X+200	90	0	window
6	DN160 CF-S	254 to axis	X+200	-90	0	LEED
7	DN160 CF-S	203 to axis	X+200	0	-90	turbomolecular pump
8	DN40 CF-R	140 to axis	X+250	0	90	gas dosing
9	DN40 CF-R	190 to sample	X+430	140	40	(future) metal evaporator
10	DN40 CF-R	190 to sample	X+430	-140	40	(future) metal evaporator
11	DN40 CF-R	190 to sample	X+430	-143	-30	(future) IL evaporator
12	DN100 CF-S	170 to sample	X+430	0	-90	ion getter pump and TSP
13	DN40 CF-R	140 to sample	X+430	-90	-45	reserve
14	DN40 CF-R	140 to sample	X+430	-90	0	load lock
15	DN40 CF-R	140 to sample	X+430	-90	45	microbalance
16	DN40 CF-S	125 to sample	X+430	0	90	sample garage
17	DN40 CF-R	140 to sample	X+430	90	45	window
18	DN40 CF-S	125 to sample	X+430	90	0	wobble stick
19	DN40 CF-R	140 to sample	X+430	90	-45	IL evaporator
20	DN40 CF-R	190 to sample	X+430	-53	-30	(future) organic evaporator
21	DN63 CF-S	203 to sample	X+430	40	30	window
22	DN40 CF-S	180 to sample	X+430	0	55	(future) QMS
23	DN63 CF-S	203 to sample	X+430	40	30	window
24	DN40 CF-R	180 to sample	X+430	55	0	(future) microbalance
25	DN40 CF-R	190 to sample	X+430	53	-30	(future) organic evaporator
26	DN100 CF-R	80 to chamber	X+695			connection manipulator

8.5.2 Analysis Chamber

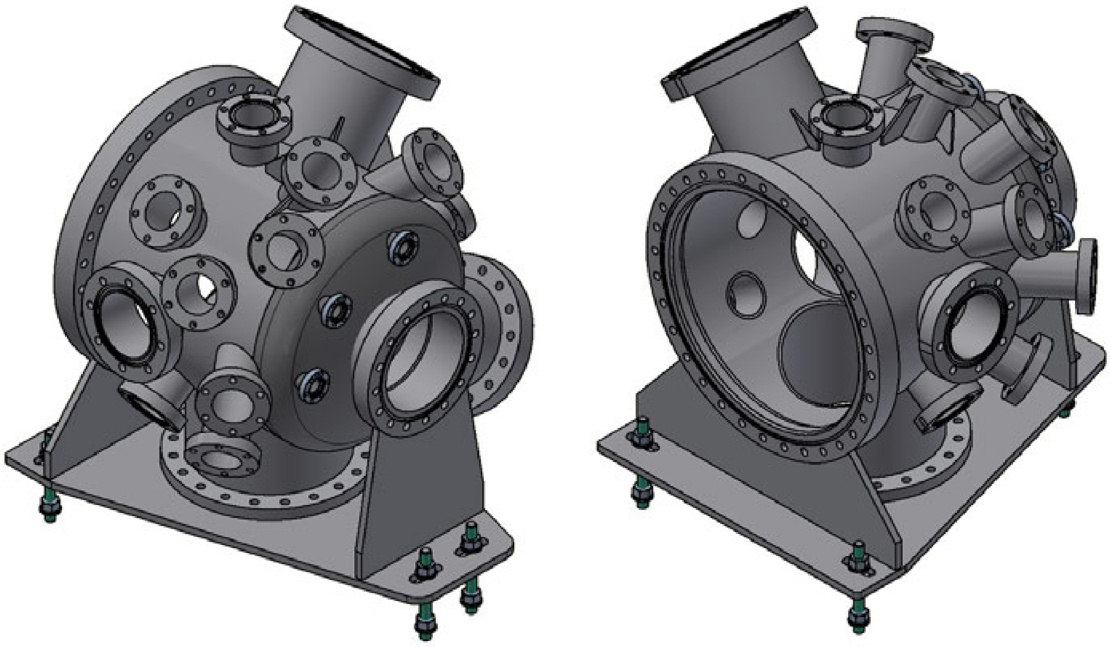

Figure 8.8: 3D drawings of the analysis chamber. Drawings by Bernd Kreß.

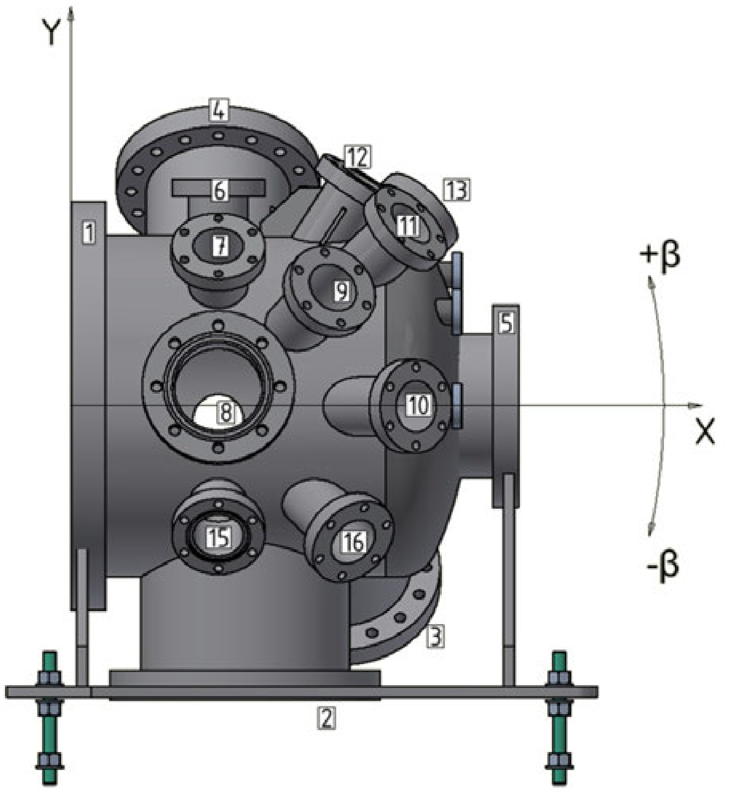

Figure 8.9: Front view of the analysis chamber. The numbers in the white boxes indicate the IDs of the flanges (see Table 8.2). Drawing by Bernd Kreß.

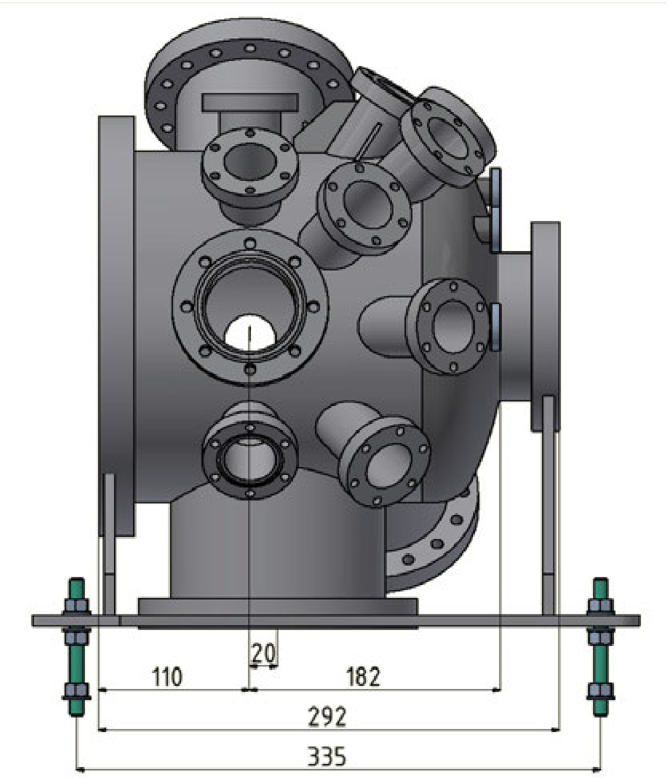

Figure 8.10: Sectional view of the analysis chamber. Dimensions are given in millimeters. Drawing by Bernd Kreß.

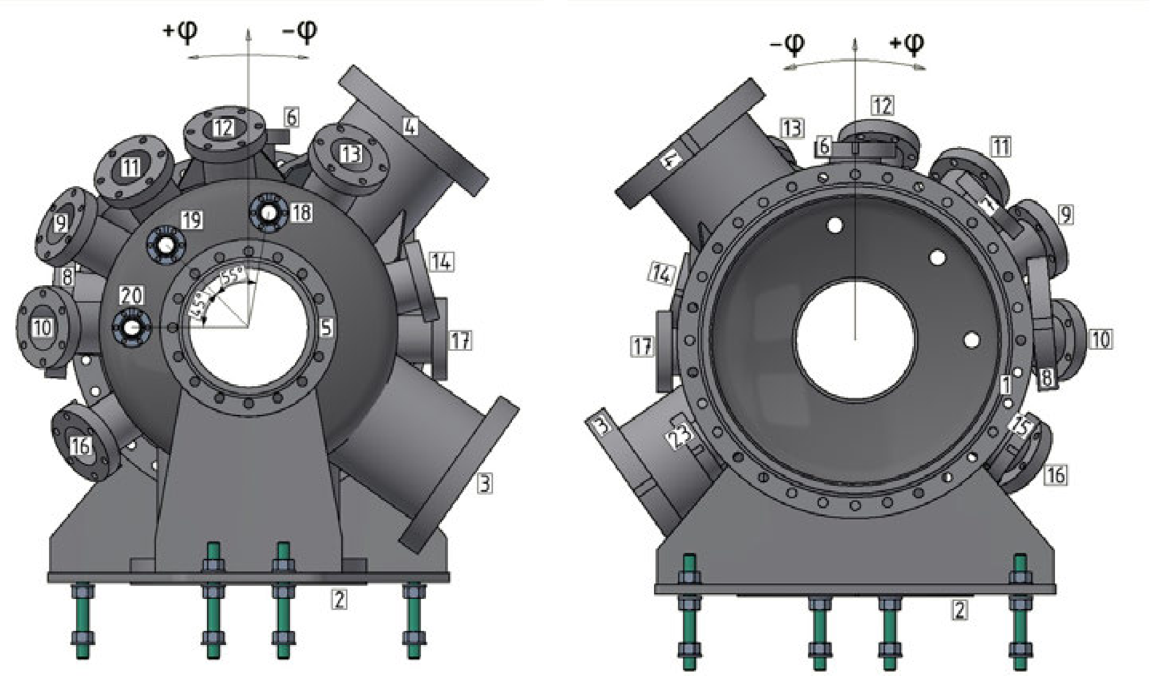

Figure 8.11: View of the analysis chamber from the side of the preparation chamber (left) and mass spectrometer (right). Compare also to Figure 3.1d. The numbers in the white boxes indicate the IDs of the flanges (see Table 8.2). Drawings by Bernd Kreß.

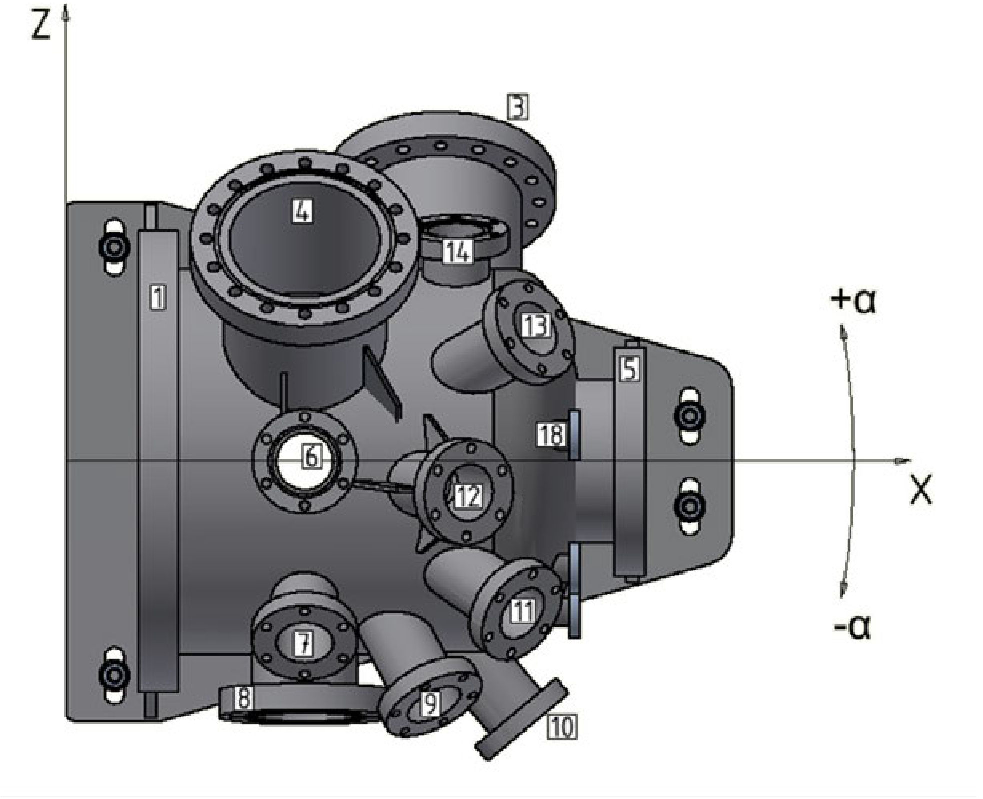

Figure 8.12: Top view of the analysis chamber. The numbers in the white boxes indicate the IDs of the flanges (see Table 8.2). Drawing by Bernd Kreß.

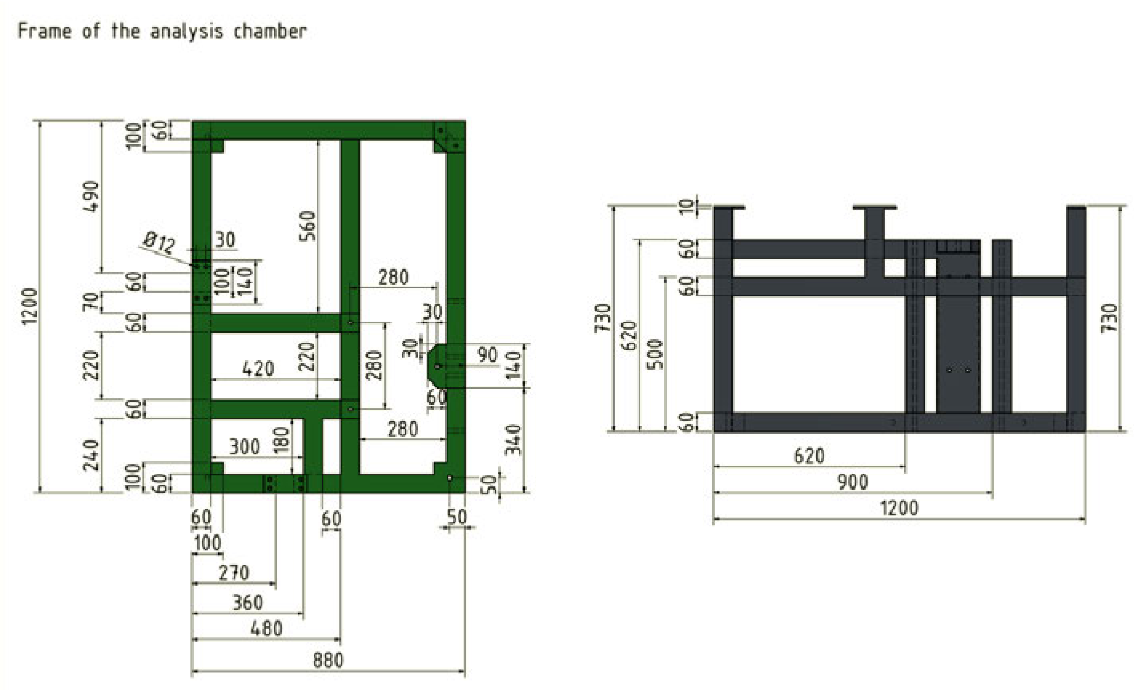

Figure 8.13: Drawing of the analysis chamber frame. Dimensions are given in millimeters. Drawing by Bernd Kreß.

Table 8.2: Flange overview for the analysis chamber. The flange IDs are indicated in Figures 8.9, 8.11 and 8.12. The angles and axes are defined in Figures 8.9, 8.11 and 8.12.

ID	size static/rot.	flange length / mm	distance / mm	angle α / °	angle β / °	use
1	DN250 CF-S		0	0		differentially pumped rotary feedthrough mass spectrometer
2	DN160 CF-S	220 to axis	X+130	90	-90	turbomolecular pump
3	DN100 CF-S	230 to axis	X+200	90	-35	ion getter pump and TSP
4	DN100 CF-S	230 to sample	X+110	90	40	analyzer
5	DN100 CF-R	70 from corpus	X+335	0	0	preparation chamber
6	DN40 CF-R	170 to sample	X+110	0	90	molecular beam
7	DN40 CF-R	170 to sample	X+110	-90	45	window with camera
8	DN63 CF-R	170 to sample	X+110	-90	5	window
9	DN40 CF-R	203 to sample	X+110	-62	26	(future) flood gun
10	DN40 CF-R	230 to sample	X+110	-50	0	X-ray bypass
11	DN40 CF-R	223 to sample	X+110	-35	38	(future) evaporator
12	DN40 CF-R	203 to sample	X+110	-10.72	57	X-Ray gun
13	DN40 CF-R	223 to sample	X+110	35	38	(future) evaporator
14	DN40 CF-S	160 to sample	X+210	90	15	ionization gauge
15	DN40 CF-R	170 to sample	X+110	-90	-35	(future) evaporator
16	DN40 CF-R	203 to sample	X+110	-55	-30	reserve
17	DN40 CF-R	170	X+110 Y-10	90	0	beam monitor
				angle ϕ / °		
18	DN16 CF-R	17 from corpus	X+292 on Ø200	-10		sample flag
19	DN16 CF-S	17 from corpus	X+292 on Ø200	+45		reserve
20	DN16 CF-S	17 from corpus	X+292 on Ø200	+90		gas dosing
23	DN40 CF-S	170 from corpus	X+70	90	-35	(future) shutter for QMS

8.5.3 Molecular Beam Chamber

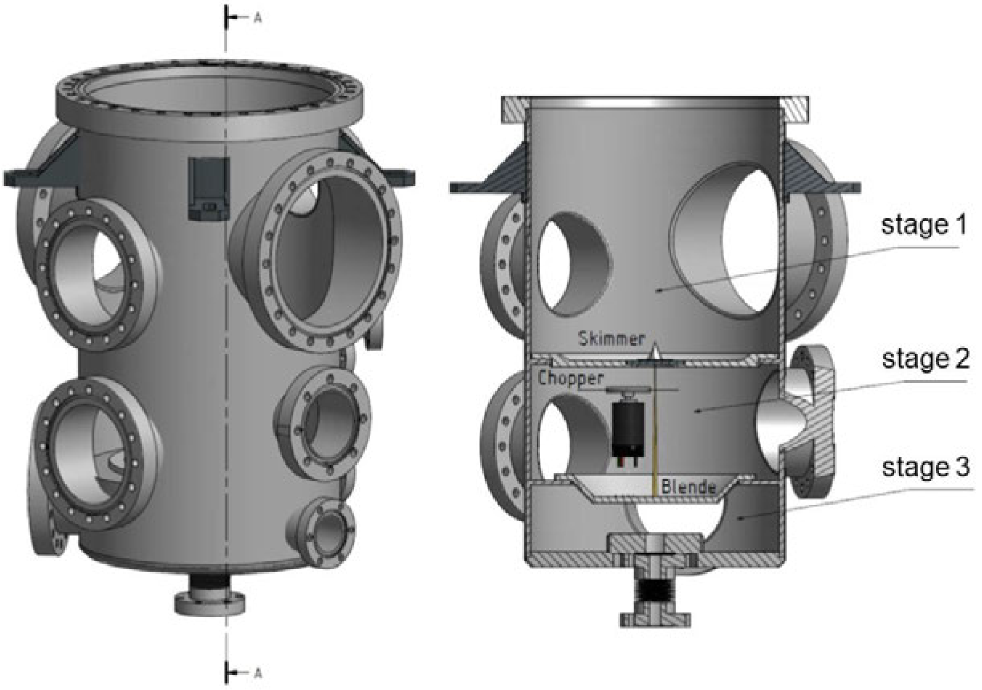

Figure 8.14: 3D drawing and cut through of the molecular beam chamber. Note that the chopper shown on the right side is not mounted so far. Drawings by Bernd Kreß.

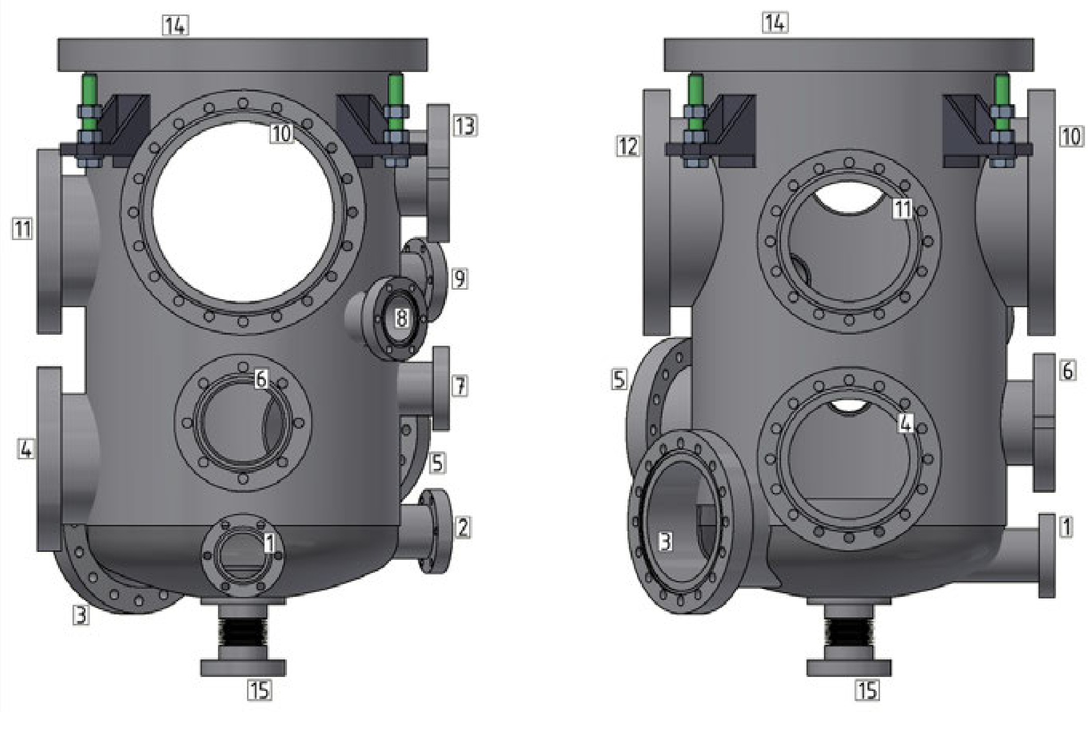

Figure 8.15: Side views of the molecular beam chamber. The numbers in the white boxes indicate the IDs of the flanges (see Table 8.3). Drawings by Bernd Kreß.

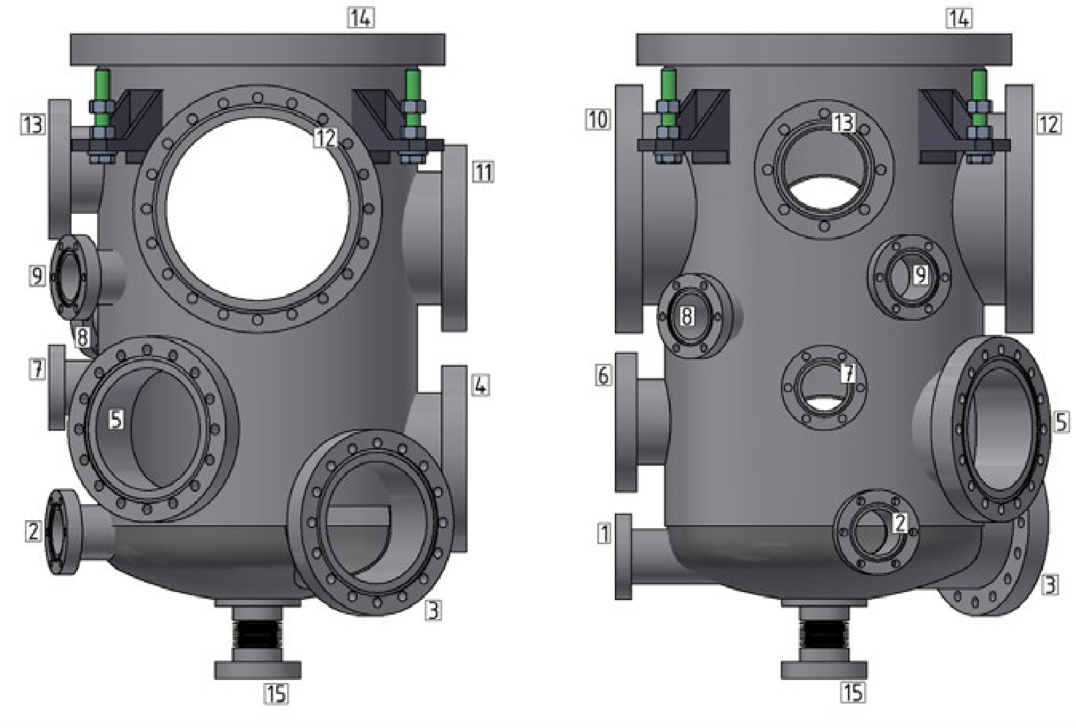

Figure 8.16: Side views of the molecular beam chamber. The numbers in the white boxes indicate the IDs of the flanges (see Table 8.3). Drawings by Bernd Kreß.

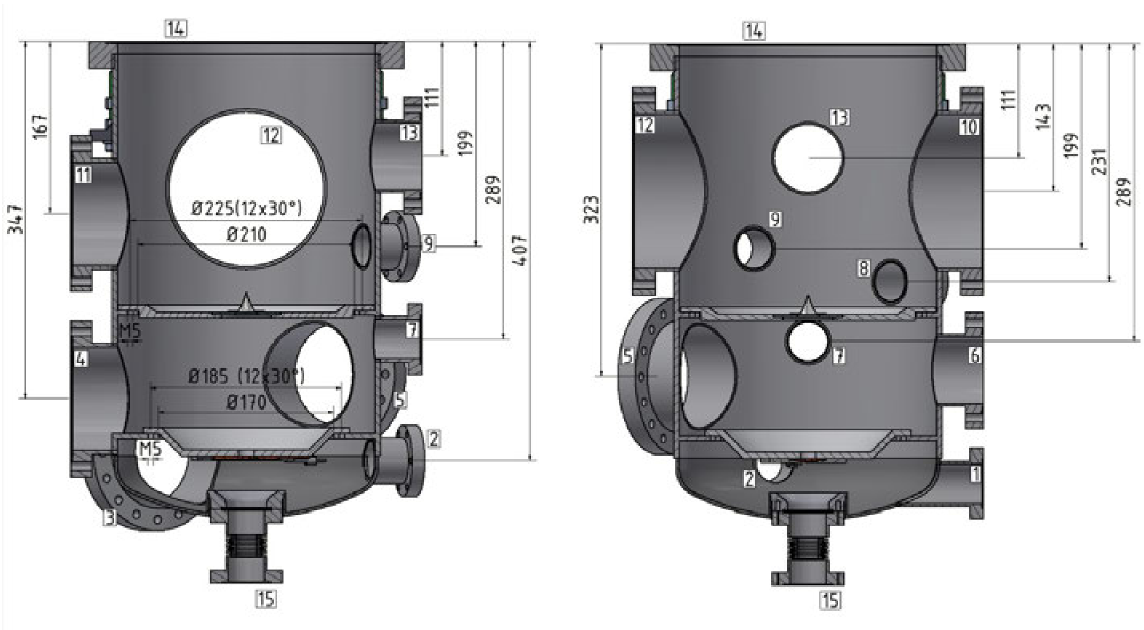

Figure 8.17: Sectional views of the molecular beam chamber. The numbers in the white boxes indicate the IDs of the flanges (see Table 8.3). Dimensions are given in millimeters. Drawings by Bernd Kreß.

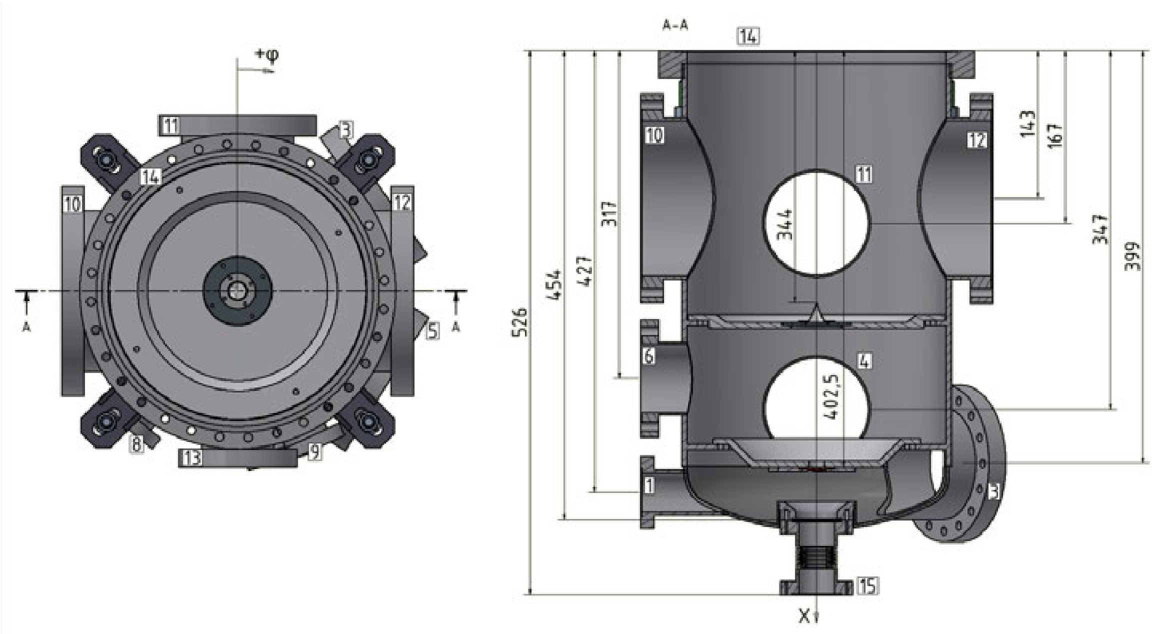

Figure 8.18: Sectional views of the molecular beam chamber. The numbers in the white boxes indicate the IDs of the flanges (see Table 8.3). Dimensions are given in millimeters. Drawings by Bernd Kreß.

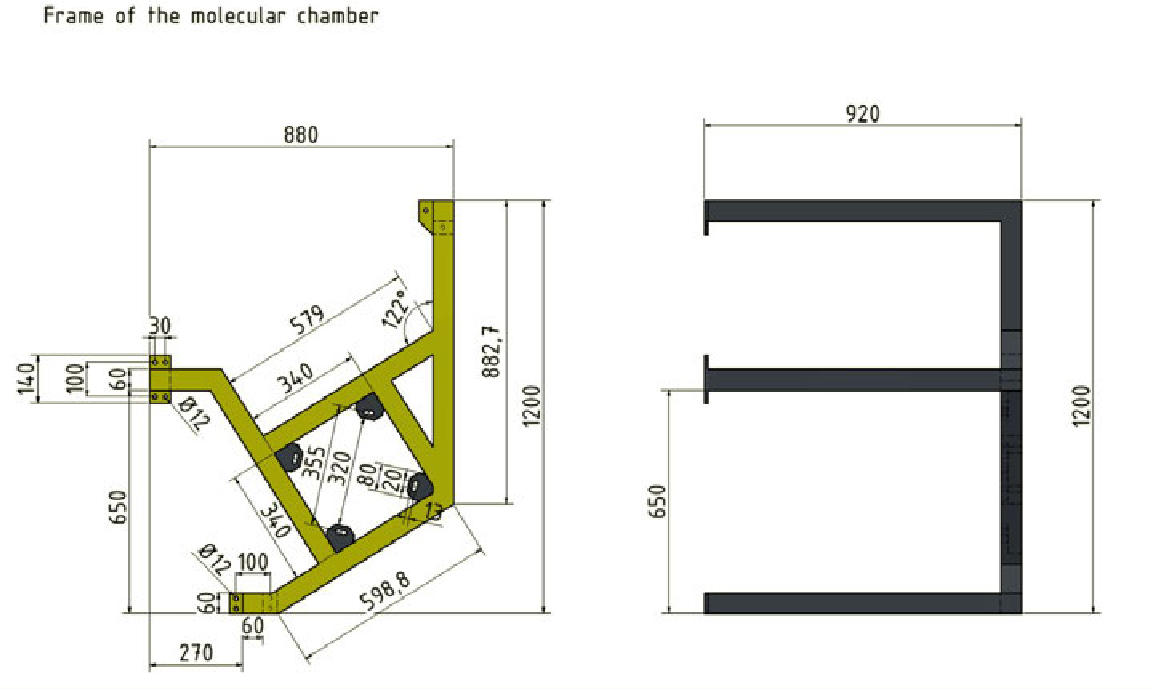

Figure 8.19: Drawing of the molecular beam chamber frame. Dimensions are given in millimeters. Drawing by Bernd Kreß.

Table 8.3: Flange overview for the molecular beam chamber. The flange IDs are indicated in Figures 8.15 to 8.18. The angle and axis are defined in Figures 8.18.

ID	size static/rot.	flange length / mm	distance / mm	angle φ / °	use
1	DN40 CF-R	170 to axis	X+427	270	ionization gauge
2	DN40 CF-S	170 to axis	X+407	165	aperture
3	DN100 CF-S	170 to axis	X+399	55	turbo HiPace 300
4	DN100 CF-R	170 to axis	X+347	0	window (future) chopper
5	DN100 CF-S	170 to axis	X+323	122	turbo HiPace 300
6	DN63 CF-S	170 to axis	X+317	270	ionization gauge
7	DN40 CF-R	170 to axis	X+289	180	beam flag
8	DN40 CF-S	170 to axis	X+231	220	reserve
9	DN40 CF-S	170 to axis	X+199	155	cold cathode gauge
10	DN160 CF-S	170 to axis	X+143	270	turbo HiPace 700
11	DN100 CF-R	170 to axis	X+167	0	window
12	DN160 CF-S	170 to axis	X+143	90	turbo HiPace 700
13	DN63 CF-S	170 to axis	X+111	180	reserve
14	DN250 CF-S	on axis	X+0	on axis	nozzle manipulator
15	DN40 CF-S	on axis	X+526	on axis	connection to the analysis chamber with CF40 bellow

8.5.4 Sample Holder

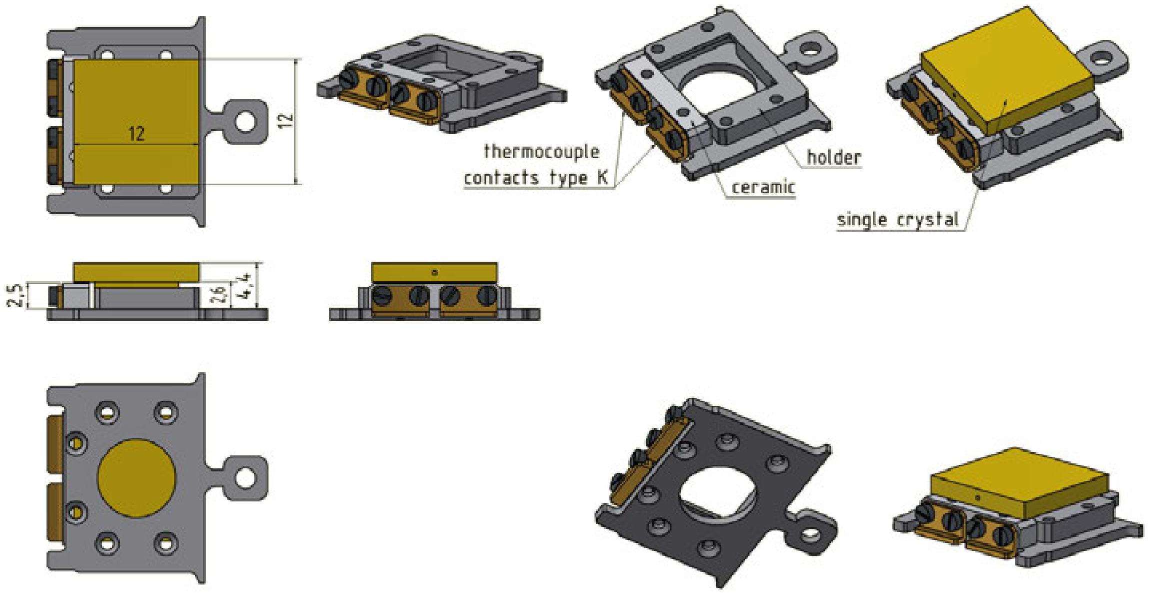

Figure 8.20: Sample holder design. Dimensions are given in millimeters. Drawings by Bernd Kreß.

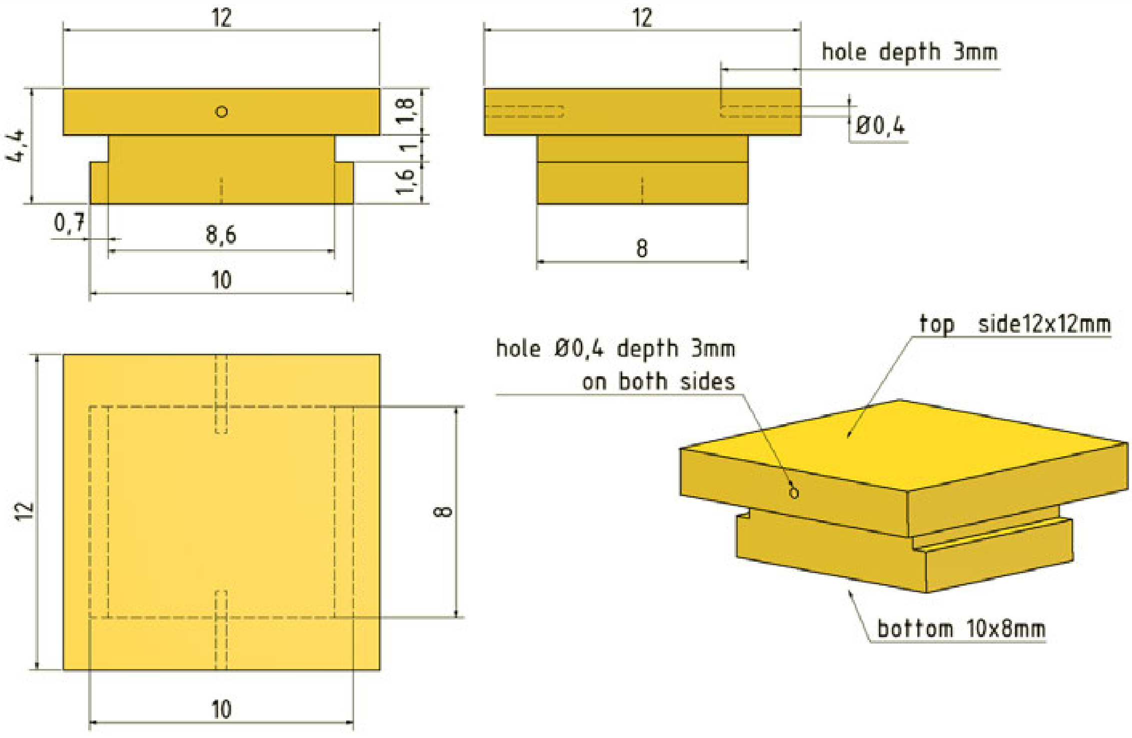

Figure 8.21: Drawings of the single crystals. Dimensions are given in millimeters. Drawings by Bernd Kreß.

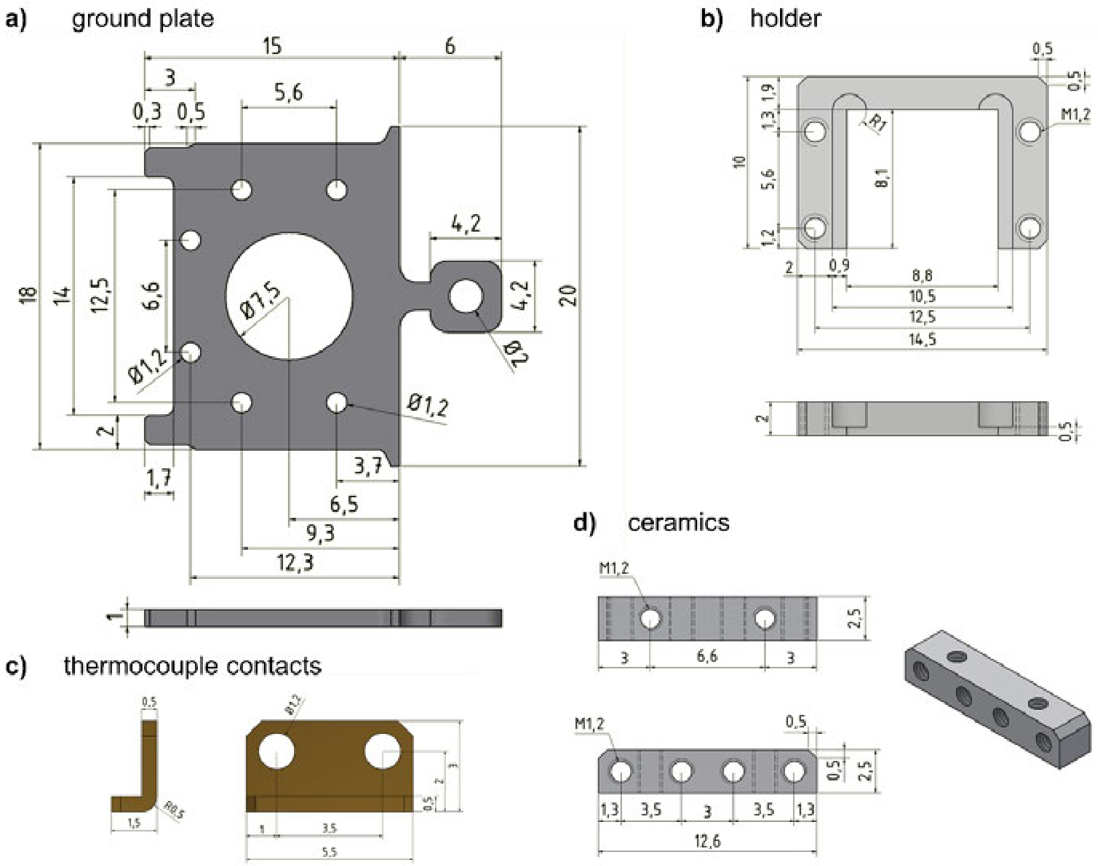

Figure 8.22: Drawings of the sample holder ground plate (**a**), crystal holder (**b**), thermocouple contacts (**c**) and insulating ceramics (**d**). Dimensions are given in millimeters. Drawings by Bernd Kreß.